Kyoto University

Dissertation

FUZZY MARKOV RANDOM FIELDS FOR OPTICAL AND MICROWAVE REMOTE SENSING IMAGE ANALYSIS: SUPER RESOLUTION MAPPING (SRM) AND MULTISOURCE IMAGE CLASSIFICATION (MIC)

Author
Duminda Ranganath Welikanna

Supervisor
Prof. Masayuki Tamura

Geoinformatics
Department of Civil and Earth Resources Engineering

2014

FUZZY MARKOV RANDOM FIELDS FOR OPTICAL AND MICROWAVE REMOTE SENSING IMAGE ANALYSIS: SUPER RESOLUTION MAPPING (SRM) AND MULTISOURCE IMAGE CLASSIFICATION (MIC)

BY

Duminda Ranganath Welikanna

A thesis submitted in partial fulfillment of the requirements for the degree of Doctor of Philosophy

Examination Comitee:	Prof. Masayuki Tamura (Chairperson) Prof. Kenji Tanaka Prof. Juinichi Susaki
Nationality:	Sri Lankan
Previous Degree:	Master of Science (Geoinformatics, Faculty of Geo-information Science and Earth Observation, University of Twente, The Netherlands)
Scholarship Donor:	Japanese Government Monbukagakusho Scholarship

Geoinformatics
Department of Civil and Earth Resources Engineering
Kyoto University, Japan

2014

Abstract

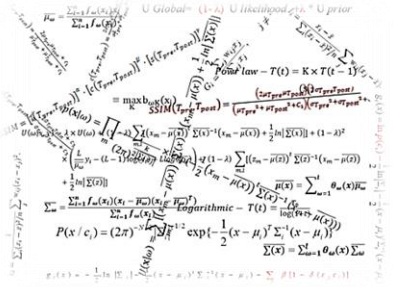

For major remote sensing applications in geographical, geophysical, meteorological and surveillance studies, image data from different sources (ex- Multispectral, Hyperspectral and Microwave) might be available for the user. With the intense developments in remote sensing image analysis techniques in the past few years, different image interpretation techniques are also available for such tasks. Among these techniques developments in the field of Markov Random Fields (MRF) and Fuzzy logic has taken strong interest in remote sensing image segmentation and restoration due to its consistency, capabilities to adopt to single and multisource imagery, quantifying the uncertainties in the results, working in contextual framework and producing super resolution maps. In the history of MRF and fuzzy techniques there has not been a setup to make them work in tandem to utilize both their advantageous.

This work proposes a novel fuzzy parameter integrated MRF models for optical as well as combined optical and microwave remote sensing images analysis. Mainly the thesis discusses in detail the application of fuzzy MRF model for super resolution mapping and multisource image classification. For the super resolution mapping (SRM) task, the study employs Worlview-2 and AVNIR-2 images. Subsequently time series AVNIR-2 images and ALOS PALSAR intensity images with autoregressive texture measures were employed for the multisource feature extraction and restoration task. The thesis details the novel formulation of both these frameworks from conventional Bayesian classification paradigms.

Other than these model formulations for SRM and multisource classification, the thesis brings in several novel and interesting modifications to the fuzzy pixel membership grades determination, energy minimization using simulated annealing and the initial class labelling for the MRF. For the pixel membership grade estimation the study propose spectral angle based class fractional values and the fuzzy c-means estimations. Simulated annealing based optimization was tested using logarithmic and power law combined annealing schemes. Initial class allocation was conducted in two different ways, where for the SRM it was random mixture while for the multisource restoration it was based on the maximum class fraction estimation.

As whole the study in depth discusses the conventional MRF models and the fuzzy integrated MRF models for single source and multisource image feature extraction. It provides the initial experimental setup for the MRF model which reduces the classification uncertainties using fuzzy membership grades and multisource image fusion.

Acknowledgement

*First and foremost I want to deeply thank my supervisor **Professor Masayuki Tamura** for supervising this PhD thesis, and trusting me as a PhD material. I am indebted to him for his encouragement and the understanding and more over the patience extended over me in the difficult times. I am really thankful to you sir.*

Secondly I want to thank my sub supervisors Professor Juinichi Susaki and Professor Yasuto Tachikawa for the great support and supervision throughout this work. My sincere gratitude always extends to Dr. V.A.Tolpekin at the department of Earth Observation Science, ITC, The Netherlands, for introducing me to Markov Random Fields and for the valuable guidance that shaped up my postgraduate studies enormously. I also want to thank Dr. Yogesh Kant and Dr. Jeganathan at the Indian Institute of Remote Sensing for being a great teachers to me.

There are number of individuals I want to extend my deepest appreciation, for standing beside me during this crucial part of my life. Among them especially my friends in Japan Dinesh, Jin, Alex, Menaka , Gayathri nangi and Ruwan ayya should be mentioned. Also all my friends back in Sri lanka who supported me deeply should me mentioned, among them Waruna, Sarath, Chanka, ,Manura, Uditha, Akshi, Bandara ayya, Rami, Derik, Krishanthi will be remembered dearly.

Finally I want to extend my appreciation and love to my family including my younger sister Piumi and brother Manoj Rajapaksha in Melborn, and my aunty Susima and younger brother Lasantha. Last but not least I want to extend my love and deep gratitude to my loving mother Nimala Devi Welikanna and my sister Manuri Welikanna and son Vidun in Toronto, for the love and caring extended towards me during one of the most difficult period of time and to my farther Mahinda Welikanna.

Unity can only be manifested by the Binary. Unity itself and the idea of Unity are already two

-Lord Buddha

Contents

List of Figures

List of Tables

Dedicated to my Loving Ammi. . . . . Gamage Nimala Devi Weliikanna

Kyoto, 2014

1

Introduction

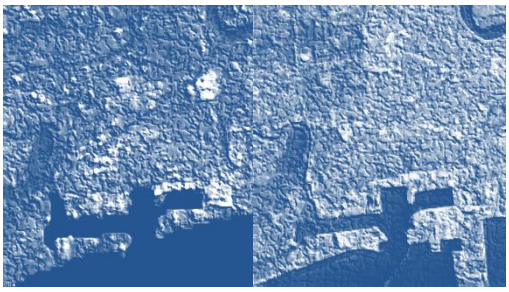

This chapter motivates the scope of this work in terms of the need for better classification mechanisms for the Synthetic Aperture Radar (SAR) images with the use of prior information assisted by the optical satellite data. The work further test the feasibility of incorporating these classification outputs for applications such as change detection and damage analysis in the case of time series satellite information. Development of Markov Random Fields (MRF) and Fuzzy class parameter integrated classification models were the central scope of this work. The study seeks into the profound application of fuzzy random field models for SAR and optical data classification. This proceeds with the challenges of a) defining fuzzy membership grades for each pixel with respect to the interested land cover categories (Especially in heterogeneous urban land scape) b) reforming the class statistical parameters on the base of fuzzy memberships c) definition of prior and likelihood energy using the fuzzy inputs for each land cover class d) performing a combined classification (fusion) using optical, SAR and SAR texture information in a MRF framework e) testing novel optimization mechanism. During the preceding of this work different textural indices generated from the SAR information based on Multiplicative Autoregressive Random Field (MAR) models, Moran's I_i Index, Geary's C_i Index and Getis-Ord G_i Index were tested for their model compatibility with the MRF framework. The chapter ends by setting objectives and research questions to be addressed throughout the rest of the thesis.

1.1 Optical and Microwave remote sensing image analysis over urban land cover

Accurate mapping over urban areas through remote sensing is always a challenging task due to the inherent complexity of the urban land cover with respect to all the other land cover types in concern (ex. shrub lands, savannas, evergreen forests, ice/snow, exposed soil and grass and water). It is important to consider the meaning of urban land cover in a remote sensing perspective with the questions being what is an urban area? How do we know it when we see it? and how do we measure the concept of urban, so that we can study it. "Urban" is a place-based characteristic that incorporates elements of population density, social and economic organization, and the transformation of the natural environment into a built environment. From a material perspective urban areas are composed of four main components: (1) concrete and soils (i.e., minerals),(2) vegetation, (3) oil products such as tar and asphalt, and (4) other

human-made materials such as refined oil products like paints and plastics (Rashed and Jurgens, 2010). Remote sensing has become the major technique to estimate the major urban land cover components such as vegetation, impervious surface and soil, (VIS) due to its low cost and convenience for mapping from local to global scales (Wu and Murray, 2003;Wu, 2004). However, there are still some open problems. First, although the VIS-based approaches have achieved success in the past decade by using both linear and non-linear models, the selection of endmember is complicated because of the diversity of impervious features (Weng and Hu, 2008). Second, the influence of seasonal variations on impervious surface estimation is catching more and more attention (Wu and Yuan, 2007; Weng and Hu, 2008). Third, shade is often confused with dark impervious surface materials, while dry soils and sands are often mixed with bright impervious surface materials (Weng et al., 2009). Moreover, in humid areas, optical remote sensing is often affected by the clouds and fails to effectively extract impervious surfaces (Jiang et al., 2009; Yang et al., 2009).

In the case of remote sensing over urban environments, urban land scape not necessarily forms a precise relationship between the actual pattern and the class label. Further it becomes a vague entity due to the rapid change of the land-cover categories within a small region, majority of land-cover types being internally heterogeneous and intermediate conditions of the class boundaries (Forster 1983; Wang 1990; Wood and Foody 1993). These conditions on the ground forms a mix spectral signature within a pixel of a satellite image (Duggin and Robinove 1990; Zhang and Foody 2001). Though the classes are mutually exclusive and discrete in the ground it might not be the case in the image due to the sensor spatial resolution. Remote sensing depends upon measuring the reflection or scattering of incident energy from earth surface features. If the incident energy is in the optical range of wavelengths (visible or near infrared) it is scattered largely by the surface of the materials being imaged. Though there is penetration into a medium such as short wavelengths into water, but by and large the energy received by an optical sensor reflects from surface of the urban area.

Because the wavelength of the microwave energy used in radar remote sensing is so long by comparison to that used in optical sensors , the energy incident of urban surface materials can often penetrates so that scattering can occur from within the medium itself as well as from the surface (Richrads J A, 2009). SAR is able to provide useful information about urban areas as it is sensitive to the geometric characteristics of urban land surfaces (Calabresi 1996; Henderson and Xia 1997; Leinenkugel et al., 2011; Soergel, 2010; Tison et al., 2004; Zhang et al., 2012), and thus SAR has been identified as an important source to help extract urban land cover especially the impervious surface with optical data (Jiang et al., 2009; Weng 2012; Yang et al., 2009). To deal with these challenges, integrating multiple data sources (e.g., optical, SAR and even Hyperspectral data) and work with contextual approaches such as MRF and address the vagueness of urban land cover classes with fuzzy approaches should be tested. A cross section of the urban remote sensing application is shown in Fig. 1.1.Both multispectral and SAR image properties and their relation for urban feature extraction is very useful in their own respective.

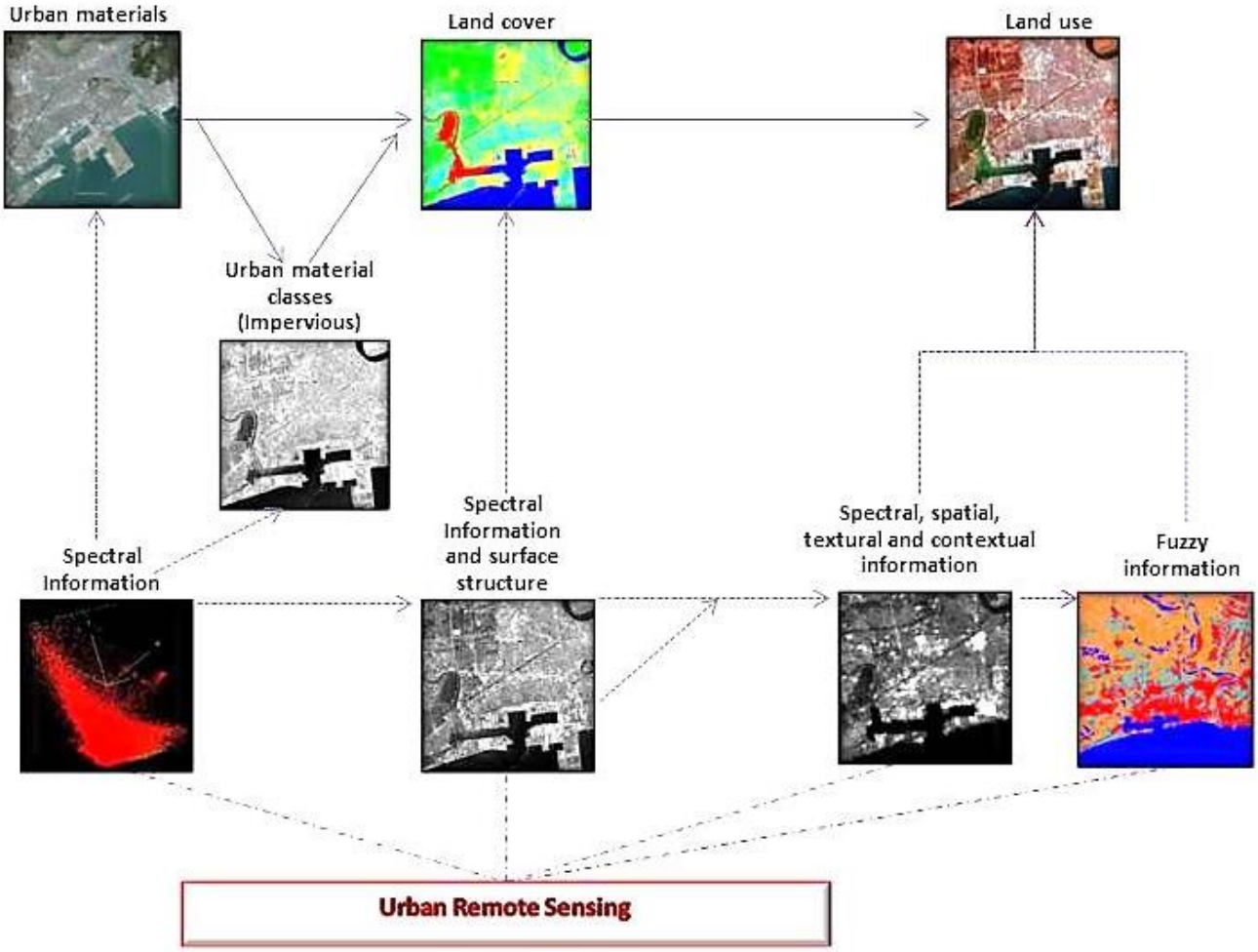

Figure 1.1 Illustration of the relationship among remote sensing of urban materials, land cover and land use (Weng, 2012)

1.2 Uncertainty in image analysis: need for context base fuzzy classification mechanisms for urban land cover

Due to the affinity of remotely sensed image pixels with different information classes, fuzziness or uncertainty can cause problems in the image classification process. Traditional classification processes such as k-means clustering approaches or the parallelepiped classifiers cannot significantly address these issues (Tso & Maher, 2009). Mixed pixels occur in both optical and SAR images. The pixel resolution is the major parameter that determines the amount of the mixed land-cover components recoded within a single pixel (Zhang and Foody 2001). This is very much obvious for pixels of the optical satellite data. In many cases this brings fuzziness or the uncertainty into the image in the form of mixed pixels (Bastin *et al*. 2002; Fisher 2010, Fisher *et al*. 2006). The conventional classification methods force this mixed pixels to get classified into a single class. Owing to these complexities many previous studies have highlighted the importance of dealing a pixel as a mixed element (Fisher 1997; Foody 1997).

Fuzzy set theories have been used extensively to address this imprecise class information in a mixel (pixel comprising mixed land cover categories) (Maselli *et al*. 1995; Zadeh, 1965). Although it should be noted that fuzzy parameter integrated classification schemes does not fully resolves the problem of class mixtures within the pixel, it provides more appropriate definition for vague land-cover classes recorded at a particular sensor spatial resolution (Fisher and Pathirana 1990). In many classification schemes defining an accurate relationship between the features in the feature space and the class labels is very important (Tso and Mather 2009). When this relationship takes the form of one-to-many a fuzzy classification output can be expected. The heavy spectral and spatial overlap of the land-cover classes also adds difficulties to their interpretation. Hence it is important to consider both the spectral and spatial dependencies to correctly classify a pixel. MRF have been potentially identified in remote sensing image classification with promising results, mainly due to its ability to integrate the contextual based information in to the classification scheme (Kasetkasem *et al*. 2005; Solberg *et al*. 1996). This practical applicability of MRF has been made possible by the equivalence between MRF and Gibbs distribution, established by the Hammersley-Clifford theorem (Li 2009; Tso and Mather 2009). This provides a convenient framework to determine the joint prior probability for the pixel labelling problem.

1.3 Interest in combining Fuzzy and Markov Random Field approaches for remote sensing image analysis

The integration of fuzzy class parameters in the MRF model brings significant novelty to the conventional approach. Addressing the vagueness of land cover interpretations within the MRF model make it more appealing in the classification process. So far very few studies have considered this setup (Tolpekin and Hamm, 2008). One of the main applications of the MRF is to produce higher resolution land-cover maps also called SRM (Super Resolution Mapping) from coarser resolution satellite images (Kasetkasem *et al*. 2005; Welikanna *et al*. 2008; Welikanna *et al*. 2012). Moreover MRF models have been widely used to resolve many of the vision problems including image restoration and segmentation, edge detection, texture analysis, data-fusion and change detection (Ardila *et al*. 2011; Dubes *et al*. 1990; Kasetkasem and Varshney 2002; Xu *et al*. 2011). SRM is relatively new in the field of remote sensing, especially for microwave remote sensing images. Available SRM algorithms in the past decade have been comprehensively reviewed to classify them on the basis of their accuracies (Atkinson 2009). Two key significant issues to consider are the estimation of the uncertainty inherent in SRM through model based approaches and the designing of a super-resolution inter-comparison study. This is important mainly because most of these algorithms did not correctly identifying the sub-pixel belongingness to a particular class and the existing SRM algorithms were not validated against each other (Atkinson 2009). Type-2 fuzzy sets have also been proposed to address higher order vagueness in land cover classes (Fisher 2010; Melin and Castilo, 2013), over type-1where uncertainty is represented by numbers in the range [0, 1] (see section 3.3. for definitions). Uncertainty is an attribute of information but it is not reasonable to use accurate membership functions to represent it. Therefor a type 2 fuzzy set can be used to address this issue. The basic difference between these two types of fuzzy sets is associated with the nature of the membership function. In the type-2 case a series of memberships for a specific pixel value with different weighting results. Fuzzy classification (FCM classifier which is controlled by the number of classes in concern and the fuzziness parameter) outcome for different values of fuzziness provide a distribution of alternative type-1 fuzzy memberships, which can be viewed collectively as an instance of a type-2 fuzzy set. Application of type-2 fuzzy sets for change detection and differential weighting in the fuzzification process needs further investigation (Melin and Castilo, 2013).

Recent efforts have been made to use the concepts of MRF based SRM and fuzzy changes to identify and monitor changes in urban trees (Ardila *et al*. 2011; Ardila *et al*. 2012). MRF based SRM methods proved to be effective in detecting urban trees from high resolution satellite images with their energy function formulated using spatial smoothness prior and conditional probabilities. Change detection approaches accounting for the fuzziness of tree crowns, using fuzzy membership images obtained from soft-classifier have been developed for urban areas. Due to the fuzzy nature of the details in remote sensing images, mixture models and MRF was used recently for unsupervised image clustering (Hou et al. 2011). A novel potential function involving the pixel intensity differences and the spatial distance between pixels in a neighborhood clique was proposed in this study. Further the FCM and max entropy criterion were also employed for initial clustering. The results suggested that the method is superior to the traditional MRF model based remote sensing image clustering. MRF technique was developed using class descriptive statistics in the form of conventional class mean and covariance to model their probability density functions. The conventional class mean vectors and covariance matrices are calculated using training pixels that assume to represent a single class (one pixel one class). This definition neglects the training pixels proportional contribution to a particular class. In contrast to conventional method a fuzzy supervised classification method using fuzzy mean and the fuzzy covariance for each land cover class of interest, shows the determination of a pixel relation to a land-cover class by the means of membership grades enabling more accurate statistical parameter determination for the classification scheme (Wang 1990). The importance of identifying the mixel and using the membership grades to utilize more of its spectral information in the classification scheme is highlighted and promoted in this study. In another effort, fully-fuzzy supervised classifications with statistical (modified fuzzy C-mean clustering algorithm) and neural network based classifiers have been tested with improved classification results (Zhang and Foody 2001). Indicator Kriging based interpolation was implemented in this study to estimate the class membership grades for the training pixels. Fuzzy parameter integrated Spectral Mixture Analysis (SMA) classification technique was also tested in another study consistently (Tang *et al*. 2007). It went on to show the improvement achieved in the classification with respect to the MLC, linear SMA and partial fuzzy methods. Much of this work resulted in improving the technique and they went on to show the importance of dealing with fuzzy land cover information within an MRF framework. Furthermore these efforts lead to deeper understanding of the performance of MRF and parameter estimation for different image configurations. As a whole the amount of work done to integrate fuzzy class descriptions in the MRF based SRM scheme recently is very limited and not a very convincing one.

1.4 Problem statement

The most investigated source of uncertainty in the remote sensing process is that of the land cover classification algorithm. The term accuracy is generally used to express the degree of correctness of a classification map. Depending on the optical and microwave data input to the classification scheme with their different image properties and model parameter estimation this accuracy can vary. This is due to the varying degree of classification error with respect to the discrepancy between what is predicted on the image and what can be found on the ground (Foody and Atkinson, 2002; Richards and Jia, 2006). Hence it is important to develop procedure to reduce the uncertainty and to communicate the uncertainty of the predictions and the errors to the end user. Finding the best classification procedure for SAR image and texture features have always been a challenging task and a topic of future research (Solberg and Jain, 1997). In this case the main difficulties to research on is the development of a complete model that can

use multisource data (ex- optical and SAR) incorporating original image information as well as different indices such as texture and also to seek for the advantageous of contextual approaches.

1.5 Main objective

The main objective of the study is to find how to integrate fuzzy class parameter within an MRF framework to model the objective functions for individual optical and microwave satellite images as well as in a fusion to minimize the uncertainty of the patterns and to perform an optimum classification scheme. Further several textural indices delineated from microwave images were also tested for time series change analysis.

1.6 Areas of interest and focus of the PhD

The study focuses and addresses several research areas of image analysis and computer vision. Though the areas are wider in its own discipline the author tries to point out the possibilities of working in a common domain incorporating them all for novel and efficient classification mechanism. All the image processing operations discussed in this thesis are spatial contextual operations, the uncertainties of the vague land cover classes were addressed using fuzzy definitions within an MRF as an extension of the ordinary MRF framework, textural descriptors in addition to the original image information were also tested within the classification scheme and Gaussian, lognormal, Gibbs and Gamma distributions were used within the MRF framework for classification process. Key terms related to remote sensing and Geo-statistics discussed and focused under the experiments conducted in this PhD work are as follows.

- Urban land cover
- Super Resolution Mapping
- Spatial Context
- MRF
- Uncertainty
- Fuzzy logic
- SAR and Optical data
- SAR Texture
- Time series analysis of texture
- Gaussian, Lognormal, Gibbs and Gamma distributions

1.7 Research questions?

Based on the objective of the work presented in this study, several important research questions were identified and answered. The findings based on these questions will bring clarity and further understanding to current research community work in the field of image classification and fusion using MRF models and multisource data.

1. What are the statistical similarities and dissimilarities in the class conditional distributions for both optical and SAR images?
2. What are the methods available to measure the fuzzy class membership grades for multisource satellite image pixels?
3. How can we model the posterior probability distributions separately for both optical and SAR images in an MRF using fuzzy class definitions?

4. What ancillary information (SAR- Texture) is available from SAR imagery, for MRF based parameter estimations and classification?
5. What is the importance of the smoothing parameter in SRM and the sensor reliability factor in multisource fusion model (λ), for the MRF model?
6. How to formulate the combined fuzzy MRF (FMRF) based feature extraction model for the optical and SAR imagery (MIC)?

1.8 General flow of the work

The general flow chart shown in Fig. 1.2, gives a quick look into the overall set up of this study. The Bayesian framework discussed in the flow chart contains two main components; those are the prior and the likelihood energy that holds the central base of the classification. The modelling of these two components has to be done in a controlled environment. Several main parameters have to be identified and defined to model these two energy functions. These parameters have to be defined carefully considering the respective pixel distribution of the optical and SAR information, the noise levels and the level of details required by the end user from the classification.

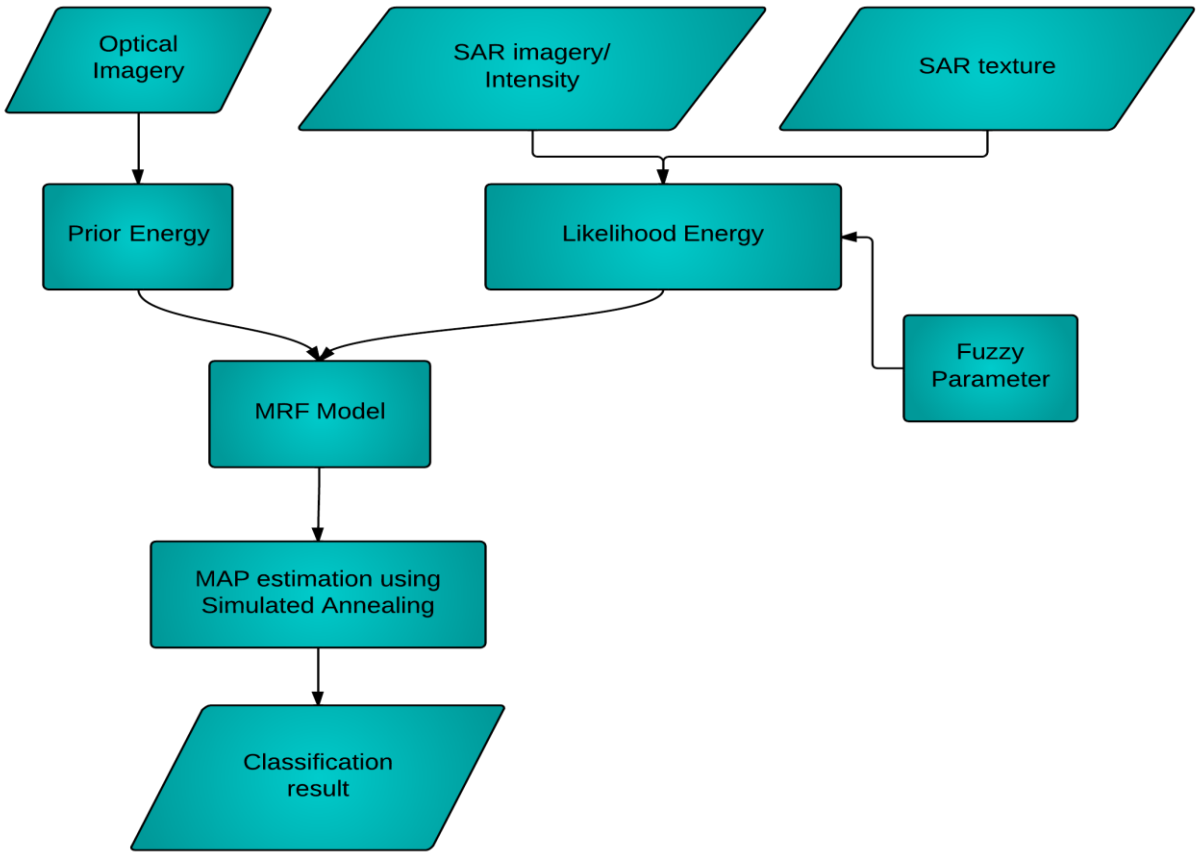

Figure 1.2 A general work flow proposed and tested in the study for the multisource image classification. A detailed flow chart follows in chapter 4

The MRF framework proposed in this study is significantly sensitive to the class parameter estimations. A considerable amount of freedom can be yielded by incorporating the fuzzy class parameters within a MRF frame work for the class training sample section. As a major improvement we discuss this inclusion in detail with relevant experiments within this study. Especially for the SAR data, the importance of the texture parameters in the classification process is highlighted using texture information in addition to the image information. Several novel texture measures namely the multiplicative autoregressive random field (MAR) based texture measures, and spatial autocorrelation based texture measures (Moran's I_i Index/Geary's C_i Index/ Getis-Ord G_i Index) and their incorporation in the classification process will be introduced in the study for SAR data. A detail description of the modelling of the MRF frame work for multisource data will be given in chapter 5.

1.9 Thesis structure

This thesis is arranged with an idea of giving the reader the best understanding of the MRF and fuzzy image processing methods with their important theoretical developments. The chapter 2 explains the main literate works which lead to the current developments of fuzzy MRF techniques explained in this thesis. Chapter 3 gives the mathematical concepts and the developments directly related to the study. Chapter 4 describes the data used in the study and the preprocessing techniques. These theoretical developments will include the statistical as well as the remote sensing theories closely related to the study. In chapter 5 we present the results while in chapter 6 we perform a detailed discussion, conclusion and the future recommendations.

2

Related work- Scientific Literature

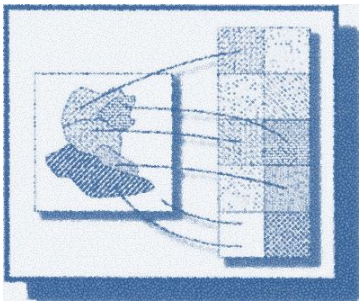

This chapter is dedicated to review the previous scientific work that motivated and promoted the work discussed in this thesis. We brief most of the work well in line with the objective of our work and to highlight the significant importance of MRF based image analysis in remote sensing.

Noncausal spatial interaction models were first introduced by Peter Whittle in his classic 1954 paper. Whittle applied 2D noncausal autoregressive models for representing spatial data and pointed the inconsistency of ordinary least-squares methods for parameter estimation. He then proceeded to derive maximum likelihood estimation techniques and hypothesis testing procedures. In a lesser known paper, Rosanov in 1967, discussed the representation of 2D discrete Gaussian Markov random field (MRF's). The 2D discrete Gaussian MRF models were introduced to the engineering literature in 1972 by John Woods, who used them for 2D spectral analysis. A big impetus to theoretical and practical consideration of 2D spatial interaction models, of which MRF's form a subclass, was given by the seminal works of Julian Besag. Since the early 1980s, MRF's have dominated the field of image processing, image analysis and computer vision.

-Rama Chellappa, june2, 2008 Maryland-

Bayesian theory and its applications had a profound influence on statistical modeling. The two key elements in a Bayesian classification formulae is the modelling of the prior and conditional probability density functions (PDF). By combining these functions a classification can be expressed in terms of maximum a posterior (MAP) criteria (Mather, 2009). A detail discussion about this can be found in

Chapter 3. The overall setup of such a frame work is given in Fig. 2.1. One of the main problems associated with such a setup is that prior information or information concerning the data distribution for the remotely sensed images might not be available. In such circumstances when the information of the data distribution is available but not the prior information a maximum likelihood criterion (ML) can be used. On the other hand depending on the images in concern (ex- Synthetic Aperture Radar (SAR)), modeling the certain data distribution within the Bayesian framework is also a challenging task. In a case where the knowledge about the data distribution is missing, maximum entropy criterion can be employed (Jaynes, 1982). In remotely sensed image classification the widely adopted maximum likelihood criterion generally uses the Gaussian distribution to model the class-conditional PDF, while neglecting the prior PDF. Hence it is evident that the use of reasonable assumptions to model the prior probabilities as well as the class conditional PDF in MAP frame work can improve the classification results. One of the solidest assumptions of modeling the prior probability is context. In the reason past there has been increasing interest in the use of contextual classification mechanisms for image analysis (Ardila et al. 2011; Dubes et al. 1990; Kasetkasem and Varshney 2002;Kasetkasem et al. 2005; Solberg et al. 1996; Magnussen et al. 2004; Ling et al.,2010; Atkinson, 2005).

Context is an important element to be considered in the form of spectral, spatial or temporal attributes. The essential use of context can allows the elimination of possible ambiguities, the recovery of missing information, correction of errors and the feasibility to attain different level of spatial details (LOD). The use of contextual information to model the prior PDF in order to interpret remote sensing images is considered to be a reasonable methodology, due to the nature and distribution of the earth surface features imaged by them. It is a well-known fact in spatial sciences that, spatial dependency is the co-variation of properties within geographic space: characteristics at proximal locations appear to be correlated, either positively or negatively. In most cases this yields that pixels within a close region represent the same features than in isolation, ex- pixels classified as soil are likely to be surrounded by pixels of the same class in desert area. With the use of context pixels are not treated in isolation but are considered to have relationship with their neighbors. Thus the relationship between the pixels of interest and its neighbors is treated as being statistically dependent (Tso and Mather, 2009).

The Markov random field is a useful tool for characterizing contextual information and has been widely used in image segmentation and image restoration. A number of very important experiments in this direction can be found in literature (Besag, 1974;Geman and Geman, 1984; Derin and Elliott, 1987; Dubs and Jain, 1989; Dubs and Jain, 1990; Geman and Reynolds, 1992; Magnussen et al., 2004; Tso and Olsen, 2005a). The use of MRF models for linear feature detection has also been tested with satisfactory results (Tupin et al., 1989). Recent efforts for super resolution land cover mapping (SRM) have shown great promise with the use of coarser resolution optical satellite imagery (Kasetkasem et al., 2005, Tolpekin and Stain, 2009, Welikanna et al., 2012). MRF applications for SAR and SAR texture classification and change detection has also been an interesting field of investigation recently (Deng and Clausi, 2004; Yang and Clausi, 2012; Solberg and Jain, 1997; Tso and Mather, 1999).

The practical use of the MRF relies on its relationship to the Gibbs random field (GRF), which provides a tractable way to apply the MRF to deal with context. Moreover, owing to the MRF's local property, the algorithm can be implemented in a highly parallel manner, which makes the MRF a more attractive.

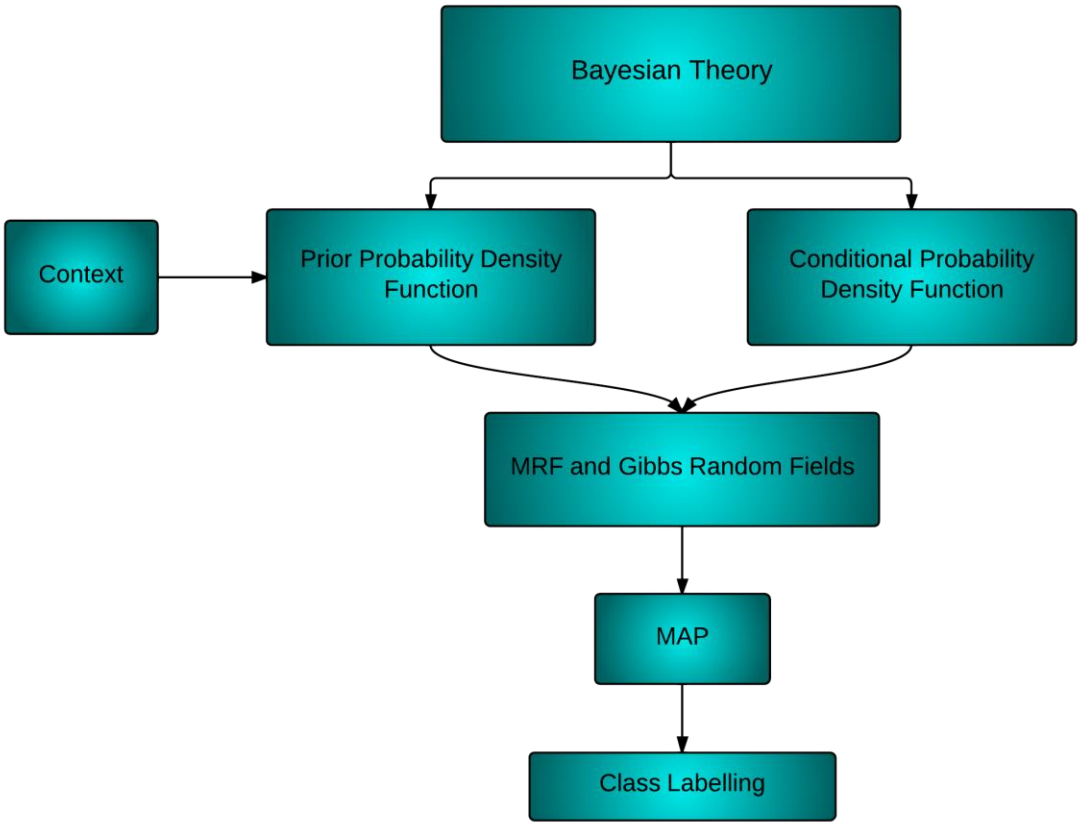

Figure 2.1The MAP MRF framework for a class labeling problem

2.1 Development of the MRF model for Image analysis

The use of MRF models in image analysis or the restoration of degraded images is a branch of digital picture processing with close relevance to image segmentation and boundary finding. Due to the extensive research work conducted in this field numerous models and applications were resulted from the early stages of 1980 (Rosenfeld, 1982). In 1984 *Geman and Geman* (Geman and Geman, 1984) adopted the Bayesian approach with a hieratical stochastic model based on Gibbs distribution and a new restoration algorithm based on stochastic relaxation and annealing to compute the maximum a posteriori (MAP) estimate of the original image given a degraded image. This algorithm exploits the equivalence between Gibbs distribution and Markov Random Fields (MRF). According to this work the stochastic relaxation algorithm developed can be explained in several major sequences.

A local change is made in the image based upon the current values of pixels and boundary elements in the immediate "neighborhood". This change is random and a class label is generated by sampling from a local conditional probability distribution

The local conditional distributions are dependent on a global control parameter *T* called "Temperature". At low temperatures the local conditional distributions concentrate on states that increase the objective function, whereas at high temperatures the distribution is essentially uniform. High temperatures induce a

loose coupling between neighboring pixels and a chaotic appearance to the image. At low temperatures the coupling is tighter and the images appear more regular and smooth.

The image restoration avoids local maxima by beginning at high temperatures where many of the stochastic changes will actually decrease the objective function. As the relaxation proceeds, temperatures are gradually lowered and the process behaves increasingly like iterative improvement. This gradual reduction of temperature simulates "annealing", a procedure by which certain chemical systems can be driven to their low energy, high regular states.

These sequences in detail describe the overall work flow and the major properties of an MRF application in image processing. Importantly the details given in this work describes the main terminologies to understand the MRF modeling which will be detailed later relevant to the objectives of this study (chapter 4). The details provided by *Geman and Geman* regarding the MRF-Gibbs equivalence, layout the fundamental theory to model the joint probability distribution as energy function. This provides a powerful mechanism to model the spatial continuity and other scene features.

In brief the original image was modeled as a pair of pixel intensities (F) and a dual matrix of edge elements (L), X={F,L}. F was referred to as intensity process and L as the line process. A degraded model which allows the noise, blurring and nonlinearities is assumed as G= $\Phi(H(\mathrm{F})) \odot N$ with H being the blurring matrix, Φ being the nonlinearity and N independent noise field with $\odot$ being a suitable additional or multiplication operator. Hence the (F,L) process is conditional on the data G. Let $Z_m = \{(i,j): 1 \leq i,j \leq m\}$ denote the $m \times m$ integer lattice, then $\mathrm{F} = \{F_{i,j}\}, (i,j) \in Z_m$, denotes the gray levels of the original digitized image. These random variables can assume a value f that is $F_{i,j} = f_{i,j}, (i,j) \in Z_m$. F was regarded as a sample realization of a random field, usually isotropic (uniformly in all orientations), homogeneous and with significant correlation well beyond nearest neighbors. F (pixel intensities) was modelled as a MRF with the probability law being a Gibbs distribution. Given a neighborhood system $\mathcal{F} = \{\mathcal{F}_{i,j}, (i,j) \in Z_m\}$, where $\mathcal{F}_{i,j} \subseteq Z_m$ denotes the neighbors of (i,j), an MRF over $(Z_m, \mathcal{F})$ is a stochastic process indexed by Z_m for which for every (i,j) and every f.

$$P(F_{i,j} = f_{i,j} | F_{k,l} = f_{k,l}, (k,l) \neq (i,j)) = P(F_{i,j} = f_{i,j} | F_{k,l} = f_{k,l})(k,l) \in \mathcal{F}_{i,j} \qquad (2.1)$$

Further it means the conditional probability can be modelled using the neighbors of (i,j), $\mathcal{F}_{i,j}$ (local properties). The MRF-Gibbs equivalence provides an explicit formula for the joint probability distribution P(F=f) in terms of an energy function, the choice of which together $\mathcal{F}$, supplies a powerful mechanism for modelling the spatial continuity and other scene features. The relaxation introduced in this study was designed to maximize the conditional probability distribution of (F, L) given data G=g, i.e., find the mode of the posteriori distribution P(X=x|G=g). This form of Bayesian estimation is known as maximum a posterior or MAP estimation or sometimes called as the penalized maximum likelihood which will have greater importance in this study. Under this MAP criterion, the estimation *log* P(G=g|(X=x)+log P(X=x) will be maximized as a function of x, where the second term is called the penalty term. Map estimation is reported to have employed successfully in spatial settings, restoration and particularly for handling general forms of spatial degradation. Importantly the distribution of the degraded model G is not needed to be determined.

The map algorithm which was introduced by "*Geman and Geman*" depends on an annealing schedule which was referred to slow decrease of a parameter called temperature (T) (this corresponds to temperature in physical systems). As T decreases, samples from the posterior distribution are forced towards the minimal energy configurations; these correspond to the mode of the distribution. Roughly this states that if the temperature T(k) employed in executing the k^{th} site replacement (i.e., the k^{th} image in the iteration scheme) satisfies the bound $T(k) \geq \frac{c}{\log(1+k)}$ for every k, where c is a constant independent of *K*, then with probability converging to one , the configurations generated by the algorithm will be those of minimal energy. Put it in another way this is a Markov Chain which converges in distribution to the uniform measure over the minimal energy configuration. It is also reported the difficulty of bringing in the theory of the annealing process in line with the experiments of the process. The changes made for this annealing process in this study and the test results will be discusses broadly in the later sections. The paper went on to discuss the application of MRF theory on the images in a way of graphs and neighborhood system. This realizes how the energy is being calculated for pixels.

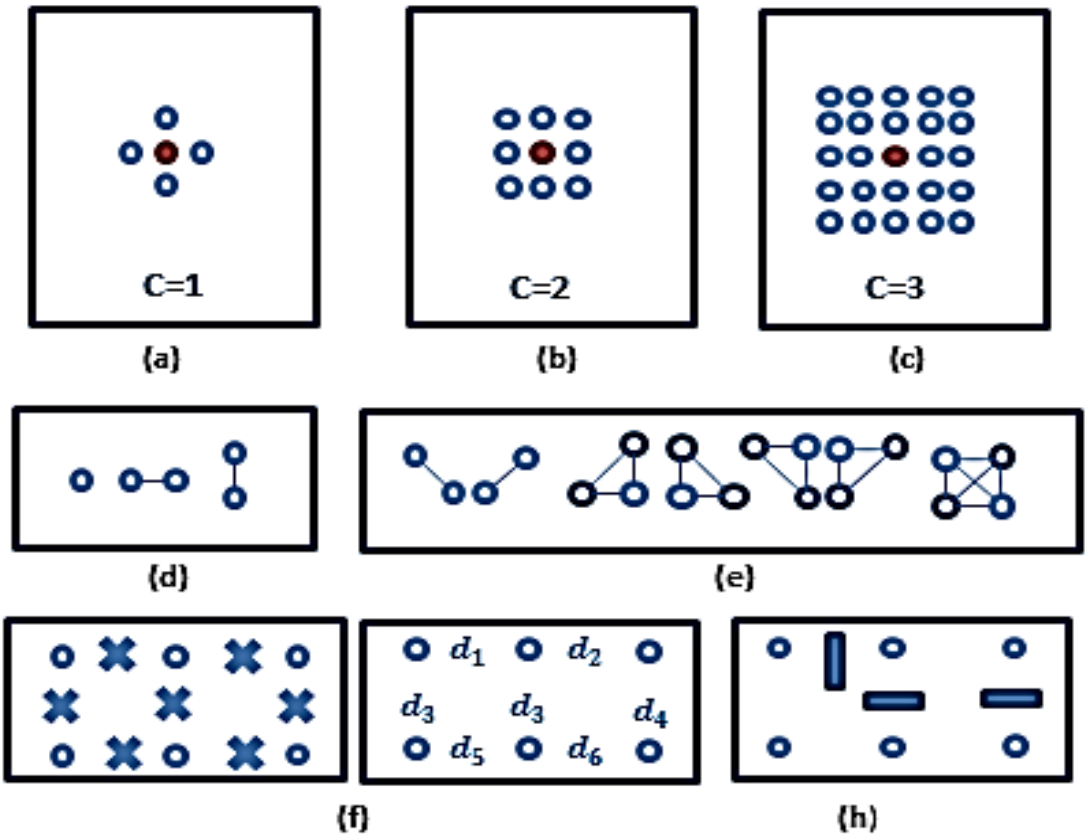

Figure 2.2 Neighborhood systems

The general theory of MRF on graphs was explained using the description of sites (pixels) and cliques (pair of distinct sites). Let S= { $s_1, s_2, \ldots, s_N$ } be a set of sites and let $\mathcal{G} = \{\mathcal{G}_s, s \in S, r \neq s, r$ a different site to $s\}$ be a neighborhood system for S, meaning any collection of subsets of S for which a) $s \notin \mathcal{G}_s$ and b) $s \in \mathcal{G}_r \Leftrightarrow r \in \mathcal{G}_s$. Here $\mathcal{G}_s$ is the set of neighbors of *s* and the pair $\{S, \mathcal{G}\}$ is a graph in the usual way. A subset $C \subseteq S$ is a clique if every pair of distinct sites in C are

neighbors. Several relevant cases can be important to understand the clique's performance. **Case1**. $S = Z_m$ $(m \times m$ interger lattice$)$, this represents the set of pixel sites for the intensity process F; $\{s_1, s_2, \ldots, s_N\}$, $N = m^2$, is any ordering of the lattice points. For a homogeneous neighboring points of the form

$$\mathcal{G} = \mathcal{F}_c = \{\mathcal{F}_{i,j}, (i,j) \in Z_m\}; \mathcal{F}_{i,j} = \{(k,l) \in Z_m : 0 < (k-i)^2 + (l-j)^2 \leq c\} \quad (2.2)$$

Noticeably the free boundary condition exists for the boundary pixels where the neighboring sites or pixels are fewer than the interior ones. Fig. 2.2 (a), (b), (c) shows the neighborhood configuration for C =1,2,8 respectively. When c=1 the first order or nearest neighbor system results where $\mathcal{F}_{i,j} = \{(i,j-1),(i,j+1),(i-1,j),(i+1,j)\}$. In each case the (*i*,*j*) is the center pixels with colored dots and the neighboring pixels are the ones with circles. The cliques for c=1 are all subsets of $Z_m$of the form $\{(i,j)\},\{(i,j),(i,j+1)\}\ or\{(i,j),(i+1,j)\}$ as shown in Fig. 2.2 (d). For c=2 all the cliques in Fig. 2.2 (d) and (e) results. Number of cliques grows rapidly with c. More complex images likely necessitate more complex energies, but a modest neighborhood size is always preferred. **Case 2**. A line process L is adjoined to F for the original image model, $= D_m$, the dual $m \times m$ lattice. Shown in Fig. 2.2 (f) are six pixel sites together with seven lines sites (D= $\{d_1, d_2, \ldots, d_7\}$) denote by an . The six surrounding are the neighbors of the middle ( ) for the neighborhood system we denote by $\mathcal{Q} = \{\mathcal{Q}_d, d \in D_m\}$. Fig. 2.2 (g) is a segment of a realization of a binary line process for which at each line site there may or may not be an edge element. Another case for the setup field (F,L), is also discussed in the study which basically follows the realization defined by the **Case 3**. Finally the study went on to show the class of stochastic process (MRF) including both the prior and posterior distributions.

For an arbitrary graph {S, $\mathcal{G}$ }, let $X = \{X_s, s \in S\}$ denote any family of random variables indexed by *s*. In a common state space (*L*-pixel intensity levels), $\Lambda = \{0,1,2,\ldots,L-1\}$, $X_s \in \Lambda$ for all *s*. Let Ω be a set of all possible labels (configurations). Then $\Omega = \{\omega = (x_{s_1}, x_{s_2}, .., x_{s_N}) : X_{s_i} \in \Lambda, 1 \leq i \leq N, s_i \in S\}$. As usual, the event $\{X_{s_1}=x_{s_1}, X_{s_2}=x_{s_2}, .., X_{s_N}=x_{s_N}\}$ is abbreviated $\{X = \omega\}$. X is an MRF with respect to $\mathcal{G}$ if $p(X=\omega) > 0 \ \forall\ \omega \in \Omega$; and $P(X_s = x_s | X_r = x_r, r \neq s) = P(X_s = x_s | X_r = x_r, r \in \mathcal{G}_s)$ for every $s \in S$ and $(x_{s_1}, x_{s_2}, .., x_{s_N}) \in \Omega$. $P(X_s = x_s | X_r = x_r, r \neq s)$is called the local characteristics of the MRF. A Gibbs distribution relative to $\{S, \mathcal{G}\}$ is a probability measure on Ω which follows the equation $P(\omega) = \frac{1}{Z} e^{-U(\omega)/T}$ where Z and T are the constants and U, called the energy function in the form of $U(\omega) = \sum_{c \in C} V_c(\omega)$, C denotes the cliques for $\mathcal{G}$. Each V_c is a function on Ω with the property that $V_c(\omega)$ depends only on those coordinates x_s of ω for which $s \in C$. Such a family $V_c, c \in C$ is called potential and the normalizing constant $Z = \sum_\omega e^{-U(\omega)/T}$ and is called the partitioning function. Finally Tstands for the temperature as mentioned above. T Controls the degree of peaking in the probability density. Choosing T small exaggerates the mode, making them easier to find by sampling, which is the principle of annealing and will be applied to the posterior distribution $P(f,l) = P(F = f, L = l | G = g)$in order to find the MAP estimate.

2.2 MRF models for super resolution mapping (SRM)

After the original developments of MRF by *Geman and Geman*, application of MRF for remote sensing applications became more inspiring (Bruzzone and Prieto, 2000; kasetkasem and Varshney, 2002; Nishii, 2003; Sarkar et al., 2002; Solberg et al., 1996; Tso and Mather, 1999; Xu et al., 2011). Yet

depending on the diversity and the formation of the remote sensing images these applications became more and more challenging. Several applications directly related to the problem discussed in this study will be detailed here.

One of the most interesting applications of the MRF is the sub pixel mapping or super resolution mapping (SRM) or sharpening (Atkinson, 2004; Foody, 1998; Mertens et al., 2003; Tatem et al., 2001; Bateson and Curtiss, 1996; Boucher et al., 2008; Nguen et al., 2006). A SRM is a map that is derived at a spatial resolution finer than the size of the pixel of a coarser spatial resolution image being classified. Tatem et al., (2002 a,b) provide an excellent review on this subject. Several algorithms based upon knowledge-based procedures, Hopfield neural networks, linear optimization, genetic algorithms and neural network predicted wavelet coefficients have been developed in the past for the super resolution mapping. Knowledge based approaches depend on the accurate identification of boundary features that split the mixed pixels into pure components at fine spatial resolution. The drawbacks of this technique are the information on accurate boundary features may not be available readily as it lacks the dependence within and between pixels. Similarly for the other techniques mentioned above, the availability of accurate sub-pixel classification derived from other techniques is a pre-requisite. Thus, the accuracy of the resulting super-resolution land cover map is limited by the accuracy of the sub-pixel classification technique. As a result MRF based SRM technique was proposed by *Kasetkasem et al., 2005*. The model developed using MRF is free from the availability of accurate boundary feature information and sub-pixel information from other classification results. Using the MRF model a statistical correlation of intensity levels among neighboring pixels can be exploited. MRF has long been recognized as an accurate model to describe a variety of image characteristics such as texture. Under this, the configuration (intensity level) of a site (pixel) is assumed to be statistically independent of configurations of all remaining sites excluding itself and its neighboring sites when configurations of its neighboring sites are given. This is the same as the configuration of a pixel given the configurations of the rest of the image is the same as the configuration of a pixel given the configuration of its neighboring pixels. This model has the feasibility to fit into a variety of remote sensing applications. As a result of this development MRF model assigns higher weights to spatial structure of a homogeneous land cover class than the isolated pixels in the case of a land cover classification. The main problem addressed in this study is the mixed pixel issues of coarse resolution satellite images (ex. Landsat ETM+, 30m) and the missing spatial information for the classification. The core of the work describes the initial SRM generation and the iterative refinement of it to become an optimal SRM. Several important concepts developed from this study will be discussed in brief hear.

Several key ideas were generated by *Kasetkasem et al., 2005*. The first is the relationship between the coarser resolution input image and the SRM or the finer resolution map. For a given observed coarser spatial resolution image Y with $M \times N$ pixels a finer spatial resolution SRM X exists with $aM \times aN$ pixels. The factor a is called the scale factor which relates a pixel of the coarse resolution image to the finer resolution SRM pixel. In general a can be any positive real number. This further means that a particular pixel in the observed coarse image contains a^2 pixels of the SRM. This also assumes that pixels of the fine spatial resolution image are pure (i.e., the attribute number $x(s)($ pixel site s), denotes one and only one land cover class) while mixed pixels can occur only in the observed coarse spatial resolution image (Fig. 2.3). This assumption is quite feasible in the case of modern day optical and hyperspectral images (ex. ASTER 15m, Hyperion 30m). If the sets of all sites (i.e., pixels) belonging to observed image and SRM is S and J respectively, then number of sites belonging to J will be a^2 times the number of sites in

the set $s \in S$. Let $J^j = \{s_1{}^j, s_2{}^j, \dots, s_{a^2}^j\}$ represent the set of all pixels in the set J that corresponds to the same area as the pixels S^j in set S. The observed coarse spatial resolution multi-spectral image is usually represented in a vector form so this pixel relationship is envisaged as $y(S^j) \in R^k$ for the pixel S^j where R denotes the set of real numbers (i.e., pixel intensity) and k the number of spectral bands. In the case of $\mathcal{L}$ number of land cover classes $x(s) \in \{1,2,\dots,\mathcal{L}\}$ can only take single integer value representing a single class at pixel s. Hence as a result there can be $\mathcal{L}^{a^2MN}$ dissimilar SRM $X_{(J)} \in \{1,2,\dots,\mathcal{L}\}_J$ each having a different class allocation in at least one pixel.

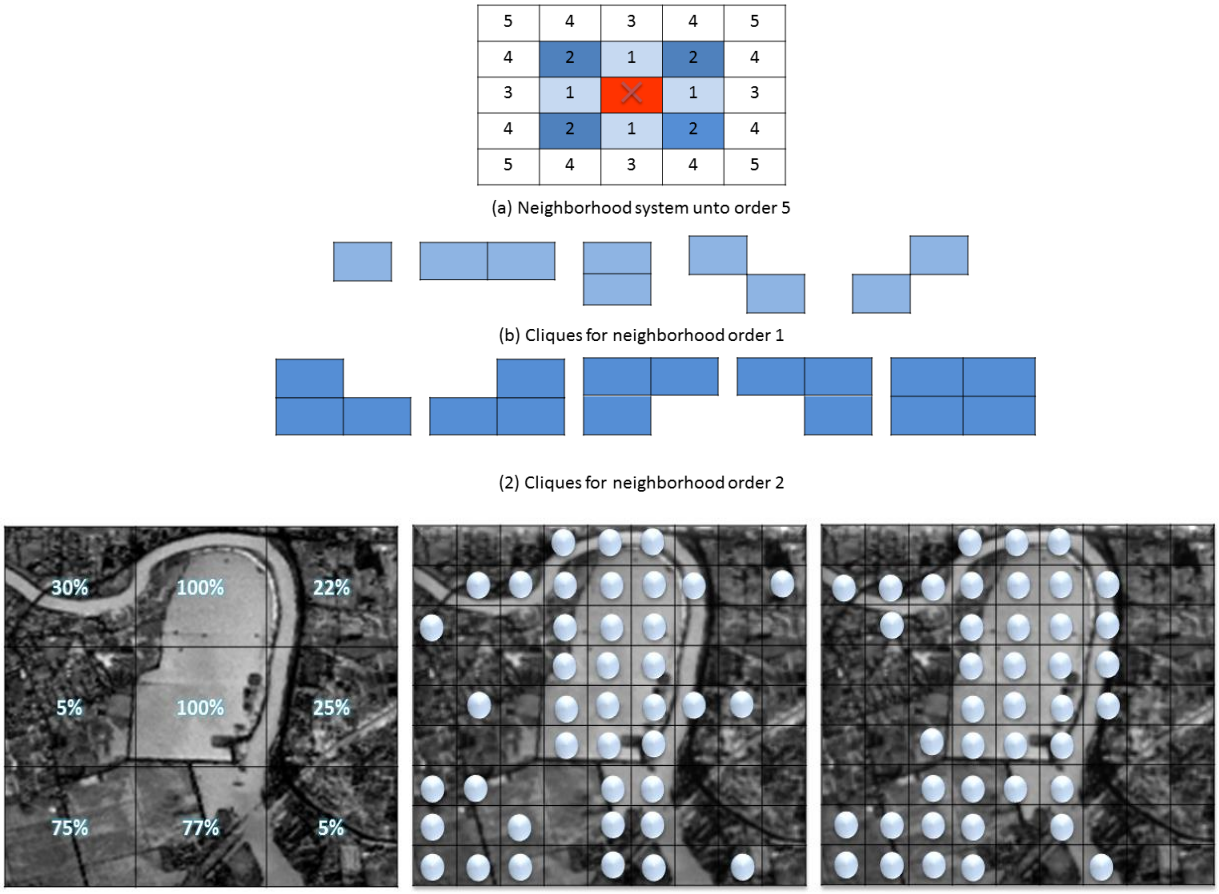

Figure 2.3 SRM (X) generation process from coarse resolution satellite image (Y) (a) coarse resolution fractional image (inundated paddy class) (b) initial SRM random class allocation (c) optimized MRF with the contextual neighborhood

Second important idea mentioned in the study is that the land cover classes occupying neighboring pixels are more likely to come from the same class than different classes, which is the property of Markovianity, (detailed in chapter 3). This can be mathematically explained by probabilities:

$$P(x(s)|X(J\backslash s)) = P(x(s)|X(N_s)) \tag{2.3}$$

where $J\backslash s$ is the set of all pixels in J excluding a pixel s, and N_s is a set of neighboring pixels of the pixel s. This equation very simply explains that in a case of land cover classification same classes are more likely to occur in connected regions than in isolation. This is an obvious situation in more homogeneous land

cover classes while to a lesser degree in heterogeneous dense urban regions. Due to this setup the conditional probability density function (PDF) gets a higher value if the configuration (class labels) of a pixel at location *s* is similar to the configuration of its neighboring pixels than in the cases when it is not. The marginal PDF which describes the distribution of a pixel *X* in the subset *J* is described by the Gibbs distribution as follows:

$$P(X) = \frac{1}{Z} exp\left[-\sum_{c \subset J} V_c(X)\right] \tag{2.4}$$

where Z is a normalizing constant , *C* is a clique and $V_c(X)$ is a Gibbs potential function as explained by Geman and Geman (Fig. 2.3 shows cliques for 4 and 8 neighborhood). The Gibbs potential function depends on the configurations of the entire SRM and the cliques. Low values for $V_c(X)$ corresponds to similar configurations, while high values represent the dissimilarities. This can be explained as follows for any different sites *r* and *s* (Bremaud, 1999; Winkler, 1995).

$$V_{\{r,s\}}(X) = \begin{cases} -\beta; if\ x(r) = x(s) and\ r \in N_s \\ +\beta; if\ x(r) \neq x(s) and\ r \in N_s \\ 0; r \notin N_s \end{cases} \tag{2.5}$$

This model was mainly used in statistical physics to describe the rotation of neighboring particles in same direction (clockwise or counterclockwise), but due to its close relation to represent land cover classes and their existence, it was also used in remotely sensed optical image classification. Finally for the complete spatial and spectral information integration accounting for the proportion of land cover in the coarser spatial resolution image, the conditional probability distribution is explained. Accordingly the fine spatial resolution image with the spatial resolution equal to the SRM with each pixel having a single class is modelled by the normal or Gaussian distribution. According to the relationship between the SRM and the coarse spatial resolution image stated earlier (*aM×aN)*, the PDF of an observed vector at pixel site *s*, *y(s*) in the coarse resolution image is also assumed to be normally distributed. If the mean vector and the covariance matrix for the classes are given by $\mu(s)$and $\Sigma(s)$the conditional PDF of the observed coarse spatial resolution image can be written as:

$$P(Y|X) = \prod_{s \in S} P(y|s)\big|b(s)\big)$$

$$= \prod_{s \in S} \frac{1}{2\pi^{\frac{k}{2}}\sqrt{|\det(\Sigma(s))|}} exp\left[-\frac{1}{2}\big(y(s) - \mu(s)\big)^T \Sigma(s)^{-1}(y(s) - \mu(s))\right] \tag{2.6}$$

where $\mu(s) = \sum_{l=1}^{L} b_l(s)\mu_l$ and $\Sigma(s) = \sum_{l=1}^{L} b_l(s)\Sigma_l$, with $b_l(s)$ being the proportion of land cover class *l* presented in J^ssuch that $\sum_{l=1}^{L} b_l(s) = 1$. Further $b(s) = [b_{l=1}(s), b_{l=2}(s), .., b_{l=\mathcal{L}}(s)]^T$. Hear both the mean and the variance of the observed coarser resolution image is a function of pixel *s*. The very meaning of this is that, because the coarser resolution pixel comprise of a combination of pure pixels at finer spatial resolution and at finer spatial resolution observation of any distinct pixel are independent, statistical mean vector and the covariance matrices are directional sum of corresponding pixels at fine

spatial resolution respectively. The classification algorithm is developed from this setup using a Maximum a posteriori (MAP) criterion, with the implementation of the Bayes rule as follows:

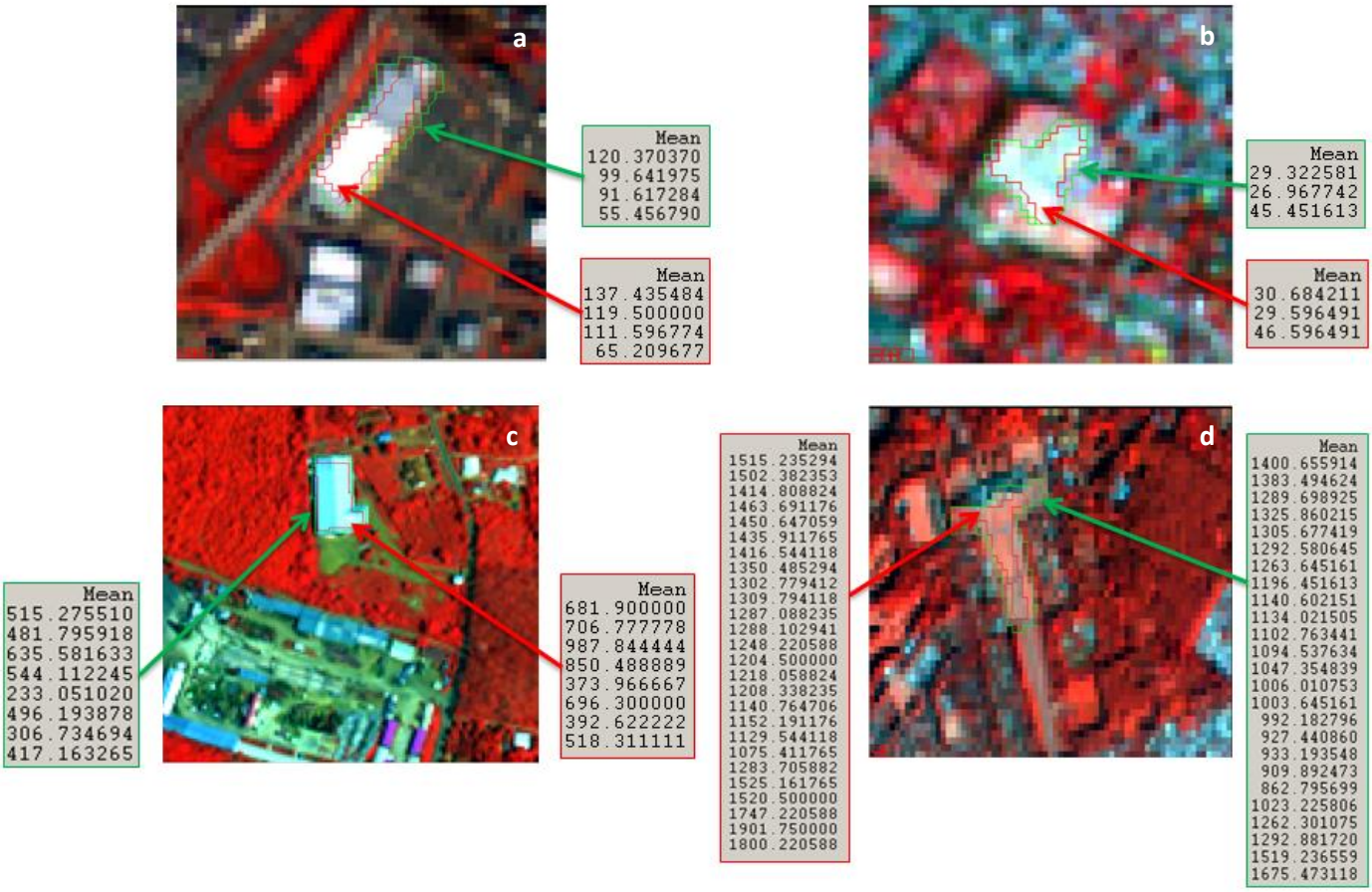

Figure 2.4 PSF effect in urban land cover at different spatial and spectral resolution (a) AVNIR-2 4 multispectral (10m) image bands 4,3,2 (R,G,B) (b) ASTER, 4 multispectral (15m) image bands 3N,2,1 (R,G,B) (c) Wordlview-II 8 multispectral(2m) image bands 8,4,3 (R,G,B) (d) EO-1 Hyperion hyperspectral (30m) image bands 42,24,16 (R,G,B)

$$X^{optimum} = arg\left\{\max_{X}\left[\frac{P(Y|X)P(X)}{P(Y)}\right]\right\} \tag{2.7}$$

The proposed methodology described as above was tested using two remote sensing images with markedly different spatial resolutions. Those are the Landsat ETM+ image at 30m and IKONOS MSS image at 4m spatial resolutions. Six land cover classes were used for the classification, shadow, grass, trees, road and two types of roofs representing top cover of tents and roof of buildings. Importantly this work concludes by highlighting that the MRF based SRM should be improved for classes which occupy

less areas on the ground and also for the classes which occupy small strips surrounded by large connected regions. Further it is suggested that these problems can be minimized by accurate estimate of the mean vector and covariance matrix of above classes or by a more suitable model of the observed data. Finally it was proposed it is needed to model the point spread function (PSF, i.e., the response of an imaging system to a point source), and the uncertainties of the land cover classes within the MRF model. The effects of PSF on mean values of the land cover components at different spatial resolutions due to factors such as optics of the instrument, the detector and electronics, atmospheric effects and image resampling (Huang et al., 2002) are shown in Fig. 2.4. In this thesis we put our attention to these problems and propose effective theoretical improvements and promising experimental results. PSF can be explained mathematically as a function $PSF(x-u, y-v)$ that maps an input pattern $g(u,v)$ in the object space into an output pattern $R(x,y)$ in the image space $R(x,y) = \iint PSF(x-u, y-v)g(u,v)dudv$, where x and y are the cross- and along-track coordinates of a pixel in the image space and u and v the cross- and along track coordinates in the object space.

2.3 MRF models for Multisource Satellite Imagery

The application of the MRF model for multisource data classification was first implemented by Solberg., et al 1996. This work lays the insightful background for the developments discussed and presented in this thesis. It proposes a MRF models to be a methodological framework which allows the images from different sensors and map data to be merged in a consistent way. The MRF model was developed to fuse optical images, SAR texture and GIS ground cover data. The study exploits the spatial dependency (spatial context) between neighboring pixels in an image and the temporal class dependencies between different images of the same scene.

The main idea behind this framework was the merging of multisource data to create a more consistence interpretation of the scene, in which the associated uncertainty is decreased. The importance of considering a pixel in context without being considered in isolation is highlighted in this study. The context was defined in three different dimensions i) the spectral ii) the spatial; and iii) the temporal dimensions. The spectral dimension referred to the different bands of the electromagnetic spectrum, which improves the separation between various ground cover classes compared to a single band image analysis. Fusion of data from different sensors allows coverage of a boarder range of the spectrum. Spatial context is defined by the correlation between spatially adjacent pixels in a spatial neighborhood. The concept of texture becomes important hear, as texture is based on the relationship between the measured intensities or pixel values of spatially neighboring pixels. In a pixel labeling problem using MRF, spatial context refers to the correlations between class labels of neighboring pixels. The third contextual dimension is the temporal context between multiple images of the same area. Using multisource data it is possible to have a better coverage of the temporal dimension, because one is no longer limited by the repeat cycle of a single satellite. It is also pointed out that the increased computational complexity in the case of multisource model is a fact to take into consideration.

Multisensor fusion can take place at either the signal, pixel, feature, or symbol level of representation. Signal-based fusion refers to the combination of signals from different sensors to create new signal with better signal-to-noise ratio than the original signal. Pixel-based fusion consists of merging information from different images on a pixel-by-pixel basis to improve the performance of image processing tasks such as segmentation. Feature-based fusion consists of merging features extracted from different signals or images. Symbol-level or decision-level fusion consists of merging information at a higher level of

abstraction, e.g., when fusing information from sensors which are very dissimilar or refer to different regions of the environment. The main methods for data fusion within remote sensing applications include statistical applications (ex., Bayesian framework), Dempster-Shafer theory and Neural Networks. Several comparisons of these three methods using a single data set can be found in literature (Benediktsson et al., 1990; Jakubowicz 1988). In these comparisons statistical methods performed the best. Among the statistical approaches for remote sensing data fusion, four main methods are reported in literature: the augmented vector approach, stratification, probabilistic relaxation, and extended statistical fusion. In the augmented vector approach, data from different sensors are concatenated as if they were measured from a single sensor and the fused data vector is then classified as an ordinary single-source measurement. Stratification (consistent assignment of pixel intensity values to predict symbols) is often used to incorporate ancillary GIS data in the interpretation process. The GIS data is stratified into categories and then a spectral model for each of these categories is used. Spatially contextual classification based on probabilistic relaxation was extended using ancillary data such as GIS. Extended statistical fusion was derived as an extension of the concepts used for classification of multispectral images involving a single data source. Each data source is considered independently, and the classification results are fused using weighted linear combination.

Contextual information for classification is mainly of two types: interpixel class dependency and interpixel feature correlation. Interpixel class dependency refers to the correlation among the class labels in a neighborhood. Interpixel feature correlation refers to the relationship between the feature vectors of spatially adjacent pixels in an image. Utilization of the interpixel feature correlation requires a model which describes the correlation between adjacent pixel values, resulting in a model with large computational complexity. Methods based on interpixel class dependency can be divided into two categories 1) classification rules based on stochastic models of the behavior of the classes in the scene and the behavior of the conditional distribution of feature vectors given the underlying classes and 2) simultaneous classification of a group of pixels in the scene, for example by constructing the MAP probability estimates. The basic elements for a multisource classification model presented by *Solberg et al.,1996* can be pointed as below.

Input data-

The input images are assumed to be geocoded and co-registered. Image registration involves a transformation of the images to a common map projection. A transformation will alter the image statics. If the images contain textured regions or significant noise with known characteristics, then the transformation is undesirable. If texture is presented for only one sensor fusion can be performed in the geometry of this sensor and the classified scene can then be transformed to the desired projection.

An image statistical model-

A sensor specific (ex., SAR, Multispectral, Hyperspectral) image statistic model should contain information about the underlying noise characteristics of the sensor and the intrinsic variability of the ground cover classes.

Ancillary information –

The backscatter signature for a ground cover measured with a specific sensor normally changes with time and season. Factors such as soil moisture, temperature, wind condition, and snow cover typically affect the signature.

A model for spatial context-

The interpixel class dependency or interpixel feature correlation is modelled for the pixels in a local spatial neighborhood.

A model for temporal context-

Temporal context can be modelled for interpixel class dependency or interpixel feature correlation in the same way as spatial context. The ground cover class of individual pixels, in most cases remains constant over small time intervals. Information about the likelihood of changes w.r.t the classes over time for a certain pixel location may provide useful knowledge about the class dependencies. Accurate modelling of temporal interpixel feature correlation for multisensor images is difficult. This task requires modelling of the temporal changes in spectral signature for each of the sensors due to different external conditions. A distinction between signature variation due to seasonal changes within the same ground cover class and the variations due to an actual change between two classes must also be made.

An interaction model-

an essential part of the fusion model is the interaction between the sensor specific modules, e.g., fusion is performed at the pixel, feature or object level.

A classification algorithm-

A classification rule must be defined to find a pixel labelling for the scene which is reasonable according to the data and the prior model. This is done by specifying a criterion function or loss function for the scene. An algorithm for optimization of the criterion function is also needed.

Parameter estimation procedures-

The parameter of different modules must be specified or estimated. For a complete multisource classification system, parameter, estimation procedures should be provided. However, standard techniques for parameter estimation might not be applicable in a complex fusion model. It is important to understand the fundamental developments presented by *Solberg et al.,1996* in her study in the overall context of this thesis. The study presents two models, the general multisource classification model and the specific model for fusion of different remote sensing images and the ancillary data. The description refers to the list of notations in Table 1 used to describe the model. Fig. 2.4 shows the set of measurement from *n* number of sensors.

Table 2 1 List of Notation for the model parameters

Symbol	Description
$\boldsymbol{M, N}$	*Image dimensions*
$\boldsymbol{X_s^t}$	*Image from sensor* **s** *at time* **t**
$\boldsymbol{n}$	*Number of sensors*
$\boldsymbol{D_s}$	*Dimension of feature vector from sensor* **s**
$\boldsymbol{K}$	*Number of classes*
$\boldsymbol{P(\omega_k)}$	*Prior probability for class* ω_k
$\boldsymbol{C^t(i,j)}$	*Class label of pixel* (i,j) *at time* **t**
$\boldsymbol{C^t}$	*Set of class labels for the scene at time t*
$\boldsymbol{l_g(i,j)}$	*Line process for pixel* (i,j) *for GIS field border map*
$\boldsymbol{l_c(i,j)}$	*Line process for pixel* (i,j) *derived from the class label* C^t
$\boldsymbol{X_s^t}$	$\{X_s^r; r \leq t\}$, *multitemporal image set*
$\mathbb{C}^t$	$\{C^r; r \leq t\}$
$\boldsymbol{Y_s, \theta_{kl}, \sigma^2, \mu_y}$	*Parameters of the SAR textural model*
$\boldsymbol{U}()$	*Energy functions*
$\boldsymbol{V}()$	*Potential functions*
Model parameters	
$\boldsymbol{\alpha_s}$	*Reliability factor source s*
$\boldsymbol{\beta_{sp}}$	*Parameter to control the spatial energy*
$\boldsymbol{\beta_{temp}}$	*Parameter to control the temporal energy*
$\boldsymbol{\beta_g}$	*Parameter to control energy associated with the map*

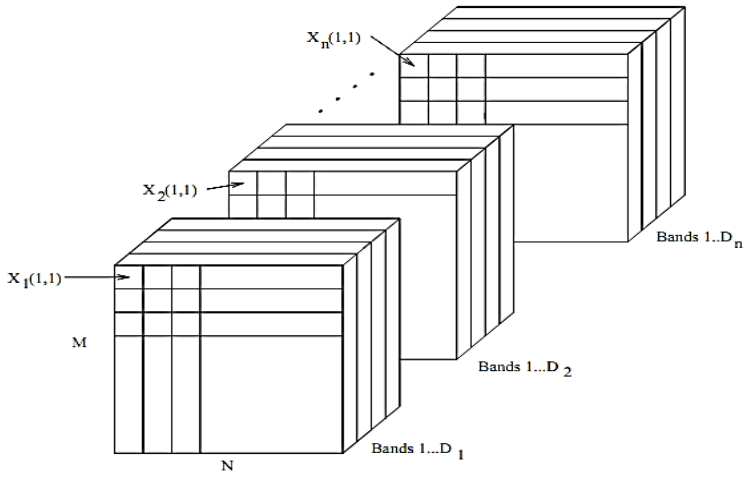

Figure 2.5 Image data, *Source Solberg et al., 1996*

Let the $M \times N$ image from sensor s consists of MN pixels or feature vectors $X_s(1,1), X_s(1,2), .., X_s(M,N), s = 1,2, .., n$ where $X_s(i,j) = (x_s(i,j,1), x_s(i,j,2), .., x_s(i,j,D_s))$, and D_s is the number of features or spectral bands for sensor s. The scene consists of K true classes, $\omega_1, \omega_2, .., \omega_k$, with the prior probabilities $p(\omega_1), p(\omega_2), .., P(\omega_k)$. We assume that the multisource images have been co-registered. The class of pixel (i,j) is denoted by $c(i,j)$. Let X_s denote the set of

pixels for the whole scene, $X_s = \{X_s(i,j); 1 \leq i \leq \text{M}, 1 \leq j \leq \text{N}$, and $C = \{C(i,j); 1 \leq i \leq \text{M}, 1 \leq j \leq \text{N}$ the corresponding set of labels for the whole scene; $C(i,j) \in \{\omega_1, \omega_2, \dots, \omega_K\}$ If the conditional probability density of feature vector $X_1, X_2, .., X_n$ given the scene labels C is $P(X_1, X_2, \dots, X_n|C)$. The main task is to assign each pixel to the class that maximizes the posterior probability $P(C|X_1, X_2, \dots, X_n)$. Using the Bayesian formulation we can define the relationship between the measurement and the prior information as:

$$P(C|X_1, X_2, \dots, X_n) = \frac{P(X_1, X_2, \dots, X_n|C)P(C)}{P(X_1, X_2, \dots, X_n)} \tag{2.8}$$

Where $P(C)$ is the prior model for class labels. The model was described considering two aspects 1) fixed time module describing the fusion of data collected simultaneously at short time interval with less class changes 2) multitemporal module describing the fusion of images captured at different dates where classes are changes. In the first part for the images sensed at same time, the posterior probability $P(C|X_1, X_2, \dots, X_n)$ is maximized taking the reliability factor of each sensor. Hear the measurements from each sensor are considered to be independent, i.e., $P(X_1, X_2, \dots, X_n|C) \equiv P(X_1|C) \times P(X_2|C), \dots \times P(X_n|C)$. For the fusion of data from optical and microwave sensors this assumption is very much reasonable. The likelihood function with different reliability factor for each sensor results as follows:

$$L(X_1, X_2, \dots, X_n|C) = P(X_1|C)^{\lambda_1} \times P(X_2|C)^{\lambda_2}, \dots \dots \times P(X_n|C)^{\lambda_n} P(C) \tag{2.9}$$

where $\lambda_s, 0 \leq \lambda_s \leq 1$, is defined as the reliability factor for source s. If the source s is totally unreliable, then α_s takes a value 0, so that $P(X_S|C)^{\lambda_S}$=1 with no contribution of the source to the likelihood estimation. To determine this reliability factor overall classification accuracy, class seperability, and genetic algorithms can be used (Tso & Mather, 2009). MRF model is used here to model the spatial context $P(C)$.

$$P(C(i,j)|C(k,l); \{k,l\} \neq \{i,j\}) = P\big(C(i,j)\big|C(k,l); \{k,l\} \in \mathcal{G}_{i,j}\big) = \frac{1}{Z} e^{-U(C)/T} \tag{2.10}$$

As explained by *Geman & Geman*, $\mathcal{G}_{i,j}$ is the local neighborhood of pixel (i,j). Maximizing $(P\big(C(i,j)\big|C(k,l); \{k,l\} \in \mathcal{G}_{i,j}\big)$ is equivalent to minimizing$U(C)$. $U(C(i,j))$ is given by

$$U(C(i,j)) = \sum_{\{k,l\} \in \mathcal{G}_{i,j}} \beta I(C(i,j), C(k,l)) \tag{2.11}$$

where

$$I(C(i,j), C(k,l)) = \begin{cases} -1, if\ C(i,j) = C(k,l) \\ 0, if\ C(i,j) \neq C(k,l) \end{cases} \tag{2.12}$$

Basically this potential function counts the number of pixels in the neighborhood assigned to the same class as the pixel in concern. If $\beta = 0$, this reduces to a noncontextual model, while β increases more homogeneous image regions will be favored. Finally the multisensor classification algorithm consists of maximizing $L(X_1, X_2, \dots, X_n|C)$, which is equivalent to the minimzing:

$$U(X_1, X_2, \dots, X_n, C) = \sum_{s=1}^{n} \lambda_s U_{data}(X_s) + U_{sp}(C) \quad (2.13)$$

Considering interpixel feature correlation the image statistical model for the optical data was modelled by multivariate normal distribution. Thus it is assumed that $P(X_s|C) = \prod_{i,j} P(X_s(i,j)|C(i,j)).P(X_s(i,j)|C^t(i,j))$ and hence can be modelled by energy functions as follows:

$$U_{data}\big(X_s(i,j), C^t(i,j)\big) = \frac{D_s}{2}\ln|2\pi\Sigma_K| + \frac{1}{2}(X_s(i,j) - \mu_K)^T {\Sigma_K}^{-1}(X_s(i,j) - \mu_K) \quad (2.14)$$

$C^t(i,j)$ represent the class label at time *t*, and $\Sigma_K$and μ_K are the class-conditional covariance matrix and mean vector for class *K* respectively. For the SAR data, the image statistics can be modelled either by PDF or a more complex model describing the speckle statistics and autocorrelation function. A general multiplicative autoregressive random field model (MAR), which incorporates textural information is used for the modelling of energy functions for SAR data. A detailed discussion of this model will be conducted in the Chapter 3. As in the case of optical data a multivariate normal distribution is used to model these texture measures. There for the feature vector $X_s(i,j)$ represents texture in this case.

For the second case of multitemporal data fusion the model is extended as with a feature vector $X_S^t = X_S^t(i,j)$ representing the measurements from sensor *S* at time *t*. Now the model allows the class changes with $C^t = \{C^t(i,j)\}$ representing the class label at time *t*. Define $X_S^t = X_S^r; r \le t$ and $\mathbb{C}^t = C^r; r \le t\}$. At each time t, a recursive estimation of the labels C^t based on the measurements, X_S^t, up to that time. Hence we maximize

$$P(C^t|X_S^t) = \frac{P(C^t, X_S^t)}{P(X_S^t)} \quad (2.15)$$

Several assumptions under the recursive labelling are made to make the model tractable:

$P(X_s^t|\mathbb{C}^t, X_s^{t-1}) \equiv P(X_s^t|C^t)$, which implies that the noise associated with a particular image frame is independent of the noise or class.

$P(C^t|\mathbb{C}^{t-1}) \equiv P(C^t|C^{t-1})$, which is the first order Markov assumption for the class labels over time.

The two assumptions give:

$$P(\mathbb{C}^t, X_s^t) = \left(\prod_{m=1}^{t} P(X_s^m|C^m)P(C^m|C^{m-1})\right)P(C^0) \quad (2.16)$$

where C^0 is the initial labelling of the scene. Then a recursive estimate of C^t, gives the previous labels and the current measurements, is

$$P(C^t|\mathbb{C}^{t-1}, X_s^t) \propto P(C^t|C^{t-1})P(X_s^t|C^t) \quad (2.17)$$

The true labels $C^{t-1}$are unknown, so the classification algorithm will be based on the estimated labels $\hat{C}^{t-1}$

$$P\left(C^t|\hat{C}^{t-1},X_s^t\right) \propto P\left(C^t|\hat{C}^{t-1}\right)P(X_s^t|C^t) \quad (2.18)$$

As matter of fact the main modification for the multitemporal images is the temporal contextual term $P(C^t|\hat{C}^{t-1})$. The Markov dependence of the class labels at time t is assumed to specify this term. An assumption is made in this development, $P(C^t(i,j)|C^{t-1},C^t(k,l);\{k,l\}\in \mathcal{G}_{i,j}{}^t) \equiv P(C^t(i,j)|C^{t-1}(q,r)\ ,\ C^t(k,l),\{k,l\}\in \mathcal{G}_{i,j}{}^t,\{q,r\}\in \mathcal{G}_{i,j}{}^{t-1}$, where $\mathcal{G}_{i,j}{}^{t-1}$ includes pixel $(i,j)$and its second-order neighbors in frame $t-1$. Fig. 2.6 shows the spatio-temporal neighborhood at time frames t and $t-1$.

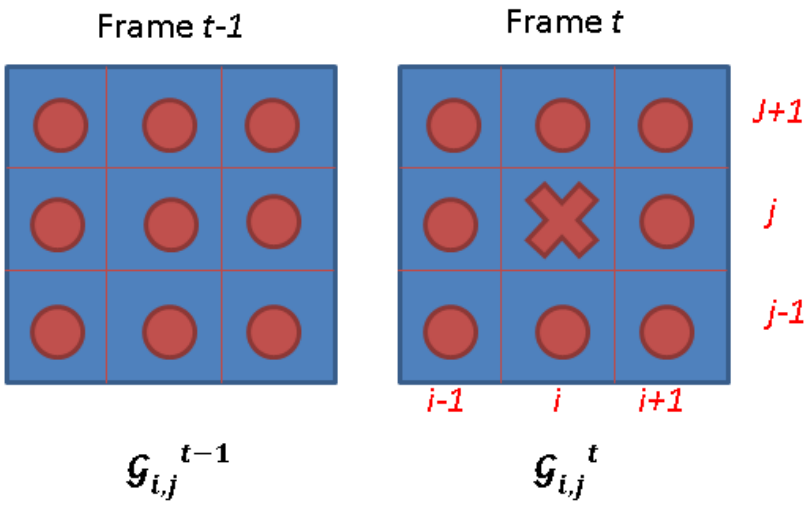

Figure 2.6 Spatio temporal neighborhood of pixel (i, j), *Solberg et al., 1996*

Hence in the form of energy functions and Gibbs random field, the above assumption can be re written as follows:

$$P(C^t(i,j)|C^{t-1}(q,r),C^t(k,l),\{k,l\}\in \mathcal{G}_{i,j},\{q,r\}\in \mathcal{G}_{i,j}{}^{t-1}) = \frac{1}{Z}e^{-\frac{U\left(C^t(i,j),C^{t-1}(q,r),C^t(k,l)\right)}{T}} \quad (2.19)$$

Due to the difficulty of specifying the above equation containing both spatial and temporal contextual information, a simplification is done assuming the seperability between the spatial and time-dependent aspects of C^t:

$$U\left(C^t(i,j),C^{t-1}(q,r),C^t(k,l)\right) \equiv U_{sp}\left(C^t(i,j),C^t(k,l)\right) + U_{temp}\left(C^t(i,j),C^{t-1}(q,r)\right) \quad (2.20)$$

Let the spatial context be:

$$U_{sp}\left(C^t(i,j), C^t(k,l)\right) = \beta_{sp} \sum_{\{k,l\}\in\mathcal{G}_{i,j}} I\left(C^t(i,j), C^t(k,l)\right) \quad (2.21)$$

and the temporal context be:

$$U_{temp}\left(C^t(i,j), C^{t-1}(q,r)\right) = -\beta_{temp} \sum_{\{q,r\}\in\mathcal{G}_{i,j}^{t-1}} P\left(C^t(i,j), C^{t-1}(q,r)\right) \quad (2.22)$$

$P\left(C^t(i,j), C^{t-1}(q,r)\right)$ is the transitin probability for a change from class $C^{t-1}(q,r)$ to class $C^t(i,j)$ between time $t-1$ and time t. β_{sp} and β_{temp} are user defined parameters. Thus the multi temporal fusion algorithm is based on minimizing

$$U(X_1, \dots X_n, C^t, C^{t-1}) = \sum_{s=1}^{n_t} \alpha_s U_{data}(X_S^t, C^t) + U_{sp}(C^t) + U_{temp}(C^t, C^{t-1}) \quad (2.23)$$

where n_t is the number of sensors active at time t .

The developed method was tested using the six non thermal bands of Landsat TM, ERS-1 SAR, MAESTRO multipolarization (HH, HV, VH, VV) amplitude 4-look SAR images and GIS ground cover data. This work is the only major work of its kind that described the theoretical model using MRF for the first time to classify multisource satellite imagery. Due to this new implementation a separate chapter (Chapter 9) describing the multisource satellite images based on this paper is resulted in Tso & Mather, 2009, famous book of "Classification methods for Remote Sensing data".

2.4 Specific application of MRF model

The theoretical development of the MRF model for SRM and multisource data, as discussed in previous sections, led to several interesting applications of it in remote sensing. *Adriella and Tolpekin, 2011*, applied the SRM technique to identify tree crowns in The Netherlands. They went on to show the potential of identifying the number of trees using the MRF based SRM quite convincingly. In the results section of this thesis we further highlight this potential in our results.

The multisource classification mechanism was tested with several improvements to identify sea ice using SAR imagery by *Deng and Clausi, 2005*. They model the SAR intensity using the Gamma distribution. Hence the PDF and the corresponding energy functions took the form as below:

$$P(X_s|C) = \frac{L^L}{{\mu_K}^L (L-1)!} {X_s}^{L-1} \exp\left(-\frac{L}{\mu_K} X_s\right) \quad (2.24)$$

$$U_{data}\left(X_s(i,j), C(i,j)\right) = \sum_K \left\{\frac{1}{\mu_K} X_s - (L-1) log X_s + L log \mu_K\right\} \quad (2.25)$$

$$U_{sp}(C(i,j)) = \sum_{\{k,l\}\in\mathcal{G}_{i,j}} \beta I(C(i,j), C(k,l)) \begin{cases} -1, if\ C(i,j) = C(k,l) \\ 1, if\ C(i,j) \neq C(k,l) \end{cases} \quad (2.26)$$

where $L$is the number of looks, X_s is the SAR pixel intensity and μ_K is the mean of class K. The use of Gray Level Co-occurrence probability (GLCP) based texture features for the SAR data is also included in this work. A detailed description of such framework will be conducted in the mathematical back ground of this thesis.

2.5 Incorporating uncertainty in the MRF model using Fuzzy techniques

In the literature it is not reported a framework using both fuzzy class parameters and MRF models for image classification. As we have pointed out using above studies the core of the MRF in any approach is the accurate class labelling of a pixel in an image. The uncertainty in this assignment to the effects such as noise in the form of PSF, speckle can be removed if we can improve the relationship definition between the class and the pixel intensity. Fuzzy set theories (Zadeh, 1965) provide the base to construct a meaningful relationship between the pixel and the class label. In this thesis we set our main goal in developing such a framework for the MRF. The success of such implementation will be tested in both SRM and the multisource classification mechanisms using MRF.

With the in-depth description of the most related previous research work and their applications, as summarized above we conclude this chapter. The work we summarized above have direct and strong influence to the developments and extensions we tested in this PhD work. From this point onward an explanation about the development of the fuzzy MRF model for SRM and multisource image classification will be detailed and explained.

3

Fuzzy Markov Random Fields

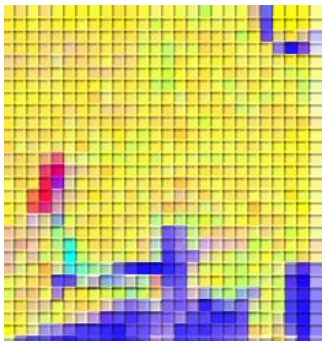

This chapter is devoted to explain the theoretical foundation of the MRF based labelling in image analysis, fuzzy sets, Optical and SAR imaging in brief with their different image properties and the texture measure associated with SAR images. A brief extension related to time series change detection theories will be discussed under the SAR texture measures to highlight the application feasibility of SAR texture measures to detect land cover changes. Overall, we will built this chapter to give a better understanding of the theoretical developments carried out under this PhD work, and to understand the image processing results and their formation presented in the latter chapters more convincingly. Major references for this chapter includes Li, 2010, Tso and Mather, 2009, Solberg et al., 1996, Kasyap and Chellappa, 1983, Franknote and Chellappa, 1987.

3.1 Labeling in image analysis

Many image analysis and interpretation problems can be posed as labelling problem in which the solution to a problem is a set of labels assigned to image pixel or features. Much better understanding about the MRF based classification can yield by using the concepts of labelling. A labelling problem is specified in terms of a set of sites and a set of labels. Let S index a discrete set m sites $S_{1D} = \{1,2,\dots,m\}$, where $1,2,..,m$ are indices. A site often represent a point or region in the Euclidean space such as an image pixel or an image feature such as corner point, a line segment, or a surface patch. A set of sites may be categorized in terms of "regularity". Sites on a lattice are considered spatially regular. A rectangular lattice for a 2D image of size $m \times m$ can also be denoted using the formulation of sites, $S_{2D} = S = \{(i,j)|1 \leq i,j \leq m\}$. Its elements correspond to the location at which an image is sampled. Sites that do not present spatial regularity are considered irregular. In MRF we treat the sites to be unordered. A neighborhood system as explained in chapter 2, maintains the interrelationship between sites. A label is

an event that may happen to a site (pixel). Let $\mathcal{L}$ be a set of labels. A label set can be a) discrete or continuous b) ordered. It is equivalent to a set of user defined information classes, for ex., in the edge detection; the label set is $\mathcal{L} = \{edge, nonedge\}$ and $\mathcal{L} = \{water, forest, pasture, residential\ area\}$ for image classification. Also a continuous label set can be ordered by the relation such as "smaller than".

3.1.2 The labelling problem

The labelling problem is to assign a label from the label set $\mathcal{L}$ to each of the sites in S. As an example, in the case of edge detection from an image, the problem is to assign a label f_i from the set $\mathcal{L} = \{edge, non\ edge\}$ to site $i \in S$ where elements in S index the image pixels. The set $\omega = \{\omega_1, \omega_2, \dots, \omega_m\}$ is called a labelling of the sites in S in terms of the labels in $\mathcal{L}$, which is the main action of the labelling problem. When each site is assigned a unique label, $\omega_i = \omega(i)$ can be regarded as function with domain S and label $\mathcal{L}$. Because the support of the function is the whole domain S, it is a maping from S to $\mathcal{L}$ that is $\omega: S \to \mathcal{L}$. A labelling is called coloring in mathematical programming. Fig. 3.1 illustrates the mapping concept for the continuous and discrete cases.

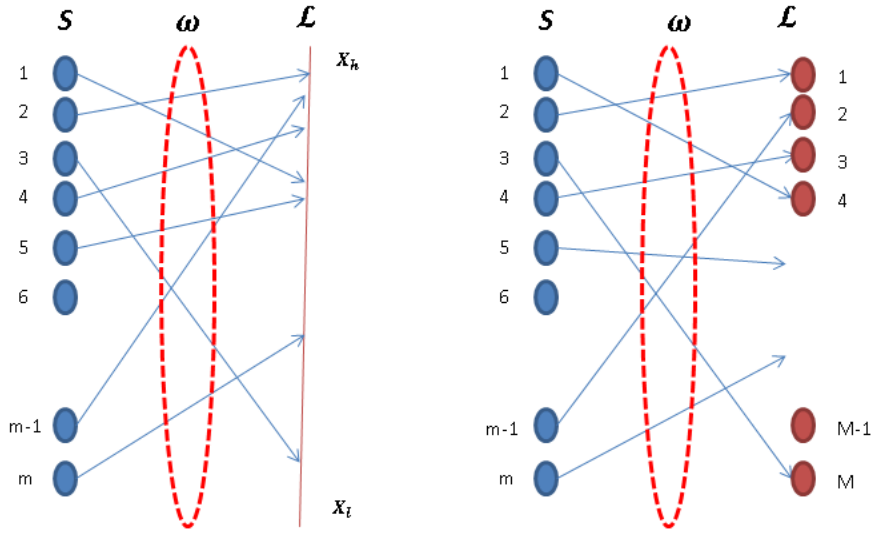

Figure 3.1 A labeling of sites is the mapping from the set of sites S to the set of labels$\mathcal{L}$, the mapping for continuous label set (left) and discrete label set (right)

According to the terminology of random fields, a labelling is called a configuration. When all the sites have the same label set $\mathcal{L}$, the set of all possible labeling (that is the configuration space) is a Cartesian product represented by $F = \mathcal{L} \times \mathcal{L} \dots \times \mathcal{L} = \mathcal{L}^m$, where m is the size of S. For a problem with m sites and M labels there exist a total number of M^mpossible configurations in F admissible images.

In image analysis depending on regularity and the continuity, the vision labelling problem can be categorized into following four categories: LP1) regular sites with continuous labels LP2) regular sites with discrete labels LP3) irregular sites with discrete labels and LP4) irregular sites with continuous labels. Restoration or smoothing of images having continuous pixels, which is the estimation of true image signal from a degraded or noise-corrupted image, belongs to the LP1.

Restoration of binary or multilevel images is an LP2, the difference is that each pixel in the resulting image assumes a discrete value and thus $\mathcal{L}$ is a set of discrete labels. Region segmentation is also an LP2. Here the observed image is portioned into mutually exclusive regions, each of which has some uniform and homogeneous properties whose values are significantly different from those of the neighboring regions. The property can be gray tone, color, or texture, where pixels within each region are assigned a unique label. Edge detection also belongs to LP2. In this case each edge site, located between two neighboring pixels, is assigned a label in {edge, nonedge} if there is a significant difference between the two pixels. Perceptual grouping is LP3. Here the sites usually correspond to initially segmented features (points, lines and regions) that are irregularly arranged. These fragmentary features are to be organized into perceptually more significant features. A label {connected, disconnected} is assigned between each pair of features, indicating whether the two features should be linked. Feature-based object matching and recognition also belong to LP3. Each site indexes an image features such as a point, a line segment, or region. Labels are discrete in nature, and each of them indexes a model feature. The resulting configuration is a mapping from the image features to those of a model object.

Post estimation from a set of point correspondences might be formulated as an LP4. A site is a given correspondence. A label represents an admissible (orthogonal, affine, or perspective) transformation. A prior (unary) constraint is that the label of transformation itself must be orthogonal, affine or perspective. A mutual constraint is that labels $\omega_1, \omega_2 \ldots, \omega_m$ should be close to each other to form a consistent transformation.

3.1.3 Labelling with context, Bayes labelling

The best way to explain contextual constraints is to explain it using probability. This can be defined using two ways. Locally by conditional probability P($\omega_i|\{\omega_{S-i}\}$), where $\{\omega_{S-i}\}$ denotes the set of labels at the site S excluding the pixel in concern i. Globally as joint probability $P(\omega)$. As local information is more directly observed, it is normal for a global inference to be made on the local properties. In situations where labels are independent of one another (no context) the joint probability is the product of local ones:

$$P(\omega) = \prod_{i \in S} P(\omega_i) \tag{3.1}$$

The above equation implies the conditional independence:

$$P(\omega_i|\{\omega_{S-i}\}) = P(\omega_i) \quad i \neq S - i \tag{3.2}$$

Hence, a global labelling ω can be computed by considering each label ω_i locally. In the presence of context labels are mutually dependent, the simple relationship in Eq. 2.1 and 2.2 do not hold anymore. Therefore to make a global inference using local information becomes nontrivial task. MRF provides trivial solution for this task. Detaille's of this will follow in the coming sections. In image labelling problems a problem is formulated as optimizing some criterion, explicitly or implicitly. The main reason behind the use of optimization principles is due to various uncertainties in the imaging and vision processes. Noise and other degradation factors such as those caused by disturbances and quantization in sensing and signal processing are sources of uncertainties. Different appearances and poses of objects, their mutual-occlusion and self-occlusion, and possible shape deformation also cause ambiguities in

visual interpretation. Under such circumstances, we can hardly obtain exact or perfect solutions and have to resort to inexact yet optimal solutions.

The three main concerns in optimization based vision are the problem representation, objective function, and optimization algorithms. In the case of problem representation, it can be done on the basis of two aspects of representation descriptive or computational. Descriptive representation concerns how to represent image features and object shapes, which relates to photometry and geometry. Computational representation concerns how to represent the solution, which relates to the choice of sites and label set for a labelling problem. In the second case, the formulation of the objective function (in the form of energy function) for the optimization is considered. This formulation determines how various constraints, which maybe pixel properties such as intensity and color and/or context such as relations between pixels or object features, are encoded into the function. There are two basic approaches to formulate the energy function: parametric and nonparametric. In the parametric approach, the types of underlying distributions are known and the distributions are parameterized by few parameters. In the nonparametric approach, sometimes called the distribution-free approach, no assumptions about the distributions are made. Hear the distribution is either estimated from the data or approximated by a pre-specified basis function. Despite the terms parametric and nonparametric, both approaches are somewhat parametric in nature, because in any case there are parameters that must be estimated. The two most important aspects of an energy function are its form and the parameters involved. The form depends on assumption about the solution ω and the observed data d. This can be expressed using the notation $U(\omega|d)$. With the set of parameters involved we can further expressed the same in more descriptive manner $U(\omega|d,\vartheta)$. Generally given the functional form for U, a different d or ϑ defines a different energy function $U(\omega|d,\vartheta)$ w.r.t ω and hence a different minimal solution $\omega^* = argmin_\omega U(\omega|d,\vartheta)$. The parameter estimation is an important area of study in MRF modelling. The energy functions discussed in this thesis for optical and SAR images and their respective parameters will be discussed further in details.

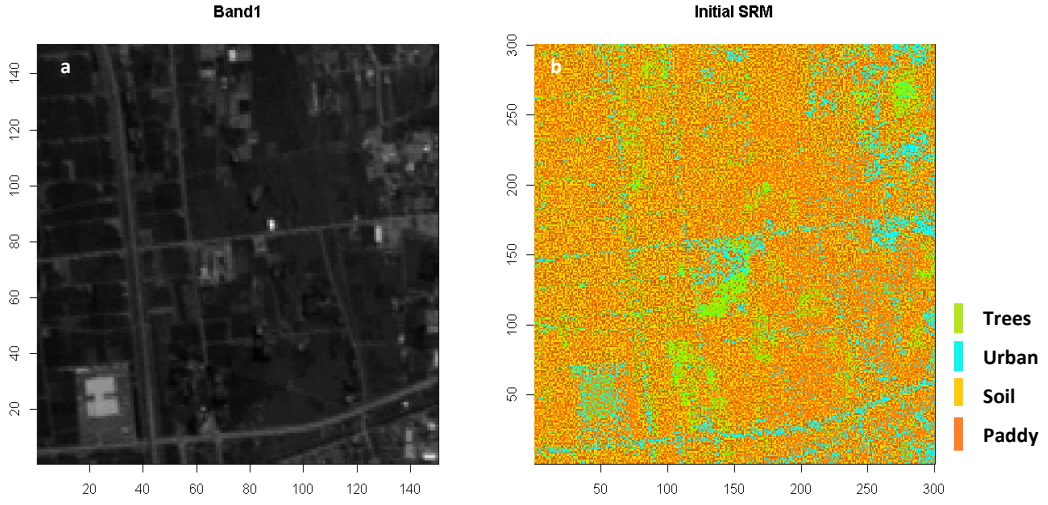

Figure 3.2 An example for the labeling of sites ($\omega: S \rightarrow \mathcal{L}$) using AVNIR-2 image and the sub pixel class fractions, (a) gray scale sites band1 (d) (b) Label set (ω)

The third is the final which is how to optimize the objective. Two major concerns are the problem of local minima existing in nonconvex functions and the efficiency of algorithm in space and time. Currently there

are no algorithms that guarantee the global solution with good efficiency. When the knowledge about the data distribution is available but the prior information is not, the maximum likelihood (ML) criterion may be used, $\omega^* = argmaxP(\omega|d)$. On the other hand, if only the prior information is available the maximum entropy criterion may be chosen, $\omega^* = argmax\{-\sum_{i=1}^{m} P(\omega_i)lnP(\omega_i)\}$. When both the prior and likelihood distributions are known, the best result is achieved by maximizing a Bayes criterion according to Bayes statistics, which will be the center of discussion in this chapter. The theorem of equivalence between MRF and Gibbs distribution establish in the coming sections provides a convenient way to specify the joint prior probability, solving a difficult issue in MAP-MRF labelling. For the details of the Bayes estimation and the MAP-MRF labelling see Appendix A.

3.2 Markov Random Fields and Gibbs Random Fields (MRF\GRF)

The sites in S are related to one another via a neighborhood system, a neighborhood system for S is defined as:

$$N = \{N_i | \forall i \in S\} \tag{3.3}$$

where N_i is the set of sites neighboring i. Importantly site is not neighboring to itself: $i \notin N_i$ and the neighboring relationship is mutual $i \in N_{i'} \Leftrightarrow i' \in N_i$. For a regular lattice S, the set of neighbors of i is defined as the set of sites within a radius of r from i:

$$N_i = \{i' \in S | dist(pixel_{i'}, pixel_i) \leq r, i' \neq i\} \tag{3.4}$$

Here *dist(A,B)* is the Euclidian distance. The neighborhood system described here relates to the details we explained in chapter 2. This can be also defined using Delaunay triangulation or its dual, the Voronoi polygon of the sites. In this thesis all the image processing activities are related to the second order neighborhood system. As explained in chapter 2, the pair $(S, N) \triangleq \mathcal{G}$ consist a graph in the ususal sense; S contains the nodes and N determines the link between the nodes. A clique c for $(S, N)$is defined as a subset of sites in S. In this study we use a single site(C_1) $c = \{i\}$, a pair of neighboring sites (C_2) $c = \{i, i'\}$, a triple of neighboring sites (C_3) $c = \{i, i', i''\}$, as an example the pair of neighboring sites will be represented as follows:

$$C_2 = \{\{i, i'\} | i' \in N_i, i \in S\} \tag{3.5}$$

Importantly the cliques are ordered, where $\{i, i'\}$ are not the same clique as $\{i', i\}$.

Let a set of random variables (x_i-Optical image pixels intensity, y_i-SAR image pixel intensity) $d = d_1, d_2, .., d_m$be defined on the set S in which each random variable $d_i (1 \leq i \leq m)$takes a label from the label set $\mathcal{L}$, which depends on the classification problem (ex., number of land cover classes). The family d is called a random field. The set S is equivalent to an image containing m pixels; d is set of pixel DN values. Among the many random field models that describe the labelling of random variables, we use the Markov random fields (MRF) and the Gibbs random fields (GRF) for our study. This choice is mainly due to the advantages of MRF and GRF as detailed in chapter 2.

Given the definition of a random field as above the configuration ω for set S is defined as ω: $d_i \rightarrow \omega_i$, where $\omega_i \in \mathcal{L}$ $(1 \leq i \leq m)$. Simply we denote the joint event as $d = \omega$, where $\omega = \omega_1, \omega_2, .., \omega_m$ is a

configuration of F. A random field w.r.t a neighborhood system is a MRF if its PDF satisfies the following three properties.

Positivity: $P(\omega) > 0,\ \forall \omega \in F$

Markovianity: $P(\omega_i|\omega_{S-i}) = P\left(\omega_i|\omega_{N_i}\right)$ (3.6)

Homogeneity: $P\left(\omega_i|\omega_{N_i}\right)$ is the same for all sites i

where $S - i$ is the set difference, ω_{S-i} denotes the set of labels at the sites in $S - i$. Also $\omega_{N_i} = \{\omega_{i'}|i' \in N_i\}$, which is the set of labels at the sites neighboring i. The joint probability $P(\omega) = P(d \to \omega)$, can be uniquely determined by local conditional properties as long as the positivity property sustains. Markovianity indicates that labelling of a site i is only dependent on its neighboring sites. The property of homogeneity specifies the conditional probability for the label of a site i, given the labels of the neighboring pixels, regardless of the relative position of site i in S. Isotropy is also another property of MRF other than the three properties mentioned above. That is the direction independence, where the neighboring sites surrounding a site i have the same contributing effect to the labelling of site i.

3.2.1 Gibbs Random Field

An MRF is defined in terms of local properties (i.e., the classification label assigned to a pixel is effected only by its neighbors), whereas a GRF describes the global properties of an image (i.e., the label given to a specific pixel is affected by the labels given to all other pixels) in terms of the joint distribution of classes for all pixels. A GRF provides a global model for an image by specifying a PDF as follows:

$$P(\omega) = \frac{1}{Z}\exp\left[-\frac{U(\omega)}{T}\right] \tag{3.7}$$

where ω is defined in section 3.1.2. $U(\omega)$ is called an energy function, T is a constant termed temperature (which is assumed to take a value 1 unless otherwise stated in this thesis), and Z is the partition function, given as below:

$$Z = \sum_{all\ possible\ cofigurations\ of\ \omega} \exp\left[-\frac{U(\omega)}{T}\right] \tag{3.8}$$

The well-known Gaussian distribution is member of this Gibbs distribution family. Z is regarded not computable for complex cases, ex., for a case of 100×100 image with 5 defined land cover classes will be $5^{100\times100}$. Based on Eq. 3.7, it can be shown that maximizing $P(\omega)$ is equivalent to minimizing the energy function $U(\omega)$, given as below:

$$U(\omega) = \sum_{c\in C} V_c(\omega) \tag{3.9}$$

c is the clique as defined in Eq. 3.5, where $C = C_1 \cup C_2 \cup C_3$. $V_c(\omega)$ is called the clique potential function w.r.t a clique type C. Thus the energy function w.r.t three clique types used for the MRF modelling in this thesis (Eq. 3.5) can be expressed as follows:

$$U(\omega) = \sum_{\{i\}\in C_1} V_{C_1}(\omega_i) + \sum_{\{i,i'\}\in C_2} V_{C_2}(\omega_i, \omega_{i'}) + \sum_{\{i,i',i''\}\in C_3} V_{C_3}(\omega_i, \omega_{i'}, \omega_{i''}) \tag{3.10}$$

The equivalence between MRF and Gibbs distribution (Hammersley and Clifford, 1971; Besag 1974), provides mathematically tractable means of specifying the joint probability of an MRF. This means that a unique GRF exists for every MRF as long as the GRF is defined in terms of cliques on a neighborhood system. This can be given as follows:

$$P(\omega_i|\{\omega_{S-i}\}) = \frac{\exp[-\sum_{c\in A} V_c(\omega)]}{\sum_{\omega_{i'}} \exp[-\sum_{c\in A} V_c(\omega')]} \tag{3.11}$$

where $A \neq C$ is the set consisting of pixels containing i. Hence Eq. 3.11 states that the conditional probability $P(\omega_i|\{\omega_{S-i}\}) = P(\omega_i|\omega_{N_i})$ depends on the neighbors of site i. The proof of this equivalence in detail is given in the Appenix A. In section 3.4 and 3.5 we will describe further the developments and the application of the MRF for super resolution mapping and multisource data classification.

3.3 Fuzzy sets as an uncertainty measure

Fuzzy set theory (Zadeh 1965) provides the conceptual framework to solve the classification problems in an ambiguous environment. In the problem of image classification if we take an event ω which is a class label and consider it to be a fuzzy subset of the universe of discourse Ω, and **x** to be a feature vector of a particular pixel, then the PDF of ω can be represented by a fuzzy membership function $f_\omega$as follows

$$P(\omega) = \int_\Omega f_\omega(\mathbf{x}) \tag{3.12}$$

A fuzzy set for class ω, ώ over Ω is defined as the set of ordered pairs:

$$\acute{\omega} = \{(\mathrm{X}, f_\omega(X)), \mathrm{X} \in \Omega\} \tag{3.13}$$

where $f_\omega(\mathrm{X})(\in [0,1])$ is termed the grade of membership or simply the membership function, of the element X to the fuzzy set ώ. Importantly all the elements X in Ω belong to ώ with different grades of memberships (Fig. 3.3). In the case of satellite images, the pattern X is described as a vector in an M-dimensional space, $X = [x_1, x_2, .., x_K], x_K \in \Omega_K, i = 1,2, \dots, K$, where Ω_k denotes the k^{th} sensor data observation space (i.e. the source universe), and K the number of sensor bands. In the case of multisensory observation space the universal set Ω is the Cartesian product $\Omega_1 \times \Omega_2 \times \dots \times \Omega_K$. If $\omega = \{\omega_1, \omega_2, .., \omega_m\}$ is a set of predefined classes then each class ω is defined as fuzzy set over Ω. Thus $f_{\omega=\omega_1}(X)$ conveys information on the degree to which the pattern $\mathrm{X} \in \Omega$ may be treated as belonging to class ω. Depending on the image input (multispectral, SAR, SAR texture) the number bands differ.

Two different techniques were presented and tested to define the fuzzy membership for each training pixel in the optical and SAR data (Zhang et al., 2011; Sohn et al., 1999; Mertens et al., 2004; Muad et al., 2012). The first case is solely for the optical data, where sub pixel class fraction in the form of spectral angle for each pixel is used as the pixel membership. While the second method in the form of fuzzy c-mean (FCM) portioning works for both SAR and optical data.

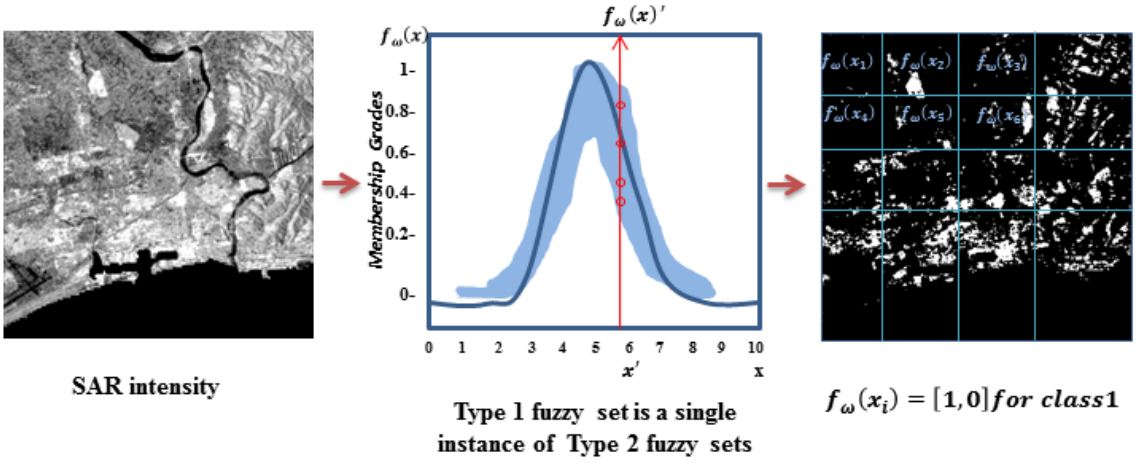

Figure 3.3 Fuzzy pixel membership generation using fuzzy functions (type 1or type 2) for SAR intensity, the central concept

The spectral angle is used to unmix the pixel to classes of interest. If $f_\omega(x_i)$ is the fuzzy membership value for the pixel vector $x_i \equiv x_m$ in the observed image **x,** the membership value was determined by calculating the spectral angle in radiance between the training pixel vector (x_i) and the reference spectra of the classes (r_i) as shown below.

$$f_\omega(\mathbf{x}) = cos^{-1}\left[\frac{\sum_{i=1}^{K} x_i r_i}{\sqrt{\sum_{i=1}^{K} x_i^2 \sum_{i=1}^{K} r_i^2}}\right] \quad (3.14)$$

To determine these membership values we use the fuzzy c-means partition matrix. The image X (when number of bands, *K***)** is portioned into a c × i matrix (*F*) with each element of the matrix ($f_\omega(x_i)$) showing the pixel membership value for class ω. Here C is the number of classes and i= *(*1,2,..,*M)* will be the number of pixels. The *J* function measures the difference between each pixel values and the cluster centers μ to estimate the *F* matrix. The clustering is performed according to the Eq. 3.15.

$$J_w(F,V) = \sum_{i=1}^{M}\sum_{\omega=1}^{C}(f_\omega(x_i) \times (x_i - \mu_\omega)^2) \quad (3.15)$$

Where V= $(\mu_1, \mu_2, \ldots, \mu_c)$ is the vector of the cluster centers, and *w* being the membership weighting exponent 1< w <∞. Parameter *w* is also known as the fuzzy exponent, controlling the level of cluster fuzziness. For a particular class of interest, different *w* values will result in different membership grades. Many optimal values for *w* (ranging from 1.1 to 1.2) have been suggested but it's less explained why one value of *w* is better than the other (Fisher, 2010). The parameter *w* was set to a usually accepted value of 2.0 (Wang, 1990) in aid to add more fuzziness to the membership assignment. A local minimum for J_w can be achieved under the condition shown in Eq. 3.16. Here w >1 and $y_i \neq \mu_\omega$

$$f_\omega(x_i) = \frac{1}{\sum_{j=1}^{c}\left[\frac{|x_i-\mu_\omega|}{|x_i-\mu_j|}\right]^{\frac{2}{(w-1)}}} \quad (3.16)$$

The number of spectral bands varies depending on the input imagery as mentioned earlier. In an instance of *K* spectral bands the fuzzy intersection operator is used to determine the membership for each pixel.

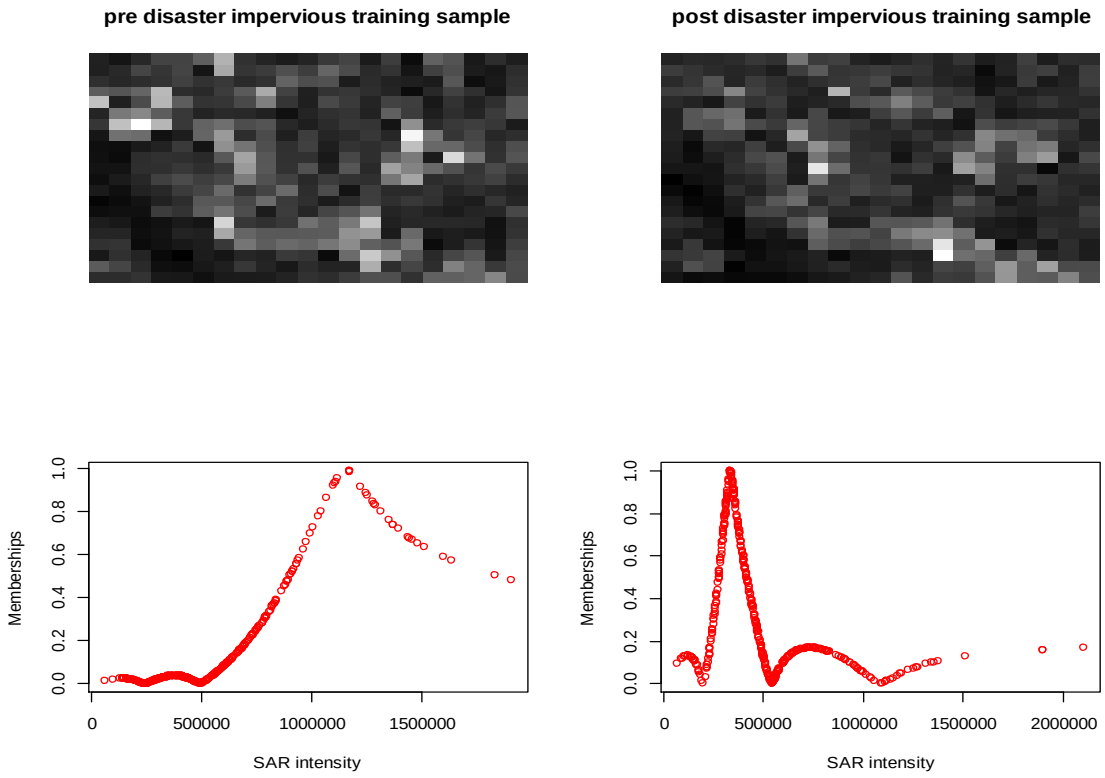

Figure 3.4 Example fuzzy membership functions for ALOS PALSAR intensity image pixels, over an impervious area

This multiple membership values for a feature vector realize to what extent it belongs to a land-cover class label; this redefines its contribution to the class mean and the variance. This is a more feasible approach to model the geometrical shapes of different clusters within the same data set. Accordingly the discrete fuzzy mean and the fuzzy covariance matrices can be derived from the definitions given by Wang (1990). Essentially this approach restructures the conventional mean and the covariance using fuzzy membership function. The incorporation of the fuzzy class parameters into the MRF model for SRM and multisource image classification will be discussed in section 3.4 and 3.5 respectively.

3.4 Markov Random Fields for super resolution mapping (SRM)

Let a set of pixel DN values in an observed image **x** with *K* spectral bands, are represented by $x_m, m = 1,2,..,M$ where *M* is the total number of pixels to be classified. The measurement vectors are represented as $x_m, m = 1,2,..,M_1 \times M_2$ in a pixel matrix $A \in (M_1 \times M_2)$ where M_1 and M_2 are the dimensions of the matrix. Let **c** be the resulting SRM defined on a pixels matrix *B*, with each of the pixel belonging to a unique class at a finer resolution than the observed image. Let an unobserved multispectral image be **y** with the same number of spectral bands as **x** but with a spatial resolution identical to **c**. The pixel location in y is represented by $y_{i,j}$. Also it is assumed that each pixel in y can be assigned to a unique class $c(y_{i,j})$. If the pixel resolution of the original image is *R* and that of the SRM is *r (<R)*, the

relation between the two images is determined by a scale factor which is denoted by *a=R/r*. Hence it can be seen that the pixel matrix $B = aM_1 \times aM_2$. In this study a is set to take an integer value for convenience. For each pixel $y_{i,j}$ a symmetric neighbourhood $N(y_{i,j})$ is defined by a window size *W*, where it is the length of the side of the squared window. Different definitions for the neighborhood system can be found in the literature (Li 2009). A second order neighborhood consisting the eight closest connected pixels (*W=3*) have been selected for this study. The classified image **c** will be modelled as a MRF with respect to the Neighborhood system $N(y_{i,j})$. MRF is defined by local properties, therefore the labelling of the pixels is considered to be effected by the neighborhood configuration (Tso and Mather 2009). It is here the MRF models take the advantage of modelling contextual dependencies, or the spatial correlation among the pixels. The set ω is referred as a random field with the probability distribution *P(ω)* describing the likelihood of finding the labels $c(y_{i,j}) = \omega \in \{1,2,..,l\}$ over the image for l number of land cover classes. The overall objective of the model is to classify all the pixels which maximize the global posterior probability *P(ω|**x**)*, which is the probability that *ω* is the correct overall scene labelling given the full set of measurement vectors **x**. According to the Bayes theorem a pixel x_m in the observed image is allocated to a class *ω* according to Eq. 3.17, where a value *ω* is selected to maximize the argument for a pixel to find the most appropriate scene label $\bar{\omega}$.

$$\bar{\omega} = argmax\{P(\boldsymbol{x}|\omega)P(\omega)\} \tag{3.17}$$

According to the equivalence of the MRF and the GRF (Eq. 3.11) the probabilities can be modelled as energy functions. Hammersley-Clifford theorem explains the existence of a unique GRF for every MRF as long as the GRF is defined by the cliques on a neighborhood system. A clique is a subset in which all pairs of the pixels are mutual neighbors (Tso and Mather 2009). Hence the prior probability P(ω) for the SRM, the conditional probability *P(**x**|ω)*, that the image **x** is observed given the true SRM and the posterior probability *P(ω|**x**)* are modelled by means of energy functions.

$$P(\omega|\boldsymbol{x}) = \frac{1}{Z} exp(-\frac{U(\omega|\boldsymbol{x})}{T}) \tag{3.18}$$

Where *Z* is the normalizing constant, *T* is the constant termed temperature and *U(ω|**x**)*, is the posterior energy function of the super resolution map **c** given the observed image **x** . Both the terms *Z* and *T* are independent of *ω* and **x**. Based on Eq. 3.18 it is clear that maximizing the probability *P(ω|**x**)* is equivalent to minimizing the energy function *U(ω|**x**)*.

3.4.1 Prior Energy for contextual dependencies

In the MRF, prior and likelihood energies are modelled individually. They account for the contextual and spectral properties of the observed image respectively. The prior energy is modelled by using the sum of pair-site interaction within the neighborhood system $N(y_{i,j})$, as follows:

$$U(\omega) = \sum_{i,j} U\left(c\left(y_{i,j}\right)\right) = \sum_{i,j} \sum_{l \in N(y_{i,j})} \beta[1 - \delta(c(y_{i,j}), c(y_l))] \tag{3.19}$$

The term $\delta(c(y_{i,j}), c(y_l))$ is called the "Kroneker delta", which takes a unit value when $\delta(c(y_{i,j})) = c(y_l)$ and 0 otherwise (Richards and Jia 2006). $\beta > 0$ controls the influence of the neighboring pixels, and can be an anisotropic or isotropic assumption made by the user. In this study this value is an isotropic expression which only depends on the Euclidian Distance *D* between the pixels $y_{i,j}$ and y_l, calculated by $\frac{1}{\bar{\omega}}[D(y_{i,j}, y_l)]^{-2}$. Where $\bar{\omega} = \sum_{l \in N_{i,j}} D(y_{i,j}, y_l) = 1$ is the normalizing constant. In Eq. 3.19 each

pixel contributes locally to the prior energy, which is denoted as $U(c(y_{i,j}))$. A single pixel in the observed optical image is assumed to follow a multidimensional normal distribution, which is determined by the mean and the variance of each spectral class. These fundamental parameters have been reformed using fuzzy definitions to determine the likelihood energy in the MRF.

3.4.2 Fuzzy mean vector and fuzzy covariance matrix

In the case of per-class covariance matrices, let the training pixels take values $x_1, x_2, .., x_n$ with n being number of training pixels for l number of classes. Then the respective fuzzy training data set can be represented as a fuzzy set $\{f_\omega(x_i) \in [0.0,1.0]\}$. The element $f_\omega(x_i)$ represents the fuzzy membership value of a training pixel $x_i (1 \leq i \leq n)$ to the class ω. The discrete fuzzy mean $\overline{\mu_\omega}$ and the fuzzy covariance matrix $\overline{\sum_\omega}$ for class ω can then be defined as follows:

$$\overline{\mu_\omega} = \frac{\sum_{i=1}^{n} f_\omega(x_i) x_i}{\sum_{i=1}^{n} f_\omega(x_i)} \tag{3.20}$$

$$\overline{\sum_\omega} = \frac{\sum_{i=1}^{n} f_\omega(x_i)(x_i - \overline{\mu_\omega})(x_i - \overline{\mu_\omega})^T)}{\sum_{i=1}^{n} f_\omega(x_i)} \tag{3.21}$$

Parameters can be estimated using the coarser resolution image. To determine the class membership grades for each pixel different approaches can be found in the literature, for an evaluation among these approaches additional research is required. The use of SA and FCM approaches provide us the means to investigate, any bias in the model to a specific membership grade definition. A single pixel in the coarser resolution image **x**, corresponds to s^2 pixels in the finer resolution SRM, **c**. Hence the PDF of an observed pixel vector x_m is assumed to be normally distributed with respect to the pixel composition with mean $\overline{\mu(x_m)}$ and covariance $\overline{\sum(x_m)}$, which can be defined using Eq. 3.22 and Eq. 3.23 as follows:

$$\overline{\mu(x_m)} = \sum_{\omega=1}^{l} \theta_\omega(x_m) \overline{\mu_\omega} \tag{3.22}$$

$$\overline{\sum(x_m)} = \sum_{\omega=1}^{l} \theta_\omega(x_m) \overline{\sum_\omega} \tag{3.23}$$

Here θ_ω is the proportion of the class ω in a pixel x_m, where $\sum_{\omega=1}^{L} \theta_\omega(x_m) = 1$. We also assume the spectral values of s^2 fine resolution pixels $y_{i,j}$ are independent and identically distributed, according to the normal distribution of the parameters of class $c(y_{i,j})$. This assumption is coming from the classical statistics in the form of sufficient statistics (REF) and probability fractions (Duda et al., 2001).

3.4.3 Fuzzy likelihood energy model

The conditional distribution of the observed image **x** with the given true class labels ω, is assumed to be Gaussian for the multi spectral images. We also assume a coarser spatial resolution pixel of the original image to contain a number of pure pixels at the fine spatial resolution. These fine spatial resolution pixels are strictly assumed to be spatially un-correlated. Therefore the fuzzy mean and the fuzzy covariance matrix of the observed pixel at a coarser resolution scale are directional sum of fuzzy mean vector and the fuzzy covariance matrix of the corresponding pixels at the fine resolution scale. Hence the conditional probability density function (PDF) in Eq., 3.18 for the observed image can be defined as follows:

$$p(\mathbf{x}|\omega) = \prod_{m} \frac{1}{(2\pi)^{K/2}\sqrt{\det(\overline{\sum(x)})}} \times \exp(-\frac{1}{2}\left(x_m - \overline{\mu(x)}\right)^t \overline{\sum(x)}^{-1} (x_m - \overline{\mu(x)})) \quad (3.24)$$

The likelihood energy in this case with respect to the relationship shown in Eq. 3.7 takes the form written by:

$$U(\mathbf{x}|\omega) = \sum_m [\left(x_m - \overline{\mu(x)}\right)^t \overline{\sum(x)}^{-1}\left(x_m - \overline{\mu(x)}\right) + Mln\left|\overline{\sum(x)}\right|] \quad (3.25)$$

The posterior energy function is established using the definitions of the Bayes theorem which combine the prior and the likelihood energy terms defined in Eq. 3.19 and 3.25 as follows:

$$U(\omega|\mathbf{x}) = U(\omega) + U(\mathbf{x}|\omega) \quad (3.26)$$

According to Eq. 3.18 the minimum of the posterior energy provides the optimum SRM $\omega \in \mathbf{c}$, which is the maximum a posterior probability solution for the SRM problem (Geman and Geman 1984). To control and balance the spectral and the contextual information flow during the SRM generation a parameter called "the smoothness parameter" $0 < \lambda < 1$is introduced to the posterior energy function in Eq. 3.26. Hence the full form of the posterior energy function can be written as:

$$U(\omega|\mathbf{x})) = \lambda U(\omega) + (1-\lambda)\mathrm{U}(\mathbf{x}|\omega) \quad (3.27)$$

The MAP estimation of the posterior energy in Eq. 3.27 is determined by using the stochastic Simulated Annealing technique (SA). This implements a Metropolis-Hasting sampling technique to reduce the energy to yield the maximum a posterior solution. A comprehensive explanation about the SA technique can be found in literature (Li 2009, Tso and Mather 2009) as well as in the end of this chapter.

3.5 Markov Random Fields for multisource image classification

The formulation of the MRF model for the multisource classification has significant changes from its design to the SRM discussed in the above section. These changes mainly occur due to the modifications of the MRF parameters to incorporate different sensor data (in this thesis Multispectral, SAR and SAR texture). This section describes the formulation of a MRF model to classify multispectral, SAR images, and its extension for more ancillary information such as SAR texture.

Let x_m and y_m denotes the observed optical (X) and SAR (Y) image pixel gray level values at a pixel location *m* respectively. The number of bands for X is *K*, while Y represents SAR polarization in the form of HH, HV, VH and VV. The intended label for each image pixel at location *m* is represented by ω_m. Depending on the number of classes l in the classification problem ω varies ($\omega_i \in \{1,2,..,l\}$). Within a considered pixel neighborhood *N* in the contextual model, a neighboring pixel label with the pixel in concern is represented by ω_n $n \in N$. According to the Bayesian theory the posterior distribution can be determined by combining both the prior and conditional probabilities of the optical and SAR images.

$$P(\omega|x_m, y_m) \propto P(x_m, y_m|\omega)P(\omega) \quad (3.28)$$

Due to the equivalence of the MRF and GRF these probabilities can be specified by means of energy functions. Hence we can write the Eq. 3.28 in its posterior energy form as

$$U(\omega|x_m, y_m) = U(x_m, y_m|\omega) + U(\omega) \tag{3.29}$$

where $U(\omega|x_m, y_m)$ is the posterior energy for a given class ω. In the case of multisource data, the measurements from different sensors are assumed to be conditionally independent. This simplifies the mathematical analysis. The validity of this assumption in the case of optical and SAR image integration is considerably higher due to the different wavelengths and different acquisition times of the images. As a result, statistically independent conditional probability distribution can be determined as below

$$P(x_m, y_m|\omega_m) \propto P(x_m|\omega_m) \times P(y_m|\omega_m) \tag{3.30}$$

Hence the MRF-MAP model for the combined SAR and optical sensors with corresponding reliability or discrimination criteria (λ) can be established as follows

$$P(x_m, y_m|\omega_m) \propto P(x_m|\omega_m)^{\lambda_1} \times P(y_m|\omega_m)^{\lambda_2} \tag{3.31}$$

According to Eq. 3.31 it is possible to include many different image indices such as SAR texture with an appropriate reliability criterion within this framework. If the SAR texture gray level at pixel location m is denoted as z_m, Eq. 3.31 can be extended to incorporate these information according to Eq. 3.32. It is important to note that the data distributions for each of the data set have to be done separately by examining their individual characteristics.

$$P(x_m, y_m, z_m|\omega_m) \propto P(x_m|\omega_m)^{\lambda_1} \times P(y_m|\omega_m)^{\lambda_2} \times P(z_m|\omega_m)^{\lambda_3} \tag{3.32}$$

Hence the class conditional energy for multisource data can be defined as follows:

$$U(x_m, y_m, z_m|\omega_m) = \lambda_1 \times U(x_m|\omega_m) + \lambda_2 \times U(y_m|\omega_m) \times \lambda_3 \times U(z_m|\omega_m) \tag{3.33}$$

The priror energy is modelled as shown in the previous section 3.4, from the multispectral data sets. The conditonal distribution for the SAR intensity and the texture is determined by using Gamma distribution and the Gaussian distribution respectively. For a pixel y_m given a true label ω_m of the multilook SAR intensity images follows a Gamma distribution. Hence the conditonal probability for SAR intensity can be defined as

$$P(y_m|\omega_m) = \frac{L^L}{\mu_\omega^L (L-1)!} y_m^{L-1} \exp(-\frac{L}{\mu_\omega} y_m) \tag{3.34}$$

where L denotes the number of looks and μ_ω is the mean value for class ω. According to the Gamma distribution (Eq. 3.34), the relative likelihood of a SAR intensity pixel to be classified to a class is mainly controlled by the class mean values. Notably this distribution function does not account for any spatial relationship among different urban land cover classes. Therefore the conditonal energy can be derived according to the MRF and Gibbs equivalnce as shown in Eq., 3.35.

$$U(y_m|\omega_m) = \frac{L}{\mu_\omega} y_m - (L-1)\log(y_m) + L log(\mu_\omega) \tag{3.35}$$

Fuzzy mean vectors for the clases in Eq. 3.35 were used instead of its conventional crisp definitons (see section 3.3). Fuzzy set theory provides the base to construct a more meaningful relationship between a pixel and a class using the grades of memberships. Intermidiate grades of membership improve the pixel belongingness to a particular class providing much better estimation for the class mean values. This pixel

weighting schemce is advantageous particularly in the case of distribution functions such as Gamma distribution, where the estimation is strongly controlled by class mean values.The discrete fuzzy mean $\overline{\mu_\omega}$ can then be defined using the Eq. 3.22. This new implementation is abrreviated as fuzzy MRF (FMRF) and the conventional approach as MRF.

The optical and SAR texture likelihood information was modelled using the multvariate gaussian distribution, in Chapter 5 we show this in detail. The prior class information is modelled always by using the optical image. For a particular pixel x_i of the observed optical image, propotion of the land cover class of interest is determined using Singular Value Decomposition (SVD) (for details see Apeendix A).

Let $b_\omega(x_i) \in b_1(x_i), b_2(x_i), \dots, b_l(x_i)$ represent the propotion of land cover in the pixel x_i for class $\omega \in (1,2,..,\mathrm{l})$ in the the observed multispectral image. Let a corresponding pixel of the initial class image (S) be $s_i \in (1,2,\dots,l)$. Then a class is assigned to a pixel based on the maximum class propotion recorded in any of the coarser resolution multspectral image pixel.

$$(\mathrm{s_m}) \equiv \max \mathrm{b_\omega(x_m)} \tag{3.36}$$

Under the assumption of pair-site interaction, in which the pixel of interest and one of its eight neighbors (2^{nd} order neighborhood) is considered, the prior energy is defined as:

$$U(\omega_m) = \sum_i \lambda \times \delta(\omega_m, \omega_n) \tag{3.37}$$

where $U(\omega_m)$ is the local contribution to the prior energy from a pixel x_m in the optical image. λ denotes the weigting parameter for each pixel and $\delta(\omega_m, \omega_n)$ takes a value 0 if $\omega_m = \omega_n$ and 1 otherwise. Combining Eq. 3.35 and Eq.3.37 and the optical and SAR texture information we can define the posteriro energy for the multisource data sets as follows:

$$\begin{aligned} &U(\omega|x,y,z) \\ &= \lambda \times U(\omega) + (1-\lambda) \sum_{m,l} [\left(x_m - \overline{\mu(x)}\right)^t \overline{\sum(x)}^{-1} \left(x_m - \overline{\mu(x)}\right) + \frac{1}{2} ln\left|\overline{\sum(x)}\right|] + (1-\lambda)^2 \\ &\times \left(\frac{L}{\overline{\mu_\omega}} y_m - (L-1)\log(y_m) + Llog(\overline{\mu_\omega})\right) + (1-\lambda) \sum_{m,l} [\left(z_m - \overline{\mu(z)}\right)^t \overline{\sum(z)}^{-1} \left(z_m - \overline{\mu(z)}\right) \\ &+ \frac{1}{2} ln\left|\overline{\sum(z)}\right|] \end{aligned} \tag{3.38}$$

The realiability factor λ controls the contributions from the optical, SAR and SAR texture imagery in the form of prior and likelihood energy for the posteriro energy determination. It is possible to regulate this factor considering two main condtions, the level of details you need in the calssification process and also in terms of the highest classification accauracy.

3.6 Simulated annealing with a combined annealing schedule

The MAP estimation of the posterior energy in Eq.3.38 can be determined by using the stochastic Simulated Annealing technique (SA). This implements a Metropolis-Hasting sampling technique to reduce the energy and retrieve MAP solution. SA algorithm allows the randomness (T-temperature), to decrease in an iterative way so that the best solution for Eq. 3.38 can be made. The temperature will be

decreased according to the criterion called annealing schedule. The process is repeated until the system becomes frozen (T→0), which means pixels stop updating. The annealing schedule is very important considering the MAP algorithm. Different annealing schedules are tested in many studies. Logarithmic and power-law annealing schedules are two of the most preferred annealing schedules. Logarithmic schedules are considered to be the most promising in the case of better solutions for the global energy minimization. But it will lead to a slower annealing process. Hence combining the two cooling schedules within the SA is tested. Eq. 3.39 and Eq. 3.40 shows the logarithmic and the power-law annealing schedules used respectively.

$$T(t) = \frac{T_0}{\log(1+t)} \tag{3.39}$$

$$T(t) = \mathrm{K} \times T(t-1) \tag{3.40}$$

where T_0 is the initial temperature, $_{\mathrm{K}}$ the cooling schedule parameter and *t* the iteration number. For better results in a complex situation, a large value for both these parameters which slows down the annealing process is recommended (Geman and Geman 1984). We start with a logarithmic annealing schedule and made it to change for the power-law schedule after the temperature (T(*t*)) drops to a certain value. This temperature value was determined by several experimental runs. Detailed explanation of the SA technique can be found in chapter 2.

3.7 Texture Measures for SAR imagery

Several important texture measures were used for the SAR data in this work. These texture measures are important they reduce the speckle noise in the SAR imagery as well as bring out spatial correlation structure into the classification mechanism. It is important for the reader to understand the formation of these texture measures in detail. Two different types of texture measures are introduced in this work, 1) Multiplicative Autoregressive Random Field (MAR) 2) spatial autocorrelation based texture (Moran's $\mathrm{I_i}$ Index, Geary's $\mathrm{C_i}$ Index and Getis-Ord $\mathrm{G_i}$ Index).

3.7.1 Autoregressive texture

Multiplicative Autoregressive Random Field (MAR) based texture models have been identified as one of the most appropriate models for SAR intensity images to capture the stochastic spatial interaction among neighboring pixels. Texture feature have received more attention, mainly because they can suppress the effect of SAR image speckle noise (Stasoll, and Gamba, 2008; Gamba and Aldrighi, 2012; Qin et al.,2004; Dekker, 2003; Derin et al., 1987; Dubes and Jain, 1989). On the context of texture, the first order statistics of the fading random variables describe their probability density functions while the second order fading texture statistics such as auto correlation function describes the relationships between pixels and its neighbors (Ulaby et al., 1996). A comprehensive discussion of the properties of second order statistics which describes how often one gray tone will appear in a specific spatial relationship to another gray tone can be found in Ulaby, 1996 and Haralick, 1973. (Ulaby et al., 1996, Haralick et al., 1973). Lognormal Random field based radar image synthesis was first proposed by Franknote and chellappa, 1987 in detail (Franknote and chellappa, 1987). MAR model based texture parameters using RADARSAT data were employed in one of the studies to detect forest fires, as a major application (Park et al, 2001). Hear it was summarized that the fusion of textural information with the information such as changes in backscatter can improve the results. Let an image *y(i,j)* be represented as a random disturbance (noise) driven multiplicative system as follows:

$$y(i,j) = \prod_{[\,r=(m,n)]\in N} y(i+m, j+n)^{\theta_r}\, v(i,j) \tag{3.41}$$

where *N* is the neighborhood set defining the model support, *v(i,j)* is the log normal white noise process which is also referred to as the driving process, and θ_r is the exponent weighting factor for a neighborhood *r*. In the case of first-order neighborhood (Mather 2009) four particular neighbors contribute to the centre pixel *(i,j)*. Then the centre pixel *y(i,j)* can be modelled as follows.

$$y(i,j) = y(i-1,j)^{\theta_{-1,0}} \times y(i-1,j)^{\theta_{0,-1}} \times y(i-1,j)^{\theta_{1,0}} \times y(i-1,j)^{\theta_{0,1}} \tag{3.42}$$

Eq. 3.42 was extended for a second order neighborhood configuration in the study. The random field *y(i,j)* is said to obey a log-normal MAR model if $x(i,j) = ln(y(i,j))$ with $u(i,j) = ln(v(i,j))$ obeys a Gaussian autoregressive random field model represented by a difference equation.

$$x(i,j) = \sum_{[r=(m,n)\in N]} \theta_r x(i+m, j+n) + u(i,j) \tag{3.43}$$

Hear θ is called the neighborhood weighting parameter and *u(i,j)* is the zero mean white Gaussian noise, with the covariance given by.

$$Cov_u(r) = \begin{cases} \sigma_u^2, & r = (0,0) \\ 0, & r \neq (0,0) \end{cases} \tag{3.44}$$

Where σ_u is the variance of *u*. Three main parameters of the MAR model can be used as texture descriptors. They are the weighting parameter θ, the noise variance σ_u^2 and the mean value δ_x of the stationary random process *x*. The neighborhood weighting parameter and the noise variance fit the logarithm of the observed data into a Gaussian random filed model. The weighting parameter is nonnegative and explains the degree of possible interaction of the neighborhood pixel values to the pixel in concern (Ord 1975). The random noise term as explained earlier is uncorrelated and normally distributed with zero means and equal variance. These parameters which characterize the image are determined by using the least square estimation with a given image *y(i,j)* of size $M \times M$ and its log transform $x(i,j) = ln(y(i,j))$. They are shown as below with the Fig. 3.5:

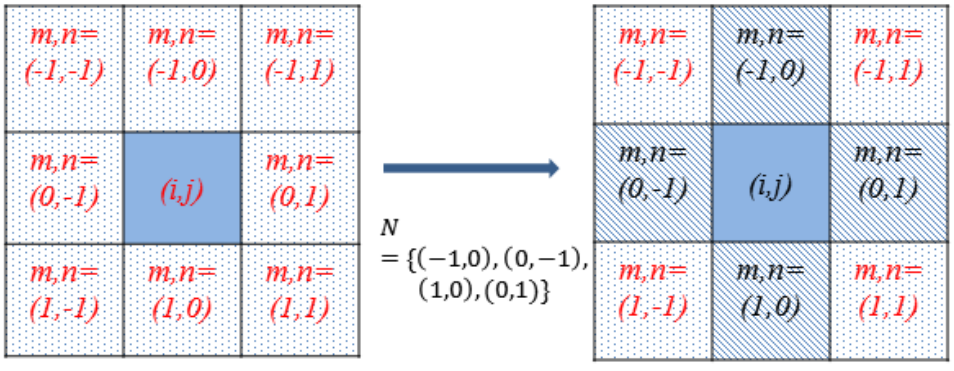

Figure 3.5 Pixel (*i,j*) and its first and second order neighborhood and the defined neighborhood set N, that contributes to the central pixel (*i,j*) when applying the MAR model

$$\delta_x = \frac{1}{M^2}\sum_{i,j} x(i,j) \tag{3.45}$$

$$z(i,j) = row(x(i+m, j+n) - \delta_x, r \in N) \tag{3.46}$$

$$\sigma_u^2 = \frac{1}{M^2}\sum_{i,j}[x(i,j) - \delta_x - \theta^T \times z(i,j)] \tag{3.47}$$

$$\theta = \frac{\sum_{i,j} z(i,j) \times (x(i,j) - \delta_x)}{\sum_{i,j} z(i,j) \times z^T(i,j)} \tag{3.48}$$

Here $z(i,j)$ is calculated as a row-scanned vector. Depending on the land surface structure represented in different images, MAR texture parameters will have different values. Hence the images with pixel values defined by each of these parameters can be considered as the synthetic representation of their original images. Theoretically any image processing operation that works on the original image can be performed using these texture parameters. In the current study we employed two of these three parameters, the neighborhood weighting parameter θ and the noise varianceσ_u^2.

3.7.2 Autocorrelation texture

More than in remote sensing in GIS (Geographic Information Systems), the use of local indicators of spatial autocorrelation is prominent. The possibility of extending these indicators for remote sensing can be done by using autocorrelation texture measures. The types of spatial autocorrelation and the most common neighborhood configuration to extract it are shown in Fig. 3.5.The three indexes proposed for the evaluation of global spatial autocorrelation of the SAR image are, Moran's I_i Index, Geary's C_i Index and Getis-Ord G_i Index.

Local Moran's I_i Index evaluates the similarity between the neighbors of each target value and the mean, providing a measure of local homogeneity. Let the set of observed SAR intensity (Y) pixel values be $y_{i=1}, y_{i=2}, \ldots, y_{i=n}$, the formulae for Moran's I_i compute a product-moment numerator between the pivotal locality *i* and all the localities *j* that have non zero connection to it, according to weight matrix **W**. The binary matrix **W,** which defines neighborhood relation**s,** being 1 the presence of connection and 0 the absence**.** The most common configurations are the so called Rook's, Bishops's and Queen's cases (Fig. 3.4). Hence the Moran's I_i measure can be formulated as follows:

$$I_i = \frac{y_i - \bar{y}}{\sum_i \frac{(y_i - \bar{y})^2}{n}} \sum_j W_{ij}\,(y_i - \bar{y}) \tag{3.49}$$

where *i* is the pivotal locality and *j* is all the other localities. I_i values range in [-1;1]. The index value decreases with correlation,-1means strong negative spatial autocorrelation, +1 strong positive spatial autocorrelation and 0 spatially uncorrelated data.

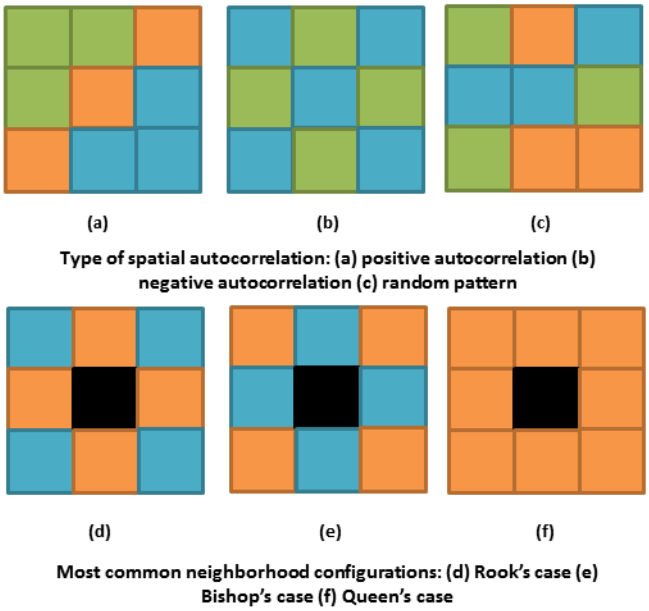

Figure 3.6 Types of spatial autocorrelation and the most common neighborhood configurations (Same colors represents same gray level values).

Geary's C_i index identifies areas of high variability between a pixel value and its neighboring pixels, providing a measure of local dissimilarity. It calculates a standardized squared distance between the pivotal locality *i* and other localities *j* that have none zero connection to it. It is useful for detecting edge areas between clusters and other areas with dissimilar neighboring values.

$$C_i = \frac{1}{\sum_i \frac{(y_i - \bar{y})^2}{n}} \sum_j W_{ij} (y_i - \bar{y}) \tag{3.50}$$

It ranges within [0,2], where 0 results in case of strong positive spatial correlation, 2 in case of strong negative spatial correlation and 1 denotes uncorrelated data.

Getis-Ord G_i Index identifies hot spots, such as areas of very high or very low values that occur near one another. It sums the variates attached to all the localities neighboring the pivot and divides by the sum of all the localities.

$$G_i = \frac{\sum_j W_{ij}\, y_j}{\sum_j y_j} \quad j \neq i \tag{3.50}$$

G_i Index is usefull determine clusters of similar values, where concentrations of high values result in a high-G_i value (> 0) and concentration of low values result in a low-G_i (< 0). The use of these texture measures for SAR data preprocessing will be discussed in the next chapter.

3.8 Change detection algorithms

The main purpose of these texture measures is to incorporate them in the MRF based multisource satellite image classification as ancillary information. In addition to that experiments were also carried out

to examine the possibilities of using texture for time series change analysis using SAR data. Here we employed several recent contextual change detection algorithms to see the effect of texture measures to identify spatial changes in the land cover.

3.8.1 Semivariogram's

Both the log transformed radar image pixel values and their texture descriptors are associated with ground locations. Hence these random variables can be considered as regionalized variable with their known position in space. Variograms measure the spatial variation in these regionalized variables (Woodcock 1988a; Woodcock 1988a; Curran 1988). It is thus possible to use variograms to investigate the spatial structure of the urban landscape represented by both the log normal and the MAR model based texture variables for the SAR images.

If a transect of pixels M on top of a particular land cover class of interest is selected from the log transformed SAR image and the texture image, given its digital number y at pixel position *i* (i=1,2,..,M,) the relationship between a pair of pixels at a lag distance *h* can be defined using the average variances of the differences between all such pairs. With the single pixel variance being half of all such combinations, semivariance s^2 for a lag distance of *h* can be given by:

$$\gamma^2 = \frac{1}{2}[y(i) - y(i+h)]^2 \tag{3.51}$$

For a transect or a subset of M pixels in a particular land cover class with a predefined lag distance, an unbiased estimation of the average semivariance in *m* pairs can be defined as follows:

$$S^2 = \frac{1}{2m}\sum_i^m [y(i) - y(i+h)]^2 \tag{3.52}$$

Effects of natural disasters are directional independent in many of the instances. However it is useful to model the variograms to suit the presence or absence of the isotropy. In this study we compute the variograms along a transect taking into account different directions using a radius defined by N number of pixels. For *i*=1,2,..,M and *j*=1,2,..,N on a regular lattice ($M \times N$), the sample semi-variogram at lag (h, k) then becomes:

$$g(h,k) = \frac{1}{2(m-h)(n-k)}\sum_i^m\sum_j^n \{[x(i,j) - x((i+h),(j+k))]^2\} \tag{3.53}$$

3.8.2 Structural Similarity Index Matrix (SSIM)

SSIM is a very recent objective image quality measure used for image quality evaluation. The application of these measures to extract the temporal changes from SAR texture images is very recent and new. The general formula for the SSIM in the case of pre and post disaster MAR weighting parameter based texture is as follows:

$$SSIM = \left[l\left(\theta_{y(t1)}, \theta_{y(t2)}\right)\right]^{\alpha} \cdot \left[c\left(\theta_{y(t1)}, \theta_{y(t2)}\right)\right]^{\beta} \cdot \left[s\left(\theta_{y(t1)}, \theta_{y(t2)}\right)\right]^{\gamma} \tag{3.54}$$

where

$$l\left(\theta_{y(t1)},\theta_{y(t2)}\right)=\frac{2\mu_{\theta_{y(t1)}}\mu_{\theta_{y(t2)}}+c_1}{\mu^2_{\theta_{y(t1)}}+\mu^2_{\theta_{y(t2)}}+c_1}$$

$$c\left(\theta_{y(t1)},\theta_{y(t2)}\right)=\frac{2\sigma_{\theta_{y(t1)}}\sigma_{\theta_{y(t2)}}+c_2}{\sigma^2_{\theta_{y(t1)}}+\sigma^2_{\theta_{y(t2)}}+c_2} \quad (3.55)$$

$$s\left(\theta_{y(t1)},\theta_{y(t2)}\right)=\frac{2\sigma_{\theta_{y(t1)}\theta_{y(t2)}}+c_3}{\sigma_{\theta_{y(t1)}}\sigma_{\theta_{y(t2)}}+c_3}$$

$\theta_{y(t1)},\theta_{y(t2)}$ are the weighting texture measures generated using MAR models for the two time series log transformed images ($y(i,j)$) respectively. The first term in Eq. 3.55 is the luminance comparison function which measures the closeness of the mean luminance of the two textural images. The second term which is the contrast comparison functions measuring the closeness of the contrast between the two images. Contrast is defined as the standard deviation of the two images ($\sigma_{\theta_{y(t1)}},\sigma_{\theta_{y(t2)}}$). The third is the structure comparison function, where $\sigma_{\theta_{y(t1)}\theta_{y(t2)}}$is the covariance between the images. This third element relates to the correlation coefficient between the resulting image and the reference. The positive constants $c_1, c_2\ and\ c_3$ avoid the null denominator. A simplified version of the SSIM results as below (Zhou 2004; Hore and Ziou, 2010) :

$$SSIM\left(\theta_{y(t1)},\theta_{y(t2)}\right)=\frac{\left(2\mu_{\theta_{y(t1)}}\mu_{\theta_{y(t2)}}+C_1\right)\left(2\sigma_{\theta_{y(t1)}\theta_{y(t2)}}+C_2\right)}{\left(\mu_{\theta_{y(t1)}}{}^2+\mu_{\theta_{y(t2)}}{}^2+C_1\right)\left(\sigma_{\theta_{y(t1)}}{}^2+\sigma_{\theta_{y(t2)}}{}^2+C_2\right)} \quad (3.56)$$

The c_1 and c_2 parameters were set to take two small contestant values of 0.01 and 0.03 respectively, for more stability in the measurement (Wang et al. 2004; Wang and Li, 2011). A value 0 for SSIM shows no correlation among the images, while a value 1 suggests that the images are almost similar. Hence the resulting SSIM maps will corresponds to dark tones in the areas where spatial changes are resulted. The use of SSIM index with texture for the temporal changes is a novel approach associated and tested in this study.

3.8.3 Mean Ratio Detector (MRD)

MRD assumes the changes to occur as a modification of the local mean values in a particular spatial neighborhood of the two images (Inglada 2007). Eq. 3.57 defines the MRD. The spatial neighborhood considered for this measure was tested from a pixel combination of 3×3, 5×5 to7×7. The effect of these neighborhood configuration for the results found to be very close, hence the results reported in this study is from a neighborhood size of 3×3.

$$r_{MRD}=1-min\left\{\frac{\mu_{Ny(t1)}}{\mu_{Ny(t2)}},\frac{\mu_{Ny(t2)}}{\mu_{Ny(t2)}}\right\} \quad (3.57)$$

Here μ_N is the mean value determined for an N^{th} order spatial neighborhood of the log transformed image y. MRD based changes were determined for the log estimation as well as the MAR based texture.

3.8.4 Gaussian Kullback-Leibler detector (GKLD)

A pixel can be considered to have changed during time if its statistical distribution is changed from one image to another. In order to quantify this change, a measure which maps the two estimated statistical distributions (one for each date at a co-locate area) into a scalar change index is required. The Kullback-Leibler divergence can be very useful in such instances. Let $P_{y(t1)}$ and $P_{y(t2)}$ be two probability laws of the time series random variable $y(t1)$ and $y(t2)$. The Kullback-Leibler divergence from $y(t1)$ to $y(t2)$, in the case where these two have the densities $f_{y(t1)}$ and $f_{y(t2)}$, is given by:

$$K\big(y(t1)\big|y(t2)\big) = \int log\frac{f_{y(t1)}}{f_{y(t2)}} f_{y(t1)} d\big(y(t1)\big) \tag{3.58}$$

Since Kullback-Leibler divergence can be understood as the entropy of $P_{y(t1)}$ relative to $P_{y(t2)}$, it is also called the information gain. It can be proven that $K\big(y(t1)\big|y(t2)\big) \geq 0$; $K\big(y(t1)\big|y(t2)\big)$ vanishes only when the two laws are identical. $K\big(y(t1)\big|y(t2)\big)$ can be used as a measure of the divergence from $P_{y(t1)}$ to $P_{y(t2)}$. This measure is not symmetric but a symmetric version may be defined by writing:

$$D\big(y(t1)|y(t2)\big) = D\big(y(t2)|y(t1)\big) = K\big(y(t2)|y(t1)\big) + K\big(y(t1)|y(t2)\big) \tag{3.59}$$

Eq. 3.59 is called the Kullback-Leibler distance (KLD). If the local statistics have to be compared up to the second order, the local random variables, $y(t1)$ and $y(t2)$ maybe assumed to be normally distributes. Then the pdf $f_{y(t1)}$ can be written as:

$$f_{y(t1)} = \frac{1}{\sqrt{2\pi\sigma^2_{y(t1)}}} e^{-\frac{(y(t1)-\mu_{y(t1)})^2}{2\sigma^2_{y(t1)}}} \tag{3.60}$$

Same follows for the PDF $f_{y(t2)}$. Using this Gaussian model in Eq. 3.59, it yields the Gaussian Kullback-Leibler detector (GKLD).

$$r_{GKLD} = \frac{\sigma^4_{y(t1)} + \sigma^4_{y(t2)} + \big(\mu_{y(t1)} - \mu_{y(t2)}\big)^2 \big(\sigma^2_{y(t1)} + \sigma^2_{y(t2)}\big)}{2\sigma^2_{y(t1)}\sigma^2_{y(t2)}} - 1 \tag{3.61}$$

From Eq. 3.61 it can be seen that even in the case of identical mean values, this detector is able to underline the shading texture which is linked to the local variance evolution. These models cannot be used with SAR intensity vales as they deviate from Gaussian assumptions having always positive values.

3.8.5 Image ratio and the principal component transformation (PCA)

In addition to the three main approaches for the temporal changes we implemented two fundamental and well known change detection methods to extract the damage areas as our references. They are the image ratio and the principal component transformation (PCA). A normalized ratio measure is attained as shown in Eq. 3.62 by using the two log transformed images.

$$R(T) = \frac{y(t_1) - y(t_2)}{y(t_1) + y(t_2)} \tag{3.62}$$

Where *R(T)* is the ratio of the log transformed images $y(t_1)$ pixel i, j at time t_1. If the log estimation for a pixel of the two images is nearly the same then *R(T)* will take a value close to zero indicating no change while for a change this will be a larger value (Singh 1989). In the case of principal component (PC) transformation the original data is mapped to a new set whose covariance matrix is diagonal so that the data can be represented without correlation. This analysis is made possible because the unchanged areas which have high correlation between the pre and post disaster images with common variance in the two days can be explained using the first PC which account for the maximum possible variance in the case of time series images. On the contrary changed areas which occupy a small region in the two images would be presented in the second principle component. For this purpose the pre and post disaster images are stacked to perform a single image, and this combined image is transformed to its PC components. If the stacked image is y_s with a dimension of l =1,2..,L mathematically as a set $y_{s_l}^T = [y_{s_1}, y_{s_2}, \dots, y_{s_L}]$, with the covariance matrix being $\sum$, the principle components p_l of the set can be expressed by the Eq. 3.63.

$$p_l = e_{l1} y_{s_1} + e_{21} y_{s_2} + \cdots . + e_{L1} y_{s_L} \tag{3.63}$$

Here T denotes the transpose of the matrix and $e_l^T = [\, e_{l1}, e_{l2}, .., e_{L1}]$ is the eigenvectors of the covariance matrix Σ. There will be high correlation between the two images for the unchanged area while in the case of changes it will be low (Liu 2004). In this work we used the log transformed polarimetric components as the input for the PCA based change analysis.

3.5: Error measures for validation of the classification

Several error measures are used for the accuracy assessment of the MRF based classification results and the change detection results. The comparison of classification results is a difficult task considering the problems of the co-registration between the data sets as well as the lack of reliable ground truth information. The main error measures used of the MRF based classification results are the overall accuracy (OA) and Cohen's kappa statistics (Congalton 1991), which is also known as kappa coefficient using the contingency tables. Additionally three error measures were also employed, root mean square error (RMSE), correlation coefficient (CC) and the area error proportion (AEP) as mentioned in Eq. 3.64, 3.63, and 3.66.

$$RMSE = \sqrt{\frac{1}{MN} \sum_i t_{\omega i}^1 - t_{\omega i}^2} \tag{3.64}$$

$$CC_\omega = \frac{\sum_i \left(\overline{t_\omega^1} - t_{\omega i}^1\right) . \left(\overline{t_\omega^2} - t_{\omega i}^2\right)}{(M.N - 1.) . S_{t_\omega^1} . S_{t_\omega^2}} \tag{3.65}$$

$$AEP_\omega = \frac{\sum_i \left(t_{\omega i}^1 - t_{\omega i}^2\right)}{M.N} \tag{3.66}$$

Here $t_{\omega i}^{1}, t_{\omega i}^{2}$ are the fractional estimation of the damaged class ω within a user determined neighborhood of an M×N, in the two images. $\overline{t_{\omega}^{1}}, S_{t_{\omega}^{1}}$ are the mean and the standard deviation of class α in the first image.

With this discussion of the detailed fuzzy MRF theories for SRM and multisource image classification, SAR texture and change detection using time series images, we conclude this chapter. Appendix C will provide details of certain proofs and probability theories necessary for complete understanding.

4

Test sites and preliminary data processing

This chapter is devoted to detail the test sites, data descriptions and data preprocessing steps. This description is important for the reader to understand the image and the object space focused in the study. The descriptions of the preprocessing operations are mainly important to understand the image statistics, and the integration in the MRF model.

4.1 Test sites

Two test areas in Asia were selected for this study. The first is the western coastal area of Sri Lanka and the second is the eastern coastal zone of Japan. Both of these areas represent urban land cover. But interestingly the topographic and the atmospheric conditions varied heavily due to the difference in geographic location.

The fuzzy MRF based SRM technique was tested using real satellite images. For the experiments we selected the southwest urban coastal zone (Colombo south) of Sri Lanka as the first test site. Colombo lies in between 6^{o} $55^{'}$ $54^{"}$ N Latitude and 79^{o} $50^{'}$ $52^{"}$ E Longitude with the mean sea leave elevation of 1m. In particular, this area is subjected to a major construction in the form of a highway running from the south to north direction. Due to these heavy construction activities the Land-covers of the region is exposed to considerable amount of changes. The major land-use/land-cover classes occurred in this region includes vegetation, impervious surface ranging from low to high albedo, exposed soil and grass and water. Out of these major land-cover classes' three main classes are considered for the study, Vegetation (V), Impervious surface (I) and exposed grass and Soil (S). This selection was influenced by Ridd`s (Ridd 1995) V-I-S model to determine the urban composition. As a result of these construction activities a significant portion of the vegetation class in the vicinity is transforming to be impervious. With respect to the existing heterogeneity of the land-cover categories and their alterations it was observed that the area is changing towards to a more complete urban settlement. Fig. 4.1 provides the details of the study area, with the Google map images showing the land cover changes from the year 2007 to year 2009.

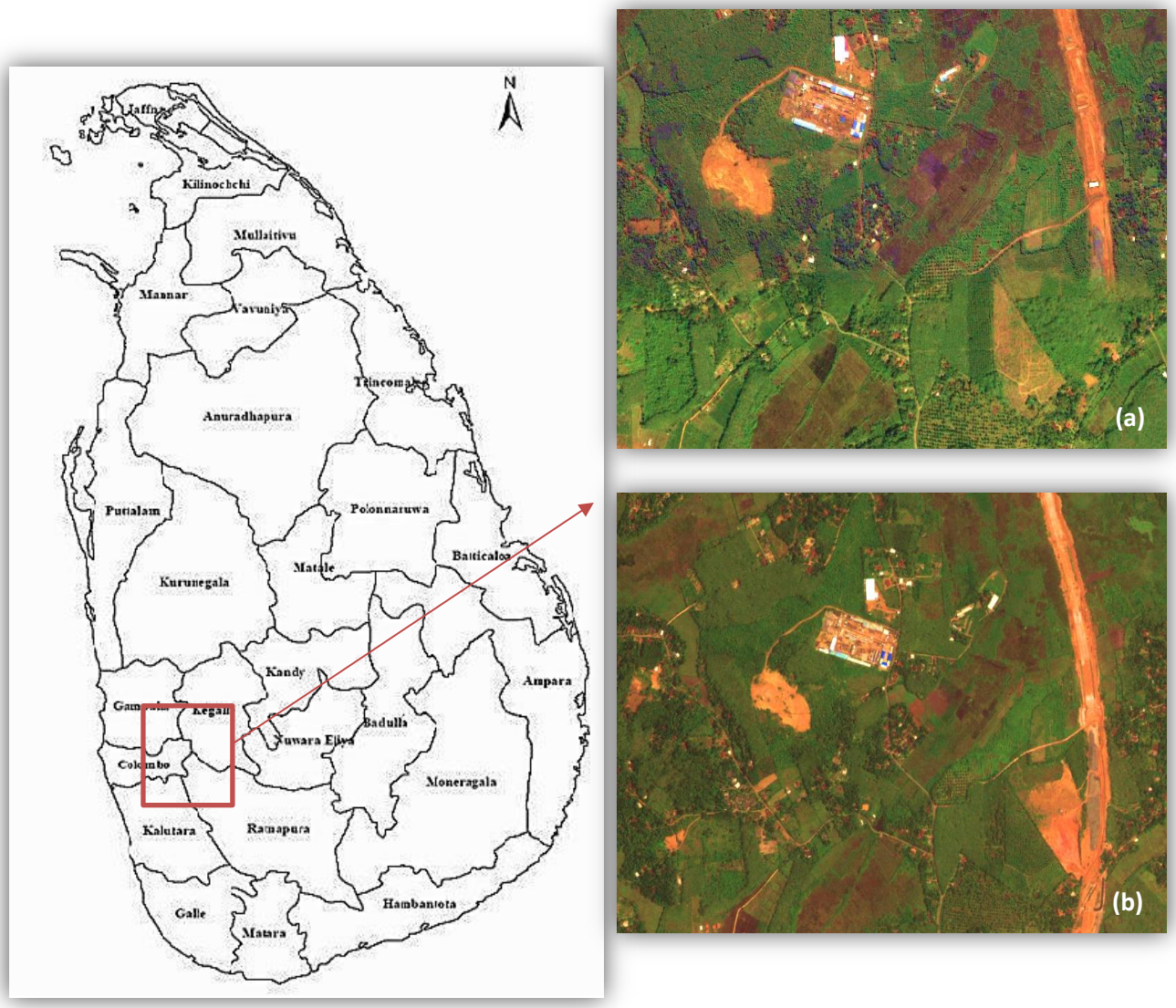

Figure 4.1 Google map image of the Study site in the west coast of Sri Lanka, for (a) year 2007 and (b) year 2009

The second study region was selected from the eastern coast of Japan. This area covers the heavily damaged Ishinomaki and Onagawa areas due to the March 11th off the pacific coast earth quake and tsunami. The Ishinomaki city lies in between 38^{o} 25$^{'}$ 00$^{''}$ N Latitude and 141^{o} 18$^{'}$ 00$^{''}$ E Longitude with the mean sea level elevation of 1m. Ishinomaki city and the areas north to the city are located in a flat basin. Two main rivers flow through the area; one which runs to the south through Ishinomaki city (Old-Kitakami river) and the other which runs eastward through Ogatsu area (Kitakami river). Many of the primary land covers of the area belong to cultivated paddy lands while the impervious, soil and vegetation dominates the rest. Fig. 4.2 shows the area map and the AVNIR-2 true color image of a part of the area. The multisource data classification was performed based on this second study site. Fig. 4.3 shows a complete cross section of the study area and the main image indices available with pixel and sub pixel based measurements from the multispectral images and the SAR images.

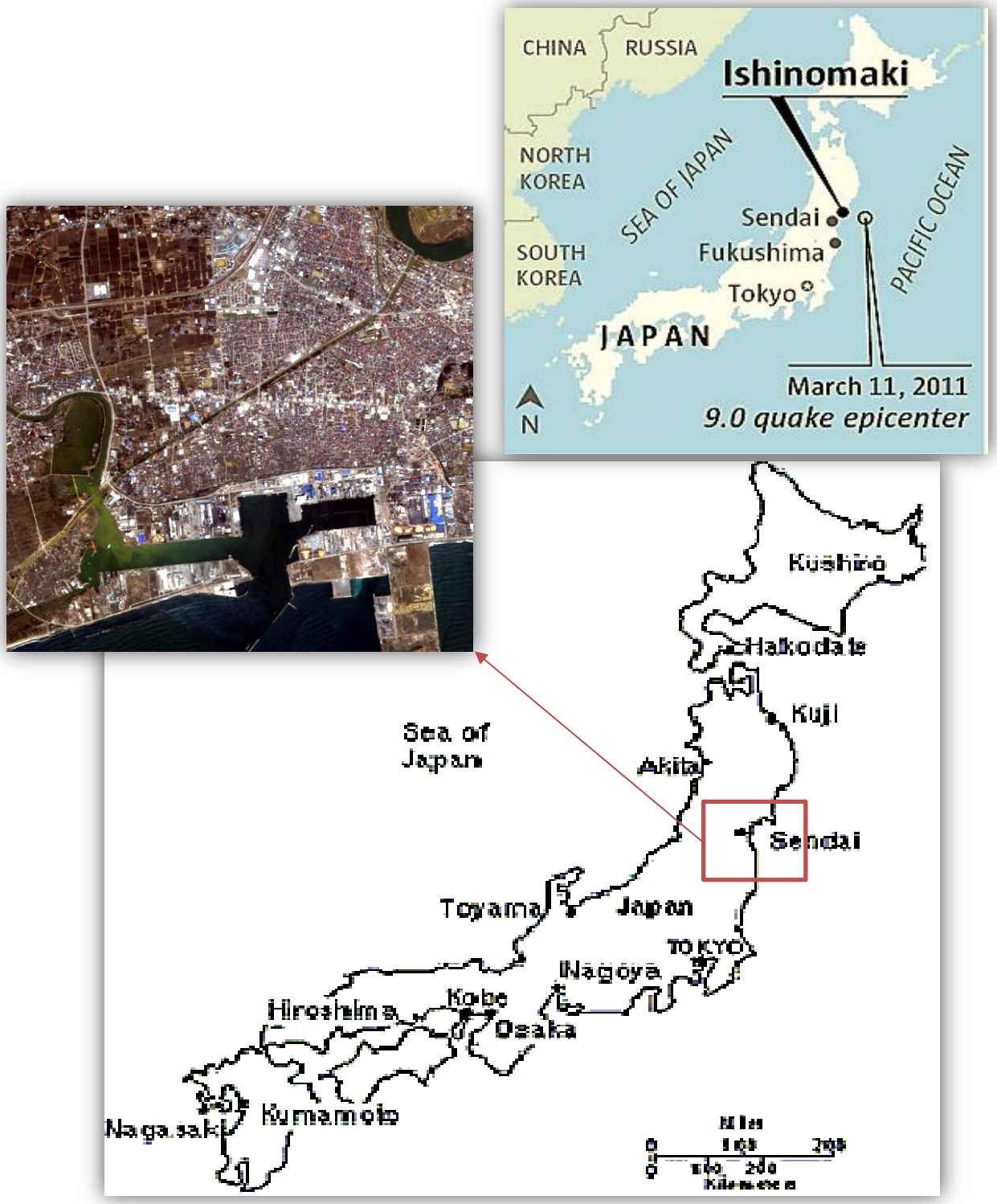

Figure 4.2 Study area map and earth quake epicenter (source-USGS) of the Tohoku region, Japan (a) AVNIR-2 true color image of the area (b) earth quake epicenter (source-USGS) on 11th March 2011

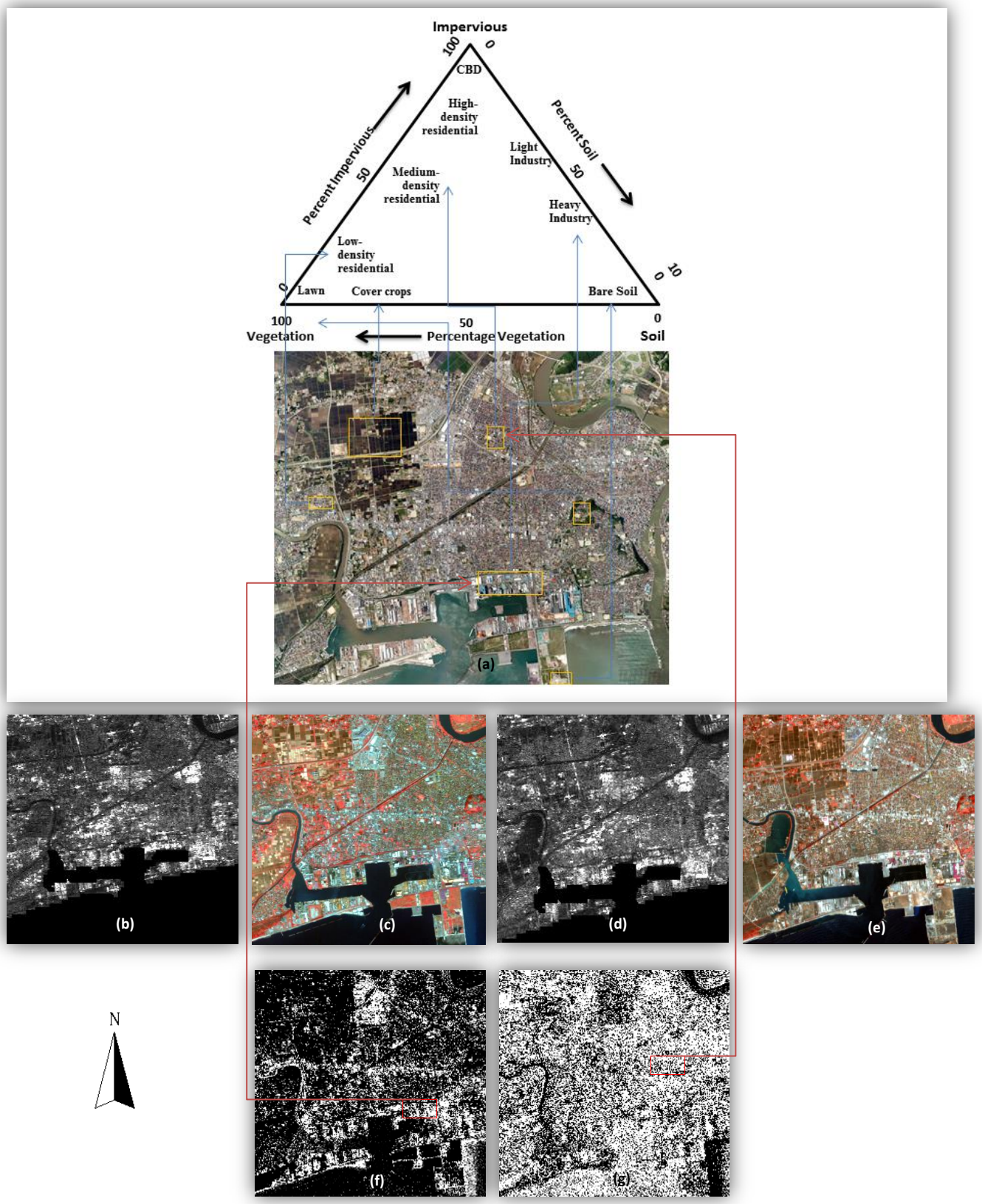

Figure 4.3 Urban land cover over the test site and image indices that can be used to represent the V-I-S components (a) areal image controlled mosaic (b) HH+VV/2 pre disaster (c) AVNIR-2 false color image pre disaster (d) HH+VV/2 post disaster (e) AVNIR-2 false color image post disaster (f) and (g) industrial and residential sub pixel fraction images using SVD respectively

4.2: Test Data

4.2.1 Worldview-2 multispectral images of test site 1

The image used for the first study site in Colombo, Sri Lanka, was a subset from the DigitalGlobe's WorldView-2 satellite acquired on 29th January 2010. Worldview-2 satellite provides coastal (400-450nm), yellow(585-625nm), red edge(705-745nm) and Near-IR2(860-1040nm) bands at a spatial resolution of 1.84m at nadir, and 2.08m at 20° off-nadir in addition to the typical multispectral bands: Blue (450-510nm), Green (510-580nm), Red (630-690nm) and Near-IR (770-895nm) (DigitalGlobe 2011). Fig. 4.4 shows the WorldView-2 satellite image and the subset chosen for the further processing.

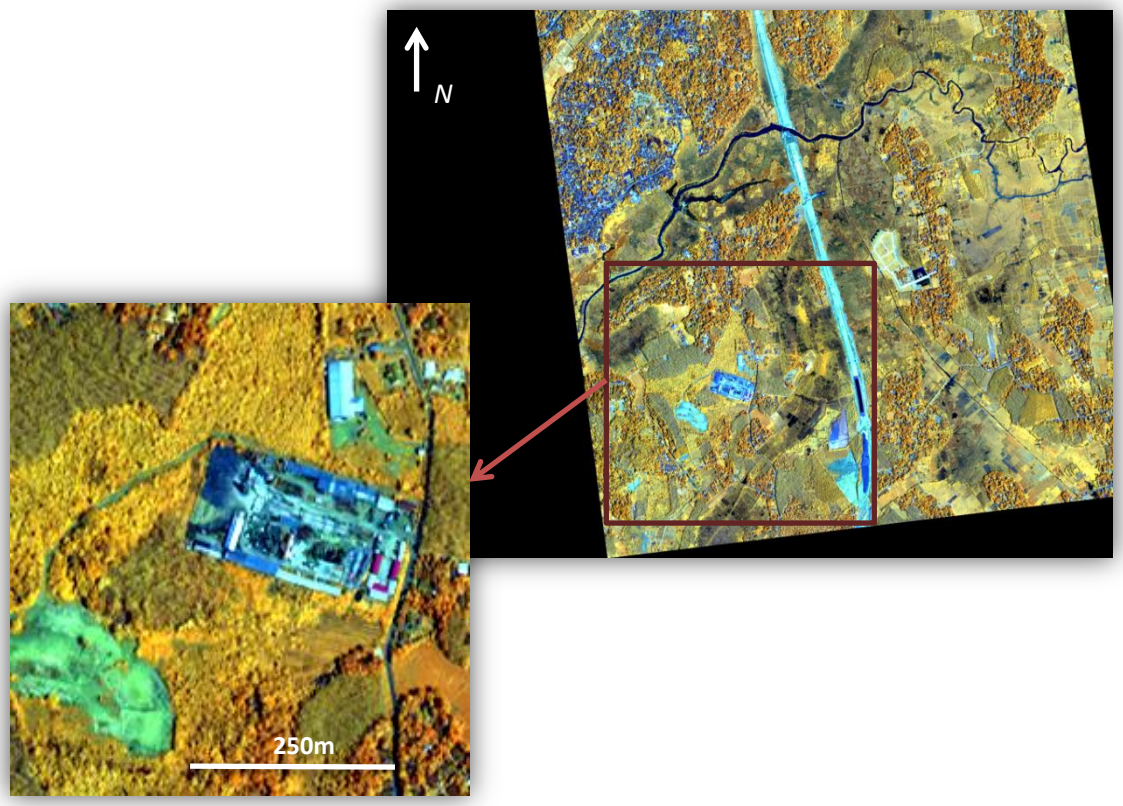

Figure 4.4 Urban land cover over the test site 1, Worlview-2 8 multispectral (2m) image bands 8,6,3 (R,G,B)

4.2.2 AVNIR-2 multispectral images of test site 2

Both multispectral as well as SAR data sets were used for the second study site in Ishinomaki area, Japan. A combination of pre and post disaster Advance Land Observation Satellite (ALOS) phased array type L-band synthetic aperture radar (PALSAR) data and Advanced Visible and Near-Infrared Radiometer-2 (AVNIR-2) data sets were used in this study. In the case of AVNIR-2 data sets, the images acquired on 5th November 2007 and 10th April 2011were taken as the pre and post disaster images respectively. These images are shown in Fig. 4.5.

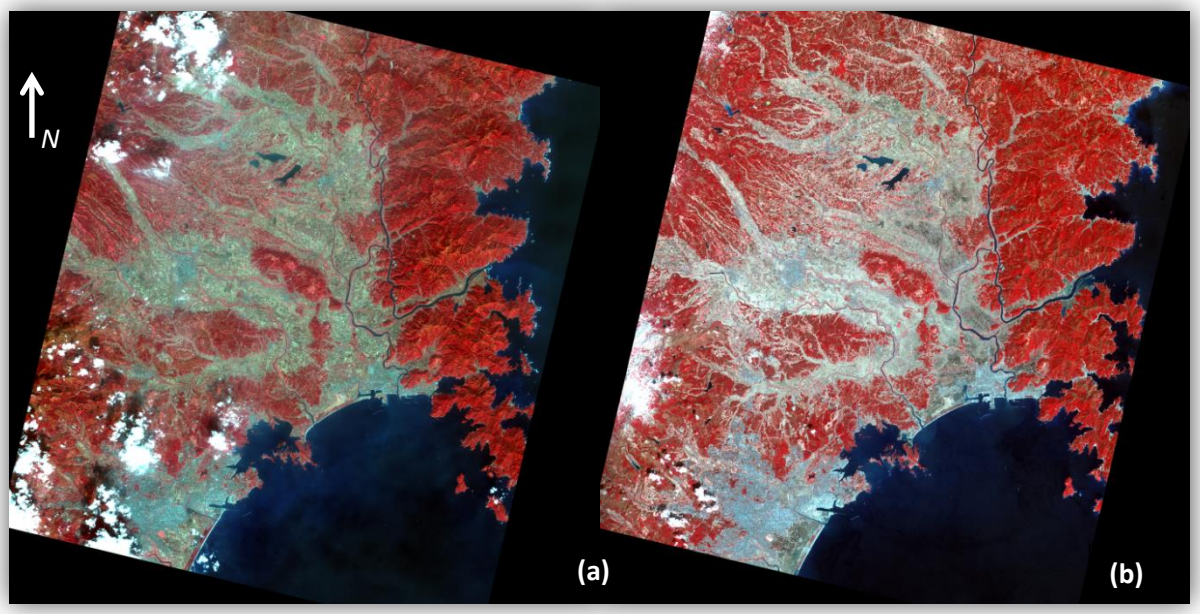

Figure 4.5 AVNIR-2 multispectral (10m) image bands 4,3,2 (R,G,B) over the test site 2 Image acquired on (a) 5th November 2007 (b) 10th April 2011

These images were resampled using nearest neighbors from 10m to 25 m spatial resolution to have the same pixel resolution of the SAR image in the case of multisource data classification. The assumption, that the higher resolution image contains pure pixels than the coarser resolution provides the possibility for this resample. The time interval between the pre disaster multispectral and SAR images are much larger (3 years) than in the case of post disaster (2 days).

4.2.3 Radar for remote sensing

4.2.3.1Power density

Active microwave remote sensing is based on the principles of radar in order to achieve practical spatial resolution (Richards, 2009). Development of radar as an imaging system is based on the power and the power density. The properties of the electric and the magnetic fields that carry the power to and from the earth surface are important in this development. Power or power density is carried forward as a result of both an electric field and a magnetic field that oscillate right angles to each other and to the direction of propagation. The electric and the magnetic fields have four important properties, the frequency at which they oscillate corresponding to the wavelength of the radiation being used, their amplitudes, their relative phase angles and directions in which they point in space. This can be shown as $\boldsymbol{E} = Ee$ (volts/meter) for electric field and $\boldsymbol{H} = Hh$ (amperes/meter) for magnetic field. Here e and h are vector of unit magnitude that point in the direction of oscillation of the respective field vector. The magnitudes of the field vectors can be expressed using these properties as follows.

$$E = E_0 expj(\omega t + \phi_e) \tag{4.1}$$

$$H = H_0 expj(\omega t + \phi_h) \tag{4.2}$$

in which E_0 and H_0 are the amplitudes of the fields and ϕ_e and ϕ_h are their phase angles. The complete backscatter arguments are generically called phases of the respective sinusoids. The radian frequency ω is related to the commonly used measure of frequency f(Hz), $\omega = 2\pi f$ rad^{-1}. The description about the development of the radar as an imaging system is given in below figure (Fig. 4.6).

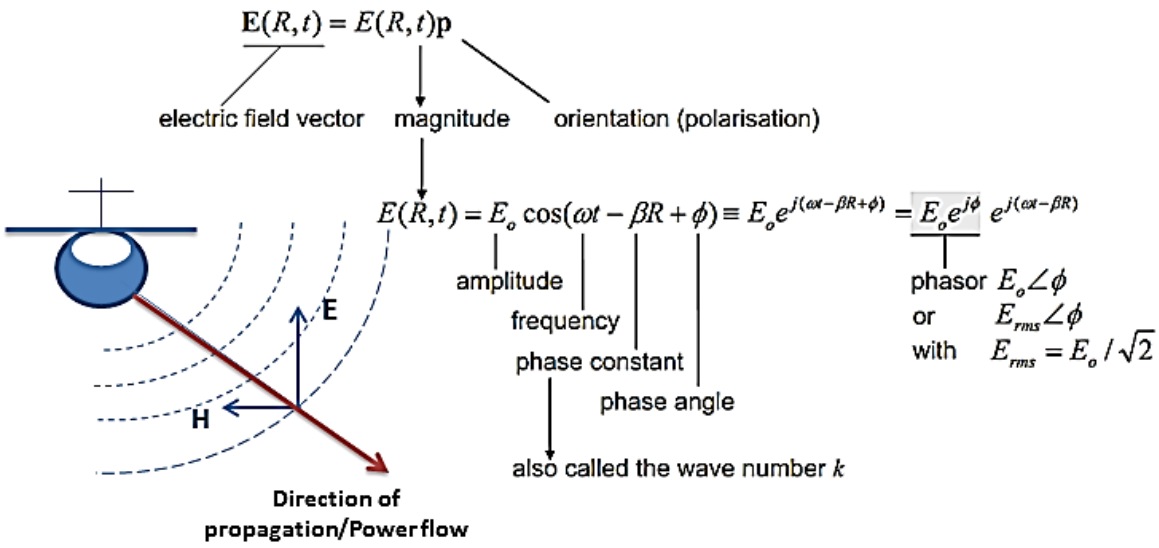

Figure 4.6 Showing the power carrying towards the earth surface as an electric and magnetic field and the complete definition of the electric field which can be extended to the magnetic fields

Polarization is the orientation of the electric and magnetic field vectors. Depending on the polarization, when radiation strikes the ground the response of surface materials can differ. Hence there are mainly two types of polarizations in the case of electric field, the parallel polarization when the electric field vector lies in the plane of incidence, and the perpendicular polarization where the electric field vector lies perpendicular to it. They are also known in remote sensing as horizontal and vertical polarizations respectively. We can write the electric field vector by using the horizontal (h) and vertical (v) unite vector length components to illustrate the polarization effect as follow:

$$E = E_H h + E_v v \tag{4.3}$$

Accordingly the component magnitudes using the horizontal and vertical components of the electric field can be described as follows:

$$E_H = a_H \cos(\omega t - \beta R) \tag{4.4}$$

$$E_V = a_V \cos(\omega t - \beta R + \delta) \tag{4.5}$$

in which a_H and a_V are the amplitudes of the two components, R ior generally s the direction of propagation and δ is a phase difference between them. The Stokes parameters provide a very convenient means by which to describe the power density relationships in an electromagnetic wave in radar, whether

it be the wave used to irradiate the earth surface of that which is scattered. For a single frequency this is defined as below:

$$S_0 = a_H^2 + a_V^2 \tag{4.5a}$$

$$S_1 = a_H^2 - a_V^2 \tag{4.5b}$$

$$S_2 = 2a_H a_V cos\delta \tag{4.5b}$$

$$S_3 = 2a_H a_V Sin\delta \tag{4.5b}$$

S_0 is equal to the amplitude squared or intensity of the actual field vector and thus directly proportional to the power density being carried by the wave. S_1 indicates whether the wave is more horizontal than vertically polarized. S_2 and S_3 indicate the ellipticity of the wave polarization. The relationship between these parameters follows $S_0^2 = S_1^2 + S_2^2 + S_3^2$. If the two orthogonal components in H and V directions described above are totally random so that there is no preferred polarization then their average squared amplitude will be the same with $S_0 = 2\langle a_H^2 \rangle$ while $S_2 = 0$. Similarly, since the relative phase is random $S_3 = S_2 = 0$.

4.2.3.2 Range and azimuth resolutions

In the case of SAR image classification it is essential to see the ability to separate targets in the signal received by the radar. This can be done by determining whether the returning pulses are distinguishable or not. Hence it is important to look how targets are resolved in the ground and slant ranges. The Fig. 4.7 shows the geometry of range resolutions.

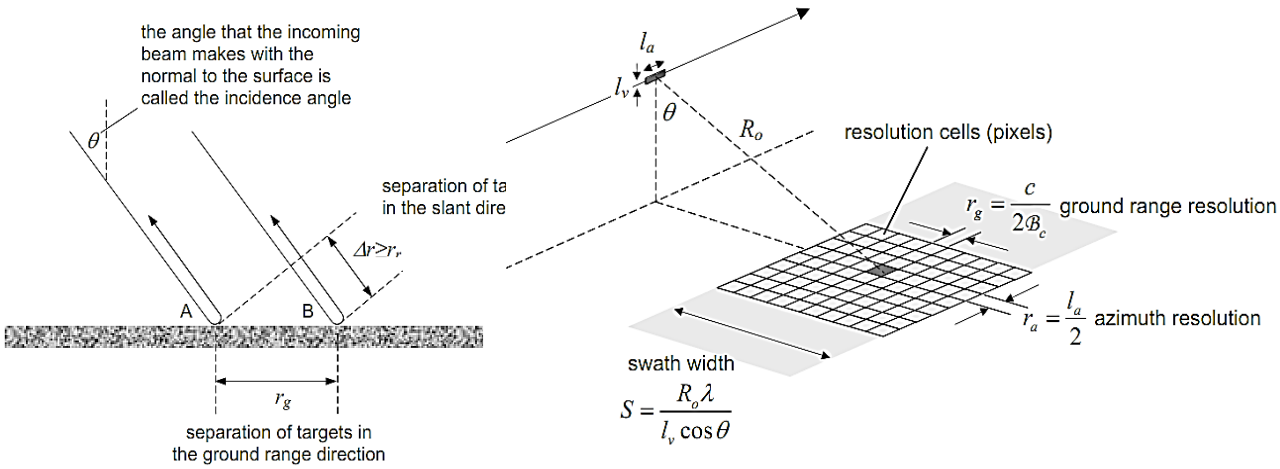

Figure 4.7 Geometry of computing the range resolution, and the ground and the azimuth resolution

If targets are Δr apart in slant range as depicted above, the difference between their echoes on reception will be $\Delta t = 2\Delta r c^{-1}$ since pulses have two way travels. We are unable to resolve in time better than the width τ of the pulse so that the lower limit on Δt is τ, the corresponding spatial resolution Δr in the slant

range direction is the slant range resolution given by $r_r = c\,\tau/2$ m, with the incident angle of θ, the spatial resolution in ground range direction (ground range resolution) can be calculated as:

$$r_r = \frac{c\,\tau}{2sin\theta}\,\mathrm{m} \tag{4.6}$$

For an antenna of length $l_a$in the along-track direction, the angular beam width subtended by the antenna is given by antenna theory $\Theta_a = \lambda/l_a$ rad. There for the along track dimension of the antenna foot print which defines the azimuth resolution for this simple system will be:

$$r_a = \frac{\lambda}{l_a} R_0\,\mathrm{m} \tag{4.7}$$

where R_0 is the slant distance from the platform to the ground, at which the azimuth resolution being considered. The azimuth resolution obtained by SAR with an antenna length of l_a is :

$$r_a = \frac{l_a}{2}\,\mathrm{m} \tag{4.8}$$

4.2.3.3 Interaction of the incident radiation with earth surface

For a target at position R, an area or cross section to the incoming radiation will absorb a certain part of the incident energy while generally reflecting or scattering a significant portion of the energy. Hence this provides the base to look at this by introducing the targets radar cross section (RCS). RCS described by σ m^2, has dimensions of area orthogonal to the incident radiation. It describes how much power is the target extracts from the power density of the incoming wave. Most of the interacted power will be scattered. Irrespective of its shape the target is assumed to scatter the intercepted power isotropically. Using the incident and the received electric field vector the radar cross section can be defined as follows:

$$\sigma = \lim_{R\to\infty} 4\pi R^2 \frac{|E^r|^2}{|E^i|^2} \tag{4.9}$$

To express the RCS in decibels a common reference level $\sigma_{ref} = 1\mathrm{m}^2$ is used, then RCS is expressed in the units dBm^2 as below:

$$\sigma = 10log\frac{\sigma}{1\mathrm{m}^2}\,\mathrm{dBm}^2 \tag{4.10}$$

RCS as a concept strictly refers only to discrete targets. To help formulate an alternative suited to distributed cover types consider a region composed of an infinite collection of infinitesimal elements of effective area, many of which make up an individual pixel. Further suppose the RCS of each of those infinitesimal area is $d\sigma$. On the average therefore the region exhibits a RCS per unit area of $d\sigma/ds$. This is called the scattering coefficient (sigma nought) of the region and denoted as σ^0 $\mathrm{m}^2\mathrm{m}^{-2}$. The scattering coefficient σ^0 is expressed in decibels, using a reference of $1\mathrm{m}^2\mathrm{m}^{-2}$ as follows:

$$\sigma^0 = 10log\frac{\sigma^0}{1\mathrm{m}^2\mathrm{m}^{-2}}\,\mathrm{dB} \tag{4.11}$$

To account for the fact that the scattering coefficient is polarization dependent we write it with subscripts σ^0_{PQ}which signify the polarisation of the incident wave and that of the wave scattered and received by the

radar. The first subscript *P* indicates the received polarization and the second *Q* the transmitted or incident polarization. The radar images used in this study radiate both vertically and horizontally, and receive both horizontal and vertical components of the scattered wave. Hence four relevant scattering coefficients, brought together in a matrix called sigma matrix, given as below:

$$\begin{bmatrix} \sigma^0_{HH} & \sigma^0_{HV} \\ \sigma^0_{VH} & \sigma^0_{VV} \end{bmatrix} \tag{4.12}$$

For monostatic radar systems that the two cross-polarized components σ_{HV} and σ_{VH} are the same, whereas the co-polarised components σ_{HH} and σ_{VV} can be quite different to each other.

4.2.3.4 The Scattering matrix

For many applications it is sufficient to use the scattering coefficients to describe the earth surface properties of interest. Just like the scattering coefficient it is a property of the scatterer itself and embodies the landscape information of interest to us. Fig. 4.8 shows the coordinate systems for the horizontal and vertical field components involved in backscattering from a discrete target, or from pixel on the ground.

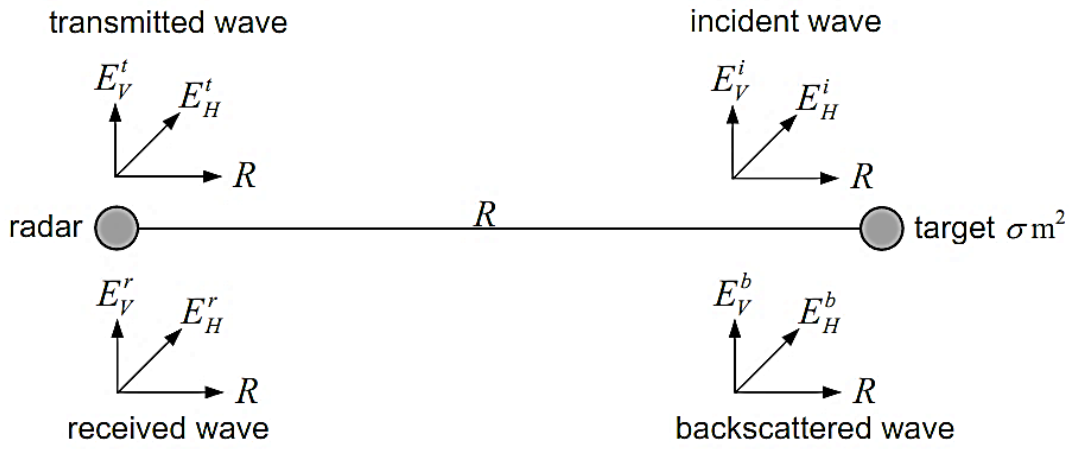

Figure 4.8 Field components relevant to the scattering matrix, assuming that all components are transverse to the direction of propagation

Backscattering occurs in –*R* direction. The only difference between the incident and transmitted fields is a result of propagation from the radar to the target. There will be a phase delay because of the travel of the wave over the distance *R*, and a drop in signal strength. As mentioned earlier not that the power density falls in an inverse square fashion with distance. Thus the field amplitudes fall in an inverse distance fashion with distance. Just as with the transmitted and incident waves, the only difference between the backscattered and received waves is a phase difference and an inverse distance drop in amplitude. It is the comparison of the incident and the backscatter waves that is of most interest to us, because that is what contains information directly about the scattering properties of the target and ultimately, biophysical properties of the target itself. The relationship shown in above figure for the incident and the backscatter fields can be explained further using the following equation.

$$\begin{bmatrix} E_H^b \\ E_V^b \end{bmatrix} = \begin{bmatrix} S_{HH} & S_{HV} \\ S_{VH} & S_{VV} \end{bmatrix} \begin{bmatrix} E_H^i \\ E_V^i \end{bmatrix} \tag{4.13}$$

where the matrix with the components $S_{HH}, S_{HV}, S_{VH}, S_{VV}$ is referred to as the Scattering or Sinclair matrix of the target. The elements of the scattering matrix contain all the information we need about the target. Each is a complex quantity (having both amplitude and phase angle) that is dependent on the frequency, or wavelength, of operation and the incidence angle at the earth's surface. In principle it is also dependent on the azimuth angle with which the target is viewed, although that is generally fixed by the broadside direction to the motion vector of the platform. Given that each element has an amplitude and phase, the scattering matrix contains eight pieces of information about the target, or region on the ground. In practice we don't measure the backscattered components right at the target, nor are they theoretically available at the target itself. Therefore Eq. 4.13 can be written as though the scattering properties are observed back at the radar.

$$\begin{bmatrix} E_H^r \\ E_V^r \end{bmatrix} = \frac{e^{j\beta R}}{R} \begin{bmatrix} S_{HH} & S_{HV} \\ S_{VH} & S_{VV} \end{bmatrix} \begin{bmatrix} E_H^i \\ E_V^i \end{bmatrix} \tag{4.14}$$

Under the assumption that the backscattering coefficient is constant across a pixel we can equate the scattering matrix element to the backscattering coefficient multiplied by the area of the pixel $r_a \times r_g$ as follows:

$$\sigma_{PQ}^0 = 4\pi \frac{\left|S_{PQ}\right|^2}{r_a r_g} \tag{4.15}$$

In the case of the scattering matrix we can assume $S_{HV} = S_{VH}$ in backscattering; this is called the reciprocity condition.

4.2.3.5 The target vector

The elements of the scattering matrix can be used to derive other pixel descriptors perhaps more suited to analysis by the classification mechanisms discussed in this thesis. A target vector which summarizes the properties of the target can be defined by arranging the scattering matrix in a column form:

$$K = \begin{bmatrix} S_{HH} \\ S_{HV} \\ S_{VH} \\ S_{VV} \end{bmatrix} \tag{4.16}$$

Different target vectors can be formed using combinations of scattering matrix elements. The most common alternative derived from Pauli basis can be given by:

$$K_p = \frac{1}{\sqrt{2}} [S_{HH} + S_{VV}\ S_{HH} - S_{VV}\ S_{HV} + S_{VH}\ \ j(S_{HV} - S_{VH})]^T \tag{4.17}$$

With the two target definitions, two more different expressions for the target can be given. Using the scattering matrix elements we define the target through the covariance matrix, which is the expected value, $C = \mathrm{E}(KK^{*T})$. The simplified form of the covariance matrix is presented as below:

$$C = \begin{bmatrix} \langle |S_{HH}| \rangle^2 & \langle S_{HH} {S_{HV}}^* \rangle & \langle S_{HH} {S_{VH}}^* \rangle & \langle S_{HH} {S_{VV}}^* \rangle \\ \langle S_{HV} {S_{HH}}^* \rangle & \langle |S_{HV}| \rangle^2 & \langle S_{HV} {S_{HH}}^* \rangle & \langle S_{HV} {S_{VV}}^* \rangle \\ \langle S_{VH} {S_{HH}}^* \rangle & \langle S_{VH} {S_{HV}}^* \rangle & \langle |S_{VH}| \rangle^2 & \langle S_{VH} {S_{VV}}^* \rangle \\ \langle S_{VV} {S_{HH}}^* \rangle & \langle S_{VV} {S_{HV}}^* \rangle & \langle S_{VV} {S_{VH}}^* \rangle & \langle |S_{VV}| \rangle^2 \end{bmatrix} \quad (4.18)$$

The diagonal elements of the covariance matrix are, to within multiplicative constant, the four scattering coefficients of the pixel: $C_{11} \propto \sigma^0_{HH}, C_{22} \propto \sigma^0_{HV}, C_{33} \propto \sigma^0_{VH}$ and $C_{44} \propto \sigma^0_{VV}$. The off-diagonal terms describe the interactions or correlation among the set of scattering mechanisms. Alternative to the covariance matrix is the coherency matrix developed by the Pauli basis target vector, $C = \mathrm{E}\left(K_p {K_p}^{*T}\right)$.

$$T = \frac{1}{2}\begin{bmatrix} \langle K_a {K_a}^* \rangle & \langle K_a {K_b}^* \rangle & \langle K_a {K_c}^* \rangle & \langle K_a {K_d}^* \rangle \\ \langle K_b {K_a}^* \rangle & \langle K_b {K_b}^* \rangle & \langle K_b {K_c}^* \rangle & \langle K_b {K_d}^* \rangle \\ \langle K_c {K_a}^* \rangle & \langle K_c {K_b}^* \rangle & \langle K_c {K_c}^* \rangle & \langle K_c {K_d}^* \rangle \\ \langle K_d {K_a}^* \rangle & \langle K_d {K_b}^* \rangle & \langle K_d {K_c}^* \rangle & \langle K_d {K_d}^* \rangle \end{bmatrix} \quad (4.19)$$

in which

$$K_a = S_{HH} + S_{VV}\,, K_b = S_{HH} - S_{VV}\,, K_c = S_{HV} + S_{VH}\,, K_d = j(S_{HV} - S_{VH})$$

4.2.4 Radar image products for the study

The most general product from the radar sensors is the scattering or Sinclair matrix which is given as below:

$$S = \begin{bmatrix} S_{HH} & S_{HV} \\ S_{VH} & S_{VV} \end{bmatrix} \quad (4.20)$$

for which $S_{HV} = S_{VH}$ in backscattering. Each of the elements of the scattering matrix is complex, and can thus be written

$$S_{PQ} = A_{PQ} + jB_{PQ} = \left|S_{PQ}\right| e^{j\emptyset_{PQ}} \quad (4.21)$$

The preliminary images for this study was provided in the form of a Sinclair matrix or for single polarization radar in terms of the complex scattering coefficient for that polarization, called single look complex images. These are complex images which does not have speckle reductions through look averaging. The images used for the further processing in this study were look averaged mainly for speckle reduction. If the data has been look averaged in order to reduce speckle then generally it will be provided in the form of the scattering coefficient σ^0_{PQ} that results from look summing during SAR image formation. If L look have been used to reduce the speckle by $\sqrt{L}$, and degrade the spatial resolution in azimuth, the available data is called L-look imagery.

The SAR datasets used in this study are the result from an urgent data acquisition after the earthquake on 11th March 2011. Full polarimetric observations conducted on 21st November 2010 was taken as the pre-disaster input while the observation made on 8th April 2011 was taken as the post-disaster input.

Observation mode was an off-nadir angle of 21.5° in the ascending orbit. A single look PolSAR image carries a resolution of 4.45m in azimuth and 23.14m in ground range direction. The revisit cycle for ALOS is 46 days. The temporal base line is 138 days and the perpendicular base line is about 2Km. Such large temporal and spatial baseline can induce significant decorrelation effects and produce poor interferometric coherence. The PALSAR images were geocoded using UTM projection (zone 54N) and WGS84 Datum. Multilooking (5-look) processing in azimuth direction was performed to adjust the azimuth and range pixel size to be comparable, with a resulting spatial resolution of 25m. No speckle filters were applied initially on the data. The images are shown below.

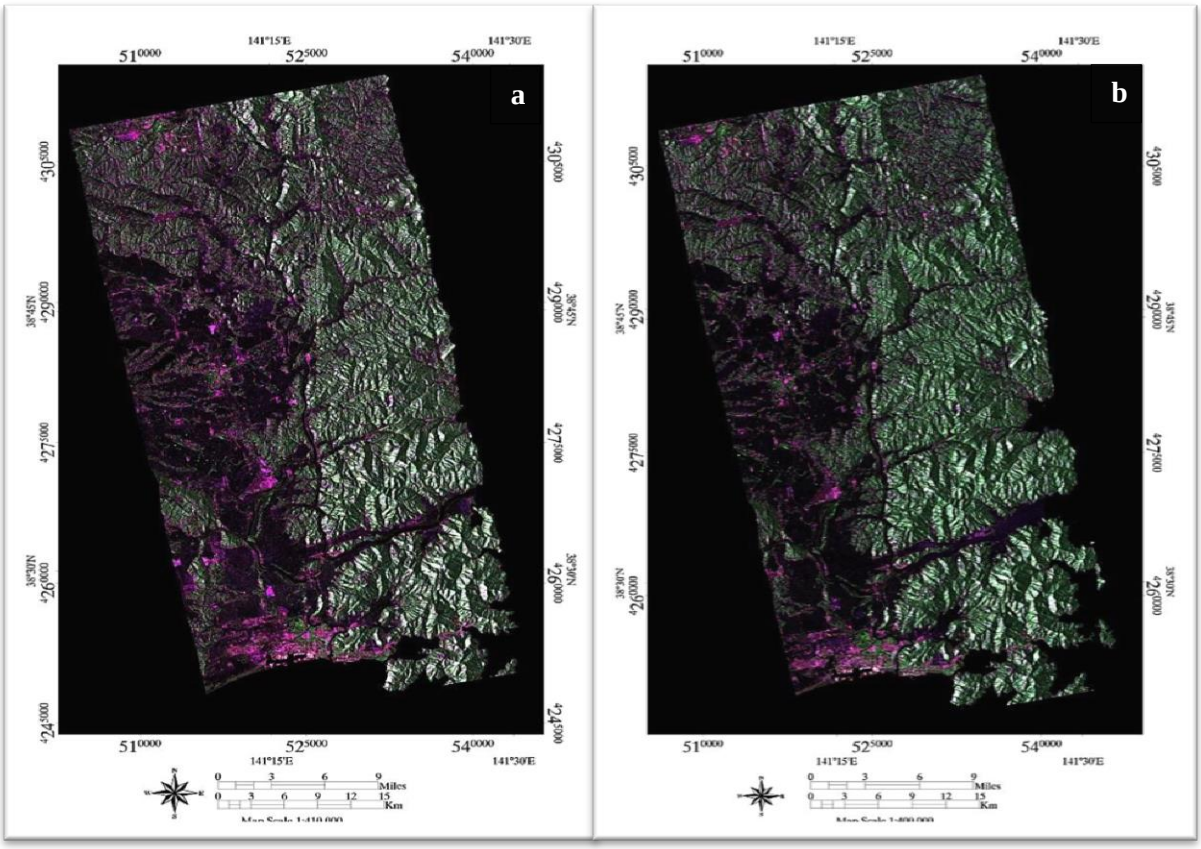

Figure 4.9 ALOS PALSAR 5 look complex images with HH, VH and VV polarization in a RGB composite (a) pre disaster 21st November 2010 (b) post disaster 8th April 2011

In the MRF based classification method presented in this thesis, classes are discriminated based on their statistical property which requires accurate statistical models. Several SAR image indices were used in this study to perform and test the MRF based classification task. Mainly we have used the co-polarized SAR intensity, logarithmic transformation, autoregressive and autocorrelation texture. These indices with their statistical properties are explained in detail in the following subsections.

4.2.4.1 Co- polarized radar image intensity

Mainly the SAR intensity and the texture can be used to distinguish land cover classes. We based our experiments using intensity and texture for MRF based classification models.

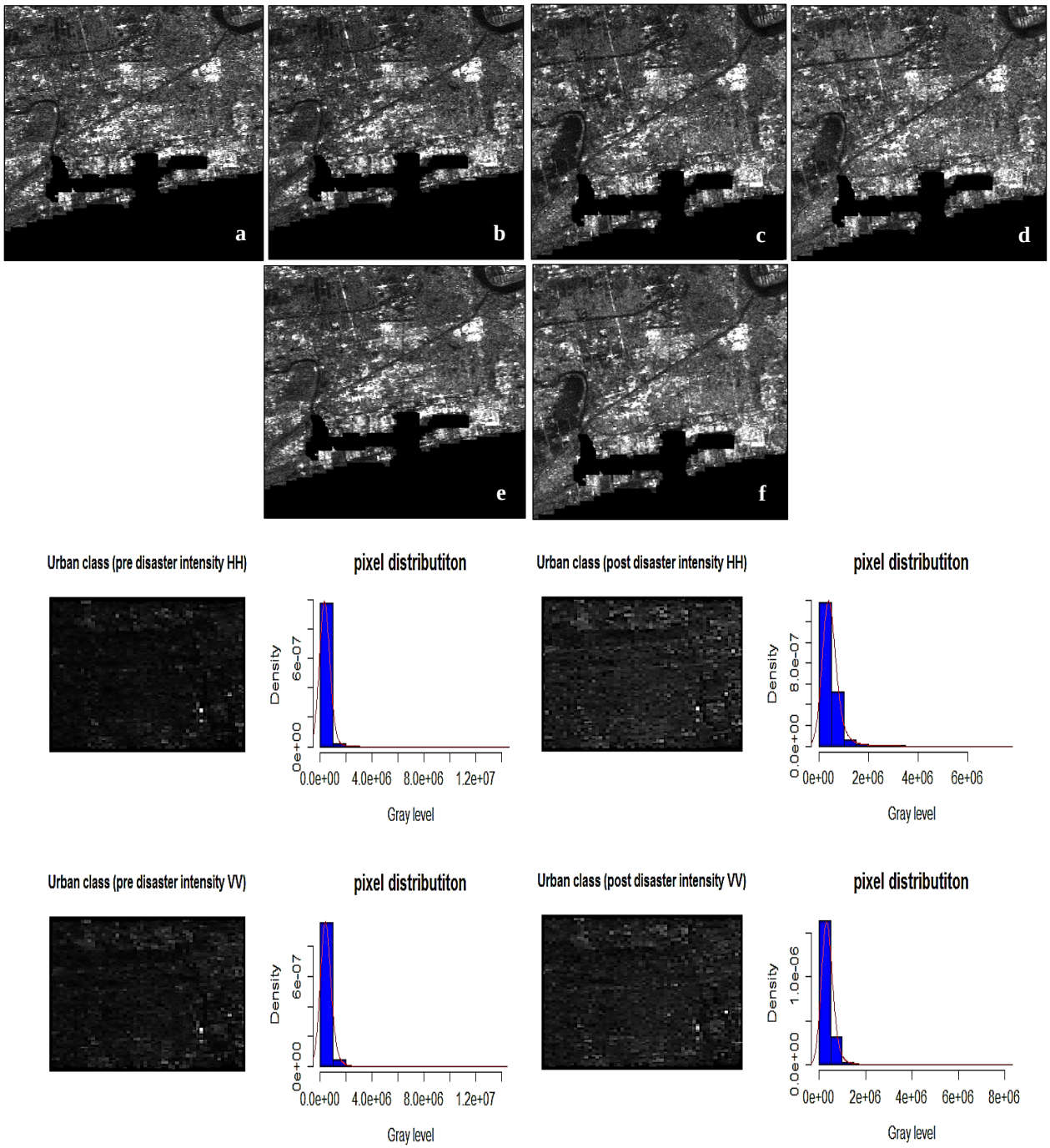

Figure 4.10 ALOS PALSAR 5 look intensity images and corresponding urban class pixel distributions (histograms) with (a), (b) pre disaster HH, and VV polarizations (c), (d) post disaster HH, and VV polarizations and (e) pre (HH+VV)/2 and (f) (HH+VV)/2 and corresponding pixel distribution

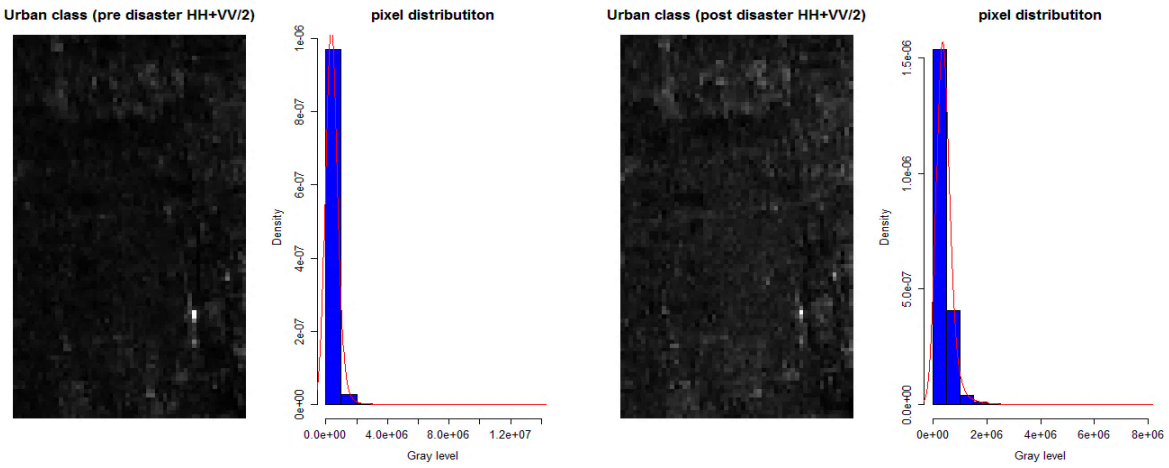

Figure 4.11 Pre HH+VV/2 and (f) Post HH+VV/2 urban pixel distribution

When electromagnetic waves are scattered from large number of targets, randomly distributed throughout a cell, with similar dimensions, which are large compared to the wave length, speckle is fully developed and homogeneous surfaces appear as stationary fields. Under these circumstances the intensity field is gamma distributed. Co polarized PALSAR intensity images and the pixel distribution following a gamma distribution function over and urban class sample is shown in the following figure. The pixel intensity is the main input for the multisource image classification using MRF. Hear we used the average pixel intensity between the co-polarized SAR images. One of the main reason for this is the average operation between the co-polarized pixel intensities reduce the effect of speckle. As can be seen in the Fig. 4.10 (e) and (f) the average polarization shows a decrease in the random noise effect. This averaging operator effects the pixel distributions shown by the histograms; interestingly it does not affect the Gamma distribution, but the range of the pixels representing the Gamma distribution for the urban class has increased. This is a useful to model the class conditional energy conveniently for a particular class. For convenience an urban class sample was taken to represent this effect but this follows for all the other major land cover types.

4.2.4.2 Speckle and speckle filtering

One of the most striking differences in the appearance of radar imagery compared to optical image data is its poor radiometric quality, caused by the overlaid speckle nature of the radar data. Radar speckle noise has a standard deviation linearly related to the mean and is often modeled as a multiplicative process. This means that higher the signal strength the higher the noise. Speckle is a direct result of the fact that the incident energy is coherent (Fig. 4.12), which means it can be assumed to have a single frequency and the wave front arrives as a pixel with a single phase. If there were a single large dominant scatterer in the pixel, such as a corner reflector or building, then the return signal would be largely determined by the response of that dominant element, and any scattering from the background would be negligible. More often, though, the pixel will be a sample of a very large number of incremental scatterers; their return combines to give the resultant received signal for that pixel. Such situation is illustrated in above figure. In this study speckle reduction was used mainly to detect the changes and to compare the results with the texture based changes. An adaptive Lee filter based on the assumption that the mean and the variance of the pixel of interest are equal to the local mean and variance of all pixels within a pixel window of 3×3 is used to filter the noise. The advantage of the Lee filters to preserve

prominent edges, linear features, point target and texture information is considered in this study to reduce the noise. Lee filtered full polarimetric SAR images are shown below.

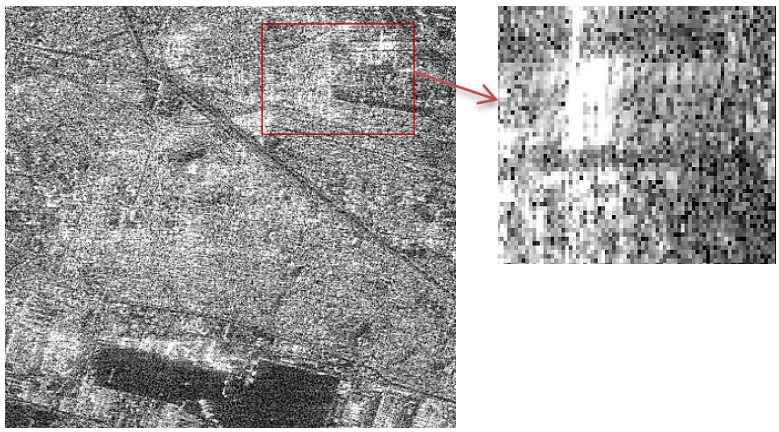

Figure 4.12 Speckle effect in ALOS PALSAR single look complex HH polarization, due to coherent interaction of the incident radiation with many incremental scatterers within a resolution cell over a residential area

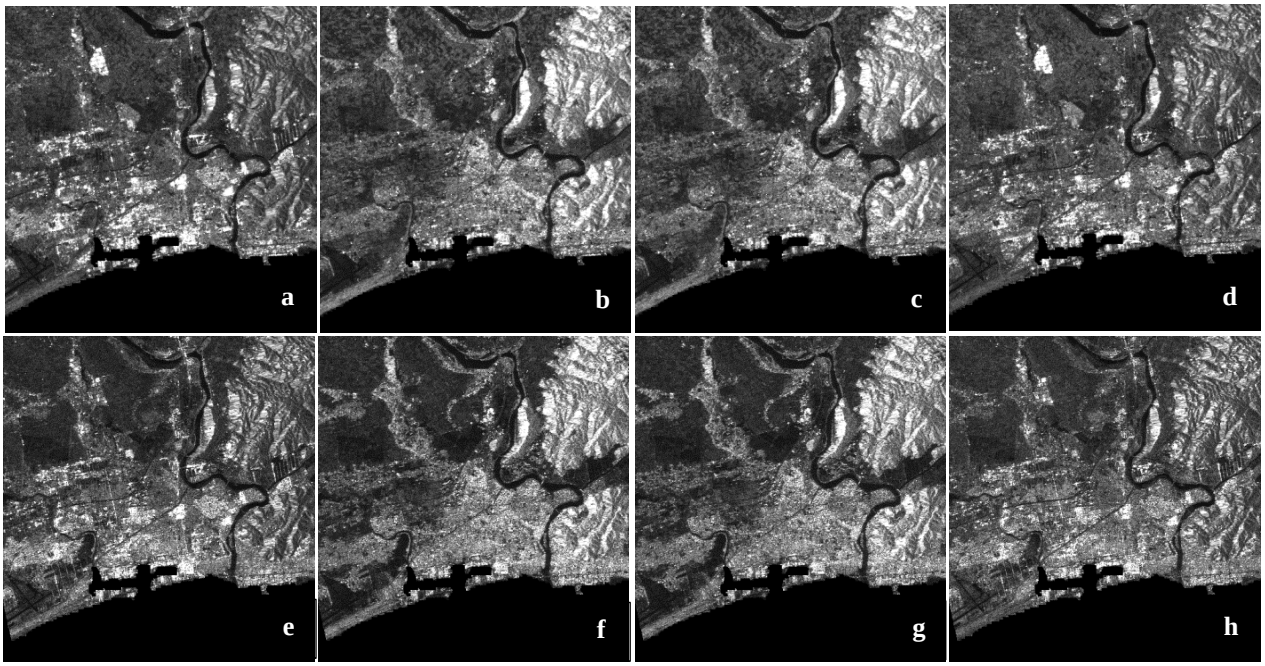

Figure 4.13 Lee filtered ALOS PALSAR 5 look intensity images (a), (b), (c), (d) pre disaster HH, HV, VH and VV polarization components (e), (f), (g), (h) post disaster HH, HV, VH and VV polarization components

4.2.4.3 Lognormal SAR images

For the generation of the MAR based texture information the main input is the logarithmic transformed intensity $x(i,j) = ln(y(i,j))$ (see Eq. 3.43). Generated logarithmic images for study region using full polarimetric components are shown in Fig. 4.14.

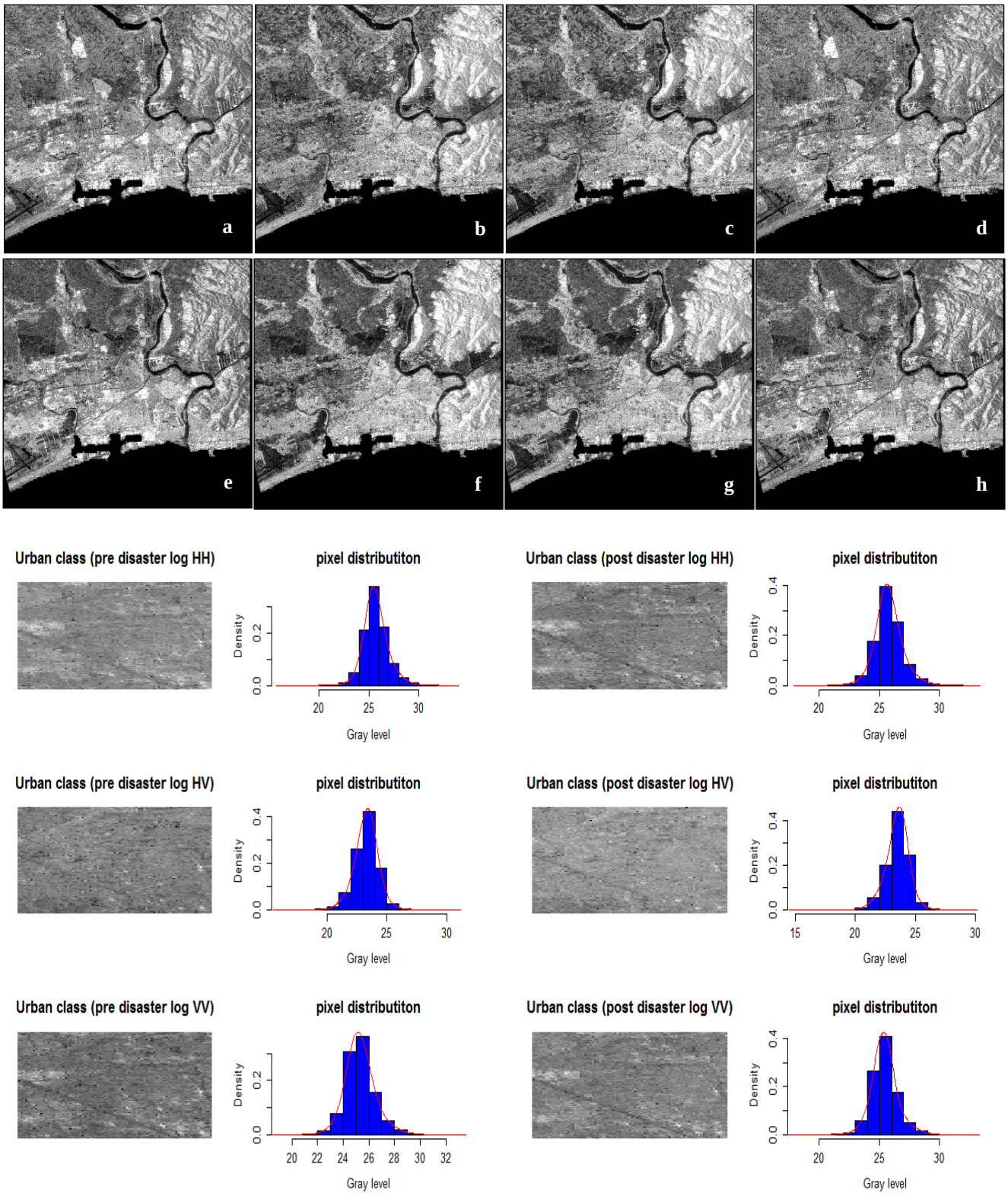

Figure 4.14 Logarithmic transformation on ALOS PALSAR 5 look intensity images and the corresponding urban pixel distribution (histograms) (a), (b), (c), (d) pre disaster HH, HV, VH and VV polarization components (e), (f), (g), (h) post disaster HH, HV, VH and VV polarization components

In the experiments a major importance is given to urban land cover classes, the distribution of the pixels in such area is always of major importance. Due to the logarithmic transformation the pixel distribution changes from Gamma to Gaussian distribution. Histograms in Fig. 4.14 show this clearly. Further the changes in the local mean values and the variance are significant between the pre and the post disaster urban class sample. Logarithmic transformation is useful and simple mathematical operation that can be used to convert the SAR image statistics to Gaussian statistics for the Bayesian image classification mechanisms. However this nonlinear transformation completely changes the speckle statistics of the image. Speckle noise transformed in this way is only additive and signal independent, but its PDF is approximately Gaussian.

4.2.4.4 Autoregressive texture the weight and noise variance

MAR texture image generation discussed in section 3.7.1 was executed using a 3×3 pixels local window as shown in below figure. A boundary pixel (Fig. 4.12) is bound to be similar to the parameters of texture B than A. By sticking to a window size in 2nd order neighborhood configuration we can reduce this effect to certain degree.

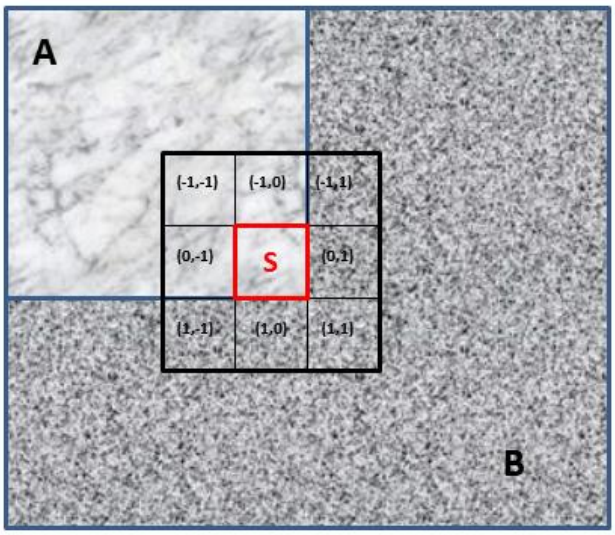

Figure 4.15 Estimating texture parameter for a pixel *S*, when it lies in a boundary condition

The MAR base neighborhood weighting parameter (θ) and the noise variance (σ_u^2) based texture images and there corresponding urban pixel class distributions are shown below in Fig. 4.16 and Fig. 4.17 respectively. These parameters describe the multiplicative spatial interaction among the SAR image pixels. Due to the variation in texture, different images show different values of θ and σ_u^2. Hence it is possible to use these parameters as the texture descriptors. For each measured block, the corresponding neighbor set *N* used for model support was defined as by (1,0), (1,1), (0,1), (-1,1), (-1,0), (-1,-1), (0,-1) and (1,-1), which is also a 2nd order neighborhood configuration. Both pixel distributions for the urban areas follow a Gaussian distribution. This is a useful property of these texture parameters to be used in Bayesian classification mechanisms. The changes to the class mean values and the variance due to the disaster can also be observed from the histograms.

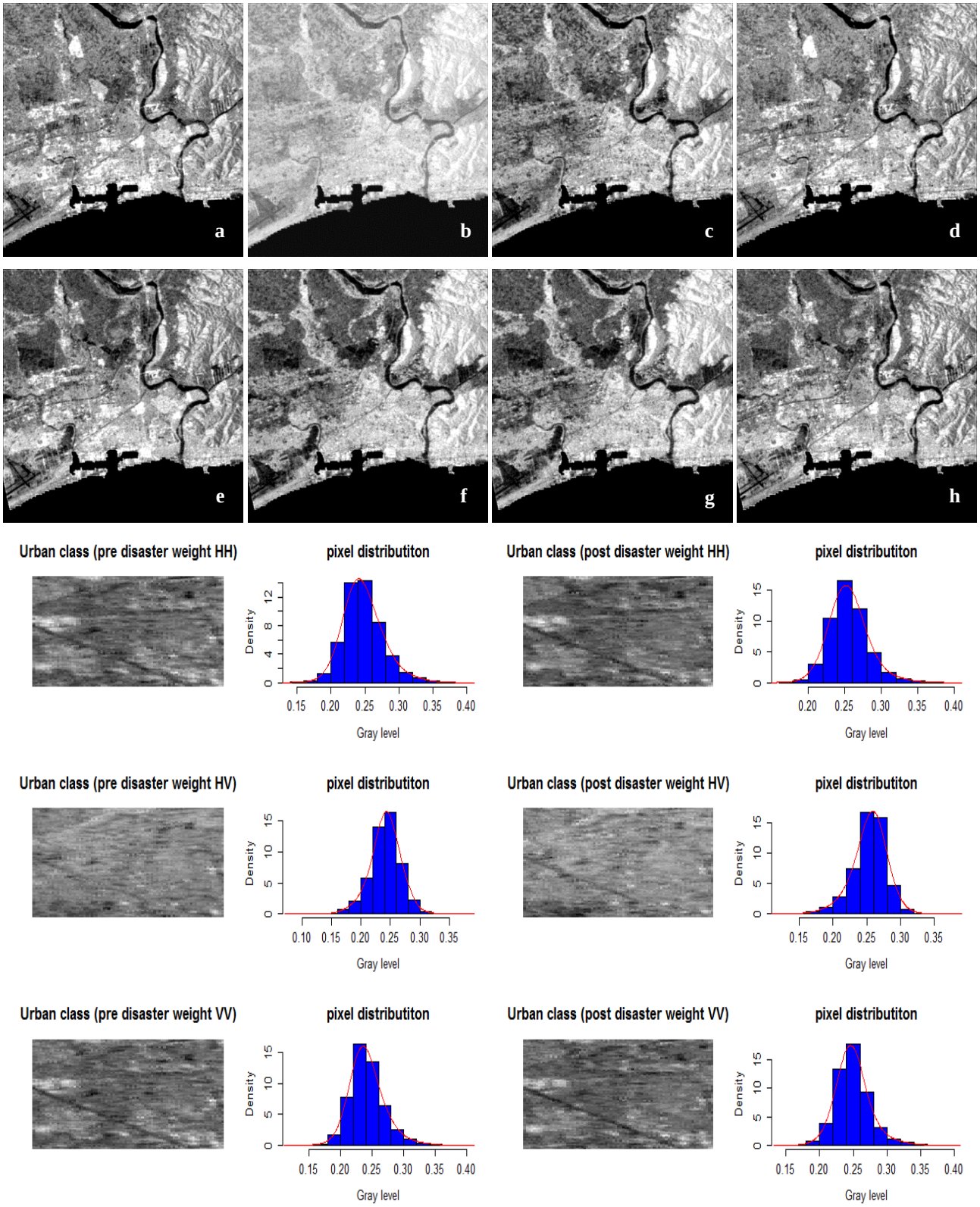

Figure. 4 16 MAR base neighborhood weighting parameter (θ) based texture and the corresponding urban pixel distribution (histograms) (a), (b), (c), (d) for pre disaster HH, HV, VH and VV polarization components (e), (f), (g), (h) for post disaster HH, HV, VH and VV polarization components

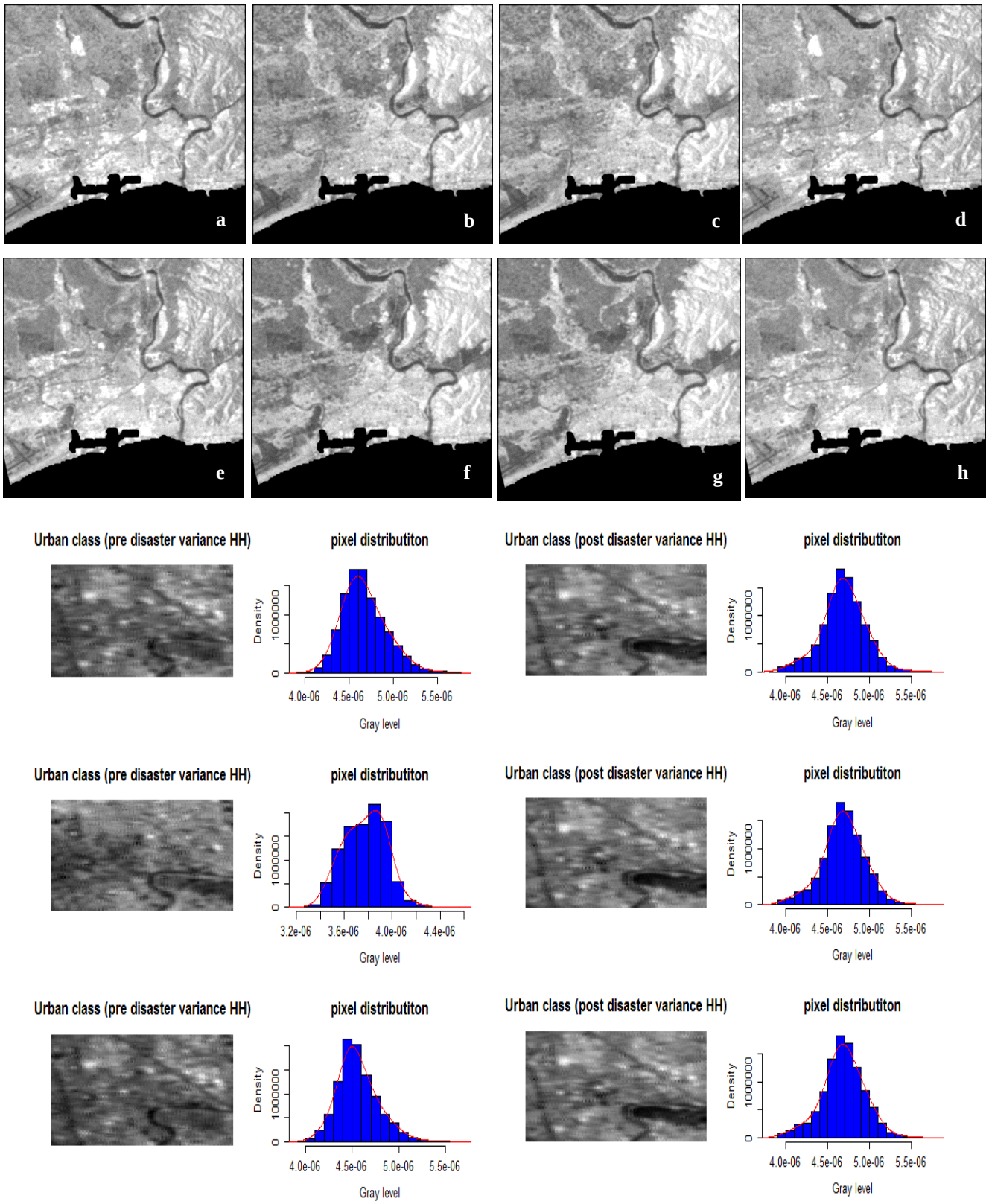

Figure 4. 17 MAR base noise variance (σ_u^2) based texture and the corresponding urban pixel distribution (histograms) (a), (b), (c), (d) for pre disaster HH, HV, VH and VV polarization components (e), (f), (g), (h) for post disaster HH, HV, VH and VV polarization components

The pixel values represented by θ and σ_u^2 are small and manageable as they represent the spatial interaction between the pixels. However, for noise-fading images, the MAR model seems to show more stable results. Note that texture classifications based on the MAR model use only two features as inputs (i.e., θ and σ_u^2). These two features appear to characterize texture very well. An added feature of the MAR model is that the computational expense is low. Therefore, the MAR model can be regarded as the most useful tool for texture quantization in the multisource MRF image classification.

4.2.4.5 Autocorrelation texture measures

The need of chracterising spatial phenomena and the importance of a statistical knowledge about bi-dimentional or multidimentional occurences is important (Stasolla and Gamba, 2008). Global autocorrelation within a given data set is an important aspect in such a case. Several number of indexes can be found for such a purpose. Among them Moran's I_i, Geary's C_i and Getis-Ord G_i gray levels can be used as important texture parameters for SAR imagery. We expect that spatial correlation like textures could be a good candidate to discriminate regular patterns, distinctive of urban areas from other land use. The high spatial correlation either positive or negative is a peculiar feature of the urban areas with formal or informal settlements especially when they are depicted from SAR imagery. The following images (Fig. 4.18, Fig. 4.19 and Fig. 4.20) show the three texture descriptors showing urban regions and linear features more prominently. The binary matrix which defines the neighborhood relationship was set to a 3×3 pixel window, while the neighborhood configuration was defined by the Rook's definition.

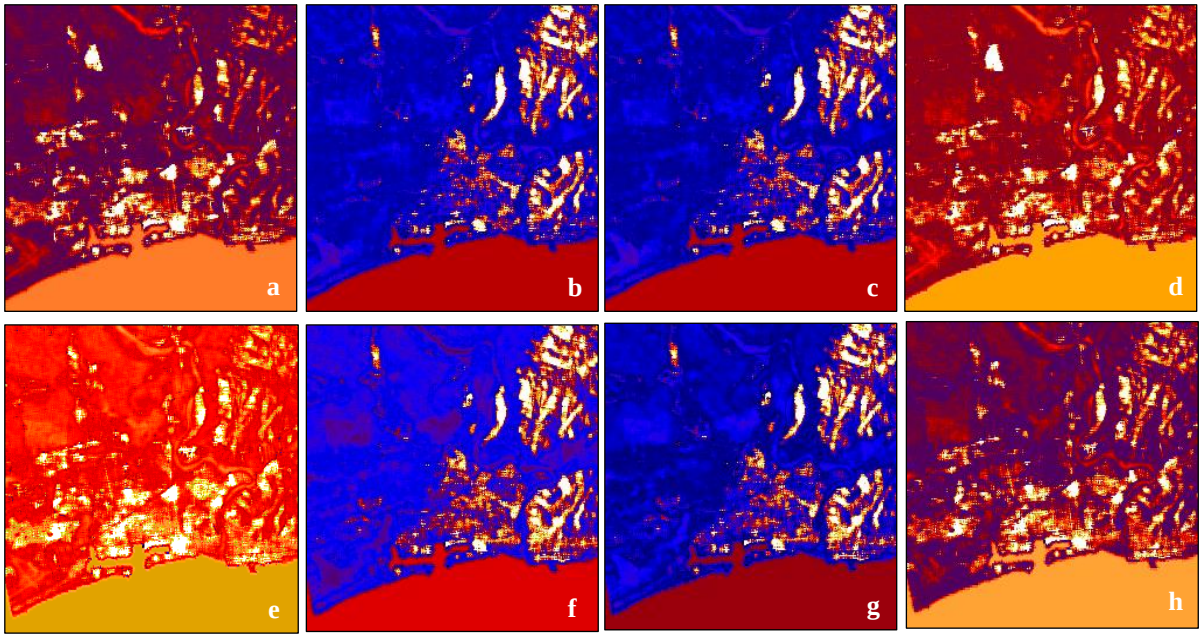

Figure 4.18 Moran's I_i gray level images (a), (b), (c), (d) for pre disaster HH, HV, VH and VV polarization components (e), (f), (g) (h) post disaster HH, HV, VV polarization components

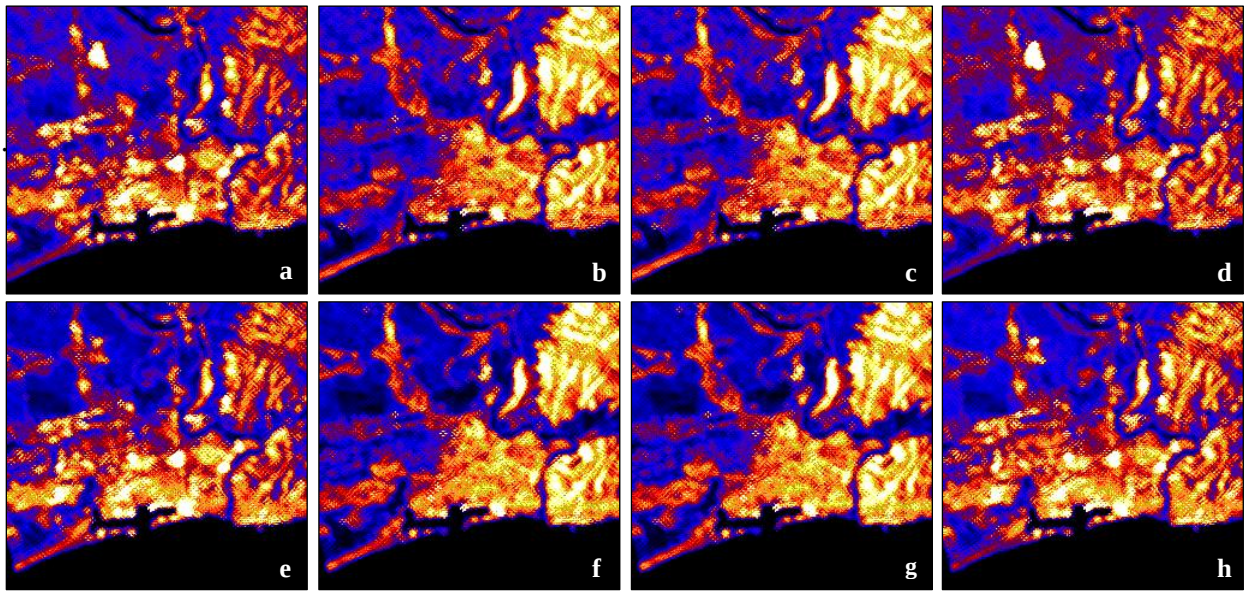

Figure 4.19 Geary's C_i gray level images (a), (b), (c), (d) for pre disaster HH, HV, VH and VV polarization components (e), (f), (g) (h) post disaster HH, HV, VV polarization components

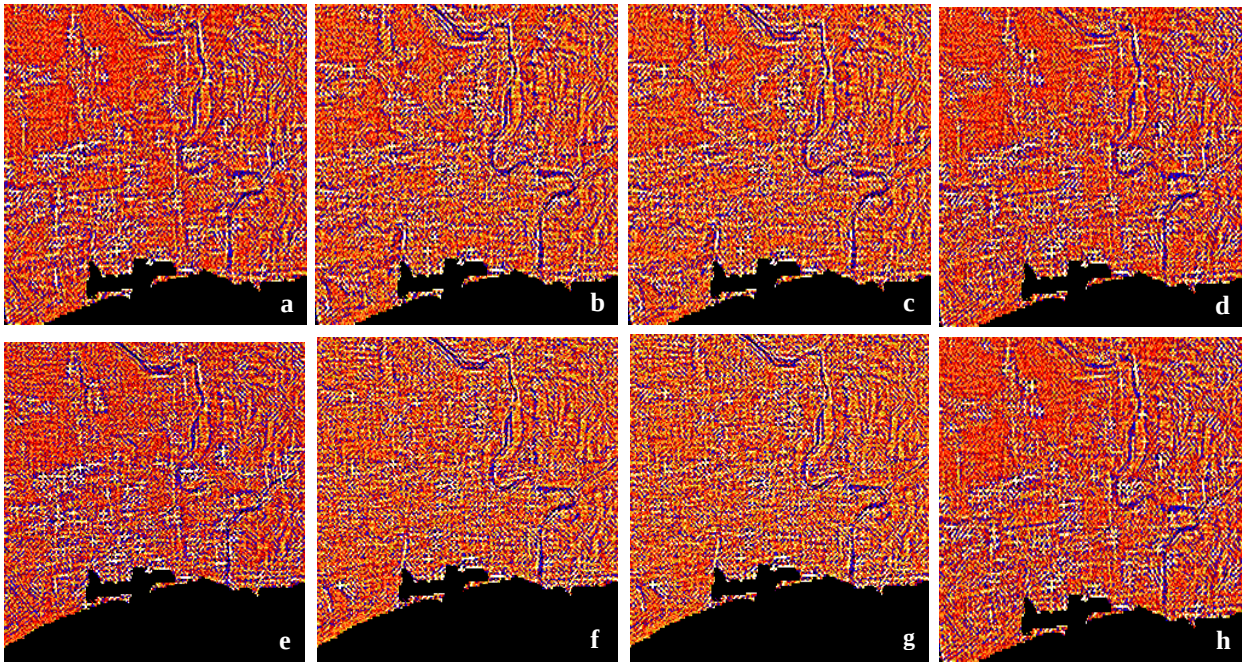

Figure 4.20 Getis-Ord G_i gray level images (a), (b), (c), (d) for pre disaster HH, HV, VH and VV polarization components (e), (f), (g) (h) post disaster HH, HV, VV polarization components

The local Moran's I_i index evaluates the similarity between a pixel in concern and the pixels of the pivotal location. As a result locally homogeneous regions such as residential areas and paddy lands will be represented by similar texture patterns. Additionally Moran's I_i and Geary's C_i provides

complementary information looking at the most evident features in the test area. Similar texture patterns with bright regions for both the Moran's I_i and Geary's C_i in the urban areas can be seen. On the other hand the Getis-Ord G_i gray level images shown above are much more suitable to fit the urban boundaries, because it can be used to identify hot spots such as areas with very high variations in neighboring pixel values.

4.2.5 Aerial mosaics for the generation of reference images

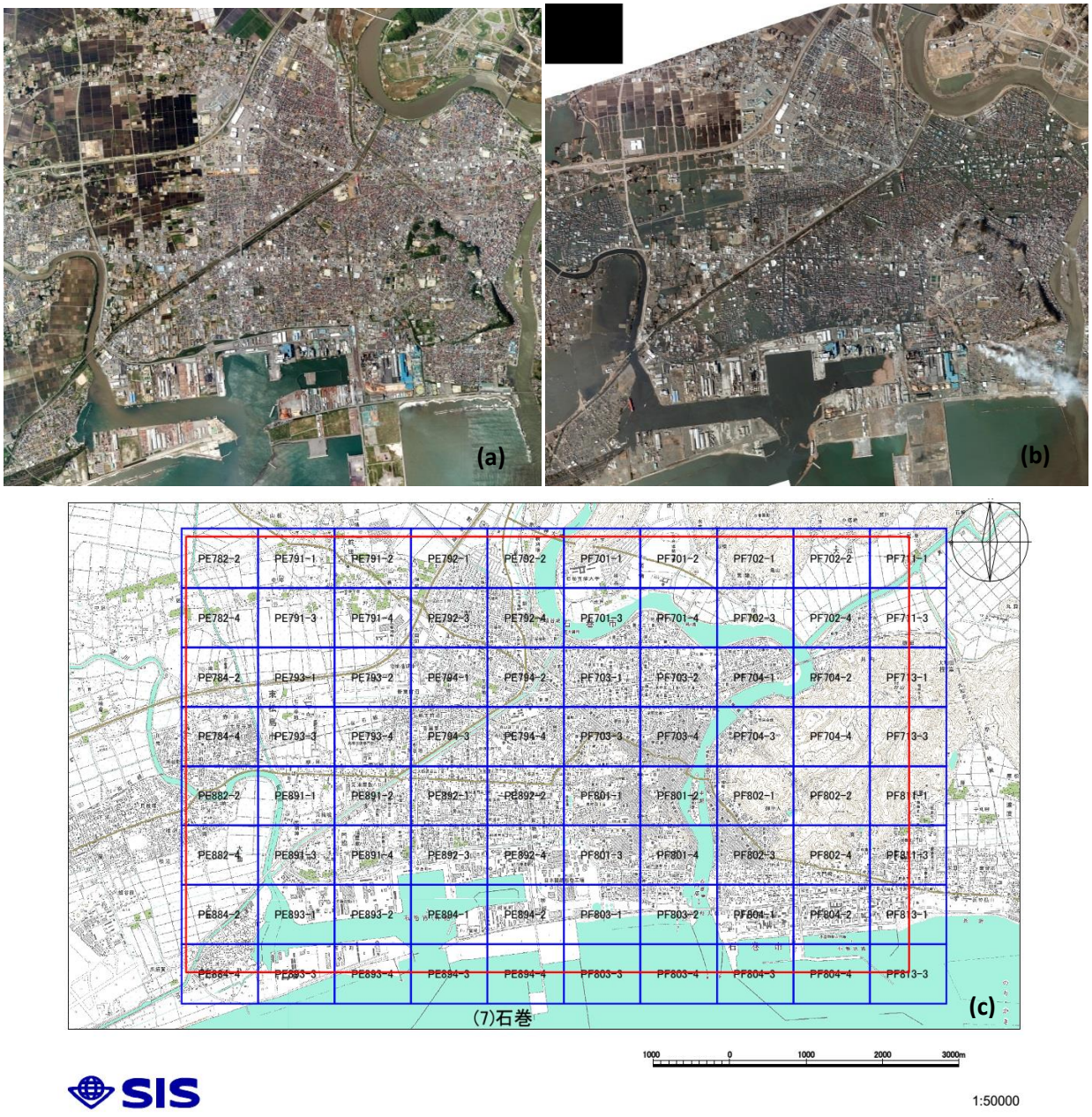

Figure 4.21 Controlled aerial mosaic of the Ishinomaki area in Japan (study region 2) (a) pre disaster flying mission on 18th May 2009 (b) post disaster flying mission on 12th march 2011 and (c) flight planning report

A high resolution controlled aerial mosaic was also employed to generate the validation information for the classification results. 72 tiles of geo-referenced aerial images acquired by an aerial survey over the study area before and after the earthquake was employed for the mosaicking process. The pre disaster flying mission was conducted on 18th May 2009 while in the case of post disaster it was 12th march 2011. As a result the post disaster aerial mosaic is a detailed aerial dataset just after one day of the disaster. These images provide strong base to understand the land cover changes in the study site due to the disaster.

4.3 Overall experimental workflow

The overall experimental process in full detail is explained in Fig. 4.22. This can be explained in three sections.

Experiments using the proposed fuzzy MRF model for the super resolution mapping- In this step the proposed fuzzy and MRF integrated model were tested on two markedly different satellite datasets. Those are the Worlview-2 with 2m and AVNIR-2 with 10m spatial resolutions. SRM's at 1m and 5m resolutions were generated using these satellite data sets respectively. The experimental results are validated using SVM and NN based classification mechanisms.

Experiments using the SAR texture for time series land cover change detection- This step is conducted mainly with two purposes in mind. The first is to understand the statistical properties of the autoregressive and autocorrelation texture measures. The second is the use of them in extracting land cover changes in a context. Several prominent contextual change detection methods, Variograms, SSIM, MRD and GKLD were incorporated and tested in the study.

Experiments using the proposed fuzzy MRF model for multisource data classification- This as the final step is the main objective of this work. Hear we experiment the developed MRF and the fuzzy MRF models for the combined classification of multispectral, SAR and SAR texture images. These experiments were conducted at the spatial resolution of the SAR imagery. The importance of the parameters in this model and the corresponding image statistics are tested in these experiments.

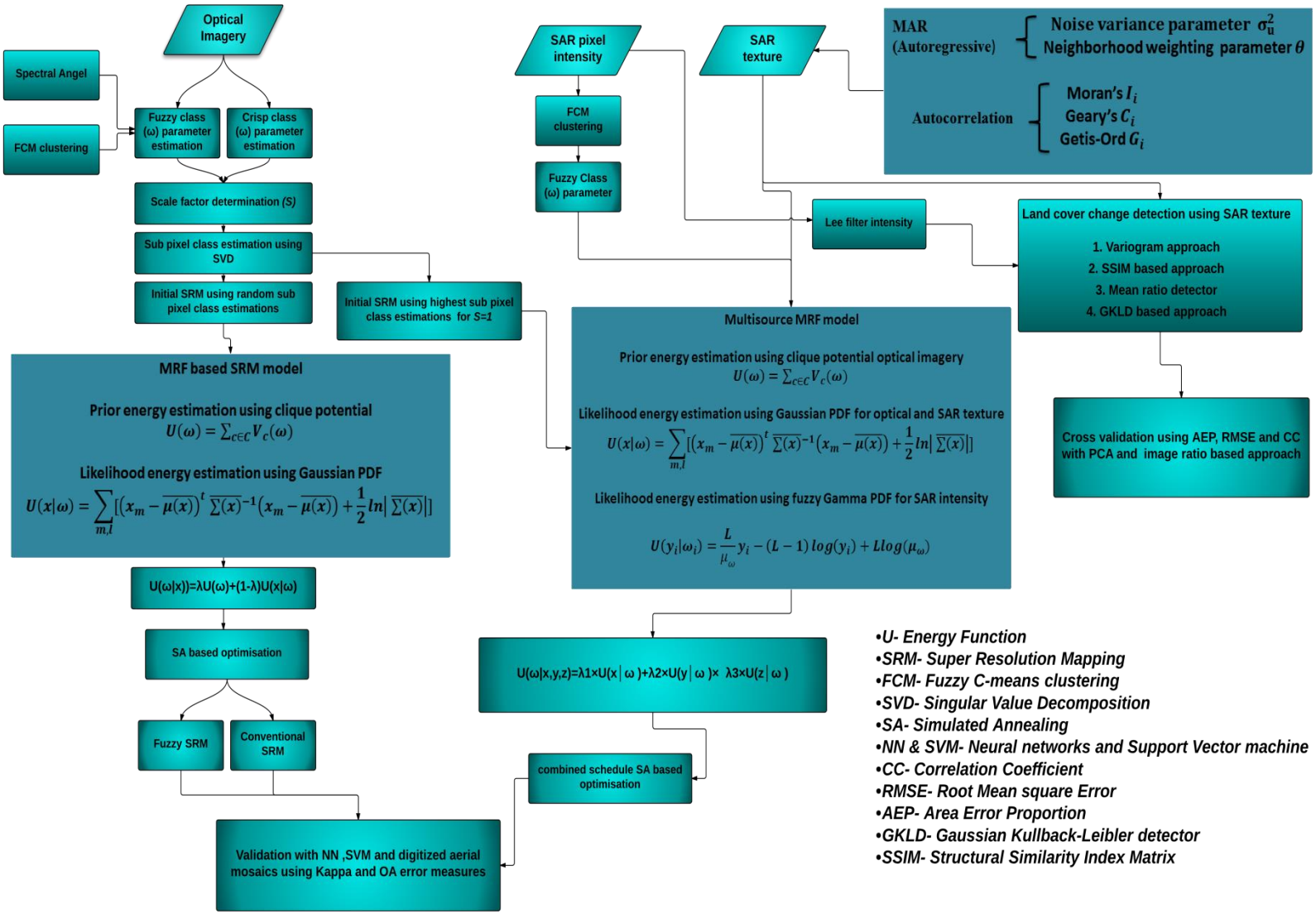

Figure 4.22 Complete flow of the experiments conducted under the study

5

Experimental results and discussion

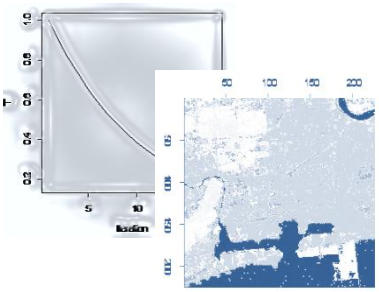

This chapter presents the experimental outcomes, along with the relevant discussion. It contains mainly of three sections. The first section describes the fuzzy Markov model development and its application for the super resolution mapping. The second section describes the use of SAR texture information for land cover change detection. The third and the last section describe the results of the multisource data classification using MRF. The positive and negative aspects and the improvements needed to be tested further will be highlighted while leaving them to be concluded in the next chapter.

5.1 Fuzzy parameter integrated MRF model for SRM

The core part of this is the class parameter estimation in a fuzzy domain. Furthermore how a class is modelled by fuzzy adaptive class mean vector and fuzzy class covariance matrix is also importance. We consider the experimental setup using two markedly different multispectral remote sensing images in the form of Worlview-2 and AVNIR-2. Adding up to the use of unbiased experimental samples, two different geographical regions as explained in previous chapter in Sri Lanka and Japan were used. These two regions are also mentioned as study site 1 and 2.

5.1.2 Experiments using Worldview-2

To simplify the calculation process the training samples were set to be square. But in any given case they can be chosen to represent the shape and the size of the land cover components needed to parameterize the class distributions. Training samples for the vegetation and the impervious surface confined a total of 900 training pixels, while for the soil class it was 400 pixels. It is important to note that when the membership values are assigned for each training pixel, the number of training pixels required to model the class probability density should necessarily decrease from the case where pixels are treated alone as crisp sets. This means that the probability distribution for a set of training pixels will be modelled by weighting them using the corresponding fuzzy membership grades determined by SA or the FCM methods. This is a very useful modification proposed as one of the central novelties in this study. As a

result the user the user gets the possibility to improve vague class mean vector and covariance matrices using the fuzzy grade of memberships.

The image was preliminary processed to determine the membership grades for each training pixel using SA and FCM clustering technique. In the case of SA, the Minimum Noise Fraction (MNF) transformation was employed to remove the correlation exists between the eight bands to identify the pure pixels. Different techniques for the selection of the image end-members can be found in the literature (Zhang *et al*. 2001, Plaza *et al.* 2011, Plaza *et al.* 2004, Small 2001). For this work, we employed a supervised end-member selection using the n-D spectral space to identify the end members. This selection of spectra from the image as end-members is the most common practice when the spectral libraries that adequately account for all the processes and the factors influencing the data spectra are not available (Bateson and Curtiss 1996). Additionally, we observed that the land cover classes in this study area hold distinct reflectance spectra among them while being homogeneous at scales larger than that of the ground field of view of the WorldView-2 sensor. Hence the use of n-D spectral space to generate the reference spectra is satisfactory for our work. After generating the reference spectra, using the spectral angle for each pixel, we unmixed the pixels into corresponding land cover components (Krus *et al.* 1993). The square homogeneous training samples chosen for these three classes to determine the fuzzy class parameters, and the fractional abundance for each of the V-I-S components are shown in the Fig. 5.1. Finally we assigned these fractional estimations as the training pixel membership values.

In the second approach, a FCM clustering membership matrix was generated for each pixel of the training samples in each band and for each class (Tso and Mather 2009). Then the average value of the 8 bands for a pixel in each class was calculated. These averaged membership values for each pixel are considered to be its final membership following that class. The statistical parameters mean and covariance generated from the conventional and the fuzzy algorithms are different. Fuzzy means for the three classes (V-I-S) and the fuzzy covariance matrices for the vegetation class generated from the conventional approach, SA and fuzzy c-means techniques are shown in Table 5.1 and Table 5.2 respectively. It can be seen from these results that the inclusions of the fuzzy class parameters makes significant changes to the class probability density functions in a Gaussian framework. Initial parameter determination was performed at a 400×400 pixel image subset, while for the MRF based SRM input it was further reduced to a 100×100 pixel image to cut down the processing time. The bench mark reference images were produced by performing a hard Maximum Likelihood classification (MLC) using the same training samples explained above. As the generated SRM spatial resolution was 1m at a scale factor of 2, prior to the MLC classification the images were resampled to 1m resolution for the pixel to pixel cross comparison. To avoid the original pixels getting over resampled with respect to the distribution of the classes in the study region, a nearest neighbor resampling technique was employed.

The initial SRM maps were generated by determining the class composition within a pixel using the Singular Value Decomposition (SVD) technique (Canty 2010). In SVD a library matrix is generated by decomposing it to two column orthogonal matrices and a diagonal matrix. A vector multiplication of this matrix with the observed image generates the least square estimate of the end member abundance (Boardman 1989). If the fractional estimation for a particular class in a pixel $x_i \in \mathrm{A}$ in the observed image is θ_i, then there will be $\theta_i \times S^2$ allocation of that class in the corresponding pixel set B of the SRM. The generated initial SRM's using the SVD fractions is shown in Appendix A, and essentially this initial configuration will be optimized with conventional MRF, SA and FCM based fuzzy MRF schemes.

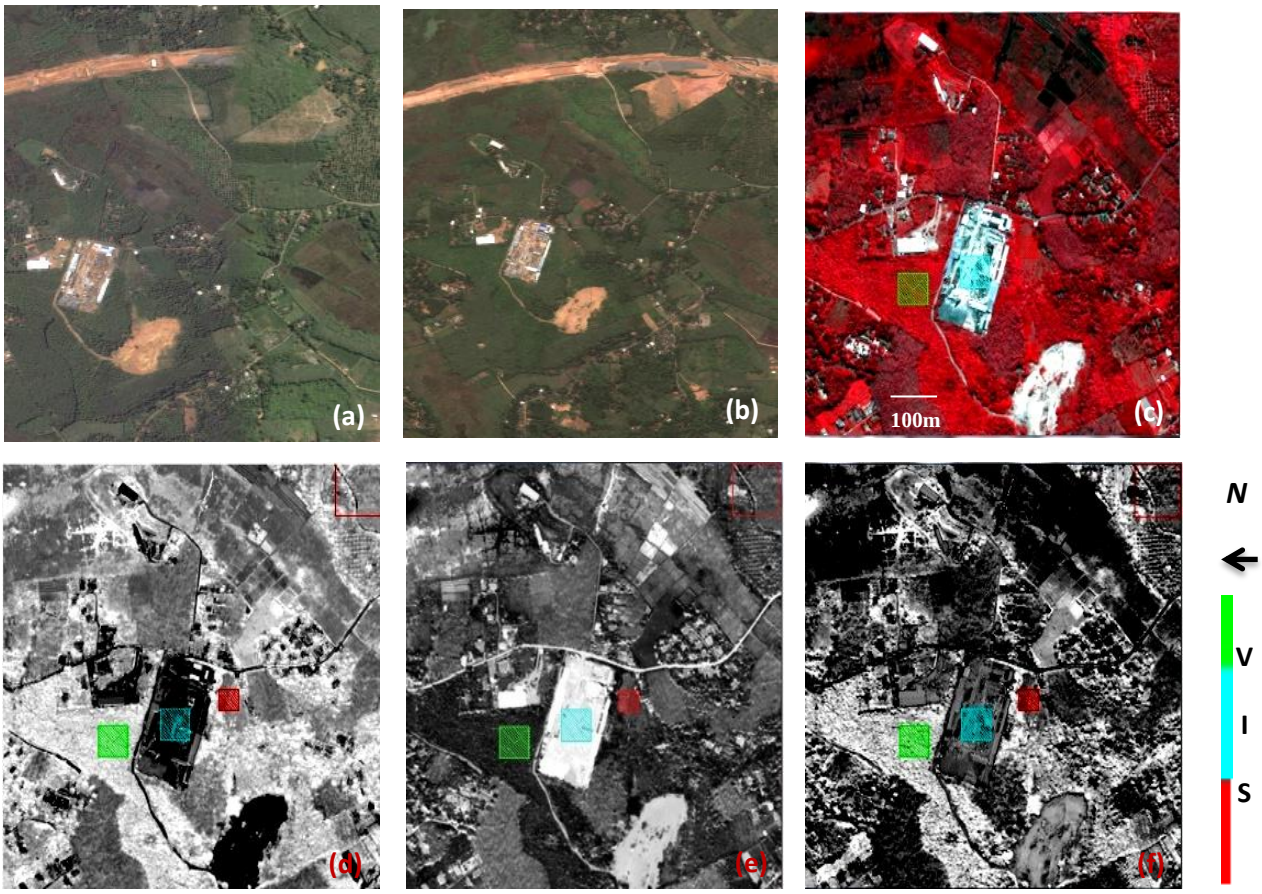

Figure 5.1 Google map image of the Study site in the west coast of Sri Lanka, (a) for year 2007 (b) 2009 (c) Worldview-II false color multispectral band composite RGB (6, 5, 4) showing the selected ground samples, (d), (e) and (f) fractional images generated by SA, for Vegetation, impervious surface and soil classes respectively

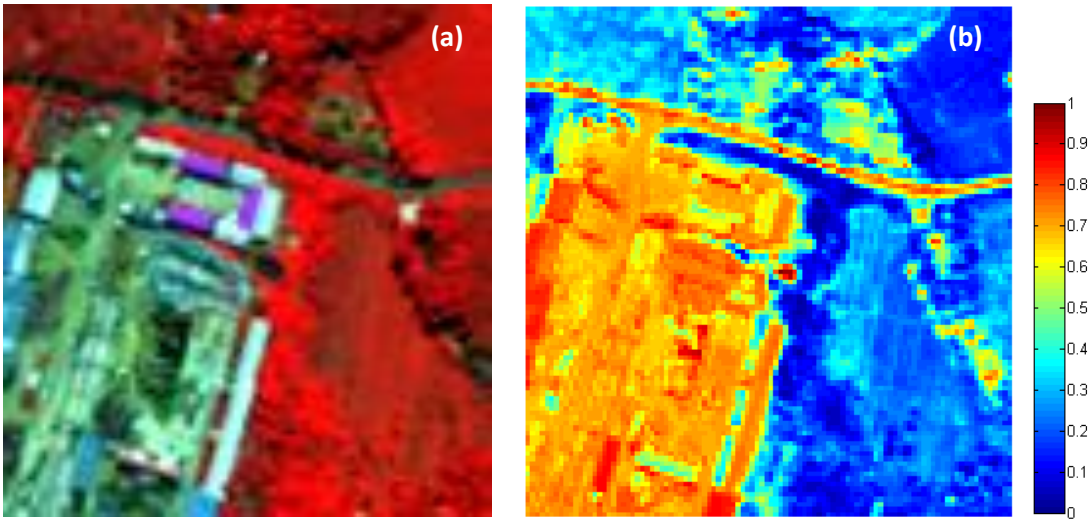

Figure 5.2 Sample image for the MRF based SRM (a) Worldview-II false color multispec nd composite RGB (6, 5, 4) (b) SA based membership image

Table 5 1 The mean values for each class in different spectral bands using conventional, SA and fuzzy c-means techniques

Worlview-2 bands		1	2	3	4	5	6	7	8
Vegetation	Fuzzy (SA)	362.99	274.47	355.50	242.71	79.46	553.95	510.57	715.65
	Fuzzy C-Mean	363.06	274.63	358.80	245.76	80.45	558.92	510.92	715.94
	Conventional	363.02	274.57	355.46	242.97	79.66	552.27	508.14	712.30
Impervious	Fuzzy (SA)	478.60	443.49	617.311	581.744	261.25	515.35	308.05	411.22
	Fuzzy C-Mean	472.41	430.27	581.64	533.93	236.64	473.91	285.74	380.71
	Conventional	476.98	441.38	614.40	579.49	260.42	516.58	310.50	415.67
Soil	Fuzzy (SA)	378.34	299.54	378.28	294.68	115.59	504.69	432.93	634.73
	Fuzzy C-Mean	378.41	299.72	378.50	294.94	115.82	503.07	431.04	632.64
	Conventional	378.33	299.36	377.15	293.87	115.28	499.10	426.93	625.40

Table 5 2 Covariance matrices for vegetation class (a) Conventional case (b) using SA (c) using fuzzy c-means

Band 1	2	3	4	5	6	7	8
8.70	8.27	26.74	25.00	10.01	68.29	53.52	77.40
8.27	16.24	48.40	41.31	19.03	103.05	84.82	117.26
26.74	48.40	319.02	229.69	69.67	838.48	714.50	917.25
25.00	41.31	229.69	212.68	69.04	625.45	452.71	652.42
10.01	19.03	69.67	69.04	33.93	135.33	88.72	132.51
68.29	103.05	838.48	625.45	135.33	3067.91	2683..14	3639..24
53.52	84.82	714.50	452.71	88.72	2683.14	2743.24	3432.85
77.40	117.26	917.25	652.42	132.51	3639.24	3432.85	4871..06

Band1	2	3	4	5	6	7	8
8.95	8.89	27.79	26.85	11.31	66.99	50.90	74.05
8.89	17.78	51.48	45.43	21.88	102.98	81.81	113.53
27.79	51.48	327.33	239.69	75.85	846.04	715.93	919.13
26.85	45.43	239.69	228.09	77.90	629.70	446.45	644.17
11.31	21.88	75.85	77.90	39.69	136.06	83.01	125.50
66.99	102.98	846.04	629.70	136.06	3097.72	2706.23	3676.97
50.90	81.81	715.93	446.45	83.01	2706.23	2768.35	3470.08
74.05	113.53	919.13	644.17	125.50	3676.97	3470.08	4931.17

Band 1	2	3	4	5	6	7	8
9.45	10.07	27.31	29.47	13.40	64.95	51.30	76.66
10.07	19.26	52.03	51.19	25.42	107.99	84.31	127.13
27.31	52.03	344.90	254.76	79.32	921.17	793.28	1027.40
29.47	51.19	254.76	249.87	89.78	664.84	485.57	708.60
13.40	25.42	79.32	89.78	47.43	136.78	79.92	135.92
64.95	107.99	921.17	664.84	136.78	3414.33	3066.42	4118.57
51.30	84.31	793.28	485.57	79.92	3066.42	3165.75	3951.29
76.66	127.13	1027.40	708.60	135.92	4118.57	3951.29	5513.88

In order to understand the fuzzy MRF performance, a combination of SRM's have been generated using conventional, SA and FCM based class PDF estimations for a range of smoothness parameters (λ). Below in the Fig. 5.2 the difference in the posterior energy estimation due to crisp and the fuzzy class estimations are shown. Energy resulting at each iteration is different from the crisp sets in the case where the fuzzy membership grades are determined for each pixel. Here it is important to note that λ is the key parameter which controls the contribution of the prior and the likelihood energy in the posterior energy determination. As an example when λ=1 the likelihood term is completely ignored in Eq. 3.27 for a

minimal posterior energy, forcing all the pixels to be classified to a single class. The validation of the SRM at both pixel level as well as the sub pixel level is a complex process. This becomes even trickier when proper ground truth information is not available. For an unbiased validation among the approaches, it is always better to estimate the class parameters using the same ground samples. This allows us to see the variability in the PDF estimation in the three methods. According to the previous experiments done on the parameters of the MRF technique it has been observed that for smaller scale factors $S \leq 4$, λ takes the values in the range of 0.7 to 0.9 (Tolpekin and Stein 2009) to generate the optimum SRM. Accordingly in the experiments for S=2, the highest accuracy of the SRM with respect to the reference image was attained at λ =0.9, for both fuzzy as well as the ordinary MRF models. These results are shown in Fig. 5.3. This figure shows the difference in the smoothness levels for different λ=0.7,0.8,0.9 .

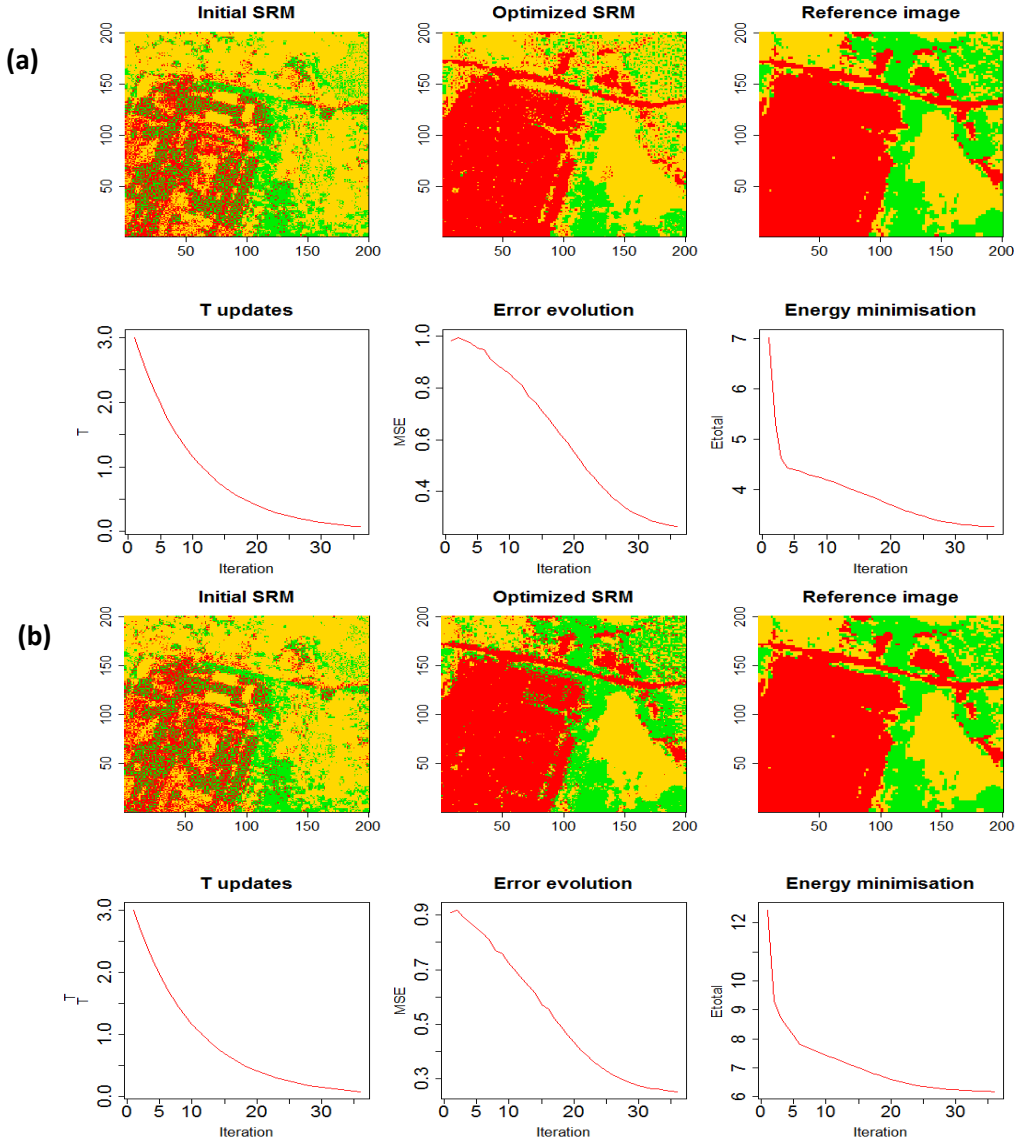

Figure 5.3 SRM process the temperature drop and the posterior energy calculation from the initial SRM using (a) fuzzy class parameters (b) conventional class parameters using Worldview-2 image

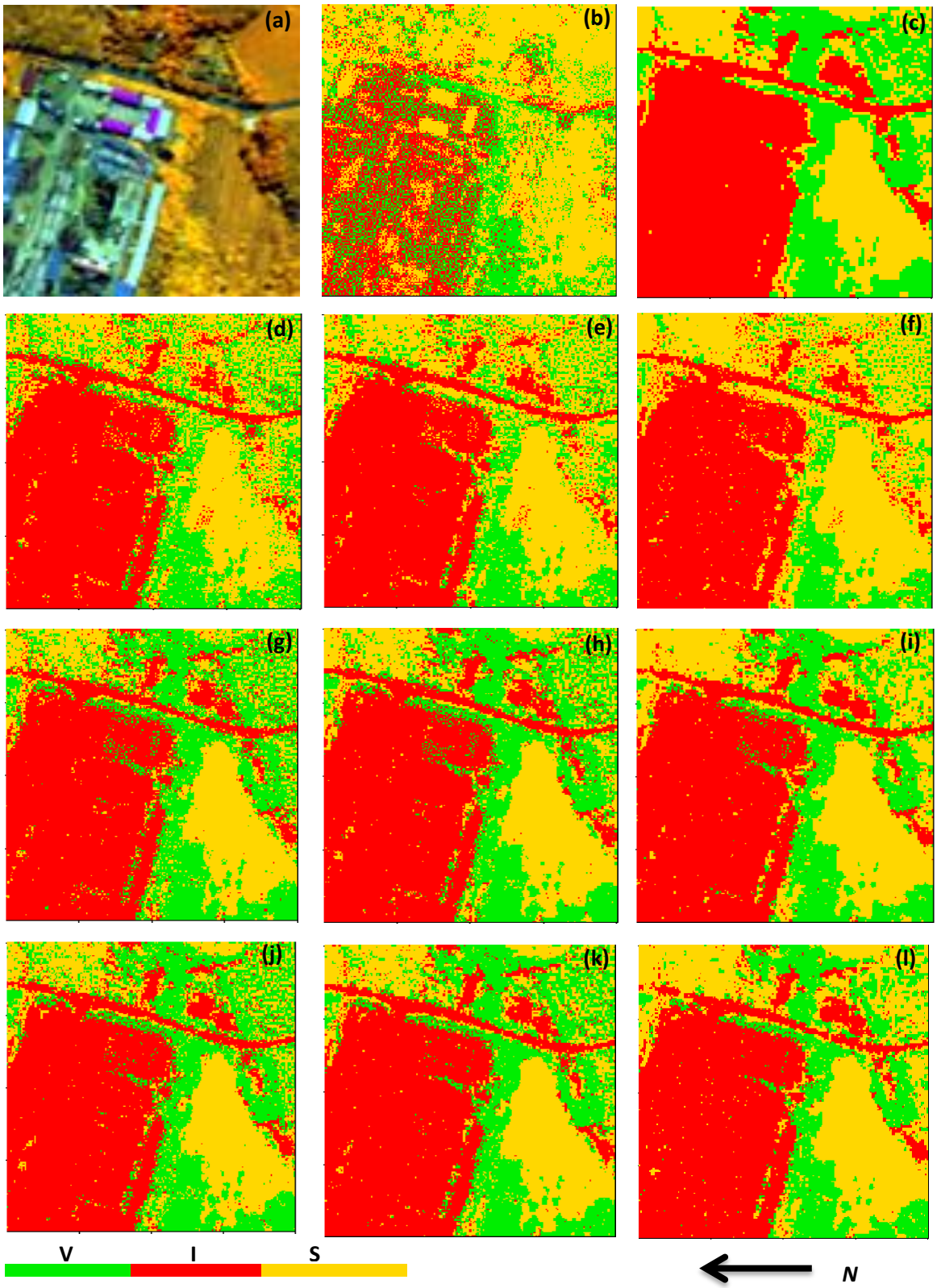

Figure 5.4 (**a**)**100 × 100** Worldview-II false color multispectral band composite RGB (8, 5, 3) (b) Initial SRM (c) MLC reference image, (d), (e), (f) optimum SRM generated at λ=0.7,0.8,0.9 for the conventional case, (g), (h), (i) optimum SRM generated at λ=0.7,0.8,0.9 using SA class parameter and MRF (j), (k), (l) optimum SRM generated at λ=0.7,0.8,0.9 using the fuzzy c-means class parameter estimations and MRF

Table 5 3 Kappa and OA, agreement for the SRM generation processes

Conventional MRF			SA parameter based MRF			Fuzzy c-means parameter based MRF		
λ	OA	Kappa	λ	OA	Kappa	λ	OA	Kappa
0.9	77.70%	0.65	0.9	85.71%	0.78	0.9	85.57%	0.78
0.8	77.26%	0.64	0.8	84.52%	0.76	0.8	85.25%	0.77
0.7	75.94%	0.62	0.7	83.04%	0.74	0.7	83.93%	0.75

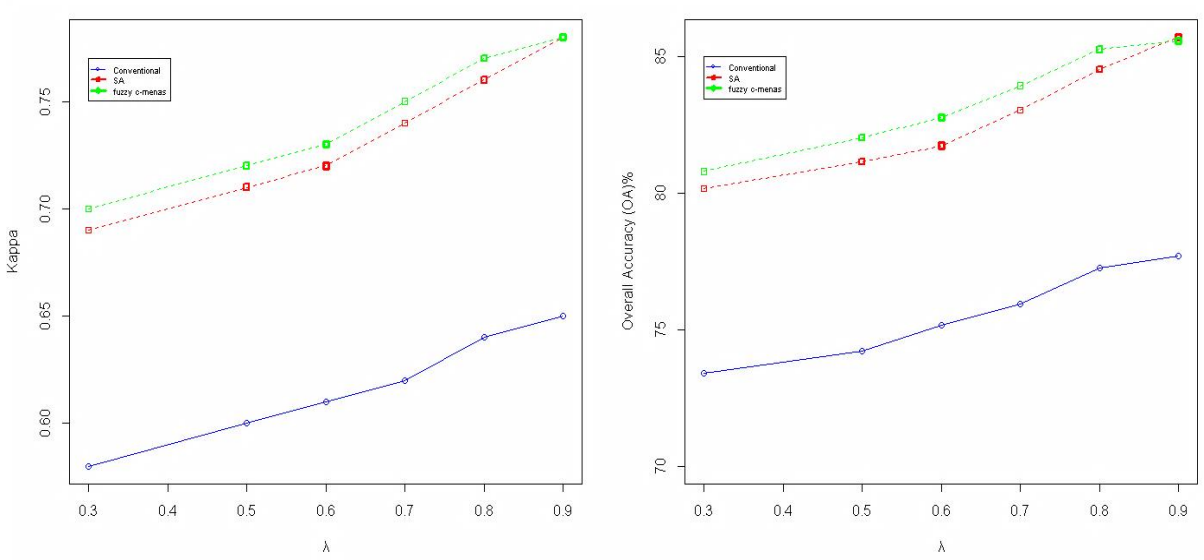

Figure 5.5 Kappa and the Overall Accuracies for the Fuzzy and the conventional MRF models for λ values ranging from 0.3 to 0.9

Table 5.3 reveals the steady increase of the kappa agreement between reference and the SRM generated at λ=0.7, 0.8, 0.9 for the three models. At λ=0.9 the highest accuracy SRM is generated with a kappa agreement of 0.78 for both SA and FCM approaches while 0.65 in the conventional approach (Table 5.3). A visual inspection of the SRM in Fig. 5.4 also justifies this result, with smoother SRM resulting in the fuzzy based approaches with respect to its conventional counterpart. For the total λ range investigated from 0.3 to 0.9 (Fig. 5.5) the FCM and SA models have produced SRM maps more close in agreement with the MLC reference map with the kappa values ranging from 0.7 to 0.78, where in the conventional case it was at 0.55 to 0.65. This clearly suggests that the fuzzy class parameter estimation inside the MRF based SRM model has a significant influence in its performance. Table 5.4 shows the error matrices generated for the fuzzy MRF model using SA and FCM approaches and the conventional SRM. From the table, the user accuracy (reliability) for the grass and exposed soil class is 74% and 72% in the fuzzy MRF models using SA and FCM definitions respectively. But in the conventional case this was 58%. Grass and exposed soil (soil) class attains a comparatively higher degree of uncertainty in the parameterization than the other two classes. This is mainly due to its higher mixture with the vegetation class. The joint distribution of normally distributed two variables is expected to be a Gaussian

distribution. The determination of the class fractions are from normally distributed pixel vectors of the class samples. These fractions assigned as the membership grades tend to preserve the original distribution and provide better probabilistic measures for classes within a pixel. This affects the pixel labelling problem with the fuzzy MRF model, demanding the pixels to have accurate statistical measure through the prior and likelihood energy determination than in the conventional method. Hence with the use of the membership grades the classification results have significantly improved for the soil class. The persistence of the classification agreement between the ground truth classes and the thematic classes for the vegetation and Impervious categories are slightly higher in the fuzzy parameterized MRF model than its conventional case. This can be seen from the diagonal elements of the error matrices.

Table 5 4 Confusion Matrices

Conventional MRF

Thematic Classes	Ground Truth Classes: V	S	I
V	4403	733	101
S	5193	9968	1932
I	452	467	16751

FCM based MRF

Thematic Classes	Ground Truth Classes: V	S	I
V	7232	893	427
S	2466	9856	1216
I	350	419	17141

SA Based MRF

Thematic Classes	Ground Truth Classes: V	S	I
V	7346	870	565
S	2296	9803	1129
I	406	495	17090

The validation was carried out mainly to compare the fuzzy and the conventional MRF results for their performance at a pixel level. But it has certain draw backs as the error matrix doesn't provide the convenience to evaluate the effect of the multiple memberships' assignment for each pixel and also the fractional agreement of the fuzzy classification. To evaluate the fractional agreement between the optimal SRM and the reference images, MAE error measure has also been employed. A fixed area size for the comparison was set to 5×5 pixel area. This fixed area size is chosen so that in this region the MLC classified output provides the necessary mixture condition for all the three classes to have fractional estimations. The definition of the fixed area can vary depending on the heterogeneity of the classes in the study region. The proportions of the classes within this fixed area of five by five pixels were determined for both the SRM and the reference images. The MAE for the fuzzy integrated MRF model and the conventional model based SRM are shown in Table 5.5. According to the table average MAE for both the SA and FCM based fuzzy MRF models are close to each other with a value of 0.03 and smaller with respect to the conventional case where it is 0.1. This is a useful result to further understand the healthier performance of the fuzzy parameter integrated schemes.

Table 5 5 MAE for the fuzzy integrated MRF models and the conventional MRF model

		V	S	I	Average MAE
MAE	SA parameter based MRF	0.03	0.05	0.02	0.03
	Conventional MRF	0.12	0.15	0.03	0.10
	fuzzy c-means based MRF	0.04	0.06	0.02	0.03

The use of PSNR and the SSIM indexes for the validation purposes is done at the sub pixel class fractional level. Hence the fractional images were generated by degrading the SRM and the reference images to their respective classes. The SSIM maps generated using the SA and FCM based SRM images and the reference images are shown in the Fig. 5.6 and 5.7. Interpreting the SSIM images to understand the description of the structural similarity measured in between the images compared is very important. In the SSIM images the areas represented by bright regions shows strong similarity while the dark regions shows the dissimilarity. The generated SSIM matrices suggested close fractional agreement between the classes determined by the MRF based SRM classifications with the fuzzy class definitions and the reference images produced by using SVM.

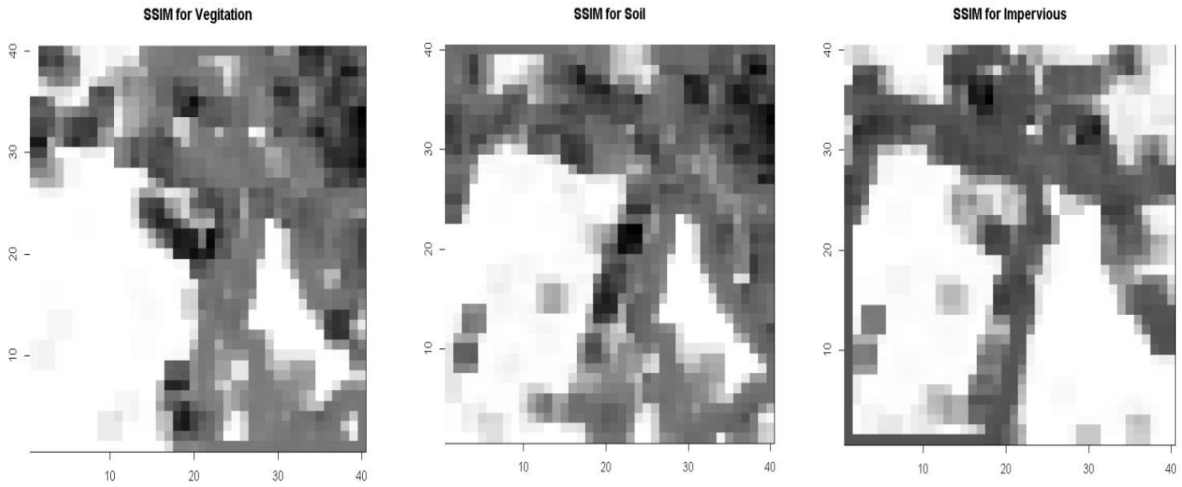

Figure 5.6 SSIM index maps generated using 3×3 sliding window between fractional images obtained by degrading the SA parameter based MRF SRM and reference images

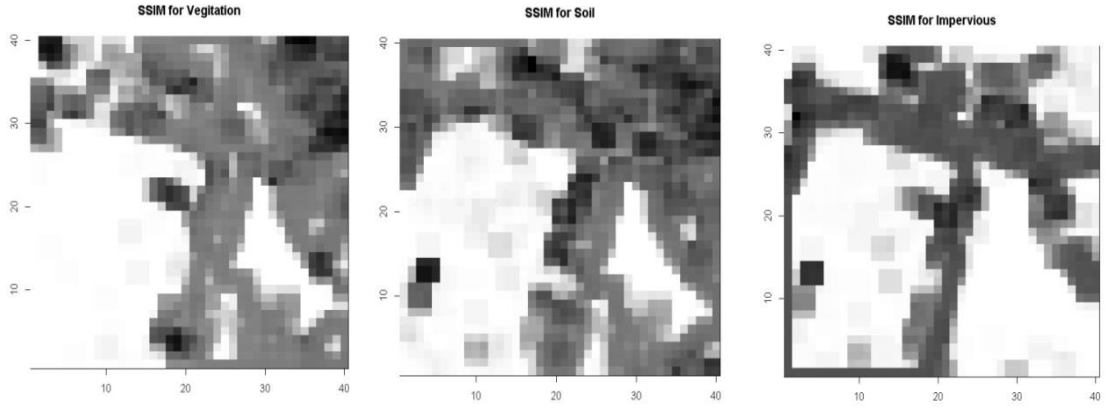

Figure 5.7 SSIM index maps generated using 3×3 sliding window between fractional images obtained by degrading the FCM parameter based MRF SRM and reference images

In the case of SSIM index, we implemented a 3×3 local sliding window on the fractional images to generate the SSIM values for each pixel. The average of the SSIM values for each class and the PSNR values are reported in the Table 5.6. The use of these two measures for classification fractional comparison is quite recent; further experiments can improve better understanding. The structural similarities represented by the fractions of the V-I-S classes in each SRM technique are more or less the same according to the PSNR and SSIM measures. Both conventional and the SA based SRM methods show an identical class fractional arrangement with PSNR values ranging from 26db to 43db and mean SSIM values ranging from 0.57 to 0.78. In the FCM based SRM method the agreement between the fractional images shows a slight improvement, with PSNR values ranging from 37.20db to 47.85db and mean SSIM from 0.54 to 0.80 for each of the V-I-S classes. The contextual refinement of the MRF based SRM method at local spatial neighborhood is significantly stronger due to the prior information modelled by the clique potential functions. More over the MRF based SRM in this study is using higher resolution data sets. Hence the resulting spatial structure of the classification outputs should emphasize strong relationship among them, as suggested by the PSNR and SSIM.

Table 5 6 MAE for the fuzzy integrated MRF models and the conventional MRF model.

		V	S	I
PSNR	SA parameter based MRF	26.66	25.81	43.79
	Conventional MRF	26.55	25.69	43.87
	fuzzy c-means based MRF	37.20	35.62	47.85
Average (SSIM)	SA parameter based MRF	0.57	0.36	0.78
	Conventional MRF	057	0.36	0.77
	fuzzy c-means based MRF	0.54	0.51	0.80

To further understand the performance of the proposed model with respect to different classification techniques SRM results were cross validated with SVM and NN based classifications. We chose a pixel based comparison using error matrices to compare these techniques. The choice of the two classification techniques SVM and NN were made mainly because of their ability to classify remote sensing images nearly as accurate as the statistical classification approaches (Foody and Matur 2006, Pal and Mather 2004). The NN was performed using a feed-forward NN classification technique, while SVM was implemented using radial basis function kernel on the resampled image of 1m resolution. Same training samples employed for the MLC has been used for both these classifications. This helps to keep the effect of the variation of size, composition and nature of the training data constant for all the classification techniques (Foody and Matur 2006). The SVM and NN classification based reference images and the optimum SRM generated at a smoothness parameter of (λ) = 0.9 are shown in Fig. 5.8 below.

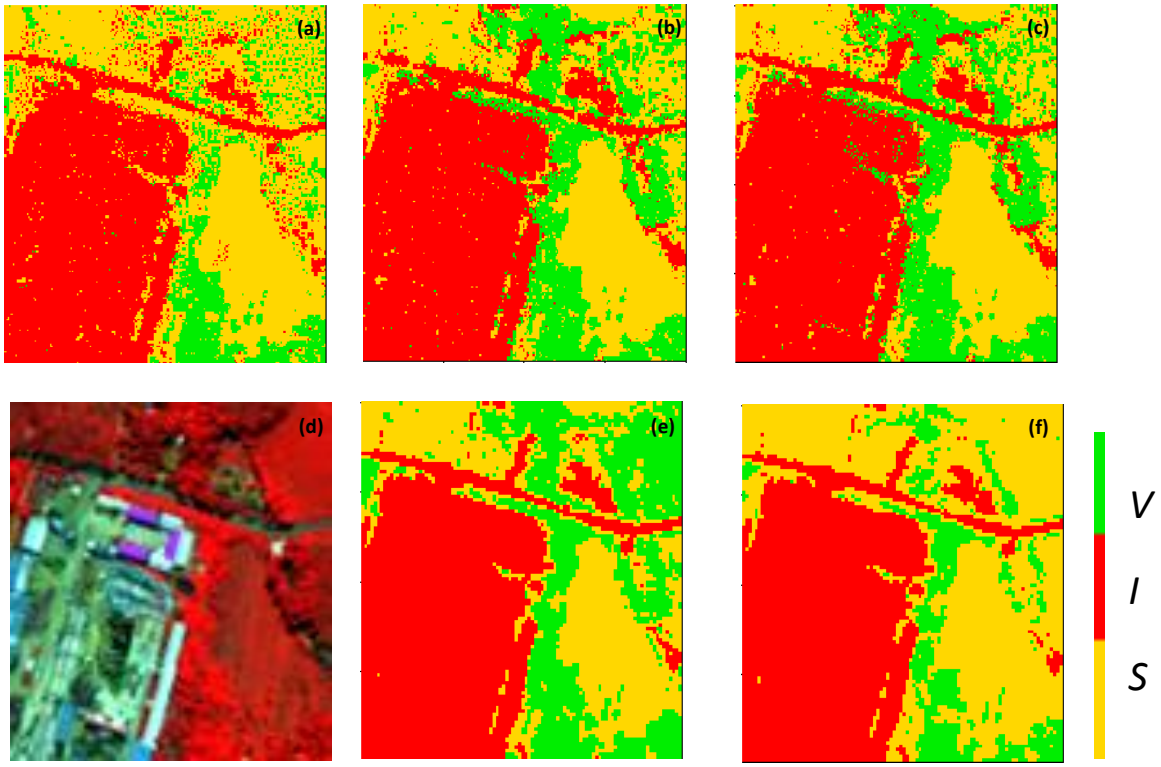

Figure 5.8 (a), (b), (c) SRM generated at λ= 0.9 conventionally, SA and FCM techniques, (d) Worldview-II false color multispectral band composite RGB (8, 6, 2) (e) (f) SVM based and NN based reference images

One of the striking features of the MRF based SRM is its contextual refinement, trying to classify the local regions as accurately as possible in a higher spatial resolution. This also preserves the local class heterogeneity as can be seen in Fig. 5.8 (b) and (c). Mostly in the SVM and NN based classifications we have to classify the image at the nominal spatial resolution and then resample it into a higher spatial resolution. This procedure does not preserve the local neighborhood statistics as the resample always try

to develop homogeneous regions with heterogeneous local spatial neighborhoods. The Kappa statistics and the Overall Accuracy (OA) agreement between two SRM and the reference maps generated using SVM and the NN are shown in the Table 5.7.

Table 5 7 Evaluation with SVM and NN based reference data respectively

Accuracy assessment with the SVM based reference data						
λ	SA based parameters		Conventional Parameters		fuzzy c-means based parameters	
	OA	Kappa	OA	Kappa	OA	Kappa
0.9	83.34%	0.74	77.78%	0.67	83.67%	0.74
0.8	82.74%	0.73	77.75%	0.65	83.71%	0.74
0.7	81.26%	0.71	76.48%	0.64	82.40%	0.73

Accuracy assessment with the NN based reference data						
λ	SA based parameters		Conventional Parameters		fuzzy c-means based parameters	
	OA	Kappa	OA	Kappa	OA	Kappa
0.9	81.70%	0.71	83.42%	0.72	82.39%	0.72
0.8	76.91%	0.64	79.35%	0.67	78.06%	0.66
0.7	75.63%	0.63	76.84%	0.63	76.67%	0.64

For both the cases, the highest agreement between the reference images and the optimal SRM were achieved at λ=0.9 as in the instance of MLC. For the SVM based comparison the SA and FCM based SRM results shows a higher kappa agreement of 0.74 while for the conventional method it is low as 0.67. In the case of NN based reference image, both the fuzzy and conventional based MRF models at λ= 0.9 show more of a similar result, with the average kappa agreement being 0.72. The poor inherent classification accuracy of the NN based reference image can have a significant effect on this result. The quality of the NN based classified image has shown a strong sensitivity to the training samples. As a condition of the study we proposed to keep the training samples same for all the techniques we tested. Visual inspection shows, a substantial confusion between the vegetation and the soil classes (Fig. 5.8(f)). Hence it is vital to use precise ground truth data in the case of NN to produce a more accurate validation dataset prior to the use of them as validation samples. The quantitative analysis and the visual inspection of overall results highlight the superiority achieved by the fuzzy class parameter definitions in the MRF models. These extended experiments reveal the consistency of the proposed SRM model with respect to more familiar and frequently used classification methods MLC, SVM and NN. The experiments carried out using the proposed fuzzy parameter integrated MRF based SRM method was further tested using the AVNIR-2 multispectral image. The testing was carried out using an image sample over an area where the PSF effect can be identified more clearly than the experiments with the Worldview-2 image sample.

5.1.3 Experiments using AVNIR-2

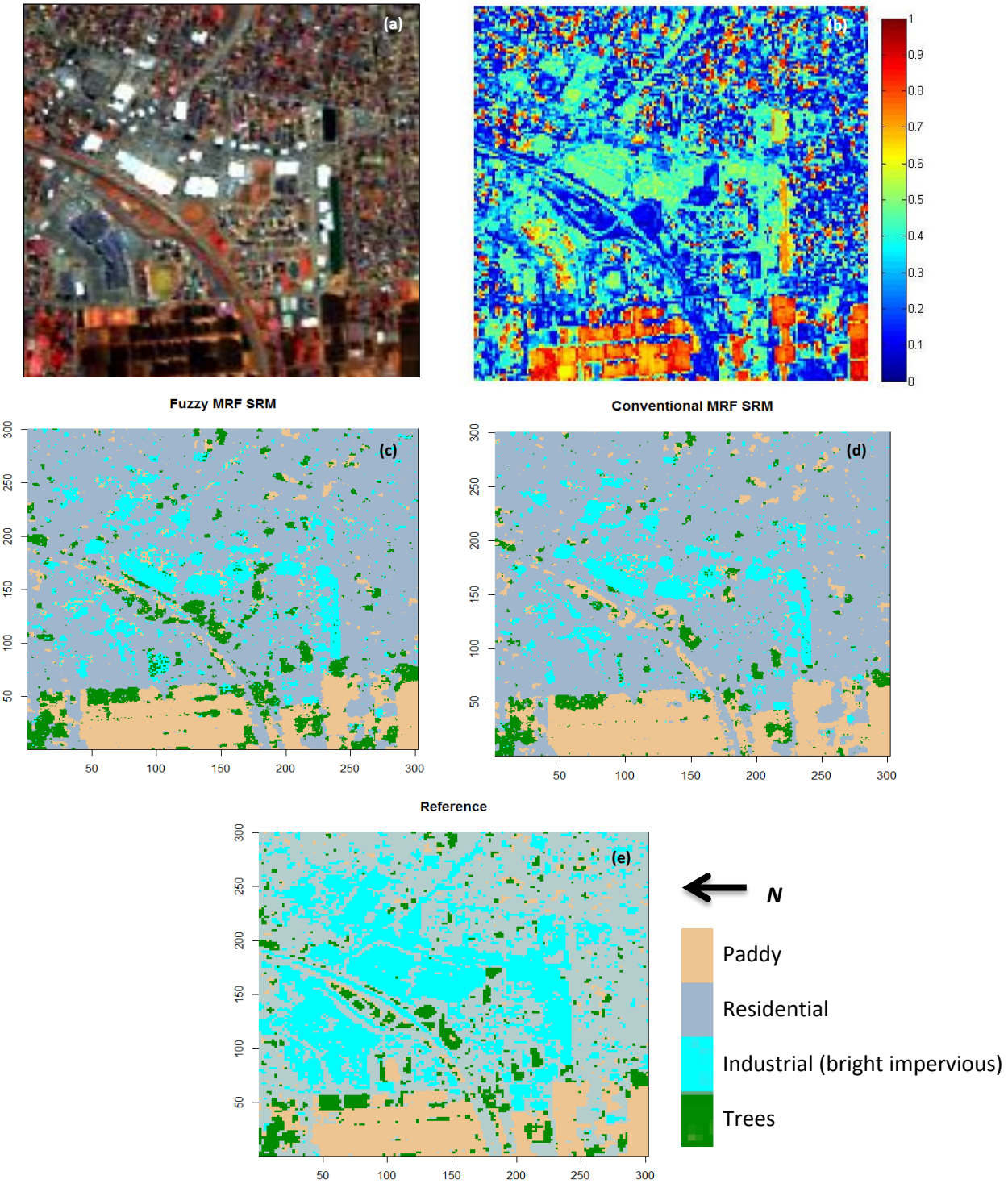

Figure 5.9 (a) AVNIR-2 false color multispectral band (10m) composite RGB (4,3,2) (b) FCM based class memberships, Optimized SRM at 5m resolution ($\boldsymbol{\lambda = 0.6}$)) using (c) fuzzy MRF (d) conventional MRF and (e) SVM based classification at 5m

The test results where the second experiment for AVNIR-2 using FMRF framework was carried out is shown in the Fig. 5.9. As result we create 5m SRM maps from the 10m AVNIR-2 images. The corresponding FMRF and MRF processes with resulting energy functions are shown below in the Fig. 5.10. As can be seen from the image the area is selected over a heterogeneous urban region (dominated by bright impervious objects) in the test site 2. These bright impervious objects mainly the buildings were selected as the main classification class of interest. These bright impervious pixels are mostly consists of pure pixels as shown in Fig. 5.11, and lies close to the convex hull showing strong end member candidacy. In most of the multispectral images at medium spatial resolutions (10m -15m) the PSF effect is linked with the impervious object due to its huge range, varying from low albedo to high albedo. Classification of these regions is always a difficult task, even with the existing strong classification mechanisms such as SVM and NN. We performed the MRF based SRM over these regions using a scale factor S=2.

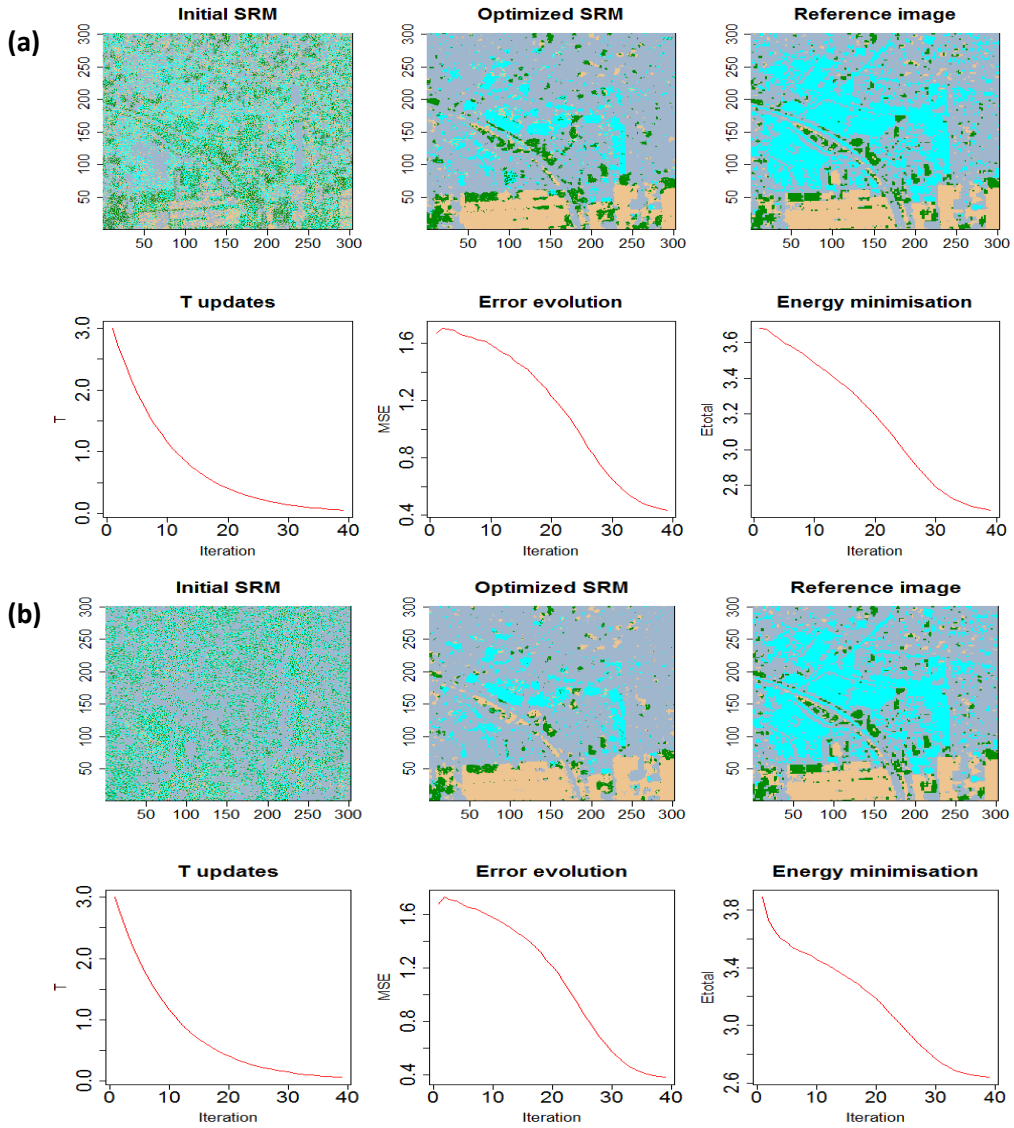

Figure 5.10 SRM process the temperature drop and the posterior energy calculation from the initial SRM using (a) fuzzy class parameters (b) conventional class parameters using AVNIR-2 image

We test the conventional and the fuzzy MRF based SRM separately on the selected image samples. The fuzzy grade of memberships for each multispectral image pixels was determined by employing the FCM clustering mechanism.

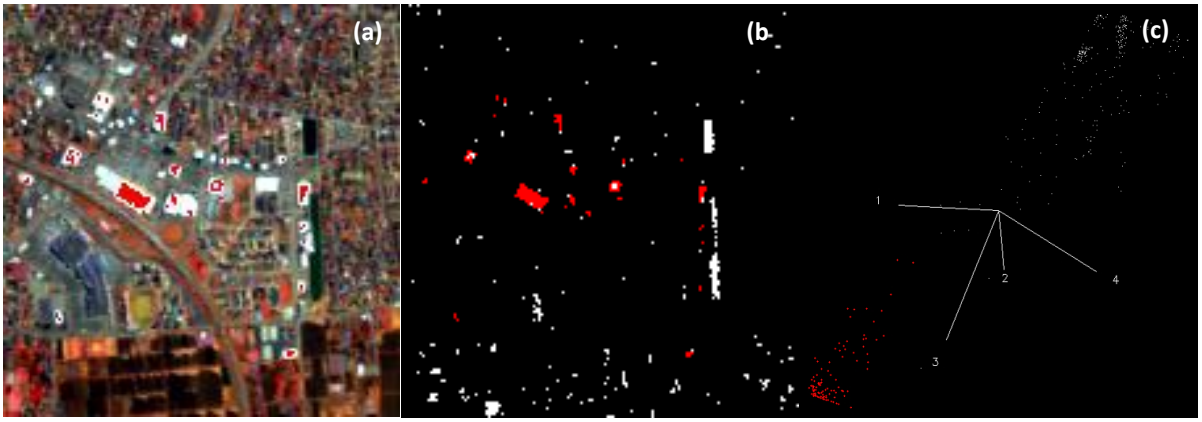

Figure 5.11 (a) Sample AVNIR-2 false color image showing the pure pixel distribution over the urban area (c) Image pure pixels (d) spectral plot of the pure pixels in the feature space

The use of membership grades generates a fuzzy membership function for the training class pixels. This function determines the contribution of each training pixel for the posterior energy estimation. This is the main difference between the crisp and the fuzzy classification mechanisms. As a matter of fact, in the crisp mechanisms this function takes either value 1 or 0. Hence the class properties represented by the mean and the covariance will change accordingly. The calculated fuzzy class mean values and the covariance for the bright impervious class are shown in Tables 5.8 and 5.9.

Table 5 8 Fuzzy and conventional class mean values for the 4 classes chosen for the classification

AVNIR-2 image bands		1	2	3	4
Industrial	Fuzzy C-Mean	168.86	152.85	145.2475	59.88
	Conventional	165.90	149.36	142.05	58.92
Residential	Fuzzy C-Mean	123.82	98.06	89.24	42.67
	Conventional	125.65	100.98	93.93	45.50
Exposed Soil and Grass	Fuzzy C-Mean	110.05	81.91	73.97	37.19
	Conventional	111.16	83.96	76.84	39.37
Vegetation	Fuzzy C-Mean	52.31	94.12	86.51	52.32
	Conventional	120.45	97.95	92.02	55.52

With the use of the fuzzy membership grades the calculated energy during the MRF process at each iteration will be different (Fig. 5.10, 5.12) providing a different SRM. Fig. 5.13 and 5.14 shows the characteristic membership function for the industrial and the residential pixels. Hence this function associates the pixels with varying membership weighting for the PDF, providing much better estimation for the posterior pixel distribution and reducing the contribution of the noisy pixels with low weights.

Table 5 9 (a) Fuzzy and (b) conventional covariance matrices for the bright impervious (industrial) class training sample

Bands	1	2	3	4
1	1817.89	2204.82	2385.17	920.58
2	2204.81	2707.72	2915.58	1124.84
3	2385.16	2915.58	3203.75	1234.85
4	920.57	1124.84	1234.85	488.72

(a)

Bands	1	2	3	4
1	1727.09	2091.41	2240.18	857.39
2	2091.41	2563.73	2733.00	1045.65
3	2240.18	2733.00	2974.22	1137.54
4	857.39	1045.65	1137.54	447.56

(b)

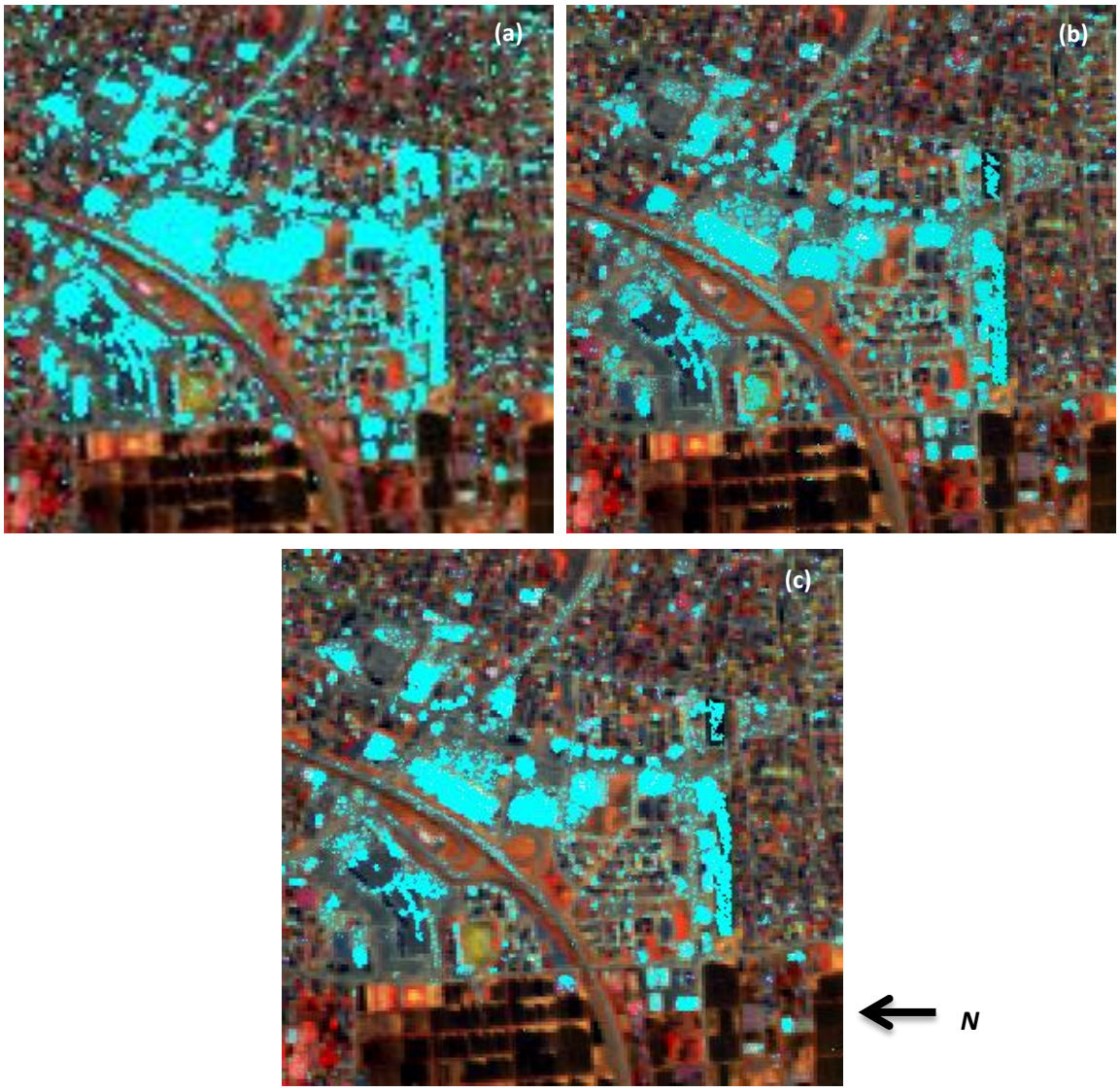

Figure 5.12 The reduction of the contribution of noise in the classification (bright impervious regions) using MRF techniques (overlay of the impervious class labels on the real image) (a) SVM technique with the images resampled to 5m (b) by the fuzzy MRF based SRM (c) conventional MRF based SRM

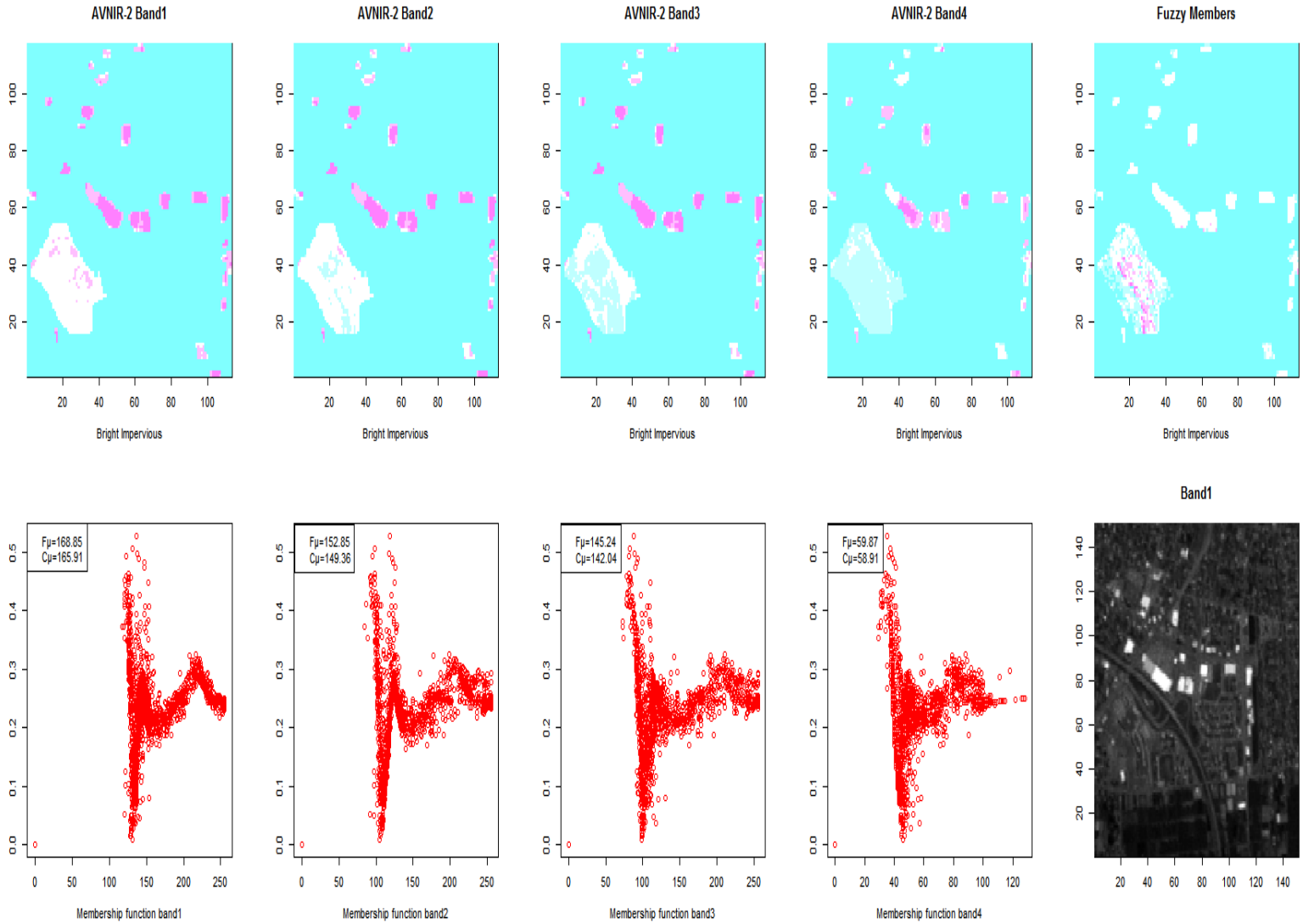

Figure 5.13 Membership functions generated for the industrial (bright impervious) region pixels using FCM clustering showing the deviation of the fuzzy mean ($F\mu$) from the conventional mean ($C\mu$)

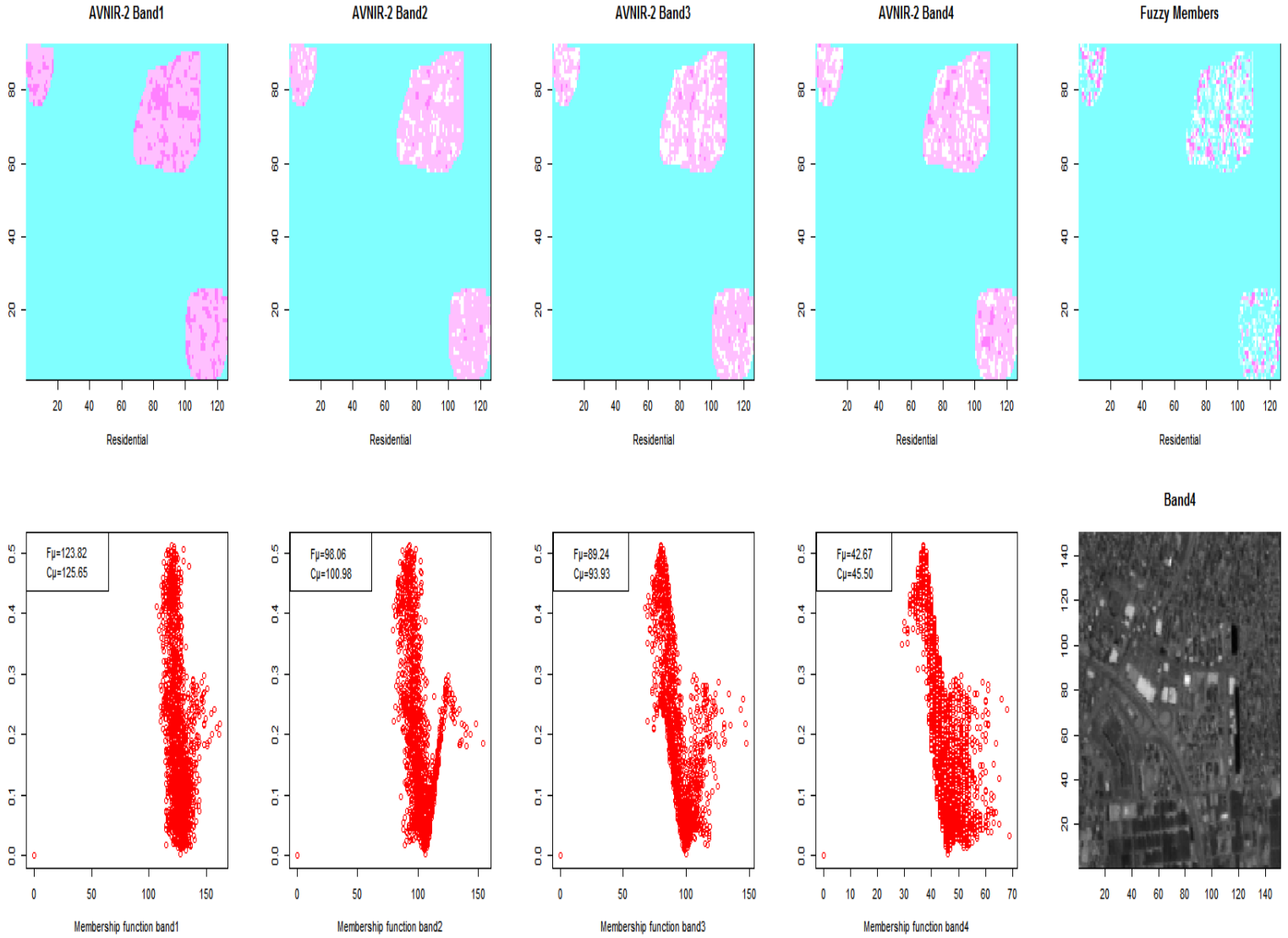

Figure 5.14 Membership functions generated for the residential region pixels using FCM clustering showing the deviation of the fuzzy mean ($F\mu$) from the conventional mean ($C\mu$)

Table 5 10 Accuracy assessments with SVM based classification results

Comparison with the SVM based classification				
λ	Conventional MRF		fuzzy c-means based parameters	
	OA	Kappa	OA	Kappa
0.3	67.50%	0.49	61.88%	0.44
0.4	69.52%	0.51	73.50%	0.58
0.5	71.19%	0.53	68.71%	0.51
0.6	72.00%	0.53	70.80%	0.53
0.7	71.99%	0.52	72.17%	0.53

The accuracy assessment of the produced fuzzy MRF and the conventional classification with the SVM based classification is shown in Table 5.10. The validation task of the MRF process is the most tedious in the setup. Very few works have been done to justify the most suitable classification accuracy assessment for the SRM maps. The problem is that to assess the accuracy of a SRM it is important to have another SRM at hand or either a detailed ground truth map. As the main objective was to implement the multisource SRM mechanism, we put less effort in this thesis to identify a proper accuracy assessment or validation mechanism as it requires a complete different research setup.

According to the above table the FMRF shows low agreement with respect to the conventional MRF results with the SVM based reference data. This is an interesting result as the reference image we have used for the validation contains significant amount of noise. Hence the more deviated agreement from this reference data can be considered as the most accurate. In another way this means closer the agreement with a noisy data set shows poor accuracy. Therefore at $\lambda = 0.5$ the FMRF results yielded an agreement of 0.51 and 68% for kappa and OA respectively while MRF reports 0.53 and 71% for kappa and OA. This can be interpreted as an improved fuzzy MRF classification result with noise to a lesser degree. Further this application and the testing of MRF in a Japanese remote sensing satellite image can be considered as the first of its kind with respect to the history and application of MRF models in remote sensing data sets. AVNIR-2 image also favors the MRF based SRM mechanism as in many other satellite images such as IKONO, ASTER, Landsat.

5.2 Autoregressive and autocorrelation SAR texture properties for change analysis

The description given in section 4.2.4 for the generation of SAR texture and the noise reduction using Lee filters are used for time series data analysis in the form of change detection in the second study region in the east coast of Japan. The Fig. 5.15 details the study area and the section 4.1 can be referred further for more description of the study area. This section which explains change detection in contrast to the MRF, was carried out mainly to test and use the MAR based texture for contextual change analysis prior to its use in the multisource data classification using MRF. From this discussion we clearly suggest the potentials of using MAR based texture for time series data applications.

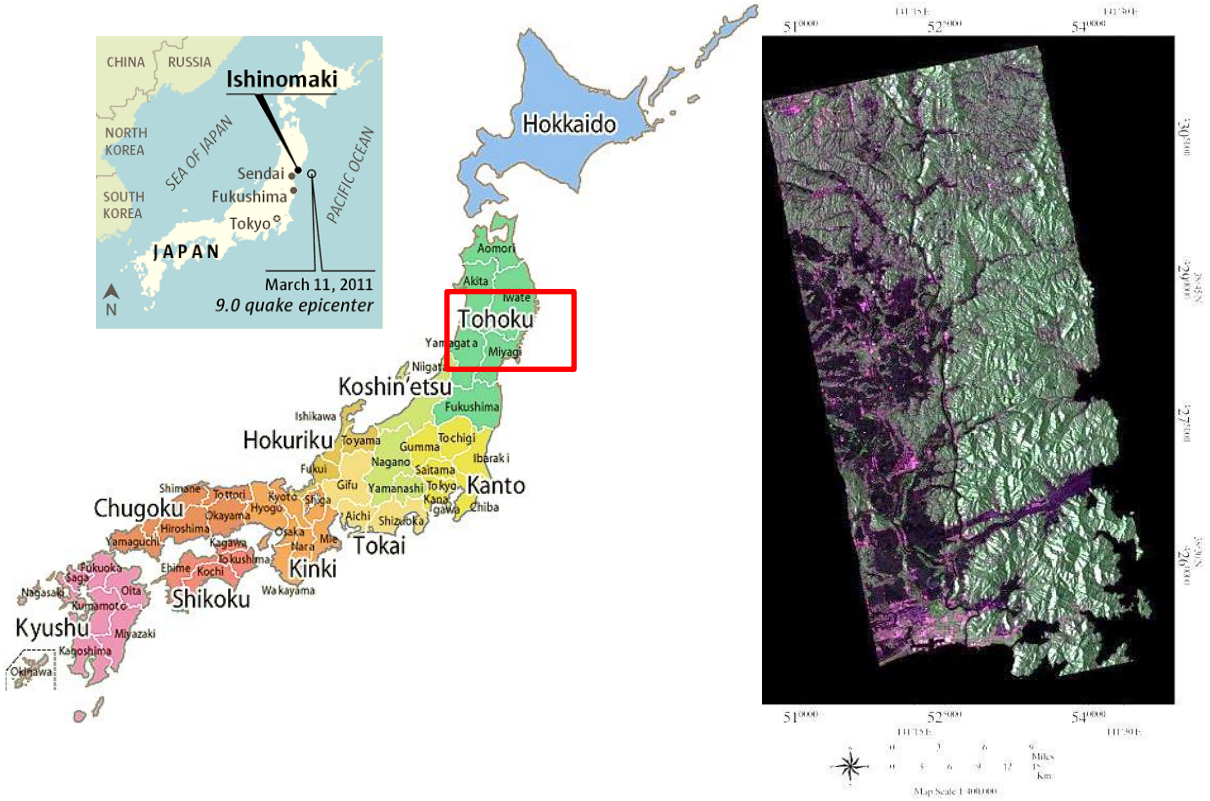

Figure 5.15 Study area map and earth quake epicenter (source-USGS) and the ALOS PALSAR 5 look complex images with HH, VH and VV polarization components in RGB respectively for the post disaster scene on 8th April 2011

Monitoring structural changes of land cover due to different magnitudes of disasters is an important usage of the earth orbiting SAR imagery. This advantage of the SAR over its optical counterpart is made possible by the capabilities of acquiring all weather, cloud insensitive multi-date digital imagery at a global scale. Backscatter intensity, texture descriptors and the interferometric coherence are the primary image features embedded in both amplitude and phase of the recorded scattered wave of the SAR sensor available for change analysis (Del Frate et al. 2008). Due to the coherent nature of the illumination, the radar image pixels are subjected to the effect of speckle noise. Attempts to reduce speckle by coherent spatial averaging, which reduces both fading and spatial resolution have met with limited success in feature extraction (Ulaby et al. 1986). Speckle as a random effect minimizes the optimal use of SAR pixels for the pre and post disaster comparison in the case of change detection. As a result SAR image pixel values become unreliable in the interpretation of spatial patterns. Hence it is useful and appealing to investigate the possibilities of extracting the spatial patterns of backscatterers using textural operators (Del Frate et al. 2008). Texture features reflect the structural arrangement of the ground objects, with

strong relationship to their changes. Temporal changes to the state of land cover can occur due to natural and manmade effects. Two kinds of changes can be considered primarily, abrupt changes corresponding to strong modifications to the state of land cover and the smooth transitions corresponding to slow evolutions (Bujor et al. 2004). Due to disaster such as earthquakes and tsunami, changes to the state of stable land cover can occur mainly from building collapses and debris in urban and barren landscapes as well as flooding in agricultural lands and lagoons.

Spatial configuration in a coastal urban area is a combination of heterogeneous land cover components such as vegetation, impervious surface and soil. The inherent nature of the spatial discontinuity of these features makes it difficult to detect them due to speckle within a single SAR image. Hence multitemporal SAR data can be useful to minimize the speckle and extract the variations. Modelling spatial correlation in radar images, using independent and identically distributed models can be considered as an over simplification of a complex process. Transforming the data to Gaussian statistics and modelling them with linear spatial interactions can be more effective in such instances. Lognormal random field models with multiplicative spatial interactions are a special case of a transformed Gaussian random field for SAR images. Multiplicative autoregressive random fields (MAR), which is a 2-D lognormal random field, is employed in this study to synthesize the radar images into texture (section 4.2.4.3 and section 4.2.4.4). The parameters of a MAR model are highly correlated with spatial distribution corresponding to the intrinsic variability of the backscattering coefficients (Dierking and Skriver 2002). Furthermore MAR model based texture for radar images become more appealing due to the ability to model both the spatial correlation structure and the distribution of the grey-levels (Dierking and Skriver 2002).

Different SAR image change detection algorithms were developed and tested for many years (Cross and Jain, 1983; Chellappa and Chatterjee 1985; Solberg, and Jain 1997; Ehrlich 2009; Bruzzone 2000; Gamba 2007;Del Frate et al., 2008). Among them, the methods based on texture feature have received more attention, mainly because they can suppress the effect of SAR image speckle noise (Stasoll and Gamba 2008; Gamba and Aldrighi 2012; Dekker 2003). On the context of texture, the first order statistics of the fading random variables describe their PDF while the second order fading texture statistics such as auto correlation function describe the relationships between pixels and its neighbors (Ulaby et al., 1986). A comprehensive discussion of the properties of second order statistics which explains how often one gray tone will appear in a specific spatial relationship to another gray tone can be found in Ulaby, 1986 and Haralick, 1973. (Ulaby et al., 1986, Haralick et al., 1973). Lognormal random field based radar image synthesis was first proposed by Franknote and chellappa, 1987 in detail (Franknote and chellappa 1987). MAR model based texture parameters using RADARSAT data were employed in one of the studies to detect forest fires, as a major application (Park et al., 2001). Here it was summarized that the fusion of textural information with the information such as changes in backscatter can improve the results. As a whole, very few efforts were carried out to use the MAR based texture for spatiotemporal changes. An investigation is made to analysis the applicability of MAR based texture parameters to extract temporal changes in an earthquake and tsunami context. These findings are reported as an alternative means to extract changes independent of the polarimetric techniques tested extensively for such purposes.

Theoretically any image processing operation that works on the original image can be performed using MAR texture parameters. In the current study we employed two of these three parameters of MAR, the neighborhood weighting parameter θ and the noise varianceσ_u^2. In second order statistics resulting from

MAR models, the Gray tones close to white represent pixels with strong relation to each other while black gray tones shows regions with isolated entities. For impervious surface, paddy and vegetation class samples, Fig. 5.16 shows Neighborhood Weight (θ) parameter based radar texture difference in the case of pre and post disaster HH and HV polarizations. The approximations of the histograms using a Gaussian fit for each of these samples are followed in the Fig. 5.17. As illustrated by the histograms the distribution of the texture measures for the SAR intensity can be modelled by Gaussian distribution. A shift in the mean values and the changes in the variance from the pre to the post disaster land cover can be observed from the histograms. This is mainly due to the changes in the geometric nature and the moisture content (due to sea water of the tsunami) of the disaster affected urban area (Richards 2009). This also provides the possibility of using MRD conveniently as the changes can be captured by the local mean values of the MAR based texture in a Gaussian framework .

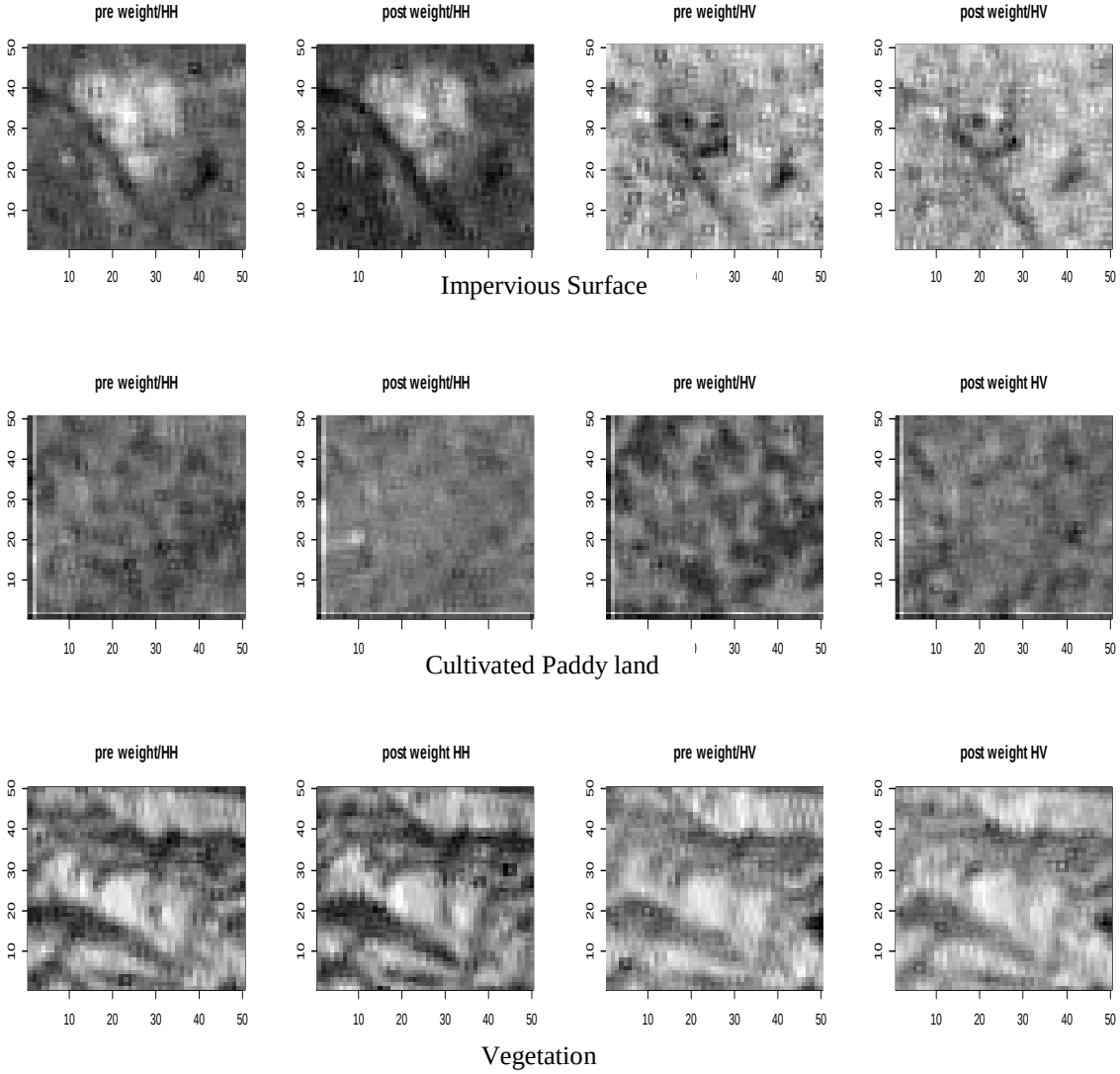

Figure 5.16 Difference in Neighborhood Weight (θ) parameter based radar texture from pre to post disaster situations in HH and HV polarization, for Impervious surface, Paddy and Vegetation class samples

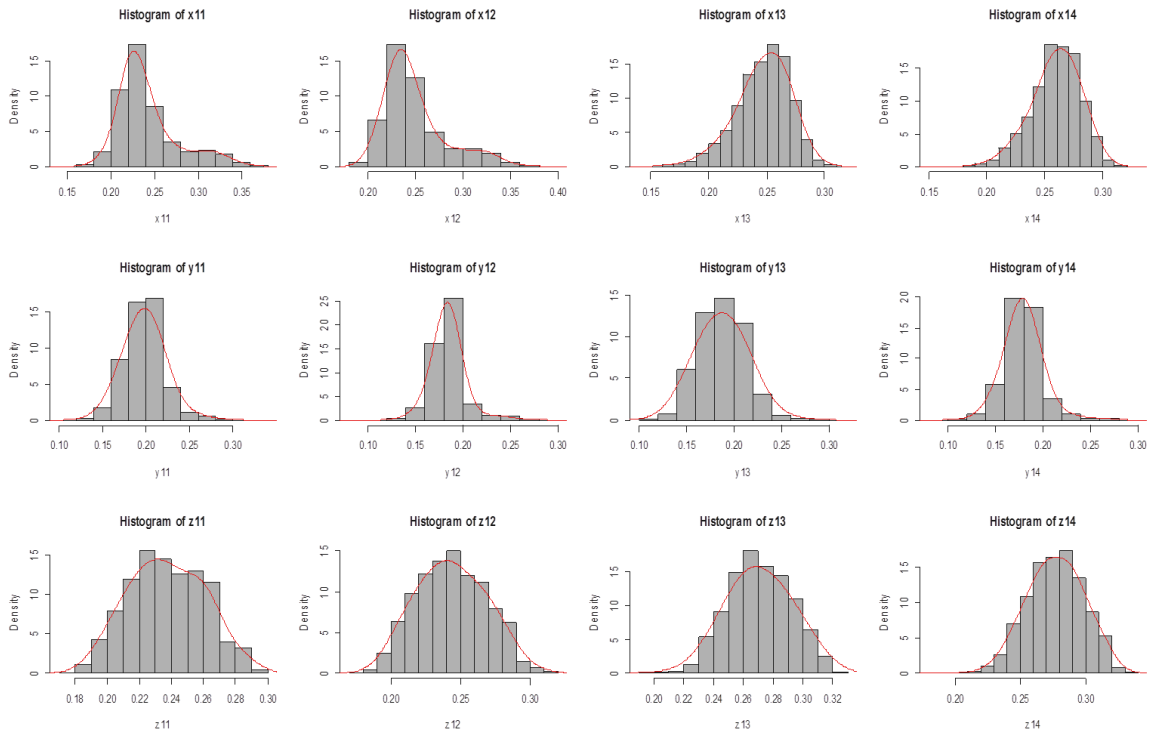

Figure 5.17 Pixel distribution and Gaussian fit for the class samples shown in figure 2 for Neighborhood Weight (θ for 2nd order neighborhood) parameter based texture image, showing the shift in mean before and after the disaster

Generation of MAR texture images as well as the variograms, SSIM and MRD analysis were carried out using R programming environment, version 3.0.1 (R 3.0.1). The influence of the disaster on the urban spatial structure in both adaptive Lee filtered and the MAR based texture images were examined using the variograms. Interestingly they show important differences for both these cases. A 50×200 pixel transect in the urban region running from west to east for both lag distance and radius of 10 pixels was used to generate the variograms. Variogram matrices and the Variogram plots for Lee filtered HH and HV, log HH and log HV with their texture components, θ and σ_u^2 are shown in Fig. 5.18 and 5.19 respectively. Transect generated over the urban area consists of well-built city features, including planned housing networks, roads, railways and canals. It was also observed using the Google earth pre and post disaster images that the tsunami damages are significant along the coast. This balanced city structure is heavily influenced by the tsunami and earth quake. In the case of variograms generated for the filtered images (Fig. 5.18), the heights of the variograms stayed close to each other. Further in all these cases the variogram shape was similar to a spherical mode. The main difference of the pre and post disaster variograms for the MAR based texture is that in the pre disaster situation the shape of the variograms is close to a spherical model while in the case of the post disaster it is almost an exponential model. The exponential model never reaches the sill but asymptotically approaches it. The sharp rise to the sill represents a considerable variance in the size of the urban features due to the effect of the disaster.

The anisotropic variance in the variogram matrices both in the lognormal images as well as the MAR based texture images (θ, $\boldsymbol{\sigma}$) further justify the change in variance of the objects after the disaster. This

could happen due to the rubble and the significant destruction to the planned arrangement of urban objects caused by the tsunami effect. Additionally the change in the sill relates to the change in object density along the transect due to the impact of the disaster. Variograms calculated by using the MAR based texture take hold of the underlying spatial variations while the filter based approaches lack them.

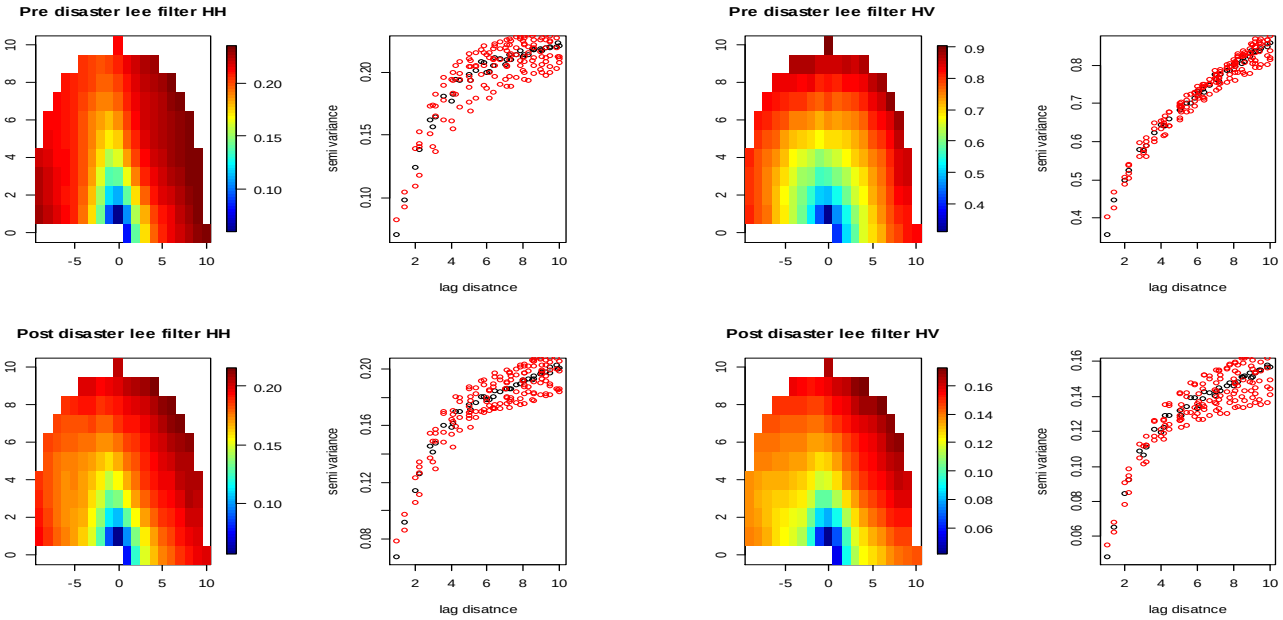

Figure 5.18 Variogram matrices and the variogram plots for Lee filtered HH, HV components respectively along a transect over the urban area before the disaster and after, showing the variograms shape being close to exponential. And the matrices show the isotropic variance with respect to lag distance corresponding to the variogram

The SSIM maps generated from the pre and post disaster speckle filtered and texture images are shown in Fig. 5.20. The use of SSIM to study the structural similarity between images is not feasible without the speckle filtering. But with MAR models the multiplicative effect of the speckle is subtracted in a local neighborhood. With the treatment of noise in this respect, it is possible to use image quality measure such as SSIM for the temporal change determination. The local statistics μ, σ for the SSIM index in Eq. 3.56 was calculated using a 3×3 local window to generate the SSIM index maps. Visually the images show that the SSIM on filtered images (Fig. 5.20 (a), (b), (c), (d)) were not fully capable to discriminate the changes, but low SSIM values resulted in the regions subjected to changes. On the contrary SSIM perform well to discriminate changes and non-changes using MAR based texture images. This is one of the significant findings of the effectiveness of MAR models to process noisy images.

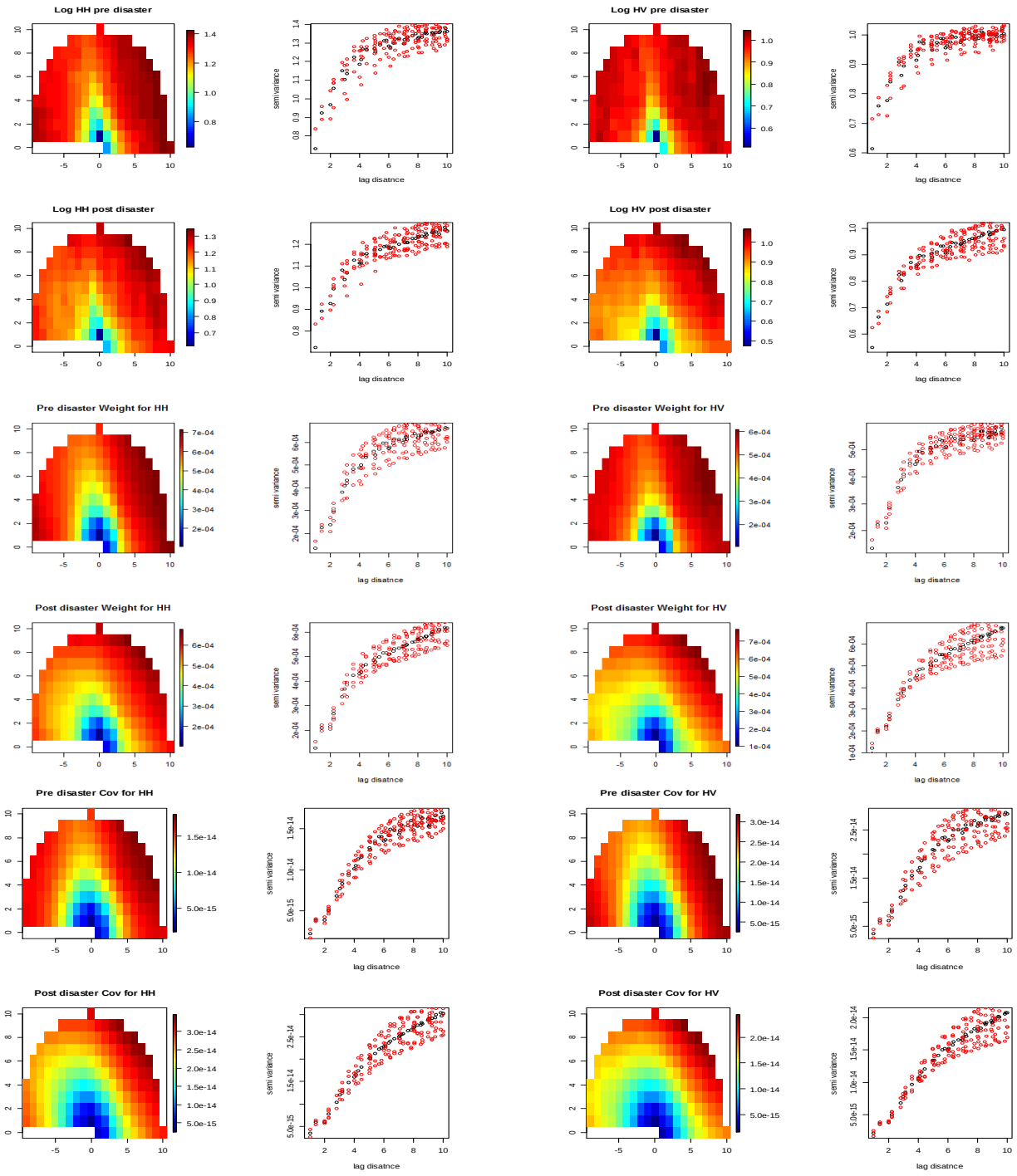

O –Sample variogram **O** –Exponential or spherical

Figure 5.19 Variogram matrices and the variogram plots for log HH, HV components and their texture components, θ and σ_u^2 respectively along a transect over the urban area before the disaster and after, showing the change of the variograms shape from spherical to exponential. And the matrices show the isotropic variance with respect to lag distance corresponding to the variogram

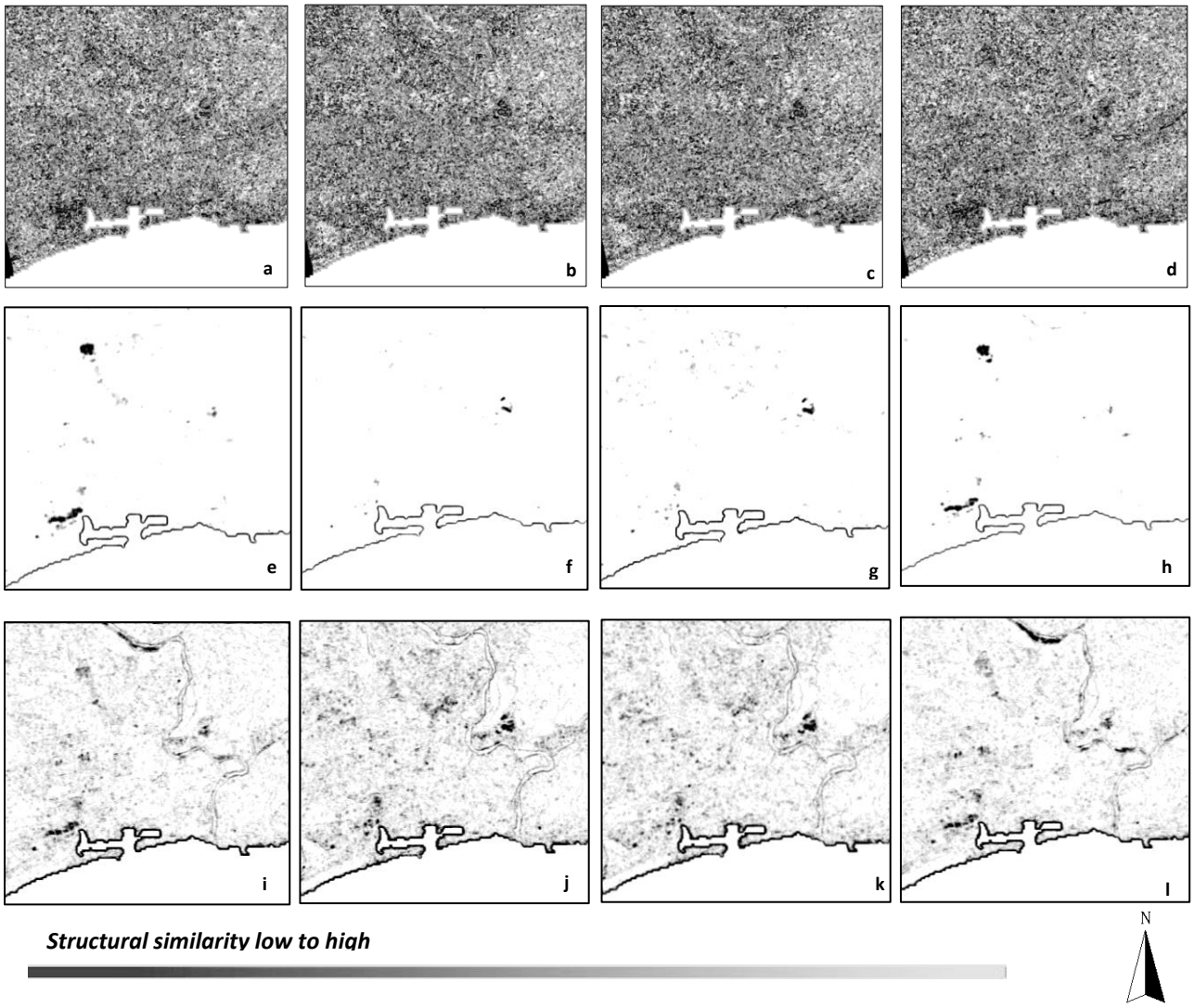

Figure 5.20 SSIM maps with brightness indicating the magnitude of the local structural similarity, the darker areas clearly relates to the changes (a), (b), (c), (d) SSIM between pre and post disaster log transformed filtered intensity images (e), (f), (g), (h) SSIM between pre and post disaster σ_u^2 (e) ,(f), (g) ,(h) SSIM between pre and post disaster θ of HH,HV,VH,VV polarization respectively. SSIM shows improved discrimination between change and no change areas using the texture measure

Finally in the case of MRD we analyzed the results with respect to the PCA and ratio based temporal changes as well as the adaptive filter based changes. The thresholds used to extract the damage levels are shown in Table 5.11. The change results based on MRD are shown in Fig. 5.21 and Fig. 5.22 for the noise filter and the textured SAR imagery respectively.

Visually the SSIM maps suggest that the coastal area has effected significant structural changes, with darker shades in the MAR based texture. Further the significant damages along the Kitakami River due to tsunami along the river basin are well represented. The cross polarized texture measures (Fig. 5.20 (f), (g), (j), (k)) show low sensitivity to the changes, with respect to the co-polarized texture. The resulting

SSIM values and error measures for the pre and post disaster despeckeled and texture images are shown in Tables 5.12, 5.13 and 5.14 respectively. The drop in the SSIM values from 1.0 of the MAR based texture to 0.5 of the filtered images suggest the poor performance in discriminating changes using the adaptive filters. This further means that the SSIM encountered significant random noise even after the filtering while determining the structural similarity from the pre to post disaster pixels. Contextual smoothing resulting from MAR based texture is important to reduce this random noise especially for the SAR data

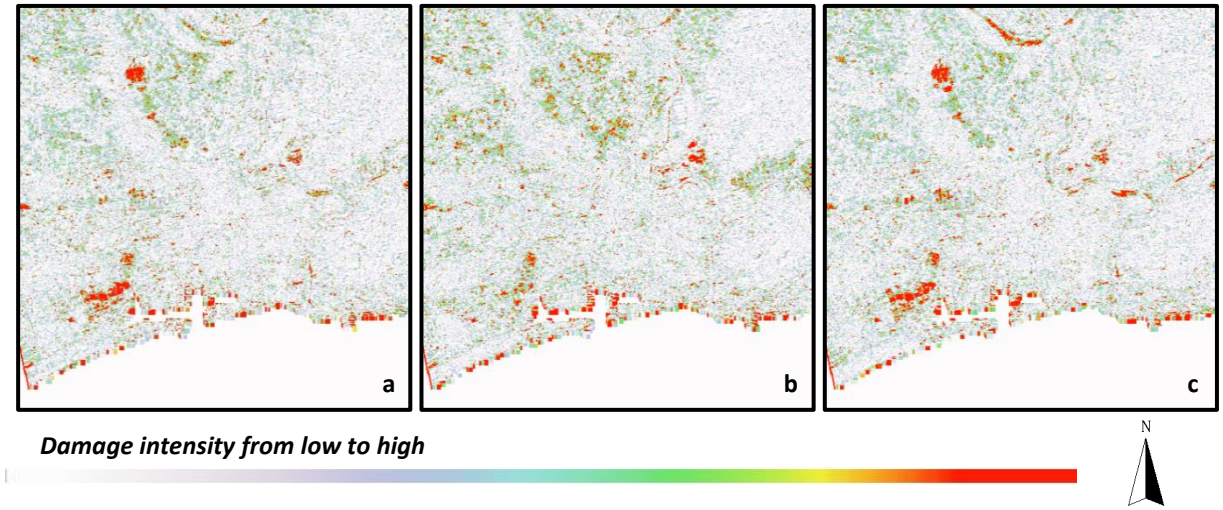

Figure 5.21 Change maps using MRD for log transformed filtered intensity images (a) (b) (c), HH, HV, VV polarization

Ground truth information for the samples was obtained by interpreting a post disaster advanced AVNIR-2 and Google earth pre and post disaster images. Visual interpretation of the results for each technique suggests that the MAR based texture parameters extracted the coastal area damages, flooded paddy lands and the damages along the river border with better contextual smoothening. According to the Fig. 5.22 all the three techniques resulted with a common disaster signature along the coastal impervious land cover, paddy lands, along the river and to the north part of the river due to tsunami flooding and earth quake. The MRD results using the filtered images as a whole shows changes close in line with the texture based results. But very clearly the change results can be seen as a mixture of change pixels and the pixels representing noise. This is clearly evident along the coast as well as along the river basins (Fig. 5.22 left bottom and right upper regions). Out of these techniques contextual based analysis conducted with MAR model parameters, have accounted for small scale variations of damages by separating them from noise, with smoother outputs. According to the error measures (Table 5.2 and 5.4), structural changes estimated using MAR texture measures based on the neighborhood weighting parameter vector and the noise variance have very high correlation in the range of 0.8 with least AEP and RMSE in the range of 0.004 and 0.06 for the co-polarized SAR images. Higher correlation between the textures (θ, σ_u^2) based change results can be seen for all the polarization components.

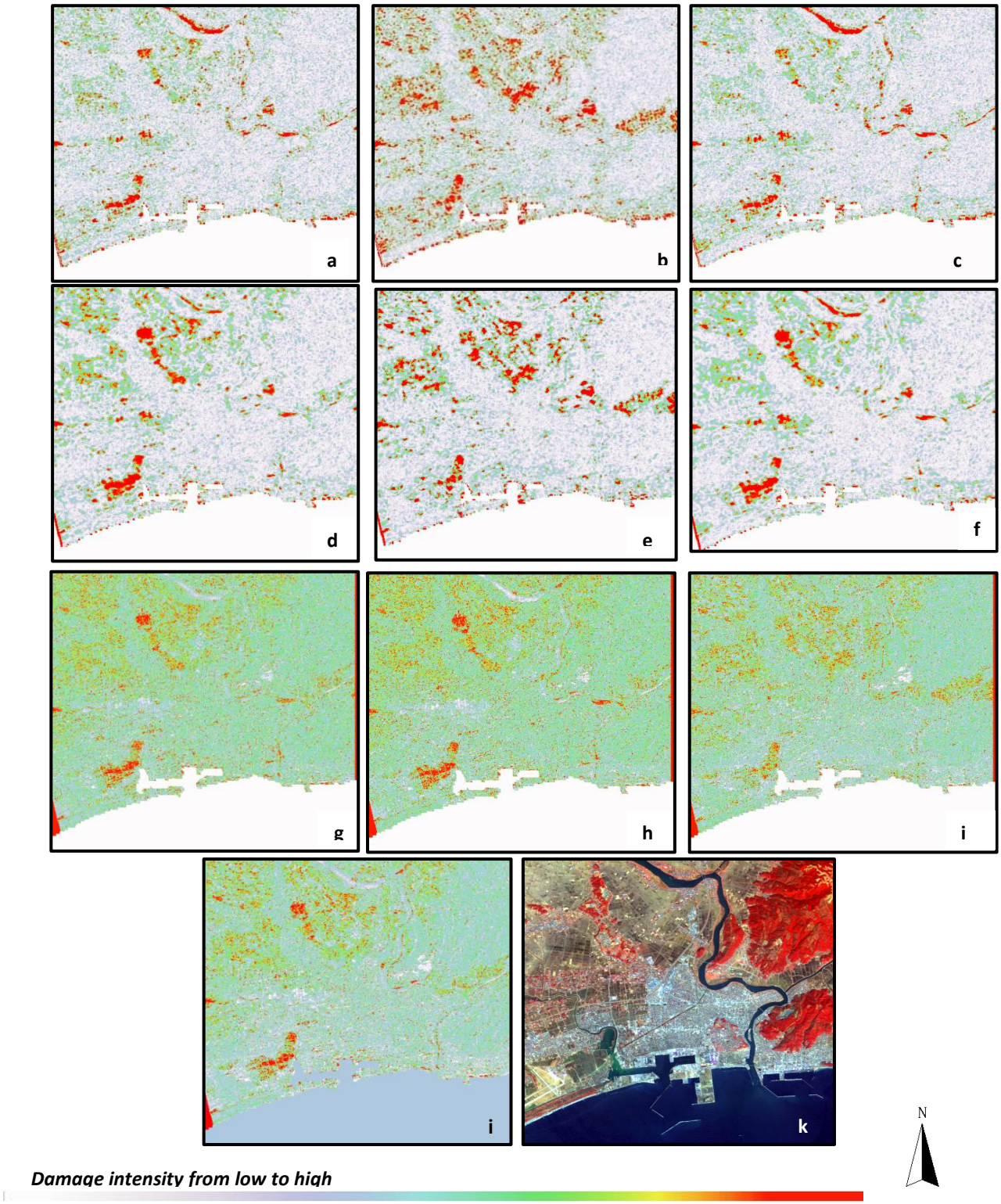

Figure 5.22 Change maps using MRD for MAR model based texture formed by using θ vector for HH, HV,,VV (a) (b) (c), MAR model texture formed by using σ_u^2 for HH, HV and VV polarization, (d), (e), (f), Mean ratio based change estimate using log estimates of SAR intensity for HH, HV and VV, using the second PCA component of the pre and post disaster log estimates of HH,HV,VH and VV components (i) and the post disaster AVNIR-2 image showing the major land cover components for the same study region (k), High level of damages are shown in red color

The comparison also suggests that the MAR texture based changes for the co-polarized components have considerably better agreement with PCA based approach than the normalized log ratio based approach with better average AEP of 0.003, RMSE 0.06 and CC of 0.74. The same results followed by the cross polarized components but with lower accuracy levels. The error measure between the MAR based texture and filtered MAR changes shows significantly high correlation in the range of 0.97 to 0.99 for both cross and co-polarized SAR images. But significant differences between them were suggested by the higher AEP and RMSE values in the range of 0.01 to 0.3 and 0.1 to 0.3 respectively. It is difficult to say from this which result is superior. Yet it provides that the changes resulting by using MAR based texture is different to the ordinary noise filtered images. Summary of the results shows that the MRD based MAR texture approach for temporal changes can be effective for smoother outputs and better fractional agreement with PCA based approaches.

Table 5 11 Threshold values to extract the damage and non-damage classes

Image	Polarization	Threshold Value
Noise variance ( )	HH	0.102
	HV	0.075
	VH	0.081
	VV	0.104
Weight (θ)	HH	0.302
	HV	0.246
	VH	0.247
	VV	0.287
Normalized Ratio	HH	1.100
	HV	1.067
	VH	1.069
	VV	1.103
PCA		2.202
Adaptive Lee filter	HH	0.064
	HV	0.070
	VH	0.071
	VV	0.068

Table 5 12 SSIM measures for the change images

Pre and post disaster images	Average SSIM
Adaptive Lee filtered intensity HH	0.5136
Adaptive Lee filtered intensity HV	0.5160
Adaptive Lee filtered intensity VH	0.5179
Adaptive Lee filtered intensity VV	0.5112
MAR based Weight HH	0.9854
MAR based Weight HV	0.9845
MAR based Weight VH	0.9849
MAR based Weight VV	0.9852
MAR based Variance HH	0.9998
MAR based Variance HV	1.0000
MAR based Variance VH	1.0000
MAR based Variance VV	0.9988

Table 5 13 Error measures between co-polarized components

Cross comparison combinations (co-polarized input) change images	AEP	RMSE	CC
MAR based Variance (HH) vs. Lee filtered (HH)	0.029	0.081	0.997
MAR based Variance (VV) vs. Lee filtered (VV)	0.026	0.080	0.997
MAR based Weight (HH) vs. Lee filtered (HH)	0.207	0.300	0.977
MAR based Weight (VV) vs. Lee filtered (VV)	0.210	0.305	0.976
MAR based Variance (HH) vs. MAR based Weight (HH)	0.004	0.059	0.865
MAR based Variance (VV) vs. MAR based Weight (VV)	0.005	0.068	0.824
MAR based Variance (HH) vs. PCA2	0.002	0.074	0.778
MAR based Variance (VV) vs. PCA2	0.001	0.076	0.780
MAR based Weight (HH) vs. PCA2	0.006	0.063	0.717
MAR based Weight (VV) vs. PCA2	0.005	0.062	0.710
MAR based Variance (HH) vs. Log Ratio (HH)	0.017	0.076	0.769
MAR based Variance (VV) vs. Log Ratio (HH)	0.015	0.080	0.758
MAR based Variance (HH) vs. Log Ratio (VV)	0.016	0.080	0.737
MAR based Variance (VV) vs. Log Ratio (VV)	0.014	0.077	0.765
MAR based Weight (HH) vs. Log Ratio (HH)	0.022	0.075	0.682
MAR based Weight (VV) vs. Log Ratio (HH)	0.021	0.077	0.645
MAR based Weight (HH) vs. Log Ratio (VV)	0.021	0.078	0.656
MAR based Weight (VV) vs. Log Ratio (VV)	0.019	0.076	0.654
Log Ratio (HH) vs. PCA2	0.014	0.046	0.881
Log Ratio (VV) vs. PCA2	0.013	0.045	0.885

Table 5 14 Error measures between cross-polarized components

Cross comparison combinations (cross-polarized input) change images	AEP	RMSE	CC
MAR based Variance (HV) vs. Lee filtered (HV)	0.018	0.064	0.997
MAR based Variance (VH) vs. Lee filtered (VH)	0.021	0.069	0.998
MAR based Weight (HV) vs. Lee filtered (HV)	0.032	0.106	0.994
MAR based Weight (VH) vs. Lee filtered (VH)	0.016	0.058	0.996
MAR based Variance (HV) vs. Mar Based Weight (HV)	0.009	0.062	0.865
MAR based Variance (VH) vs. MAR based Weight (VH)	0.018	0.071	0.800
MAR based Variance (HV) vs. PCA2	0.008	0.102	0.520
MAR based Variance (VH) vs. PCA2	0.001	0.090	0.485
MAR based Weight (HV) vs. PCA2	0.017	0.106	0.466
MAR based Weight (VH) vs. PCA2	0.016	0.107	0.434
MAR based Variance (HV) vs. Log Ratio (HV)	0.014	0.104	0.517
MAR based Variance (VH) vs. Log Ratio (VH)	0.022	0.092	0.497
MAR based Weight (HV) vs. Log Ratio (HV)	0.023	0.105	0.494
MAR based Weight (VH) vs. Log Ratio (VH)	0.023	0.107	0.416
Log Ratio (HV) vs. PCA2	0.006	0.058	0.654
Log Ratio (VH) vs. PCA2	0.021	0.064	0.681

5.2.1 KLD based change detection for the log normal SAR images

The Gaussian Kullaback-leibler based change detection was performed using the log transformed SAR intensity. The log transformation which transformed the data into Gaussian statistics provides the base to perform these experiments. The use of the first order statistics makes this experiment different from the experiment we have conducted using the MAR based changes. The main reason for us to conduct these experiments is to see how the first order statistical changes deviate from the second order statistics of the MAR texture. The change maps generated using the GKLD is shown for the fully polarimetric logarithmic SAR intensity in Fig. 5.23.

Since the SAR intensity is always positive showing a Gamma PDF, Gaussian models cannot be applied directly to the SAR data. Hence the above mentioned log transformation is an important prior procedure for the GKLD change detection. Visually it can be seen from the results the bright regions close to the value 1.0 indicates the areas with significant changes. The overall signature corresponds to the finding reported by the image ratio approach Fig. 5.22. But it is clearly visible that the contextual smoothing is lacking from the GKLD method. But the changes represented within a region using the local mean and the variance statistics can be highlighted and accounted using the GKLD method. Changes are more prominent in the co-polarized SAR log intensity than in the co-polarized SAR intensity.

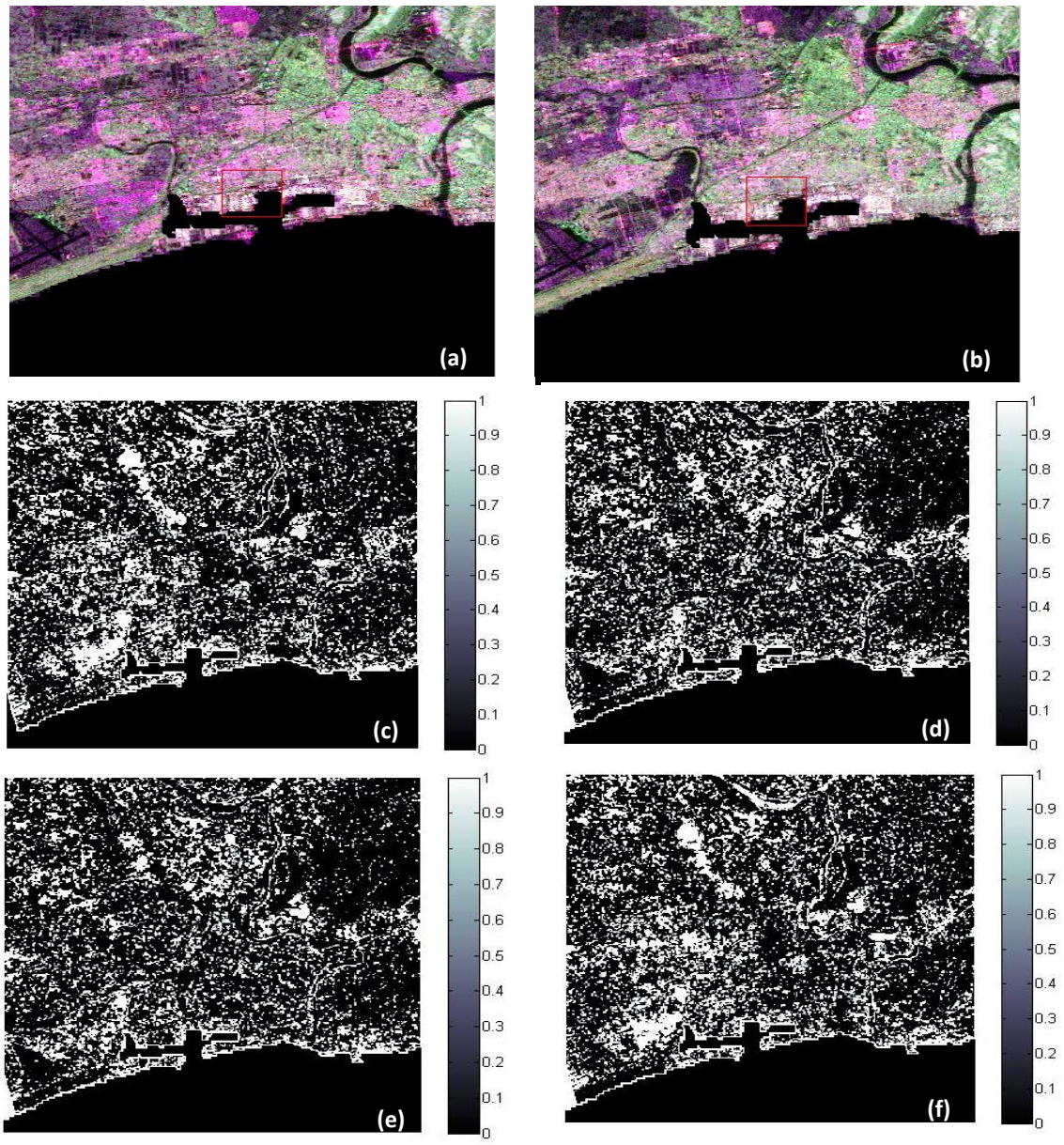

Figure 5.23 (a) Pre Disaster (2010.10.20) log transformed image (HH,HV,VV in RGB) (b) Post Disaster (2011.04.08) log transformed image (HH,HV,VV in RGB) GKLD based change maps with brighter regions showing areas with significant pixel distributional changes (c) log HH (d) log HV (e) log VH (f) log VV

MAR model parameters since their introduction; have been used successfully with Markov Random Filed base classification mechanisms for better contextual smooth classification outputs from multisource data. Yet their capabilities in time series data analysis especially to detect contextual changes in land cover have not been investigated fully. In this regard the main goal of this experiment is to investigate the performance of MAR texture measures of SAR data, to extract contextual changes resulting due to disasters. The use of MAR based texture for time series SAR data change analysis independent of polarimetric approaches is also important to note. A noteworthy finding of the experiments from this

section is the changes in the shape and height of the variograms from a spherical to exponential depending on the damages to the structure. Hence extensive use of variograms with MAR base texture at different transects over the study region can predict the areas exposed to major changes. The noise suppression setup of the MAR based texture provides the feasibility to use the SSIM for the study. The change areas always represent the dissimilarity between the pre and the post disaster scenes. The temporal changes extracted from the SSIM based analysis corresponds similar to the change detection results of the MRD. Finally MRD extracts the change pixels from the non-change one. The visual inspection shows the MAR texture parameters are more sensitive to the small scale variations of the change. Noise free results with better smoothing can be observed in the MAR texture, comparative to the PCA and normalized ratio based approaches.

5.3 MRF experiments with multisource data

This section is dedicated to explain the outcomes of the multi-source data fusion and classification mechanism proposed in this study using MRF and fuzzy theories. It highlights two experimental results. The first is the experiments conducted by using the optical and SAR imagery to model the prior and the likelihood energy terms respectively. Secondly the experiments extended to classify the optical, SAR and SAR texture images. A quick look at the area and the images used in most of these experiments are shown below in Fig. 5.24.

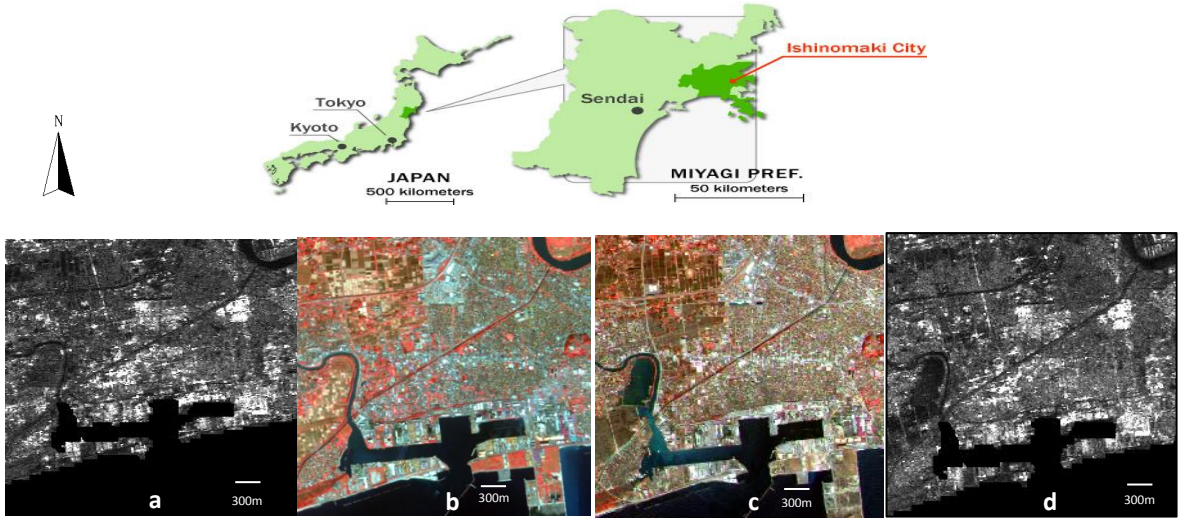

Figure 5. 24 Study area map and the images (a) average HH, VV intensity pre disaster (b) true color composite of the AVNIR-2 pre disaster image (c) true color composite of the AVNIR-2 post disaster image (d) average HH, VV intensity post disaster ALOS PALSAR image

5.3.1 Combined classification of the AVNIR-2 and SAR imagery using Fuzzy MRF

A novel model to classify multisource time series satellite images using adaptive fuzzy class mean vector and Markov Random Fields (MRF) is experimented in this section. The model uses the contextual information from the optical image pixels and the fuzzy grade of memberships for Synthetic Aperture Radar (SAR) intensity pixels to classify a heterogeneous urban land cover. Sub pixel class fractions estimated using linear unmixing from the optical image initialize the class arrangement for the MRF process (Appendix A). Pair-site interactions of the pixels were used to model the prior energy from the initial class arrangement. Fuzzy class mean vector from the SAR intensity pixels are calculated by

using Fuzzy C-means (FCM) partitioning. Conditional probability for each class was determined by a Gamma distribution. Minimization of the global energy by simulated annealing is executed using a logarithmic and power-law combined annealing schedule. The technique was tested using two time series Advanced Land Observation Satellite (ALOS)/phased array type L-band synthetic aperture radar (PALSAR) and Advanced Visible and Near-Infrared Radiometer-2 (AVNIR-2) data set over a disaster effected urban region. Proposed method and the conventional MRF results were evaluated with neural network (NN) and support vector machine (SVM) based classifications. The conventional and the fuzzy MRF results were also compared with structural similarity index measure (SSIM). From the Multilooking intensity of HH and VV polarizations an average magnitude response HH+VV/2 was generated. For meaningful estimation of HH+VV/2 response it is important that HH and VV polarizations are independent from each other. If they are highly correlated with each other than the averaging operation is not required as we can use either HH or VV magnitudes alone. According to Fig. 5.25 the correlation coefficient (r) for the pre and post disaster co-polarization is 0.17 and 0.18 respectively. This indicates the satirical independence between the co-polarization measures. Notably the classification scheme based on average polarimetric data is independent of the averaging function (Kong et al., 1990).

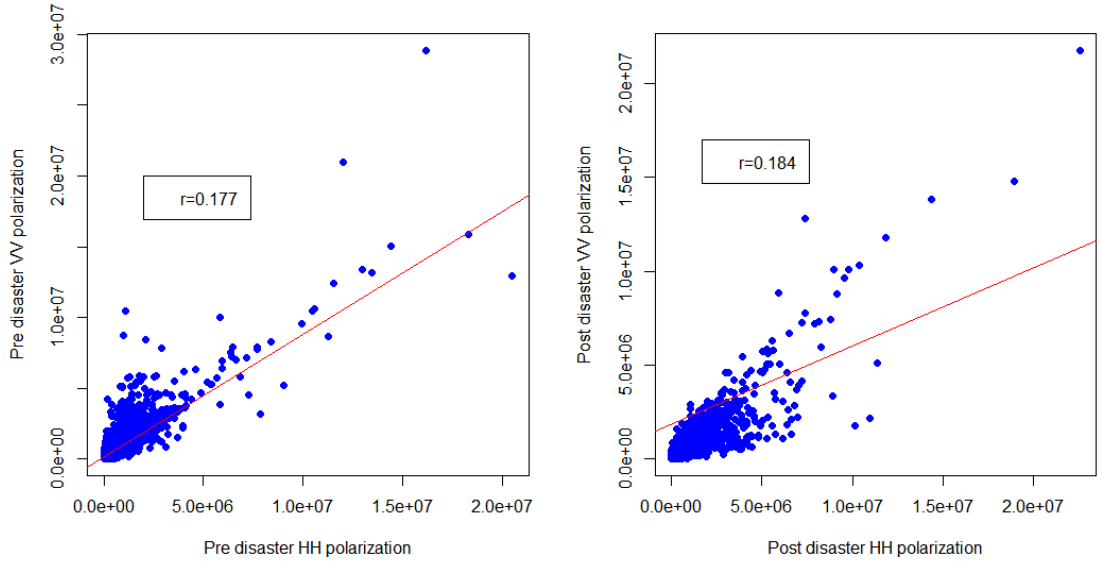

Figure 5.25 Correlation between the HH and VV polarization intensity values, significantly low correlation values suggest the statistical independence between HH and VV observations

Several key parameters have to be estimated to perform the multisource classification proposed in this study. They are the fuzzy membership grade parameter $f_\omega(y_i)$ for each intesity pixel, fuzzy class mean $\overline{\mu_\omega}$ and the source realiability factor λ. To detemine the membership grades we employed the fuzzy C-means clustering criteria. The membership values for each SAR intensity pixel after the FCM clustering are shown in Fig. 5.26. Training pixels for each land cover class were selected (Table 5.15). We first determine the FCM based membership values for each radar intensity pixel. With the use of pixel membership weights the number of pixels in a training sample necessary to model the class distribution can be reduced as mentioned earlier. The scattering mechanism recorded by fully polarimetric SAR data before and after the earthquake and tsunami changes depending on the damages to manmade structures and the disturbances to the land scape. The effect of the scattering mechanism in the SAR intensity is an important factor to consider in the case of urban area damages and inundated farmlands. As a result of the

disaster, post disaster SAR image has a significant decrease in the double bounce scattering due to the urban structural damages. This is in contrast to the increase in volume scattering power caused by the scattering from large amount of debris. This significant change in the scattering power can be seen with the rapid fluctuation of the membership grades in the post disaster SAR image compared to the pre disaster image (Fig. 5.26 (b)). Prominent double bounce scattering from stable urban buildings can be seen in the urban areas with the pre disaster fuzzy memberships (Fig. 5.26 (a)). Four main land cover clases were identified for the classification, namely water, industrial and residential (Impervious surface) and the farmlands. An additional class in the post disaster situation as exposed soil and grass were identified specifically due to the tsunami effect to the area. Hence we classify the pre disaster SAR image for four classes while the post disaster image was classified for five. The NN and SVM based refrence images were generated by using HH and VV polarizations alone. We compare the MRF and FMRF results with an NN and SVM based classification results.

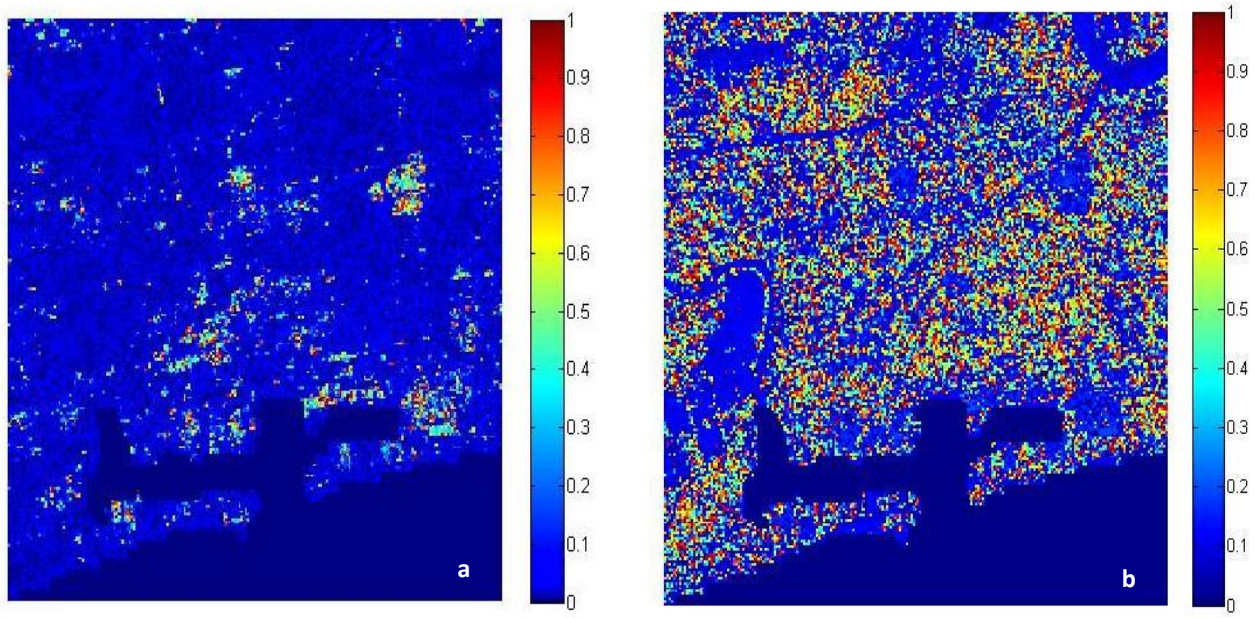

Figure 5.26 Fuzzy C-means clustering results with membership values for SAR intensity image pixels (a) Pre disaster (b) post disaster

Table 5 15 Number of pixels in the selected training samples

Land cover class	Pre disaster/no of training pixels	Post disaster/no of training pixels
Water	1137	1025
Industrial	1735	797
Residential	1398	1307
Farmlands	1216	935
Exposed soil and Grass		416

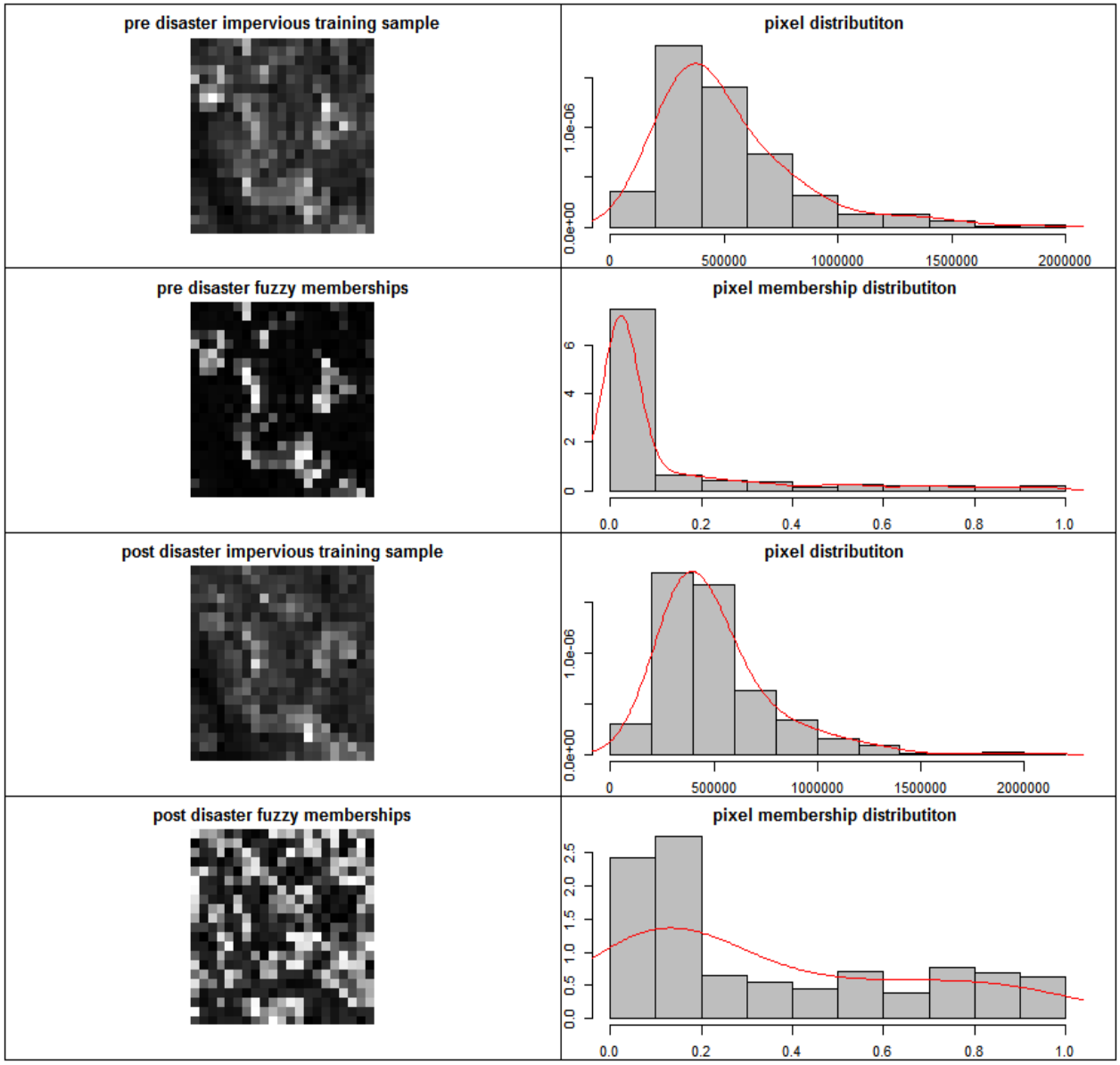

Figure 5.27 SAR intensity pixel distribution for impervious surface training sample and its associated membership distribution for the pre and post disaster situations following a Gamma distribution

Fig. 5.27 shows the intensity pixel and the corresponding membership grades distribution for an impervious surface training sample. Obviously both the distributions follow a Gamma distribution, making all the pixels to have a membership grade. The shift in the mean pixel values before and after the disaster can be observed from the distributions. Further the rise in the fluctuation of the fuzzy membership grades, especially for the post disaster condition as mentioned earlier is also clear. With the inclusion of fuzzy memberships the separability between the class means can be improved providing a better discrimination for the classes. To understand the performance of MRF classification with the fuzzy membership graded intensity pixels of the SAR data, MRF and FMRF classifications were performed

separately for the pre and post disaster images. The conventional and the fuzzy class mean values calculated are different to each other as shown in Table 5.16.

Table 5 16 Conventional and fuzzy mean values calculated for each land cover training class in the pre and the post disaster SAR intensity images

Pre Disaster land cover classes	Conventional class Mean	Fuzzy class Mean	Post Disaster land cover classes	Conventional class Mean	Fuzzy class Mean
Farmlands	190812.47	182385.10	Farmlands (inundated)	130283.64	138558.50
Water	12208.80	35371.89	Water	10834.03	64296.26
High albedo	918304.26	1272770.00	High albedo	1165112.77	1079266.00
Low albedo	345930.48	769929.50	Low albedo	348684.43	348346.40
			Exposed soil and Grass	251685.85	311111.20

Singular Value Decomposition (SVD) based pixel unmixing was carried out on AVNIR-2 images (Boardman, 1989; Canty, 2010; Krus et al., 1993). Then the pixels were labelled to a class depending on the highest class fraction estimated by SVD. Generated initial class images are shown in the Fig. 5.28. Using the posterior energy minimization in MRF and FMRF models we perform the classification using these initial class images.

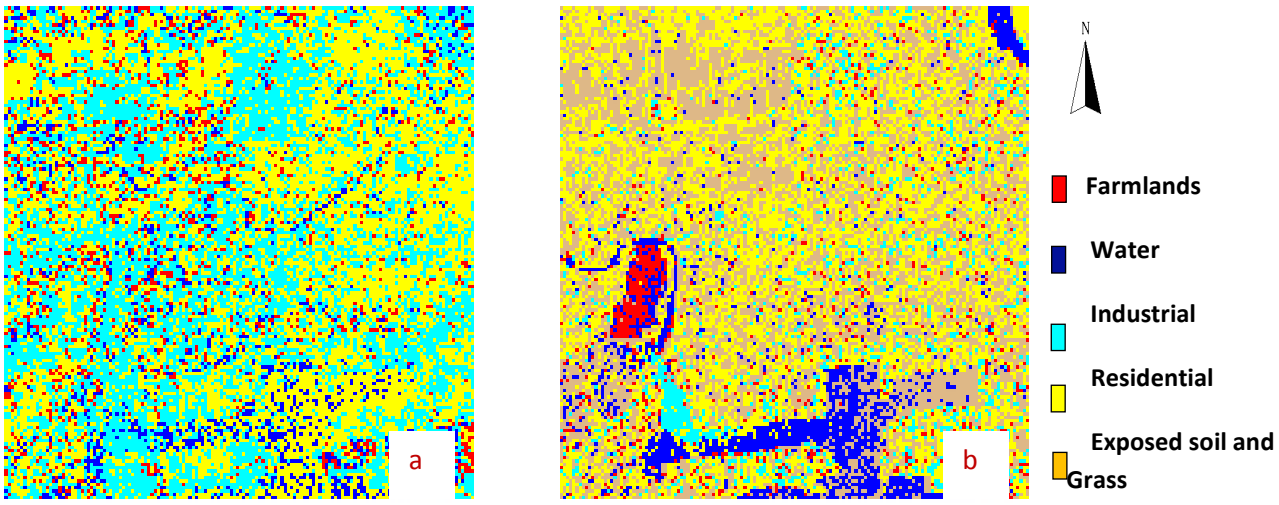

Figure 5.28 Initial class arrangement based on the maximum class fraction estimation using SVD for an AVNIR-2 image pixel (a) pre disaster (b) post disaster

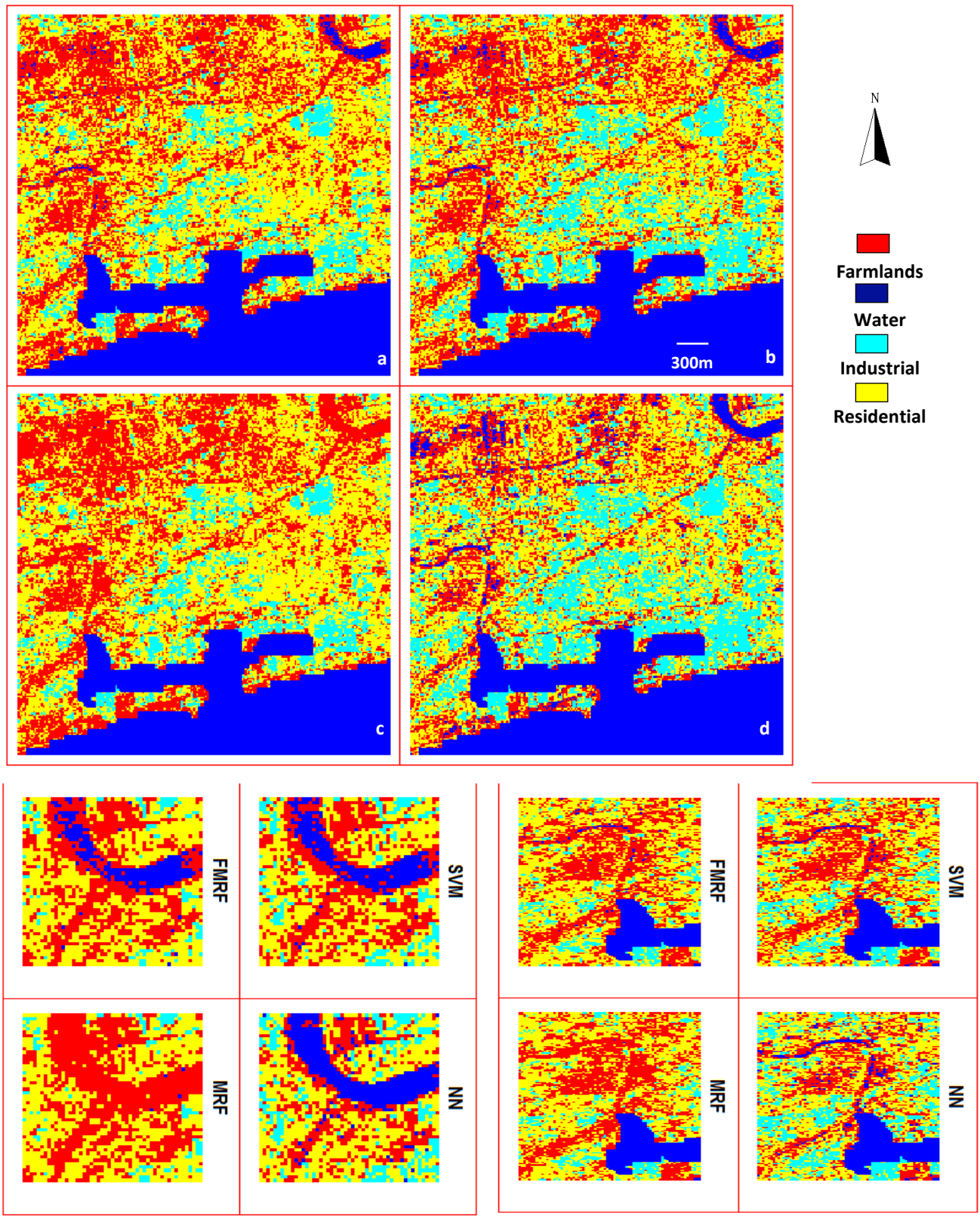

Figure 5.29 Optimal classification results using MRF and FMRF approaches for a reliability factor ($\lambda = 0.4$), (a) pre disaster FMRF (b) pre disaster SVM classification (c) pre disaster MRF (d) pre disaster NN classification

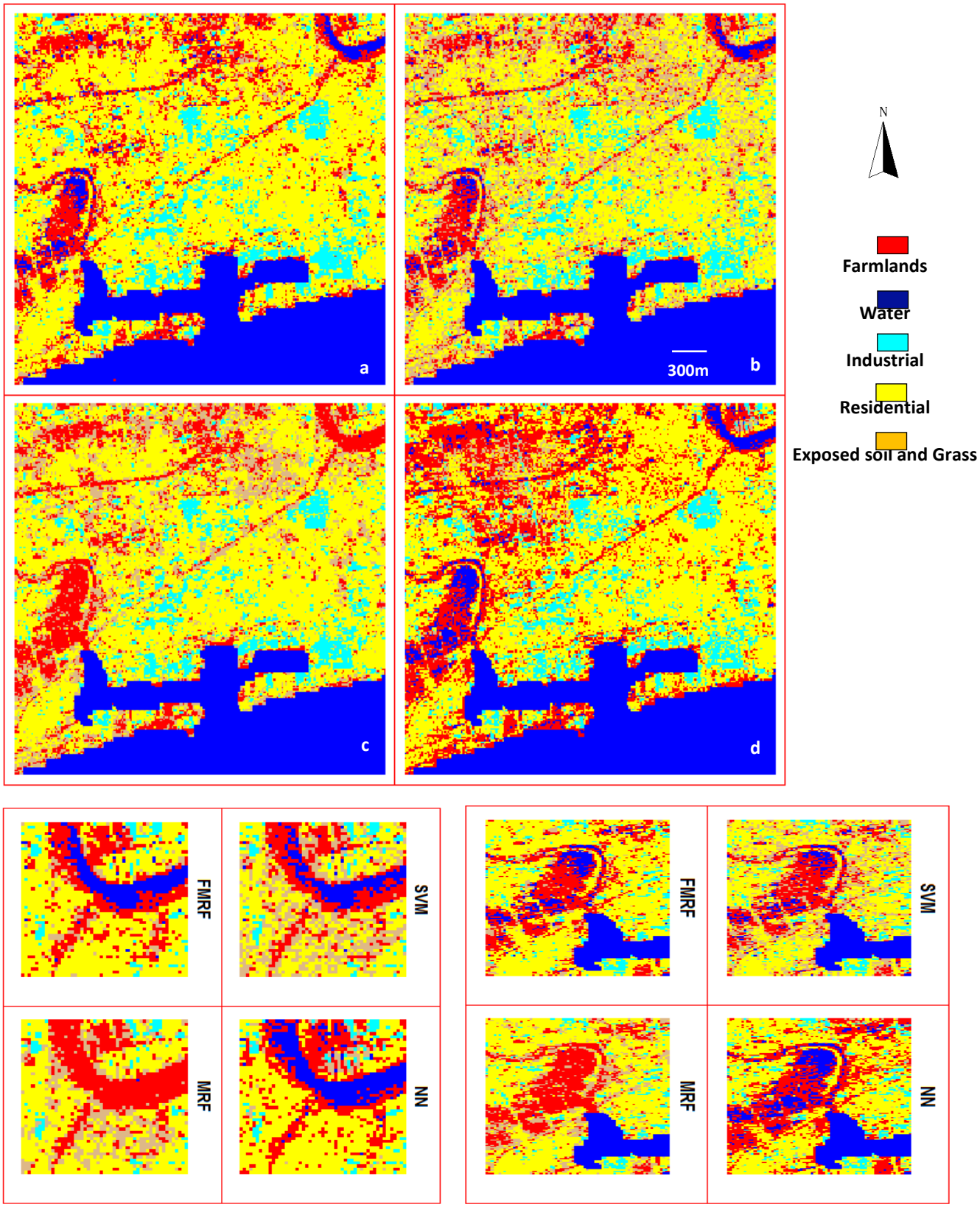

Figure 5.30 Optimal classification results using MRF and FMRF approaches for a reliability factor ($\lambda = 0.4$), (a) post disaster FMRF classification (b) post disaster SVM classification (c) post disaster MRF (d) post disaster NN

It is important to mention that the λ is a key parameter which controls the contribution of the prior and the likelihood energy in the posterior energy determination. For example when λ=1 the likelihood term is completely ignored in Eq. 3.38 for a minimal posterior energy, forcing all the pixels to be classified to a single class. After the initial setup we ran the experiment for a range of λ values. The optimum results were generated with the λ in the range from 0.2 to 0.5. Within this range the reliability of the SAR data in the classification mechanism is much higher than the optical image. As a matter of fact with the main motivation of classifying the SAR images it is important for us to give a higher reliability to the SAR image. The optimum MRF and FMRF results and the reference images are shown in Fig. 5.29 and 5.30.

Posterior energy (Eq. 3.38) was minimized using SA with Metropolis-Hasting sampler (Geman and Geman, 1984; Tso and Mather, 2009). We have implemented a new cooling schedule within the SA in this study. Initially the parameter T_0 and $_K$ was set to values 3.0 and 0.9 respectively. We tested the energy minimization with ordinary lognormal annealing scheme. It was identified that once the T reaches a value between 1.0 and 0.7 the drop in the energy becomes significantly slow. Hence we implemented the power-law annealing schedule after T=1.0 and 0.7. From this experiments, due to the considerable reduction of number of iterations and the slight difference in local energy we stick to T=1.0. The two schedules and the test runs are shown in Fig. 5.31.

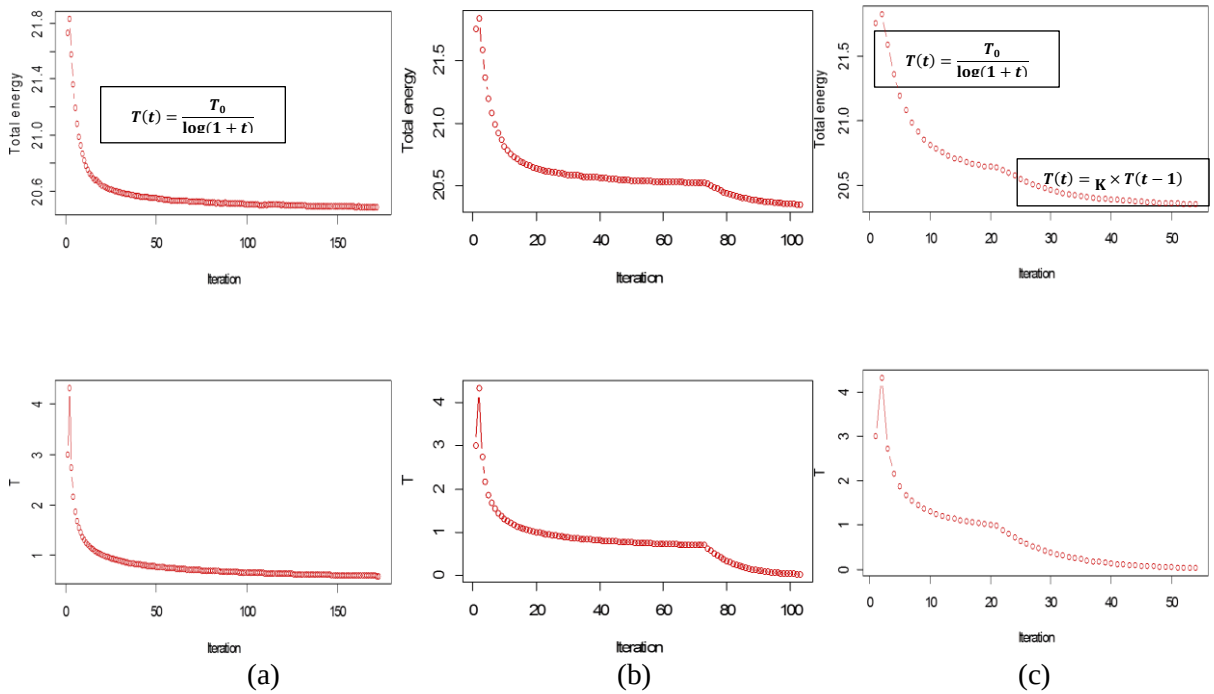

Figure 5.31 Behavior of the energy with respect to the temperature drop for the post disaster SAR images, SA with (a) lognormal annealing schedule (b) lognormal and power-law combined annealing schedule changing at T=0.7 (c) lognormal and power-law combined annealing schedule changing at T=1.0

Visual interpretation of the classified images interestingly suggests the improved ability of FMRF to classify the local water sources and the inundated farmland better than the MRF. SVM and NN based classification outputs shows salt and pepper effect with noise-like pixel labels for land cover classes

whereas both MRF being contextual approaches shows less noisy effect. Clarity in the edge information (ex. Internal water ways, live fences) resulting from MRF approaches is higher than the SVM and NN. Table 5.17 and Table 5.18 show the overall comparison results of the FMRF with NN and SVM respectively. The comparison with the NN based reference image clearly suggested the improvements in the FMRF over MRF. At λ=0.3 and 0.4 the optimal classifications were reached for the pre and post disaster images respectively. In the pre disaster case the FMRF OA improved from 77% to 80% with resulting kappa values of 0.69 and 0.72 respectively. For the post disaster, OA increased from 73% to 81% with 0.63 to 0.72 increases in kappa. The SVM based comparison also follows the same pattern but with marginal improvements for the FMRF. At λ=0.2 the pre disaster FMRF results shows 86% OA and 0.80 kappa while a OA of 84% and kappa 0.78 for the MRF. In the post disaster case the results shows better accuracy for the MRF at λ=0.2, with OA and kappa being 87% and 0.83 over FMRF OA and kappa of 83% and 0.77 respectively. To get a better understanding of the classification performance at individual classes we examine the producer accuracy for each class (Table 5.19 and 5.20). Producer accuracy for each class clearly indicates the classification accuracy enhancement using grade of membership. With the NN based comparison in the pre disaster images all the four classes improved the classification accuracy in the FMRF with average producer accuracy reaching 79% from 76%. In the post disaster producer accuracies, only the soil class shows a significantly less accuracy of 49% in FMRF with the 77% of MRF. It is difficult to say from the NN and SVM based classification methods which is the most suitable reference to assess the accuracy of the proposed FMRF model. Hence we report both methods in the analysis. The use of new SA scheme provided significantly rapid optimization by cutting down the number of iteration from 155 to 56 (Fig. 5.31).

Table 5 17 Overall accuracy and the kappa statistics resulted from the comparison of the MRF results with the NN based reference images

Overall Accuracy (OA) and Kappa statistics comparison with NN based reference				
Reliability factor λ	OA%	Kappa	OA%	Kappa
	Pre disaster MRF		Pre disaster FMRF	
0.2	77.23	0.686	80.00	0.721
0.3	77.60	0.690	80.10	0.724
0.4	77.24	0.683	79.52	0.714
	Post disaster MRF		Post disaster FMRF	
0.2	70.13	0.596	76.28	0.676
0.3	71.40	0.609	79.76	0.713
0.4	73.63	0.631	81.32	0.728
0.5	74.89	0.639	80.32	0.710

Table 5 18 Overall accuracy and the kappa statistics resulted from the comparison of the MRF results with the SVM based reference images

Overall Accuracy (OA) and Kappa statistics comparison with SVM based reference				
Reliability factor λ	OA%	Kappa	OA%	Kappa
	Pre disaster MRF		Pre disaster FMRF	
0.2	84.42	0.782	86.17	0.806
0.3	84.03	0.776	85.75	0.800
0.4	83.54	0.768	84.90	0.787
	Post disaster MRF		Post disaster FMRF	
0.2	87.72	0.834	83.28	0.776
0.3	87.27	0.827	82.22	0.756
0.4	84.52	0.787	79.79	0.718

Table 5 19 Producer's accuracy (%) for the four pre and post disaster land cover classes, compared with NN reference images

Pre Disaster	Farmlands	Water	Industrial	Residential	Average
FMRF	93.40	90.00	83.00	49.00	78.85
MRF	93.18	85.31	79.00	49.41	76.72
Post disaster	**Farmlands**	**Water**	**Industrial**	**Residential**	**Average**
FMRF	87.85	97.58	87.57	64.05	84.26
MRF	90.00	93.00	83.90	63.00	82.47

Table 5 20 Producer's accuracy (%) for the five pre and post disaster land cover classes, compared with SVM reference images

Pre Disaster	Farmlands	Water	Industrial	Residential	Soil	Average
FMRF	55.67	94.00	92.00	93.31	94.53	85.90
MRF	43.00	85.00	87.24	84.61	96.00	79.17
Post Disaster	**Farmlands**	**Water**	**Industrial**	**Residential**	**Soil**	**Average**
FMRF	93.26	99.96	99.72	84.08	49.14	85.23
MRF	88.94	91.78	97.05	88.37	76.90	88.60

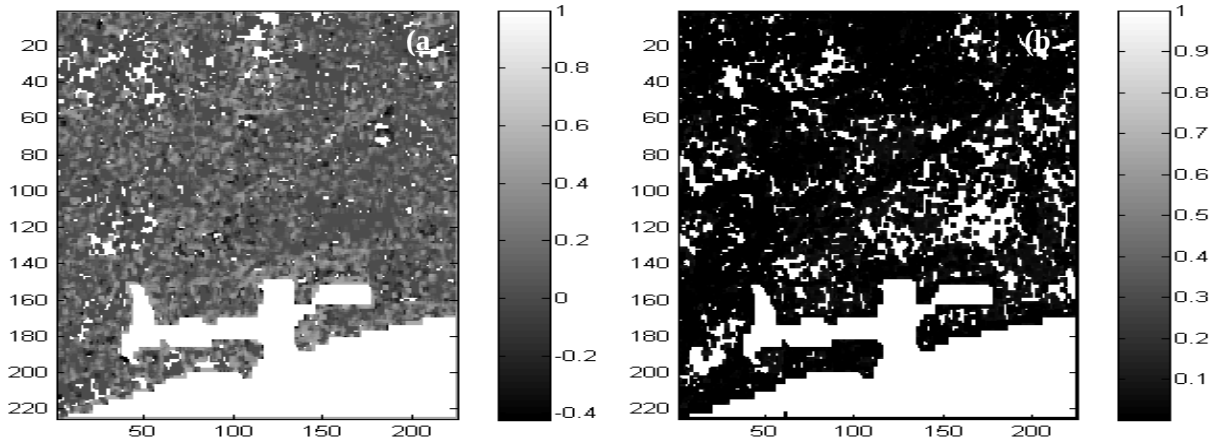

Figure 5.32 SSIM index maps showing the regions affected by the fuzzy membership graded MRF from the conventional MRF (a) pre disaster (b) post disaster

Table 5 21 Average SSIM measure between the conventional and fuzzy MRF classified images for the pre and post disaster cases

	Pre disaster MRF and FMRF	**Post disaster MRF and FMRF**
Average SSIM	0.312	0.305

The generated SSIM maps and the average SSIM values for the pre and post MRF and the FMRF images are shown in Fig. 5.32 and Table 5.21 respectively. The bright areas (white color) in the SSIM shows perfect corrlation while the dark areas show the changes. The average SSIM in the range of 0.3 suggest the MRF and FMRF have significant structural difference. This further means that the classification perfomrance of the FMRF is significantly different from the MRF at each class level. In this section we tested the MRF based classification mechanism to model the prior and the likelihood energy using multispectral and SAR imagery respectively. In the experiments, it is important to note that information regarding the spectral properties of the optical data was not modeled within the MRF. The main idea behind this is to classify the SAR information using the initial labeling performed by the optical data and to see the effect by comparison to the ordinary classification approaches using the SAR data alone. The advantageous of this setup is shown in detail and the findings were extended to a more complete model that deals with both the spatial and the spectral information of the optical, SAR and SAR texture information in the next section.

5.3.2 Extension of Fuzzy MRF for AVNIR-2, SAR and MAR based SAR texture classification

The theoretical developments of the MRF model for multisource data classification proposed and explained in the chapter 3 is tested and applied to the real satellite data. This section produces those results and discusses the issues related to the findings. The main idea behind the testing is to integrate the optical SAR and SAR texture for urban area classification and to identify the main potential outcomes of the approach. The results presented in this section are the first outcomes of the model in the ongoing experimental stage. There are several parameters that have to be defined quite accurately in the case of

the optimum results. Several research works have been done on these parameter estimations but an optimal solution for the determination of them is not clear. The main idea in this thesis is not to test about this parameter but to bring about the compound model to fuse and classify the multisource data in a single environment. We make the experiments for pre and post disaster images separately.

5.3.2.1 Pre disaster test

The proposed multisource data classification was first test on the pre disaster data sets of the test region two (see chapter 4 for details). This data set includes the pre disaster AVNIR-2 data set acquired on 5th November 2007 as the multispectral input and the ALOS PALSAR full polarimetric image acquired on 21st November 2010 as the SAR image. From the fully polarimetric SAR image we have used the average response of the HH and VV polarization (HH+VV/2) as the SAR intensity for the classification. The MAR based weighting parameter was used for the testing as the autoregressive random field based texture.

The initial class arrangement was conducted by using the SVD based class fraction estimation for each pixel from the AVNIR-2 image. Prior to this the AVNIR-2 image was resampled to 25m pixel resolution and co-registered with the SAR intensity images. Speckle filterers were not applied on the SAR images prior to the classification. One of the main reasons for this is that we wanted to leave the noise as source of uncertainty within the multisource classification. After estimating the class fractions within a single multispectral image pixel we have used the highest class fraction to assign and label an initial class label for that pixel. Hence this allocation is different from the random class allocation we have used in the SRM experiments explained in the earlier sections. This is largely due to the change in the functionality of the scale factor in the case of the multisource data classification. If we explain this in detail the classification and fusion of the experiments we have discussed hear happened at the SAR pixel resolution level (i.e 25m). Hence the scale factor or the subdivision of an optical pixel does not occur in this case, meaning that we are not generating the SRM. But this model can be used to work on generating SRM or classification at higher resolution by allowing the scale factor to have integers greater than 1 (isotropic MRF). But in that case we have to determine a way to calculate class conditional probabilities at lesser resolution for the SAR images. This yields a more complex mechanism and need a further modification of the proposed model in several different directions. This also offers several more directions to carry out further research. Interestingly in this model for the initial class labeling the SAR intensity image or the SAR texture is not required. This is convenient enough as MRF is a contextual classification mechanism and hence the multispectral image can assign class labels more appropriate to the context than the SAR images. But it should be mentioned that the time difference between these images should not be considerably large. The optimization of these initial class labels on the contrary is controlled by both the optical, SAR and SAR texture information. The initial class fractions determined by SVD and the allocation of the initial class image is shown in Fig. 5.33.

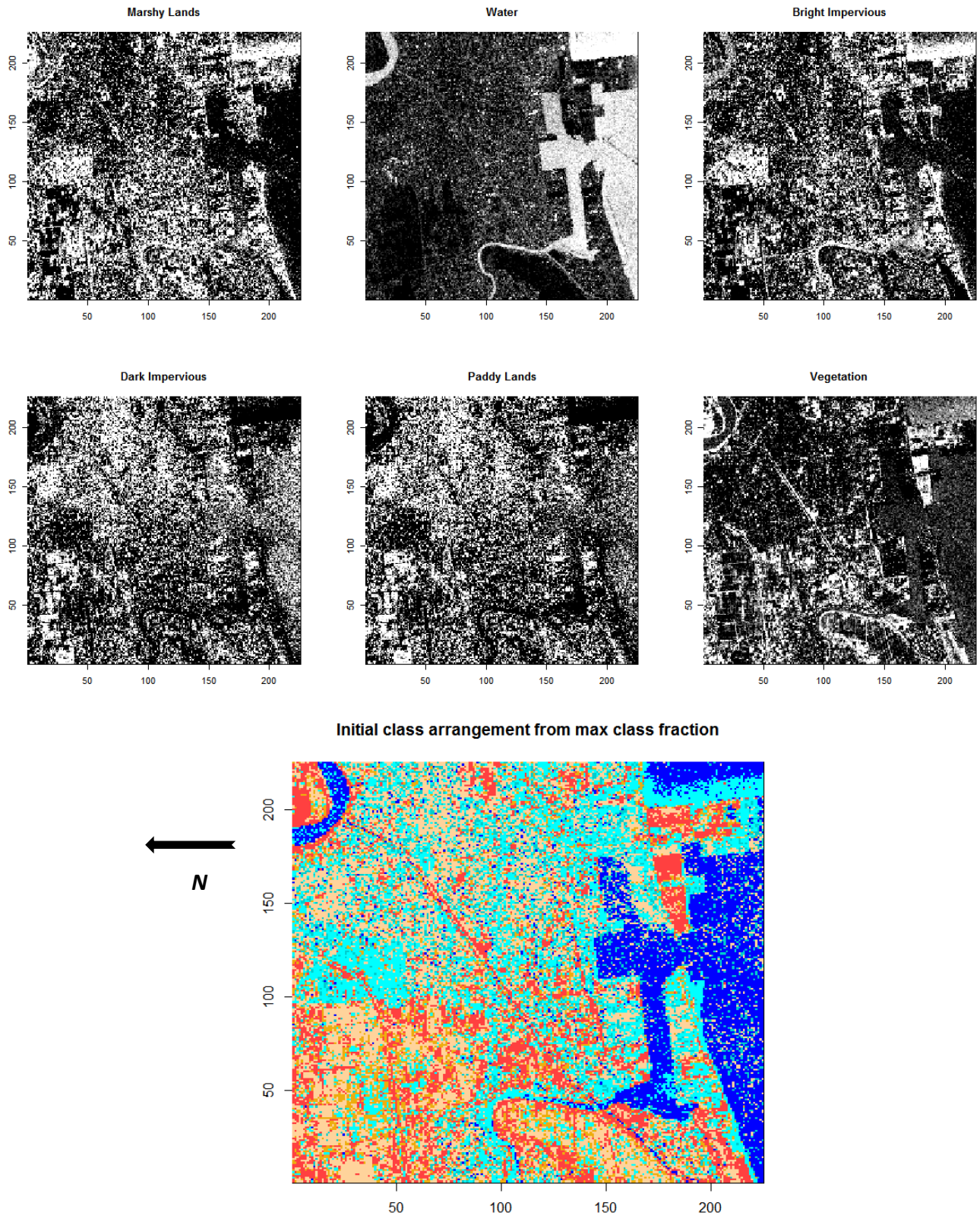

Figure 5.33 Initial class fractions determined using the pre disaster AVNIR-2 image and the initial class image generated by using the maximum class fraction

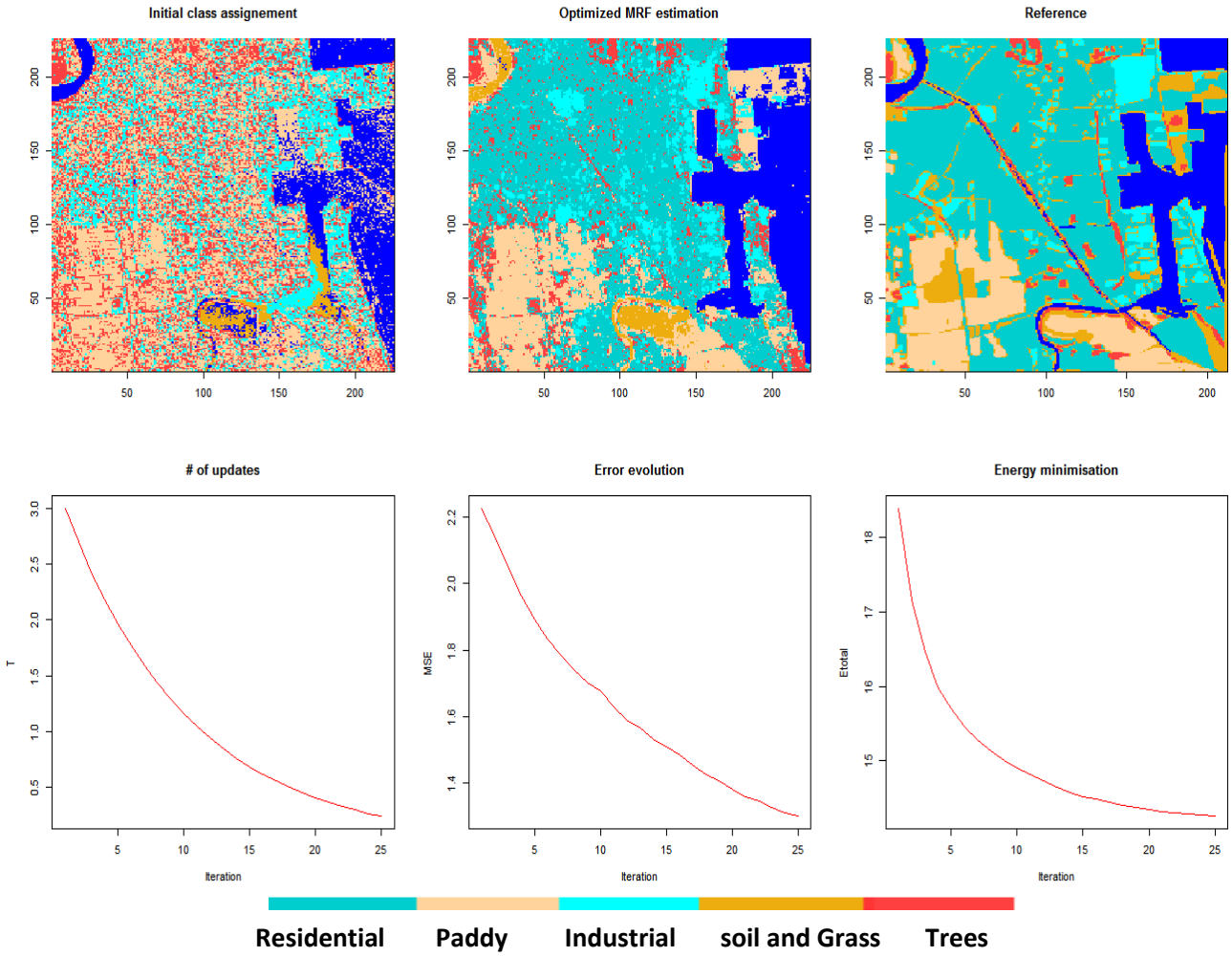

Figure 5.34 Multisource MRF classification mechanism at a reliable factor of $\boldsymbol{\lambda = 0.5}$ and the simulate annealing based optimization, using the conventional class mean vector to model the class PDF using Gamma distribution for the SAR intensity

The initial class image (Fig.5.33) generated using the maximum class fraction will be used with multisource conventional MRF to produce the optimal classified images. The optimization at a reliable factor of $\lambda = 0.5$ is shown in Fig. 5.34.

Table 5 22 Pre disaster mean vector to model the SAR intensity using Gamma distribution

Land cover Class	Marshy	Water	Bright impervious	Low albedo	Paddy	Vegetation
Conventional μ	203930.023	9218.364	1154428.199	319599.436	266916.936	309744.660
Fuzzy μ	341335.800	55182.760	952899.700	542515.500	545185.000	3434659.700

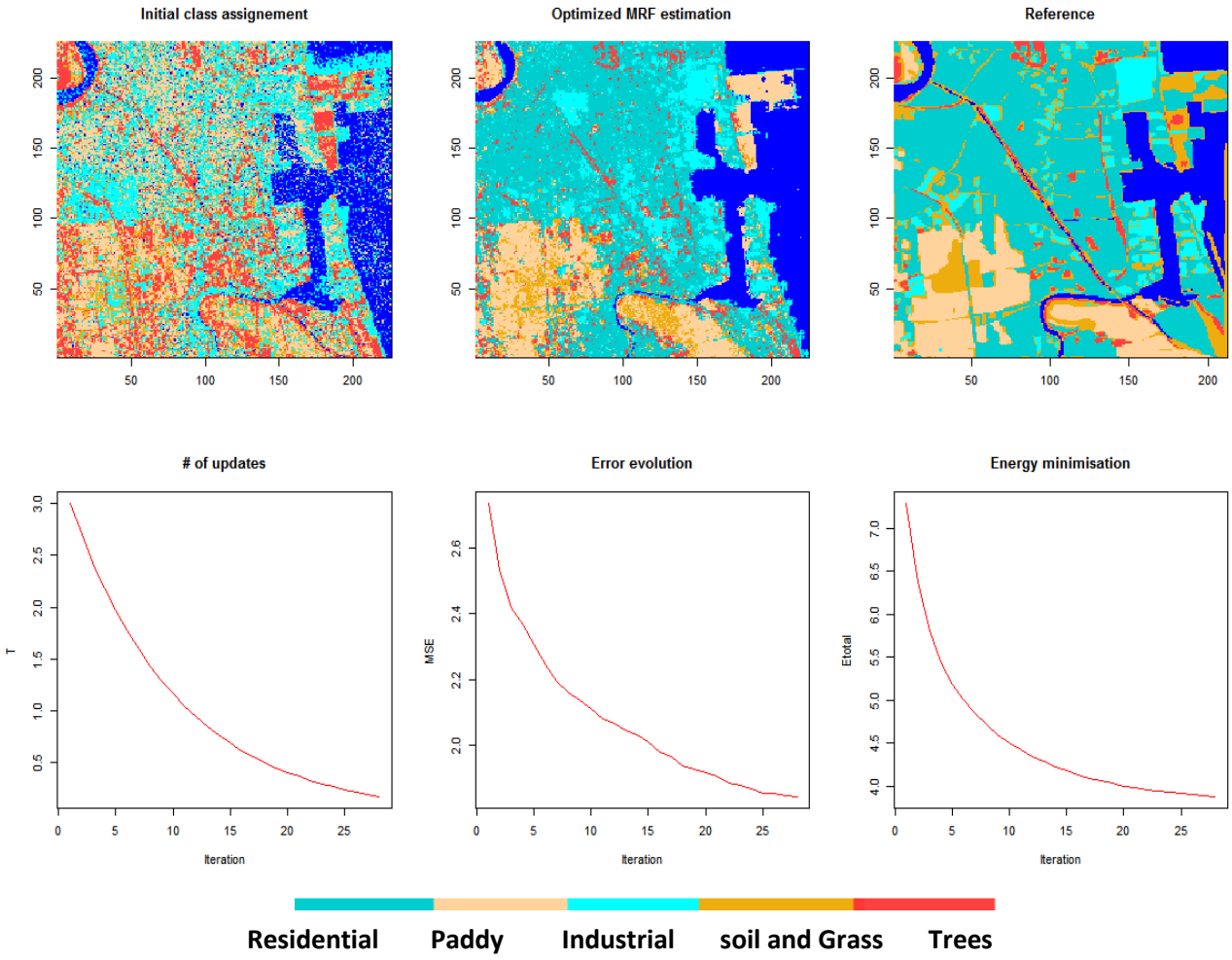

Figure 5.35 Multicourse MRF classification mechanism at a reliable factor of $\boldsymbol{\lambda = 0.5}$ and the simulate annealing based optimization, using the fuzzy class mean vector to model the class PDF using Gamma distribution for the SAR intensity

Multisource fuzzy MRF to produce the optimally classified images are shown in Fig. 5.35. The calculated fuzzy mean vector for the SAR intensity (Table 5.22) is different from the conventional case. The divergences between the class means with the inclusion of fuzzy membership grades are increased. With the use of fuzzy class parameters in the SAR Gamma PDF determination, the energy values at each iteration is different from the energy values determined in the conventional mechanism. The energy values at T=3.0 for the conventional MRF lies in the range of 18.0 while for the fuzzy MRF it decreases to the range 7.0. With the temperature drop the energy values drops within the SA to provide the maximum probability for a pixel to be classified to a class. The energy graphs in Fig. 5.34 and Fig. 5.35 shows that lower energy states are reached by the use of the fuzzy membership grades. This fuzzy pixel weighting in the PDF determination is quite useful to attain lower energy states in the optimization. The experiments were extended to see the differences between the single source MRF and the multisource MRF results.

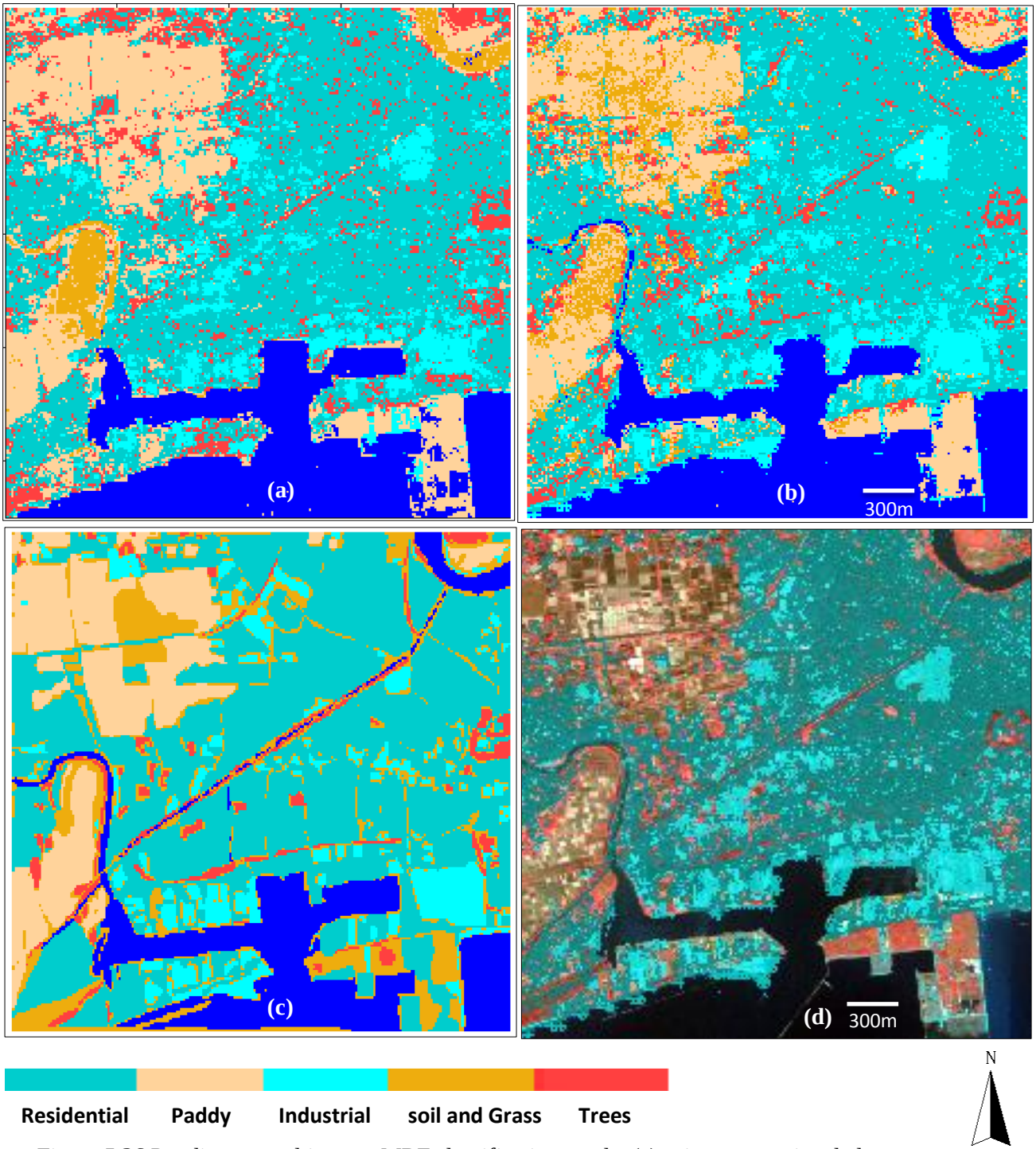

Figure 5.36 Pre disaster multisource MRF classification results (a) using conventional class parameters for the SAR intensity (b) using fuzzy class parameters for the SAR intensity (c) reference images generated by using aerial image mosaic (d) classification overlay for the urban classes over the pre disaster Avinir-2 image

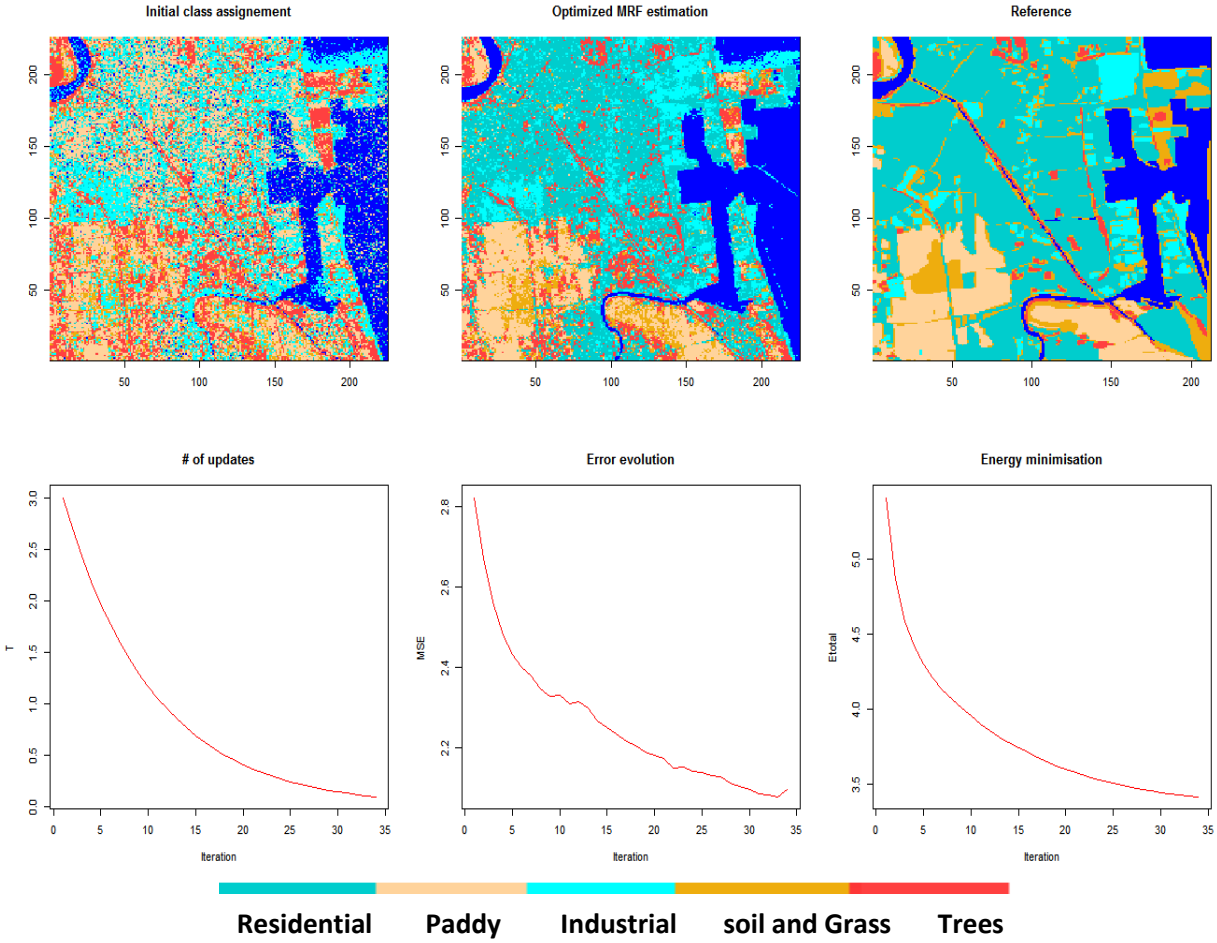

Figure 5.37 MRF classification using AVNIR-2 optical image at a reliable factor of $\boldsymbol{\lambda = 0.5}$ and the simulate annealing based optimization, using the fuzzy class mean vector

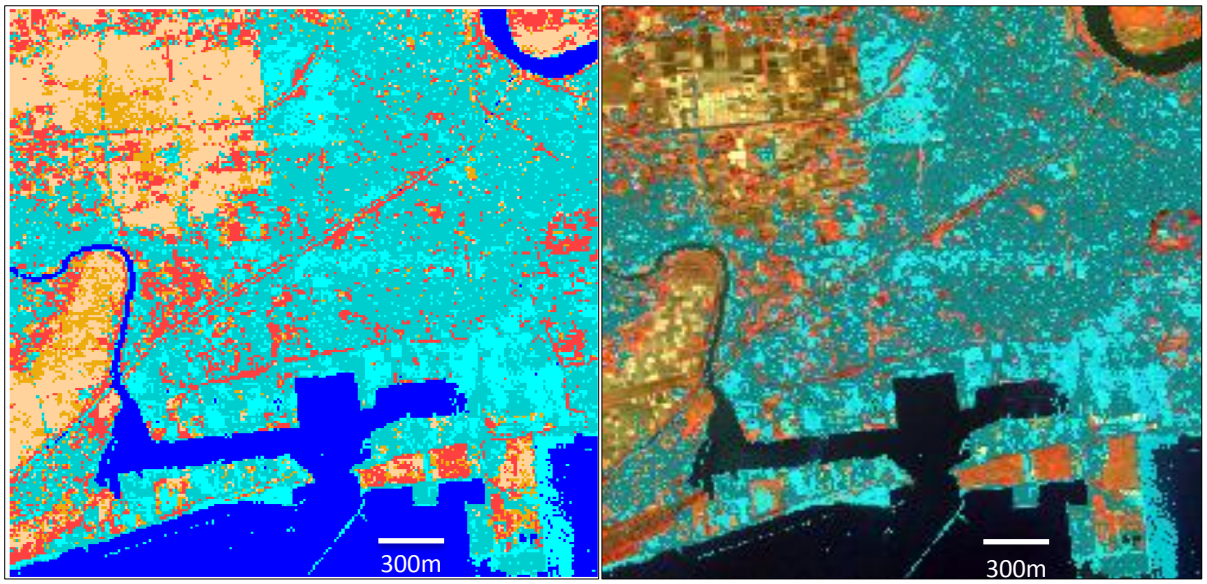

Figure 5.38 (a) optimal classification of AVNIR-2 image using MRF (b) classified impervious region overlay

The results and the experiments in Fig. 5.37 and Fig. 5.38 shows the application of the MRF model in single source multispectral imagery (pre disaster AVNIR-2 image). The visual inspection of the results Fig. 5.38 (a) shows an optimum classification for the six classes at $\lambda = 0.5$. Prominent noise levels in the harbor area are significantly visible in the classification results. The sensitivity to the local noise levels due to the contextual behavior is very high in the case of the MRF based classification. According to the results, in the multisource classification the contribution of the noise in the classification can be reduced to a significant level.

Table 5 23 Pre disaster classification accuracy assessment

Reference data type	Pre Disaster	Single source MRF model	Multisource conventional MRF model	Multisource fuzzy MRF model
Digitized aerial reference image	**OA%**	54.046%	55.853%	56.012%
	Kappa	0.401	0.414	0.420
SVM based reference image	**OA%**	55.10%	55.91%	57.30%
	Kappa	0.412	0.425	0.440

Table 5.23 shows the accuracy results between the MRF results using single source and multisource imageries with the reference image generated using the aerial photographs for the pre disaster case. This step is a difficult task in this work and which needs a further improvements. This is mainly because the difficulties of generating an accurate reference data set and the time consuming effort of a tedious digitization with the aerial photographs. Digitization based reference data generation for heterogeneous urban regions always have their own limitations. The possibility to use different classifications to assess the accuracy is also considered under this study. Hence the cross validation with the reference image generated using SVM based classification was also reported. But the significant noise levels in such reference images add lot of uncertainty in the quantitative accuracy assessments. As seen in Table 5.23, the performance of the multisource MRF model with respect to the performance with the single source seems quite close to each other. This is controversial to the visual inspection of the classification details. Comparison with the digitized reference image shows a slight increase in the accuracy using MRF models with multisource data with 56% OA with 0.42 kappa with respect to the 54% OA and 0.40 kappa of the single source classification. The second comparison with the SVM based classification shows that FMRF have 57% OA with 0.44 kappa with respect to the 55% and 0.41 of the single source classification results. This result suggests us that the multisource method has slight advantage over the single source method. More than this quantitate evaluation the visual inspection suggests more strong justification to this observation. The main problem in this evaluation is that the comparison of the MRF results is with the reference data deteriorated by noise. Hence it is important to produce more detailed reference data sets or other means of validation for such purpose. Hence we present some further evaluation using SSIM matrices in the end of this chapter. But in this thesis we will conclude with these results as our main objective was the development of the combined classification mechanism.

5.3.2.2 Post disaster test

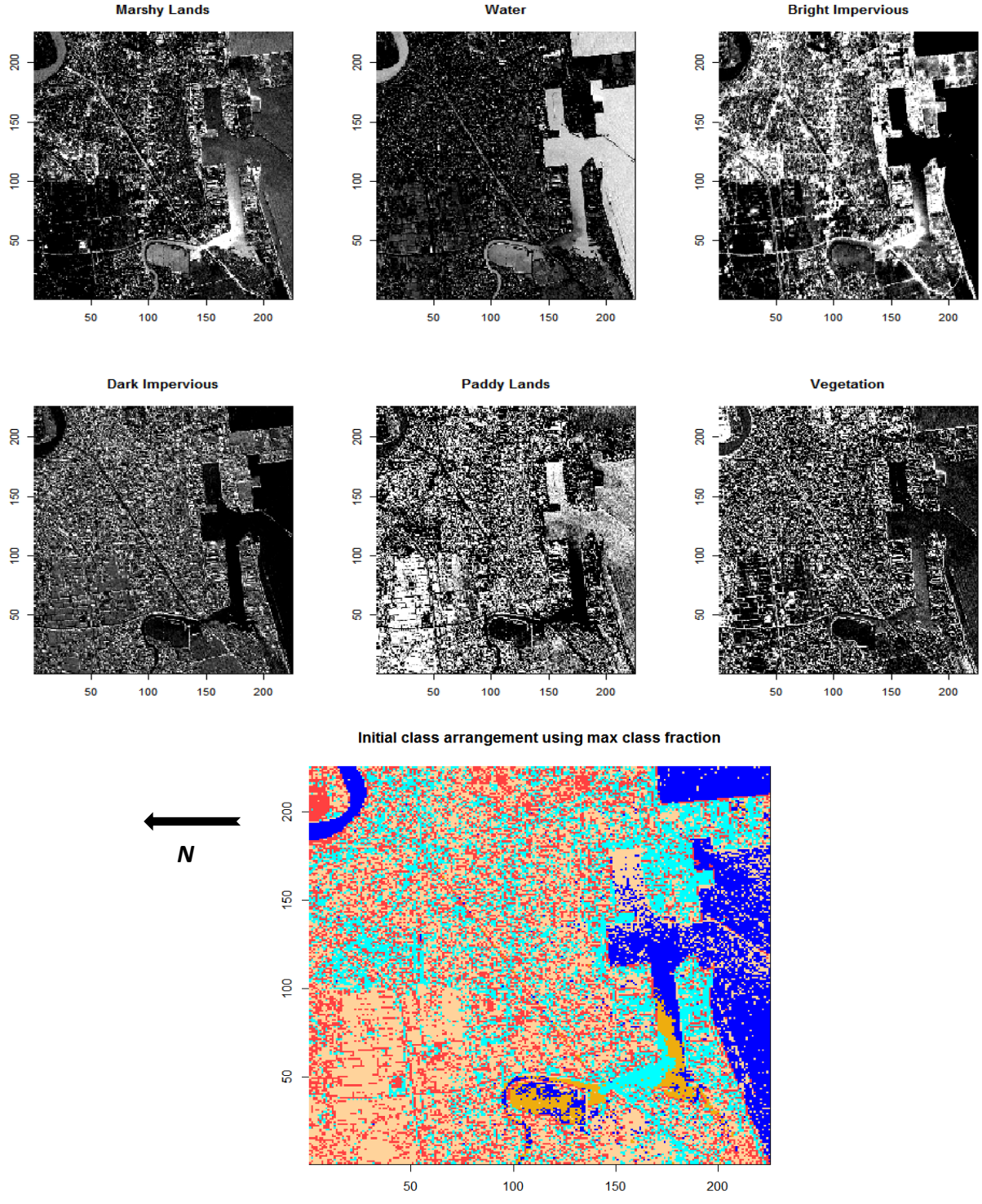

Figure 5.39 Initial class fractions determined using the pre disaster AVNIR-2 image and the initial class image generated by using the maximum class fraction

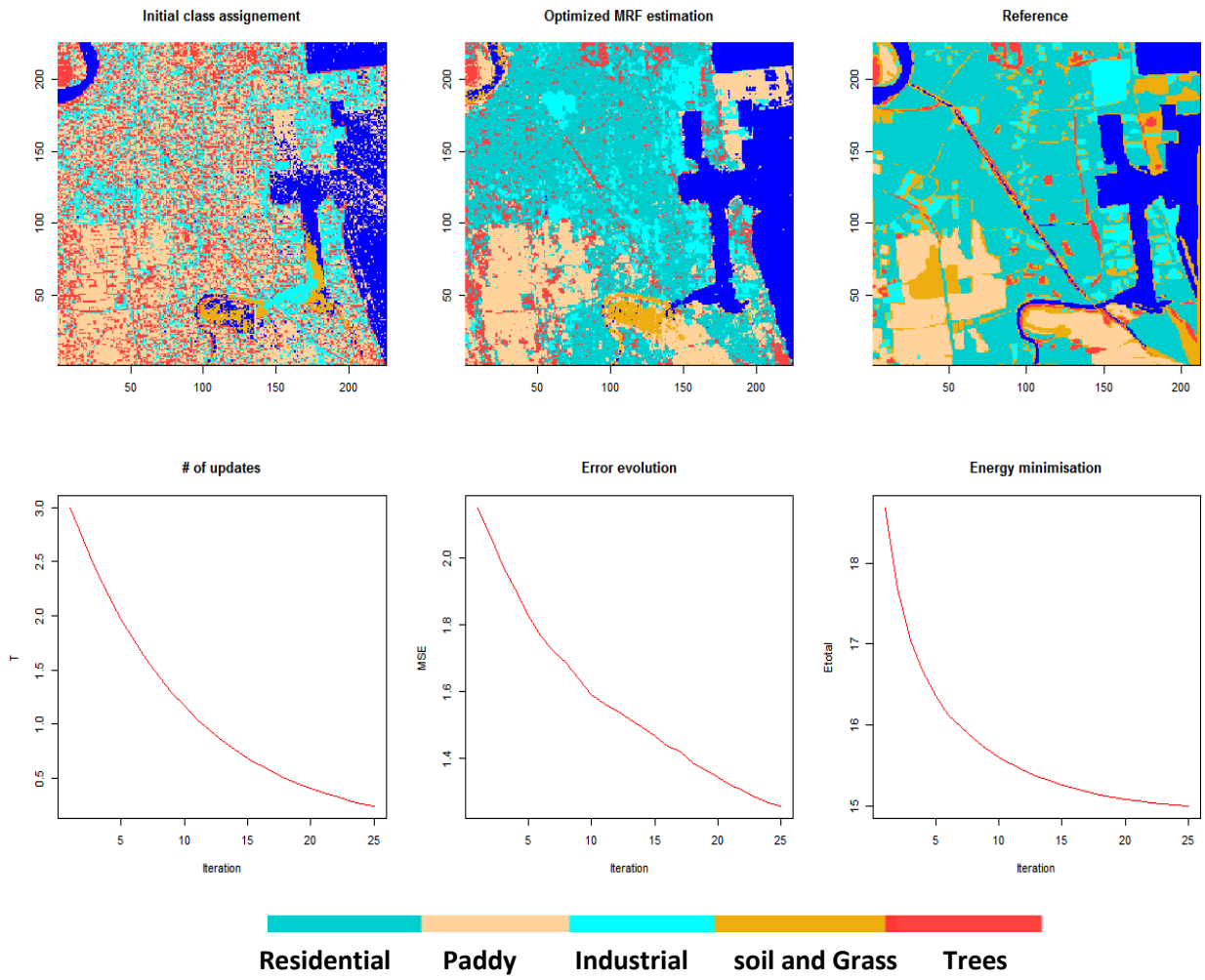

Figure 5.40 Multicourse MRF classification mechanism at a reliable factor of $\boldsymbol{\lambda = 0.5}$ and the simulate annealing based optimization, using the conventional class mean vector to model the class PDF using Gamma distribution for the SAR intensity

Table 5 24 Post disaster mean vector to model the SAR intensity using Gamma distribution

Land cover Class	Inundated paddy	Water	Bright impervious	Low albedo	Paddy	Vegetation
Conventional μ	124848.521	10999.420	1319056.703	374139.339	242463.004	367089.020
Fuzzy μ	135803.000	71089.960	1269167.000	337822.800	275259.400	337897.800

The experiments conducted by using the pre disaster multispectral, SAR and SAR texture was extended to the post disaster case. Fig. 5.39 shows the initial class fractional estimation, using SVD and the initial labeling of the MRF. Fig. 5.40 shows the optimization of the posterior energy for the conventional MRF model using the SA, and corresponding energy and the temperature drops. The class means vectors for the conventional and the fuzzy MRF models determined for the SAR intensity is shown in Table 5.24. The SA based optimization for the fuzzy MRF model using the multisource data is shown in Fig. 5.41. Due to

different class parameters the conventional and the fuzzy MRF processes works at different probability estimations for class labels. Hence the resulting energy at each iteration is different. Slight difference in the initial energy, close to 19 for conventional case and 18 for the fuzzy case can be observed. Similarly the minimal energy for the conventional MRF is close to 14 while in the FMRF it is 15. This observation is different from the pre disaster experiment where the estimated energy had large deviation. This can be mainly due to the time difference in the images. In the pre disaster optical and SAR image the time lag was nearly 3 years, while it was 2 days for the post disaster. This brings confusion between the initial class allocation from optical data and the class represented by the SAR image, providing large differences in the energy. This is an interesting observation, which is important to be investigated further.

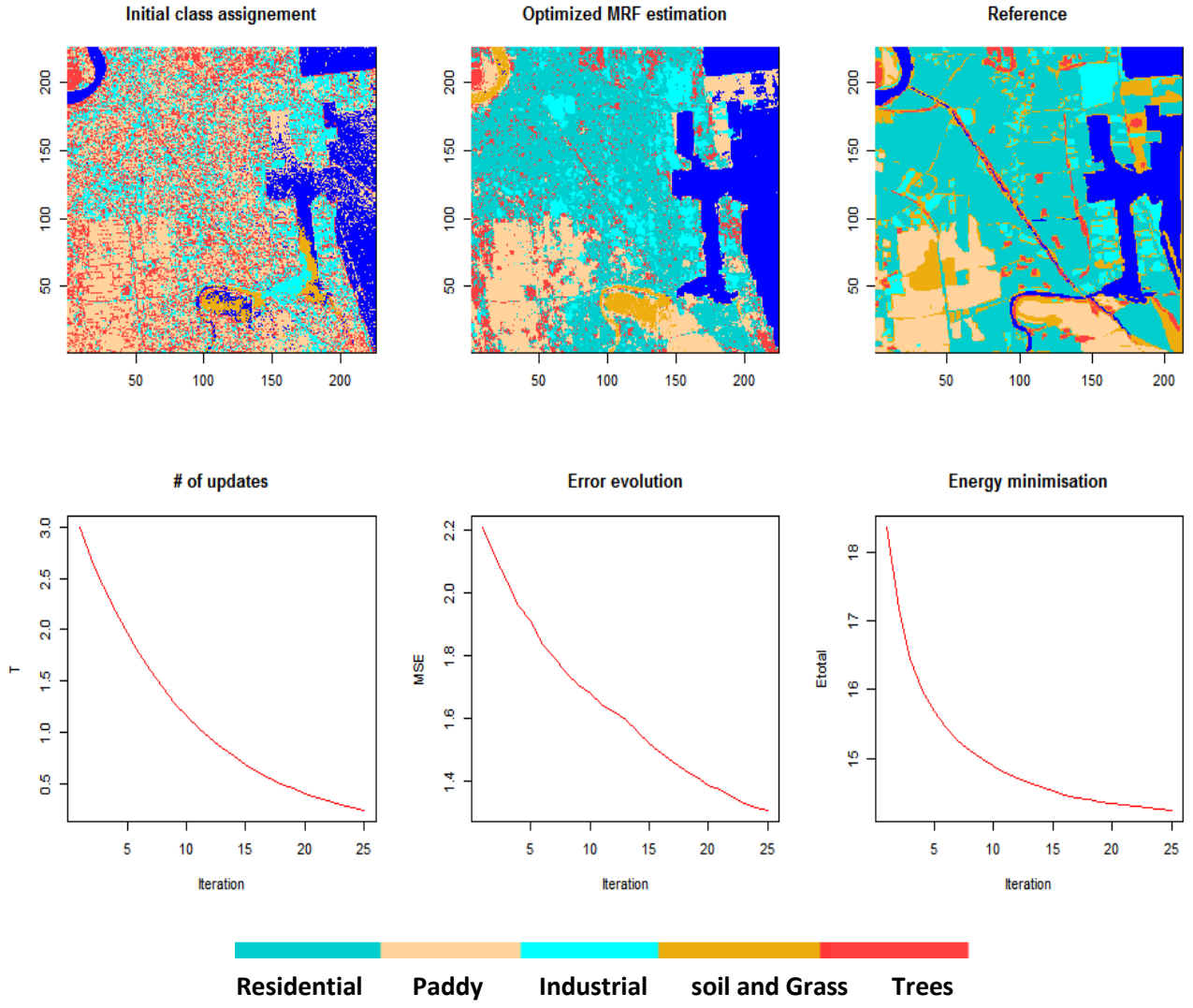

Figure 5.41 Multicourse MRF classification mechanism at a reliable factor of $\boldsymbol{\lambda = 0.5}$ and the simulate annealing based optimization, using the fuzzy class mean vector to model the class PDF using Gamma distribution for the SAR intensity

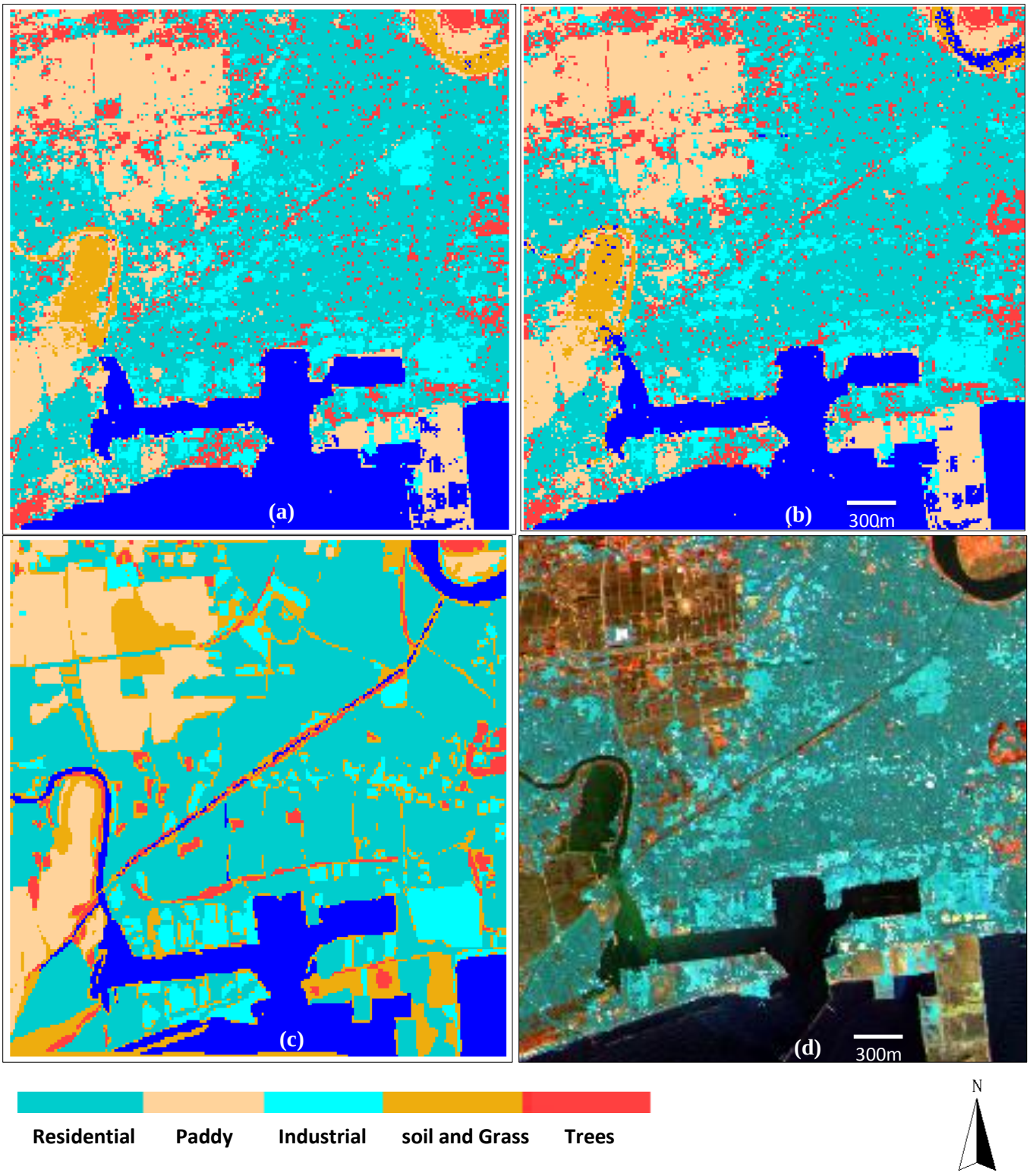

Figure 5.42 Post disaster multisource MRF classification results (a) using conventional class parameters for the SAR intensity (b) using fuzzy class parameters for the SAR intensity (c) reference images generated by using aerial image mosaic (d) classification overlay for the urban classes over the pre disaster Avinir-2 image

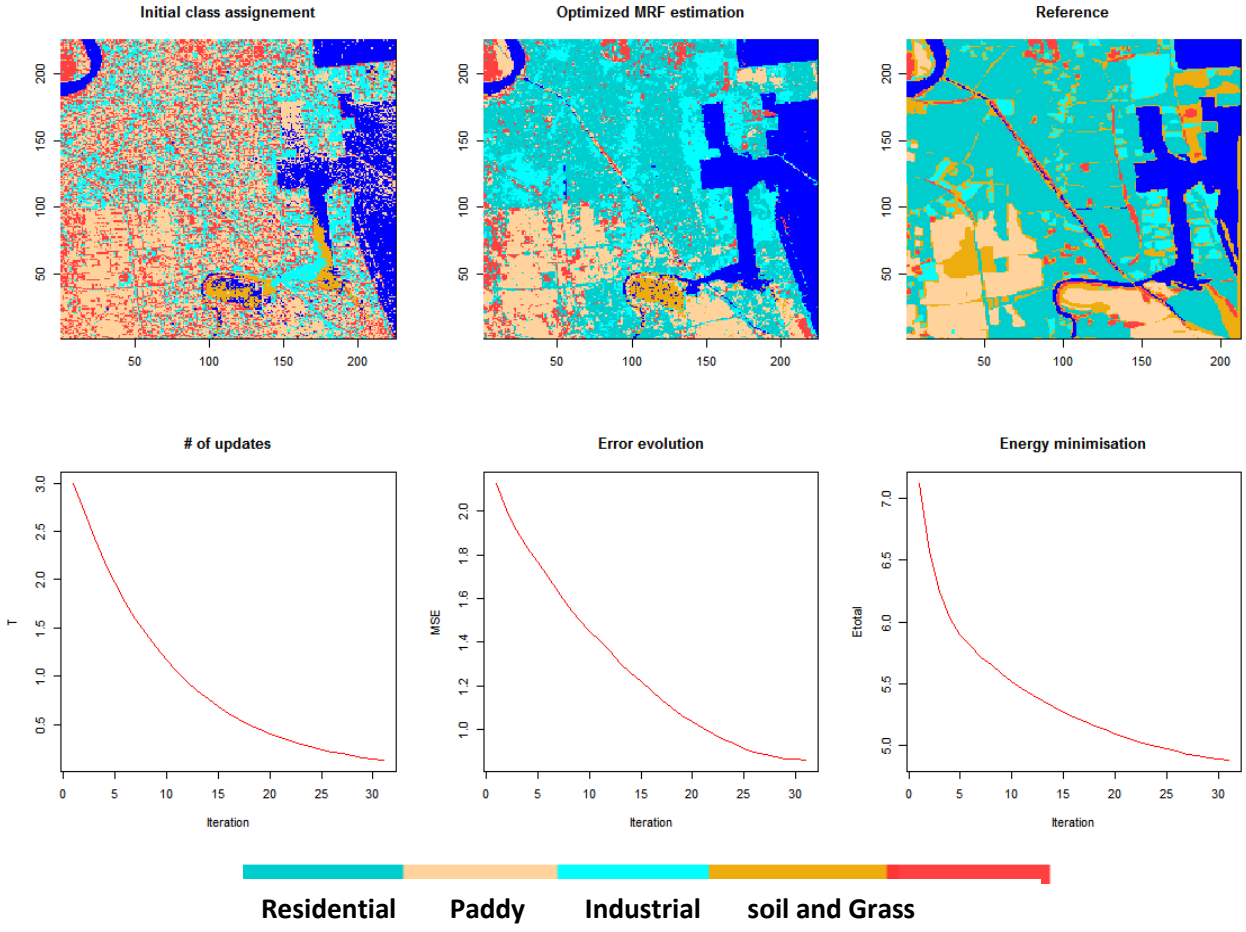

Figure 5.43 MRF classification using AVNIR-2 optical image at a reliable factor of $\boldsymbol{\lambda = 0.5}$ and the simulate annealing based optimization, using the fuzzy class mean vector

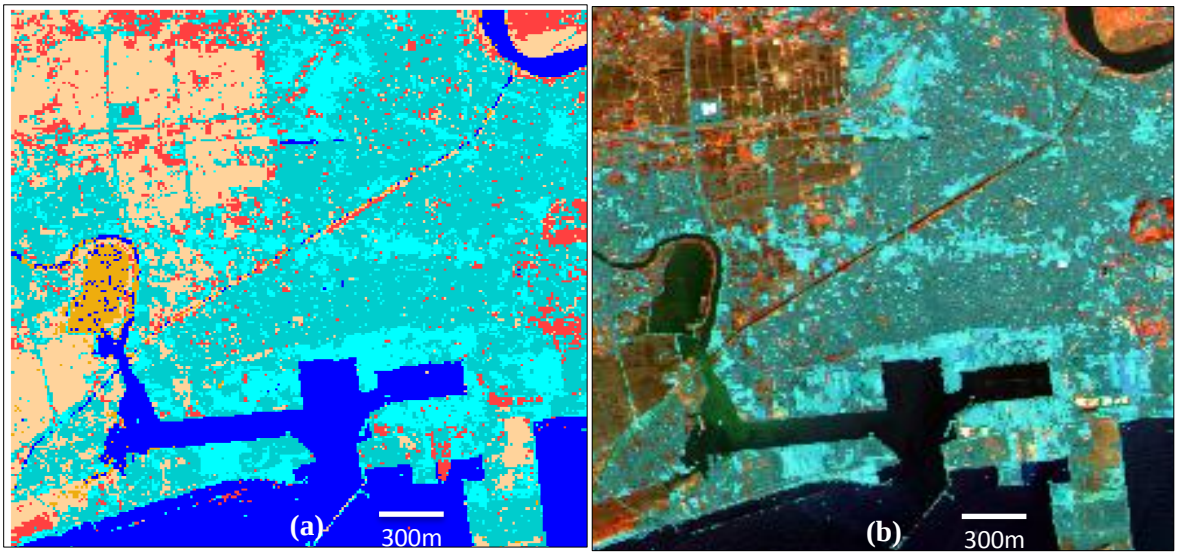

Figure 5.44 (a) optimal classification of AVNIR-2 image using MRF (b) classified impervious region overlay

Table 5 25 Post disaster classification accuracy assessment

Reference data type	Post disaster	Single source MRF model	Multisource conventional MRF model	Multisource fuzzy MRF model
Digitized aerial reference image	**OA%**	**55.175%**	**55.855%**	**57.287%**
	Kappa	**0.426**	**0.416**	**0.438**
SVM based reference image	**OA%**	**56.000%**	**51.720%**	**52.352%**
	Kappa	**0.430**	**0.370**	**0.400**

Table 5.15 shows the accuracy results between the MRF results using single source and multisource imageries with the reference image generated using the aerial photographs for the post disaster case. For both the pre and the post disaster results we have used the same digitized reference images. As seen in Table 5.25, the performance of the multisource MRF model with respect to the performance with the single source seems quite close to each other as in the previous results. This is controversial to the visual inspection of the classification details. Comparison with the digitized reference image shows a slight increase in the accuracy using MRF models with multisource data with 57% OA and 0.44 kappa, respect to the 54% OA and 0.42 kappa of the single source classification. The second comparison with the SVM based classification shows different agreement to these results. The FMRF have 52% OA with 0.40 kappa with respect to the 56% and 0.43 of the single source classification results. The contextual smoothness and the contribution of the SAR and the SAR texture cannot be assessed in this manner. In situations where the reference image is noisy compared to the model outputs inverse mechanisms of the kappa meaning the disagreement between the images is also important in the analysis.

Table 5 26 Pre disaster MRF classification comparison (Single source and multisource)

Pre disaster MRF model			
Comparison	**OA%**	**Kappa**	**SSIM**
Single source MRF vs Multi source conventional MRF	**53.59802**	**0.391101**	**0.1783118**
Single source MRF vs Multi source fuzzy MRF	**70.57383**	**0.6148729**	**0.2961719**
Multisource MRF vs Multi source fuzzy MRF	**63.54765**	**0.5054811**	**0.2448590**

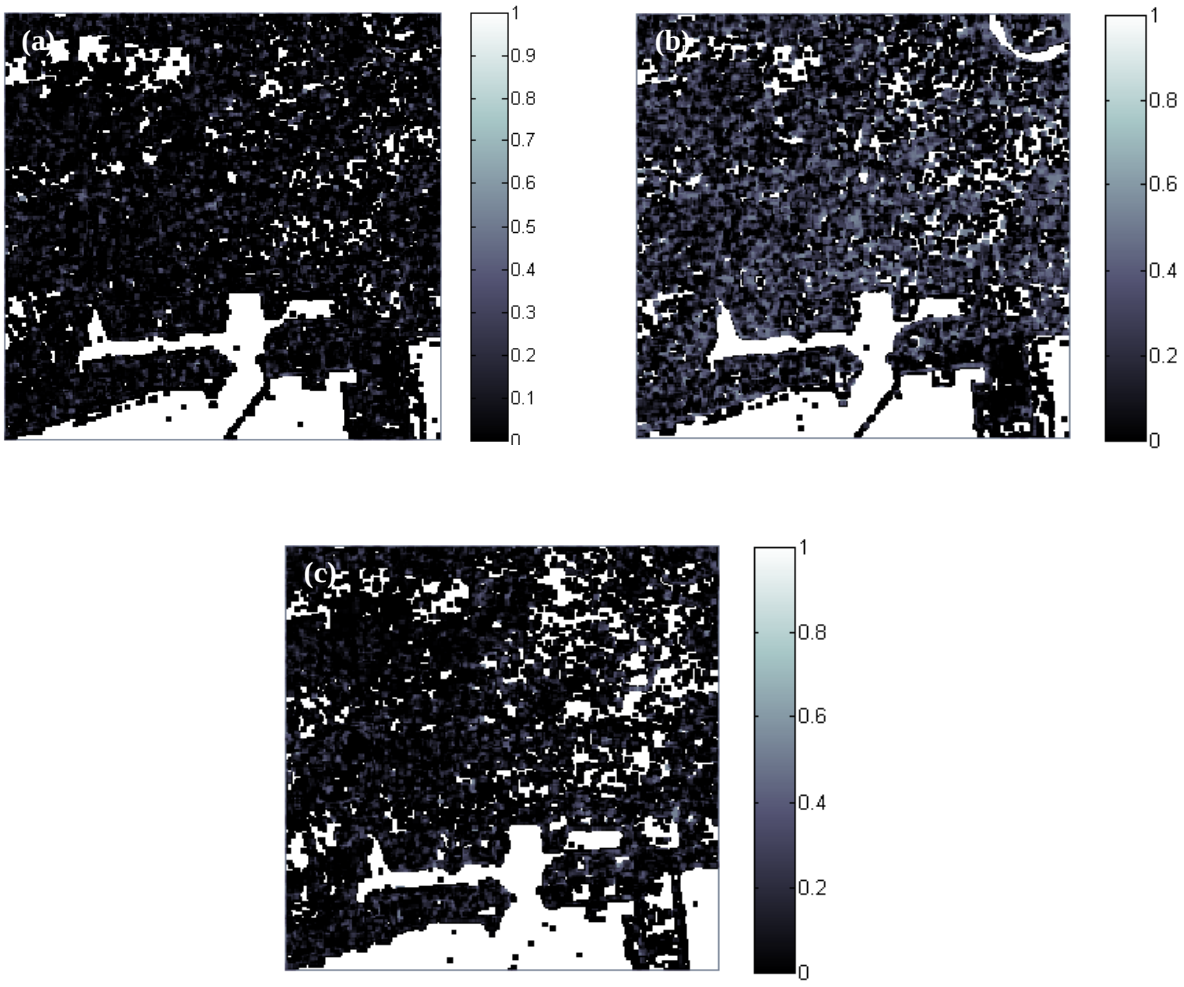

Figure 5.45 Structural Similarity Index matrices (SSIM) generated using pre disaster(a) single source MRF results and multisource conventional MRF (b) single source MRF results and multisource fuzzy MRF (c) multi source MRF results and multisource conventional MRF

Figure 5.45 and 5.46 show the SSIM matrices generated using pre and post disaster MRF results respectively. The main idea behind this analysis is to identify the similarity and the dissimilarity between the classification mechanisms using the MRF models in this study. The strongest dissimilarity was recorded in Fig. 5.45 (a) between the single source and the multisource MRF classification results. From Table 5.26 it can be seen the SSIM values shows this in the range of 0.2. It can also be seen that the fuzzy parameters within the multisource classification has also made changes to the classification with low SSIM values in the range 0.25. This pattern also revealed from the kappa and OA measures. The multisource MRF results shows close agreement with OA in the range 63% to 71% and kappa in the range 0.6 for the fuzzy and conventional post disaster MRF classification. This drops to 53% OA and 0.39 kappa with the single source imagery.

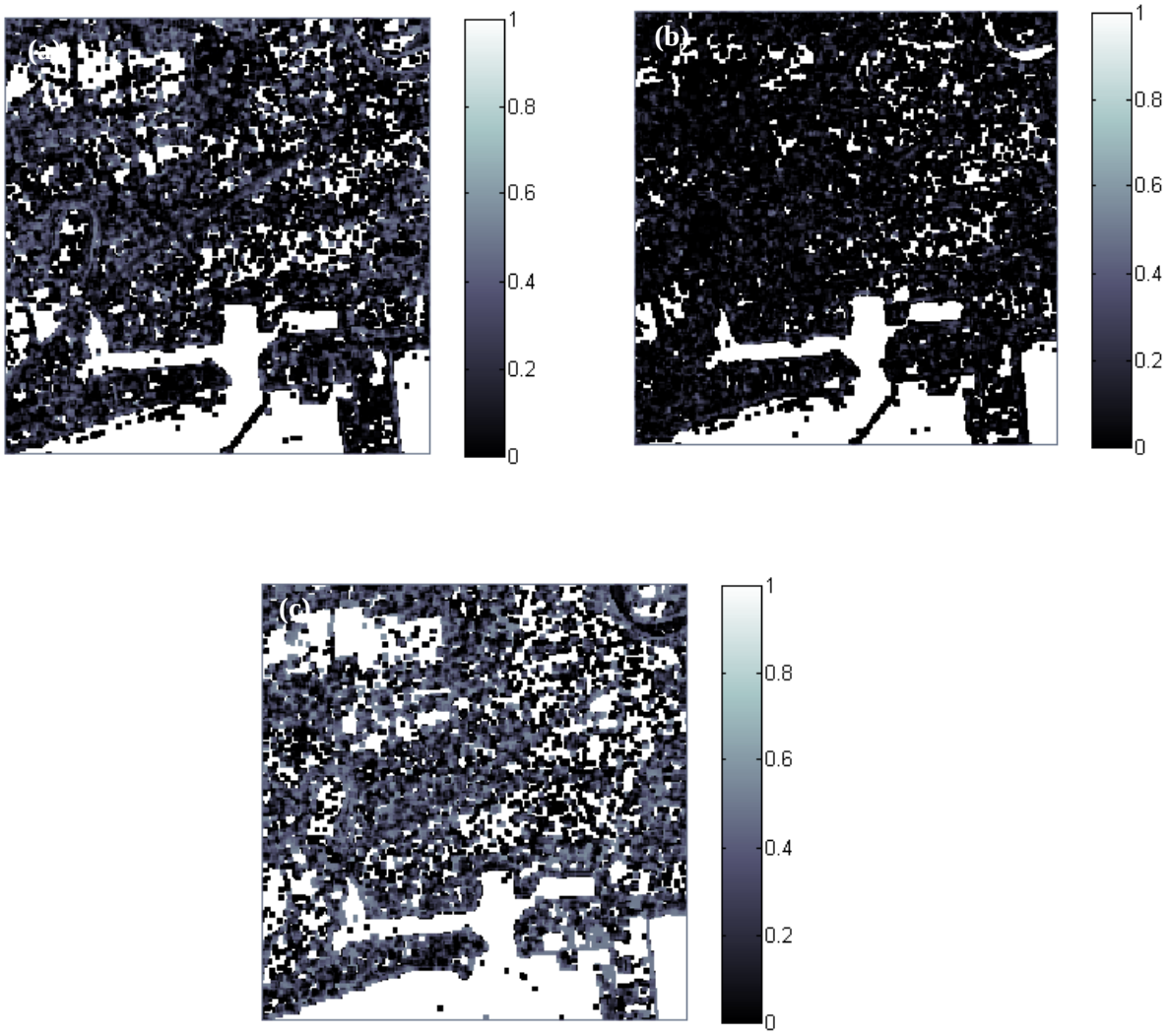

Figure 5.46 Structural Similarity Index matrices (SSIM) generated using post disaster (a) single source MRF results and multisource conventional MRF (b) single source MRF results and multisource fuzzy MRF (c) multi source MRF results and multisource conventional MRF

The strongest dissimilarity was recorded in Fig. 5.46 (a) between the single source and the multisource MRF classification results in the post disaster classification. From Table 5.27 it can be seen the SSIM values shows this in the range of 0.19. Further the fuzzy parameters within the multisource classification have also made changes to the classification with low SSIM values in the range 0.46. This pattern also revealed from the kappa and OA measures. The multisource MRF results shows close agreement with OA in the range 87% and kappa in the range 0.8 for the fuzzy and conventional post disaster MRF classification. This drops to 54% OA and 0.39 kappa with the single source imagery.

Table 5 27 Post disaster MRF classification comparison (Single source and multisource)

Post disaster MRF model			
Comparison	**OA%**	**Kappa**	**SSIM**
Single source MRF vs Multi source conventional MRF	**68.91654**	**0.58320**	**0.3259521**
Single source MRF vs Multi source fuzzy MRF	**54.66074**	**0.3955067**	**0.1999618**
Multisource MRF vs Multi source fuzzy MRF	**87.0084**	**0.8236323**	**0.4632268**

With the detailed experiments conducted in this study on MRF based SRM, SAR texture based time series change analysis and finally the MRF based multisource data classification the comprehensive discussion about the MRF models for feature extraction and its promising out comes will be concluded. The necessity to conduct more experiments to get a strong understanding about the MRF performance and the possibility to improve it and also to perform it with different parameter settings and the best parameters is long way. Our main aim in this study was to extend MRF based image analysis to different directions and to show its performance and the feasibility. To do this we have also taken a complex setup with all the study regions are resulting in the urban environments. The results we have experienced in the heterogeneous urban study regions shows that the model can be implemented with more promise for homogenous land cover classes. One of the most important implementation of this findings is the information restoration for the optical data with the all whether SAR imagery or image texture.

Conclusion and recommendations

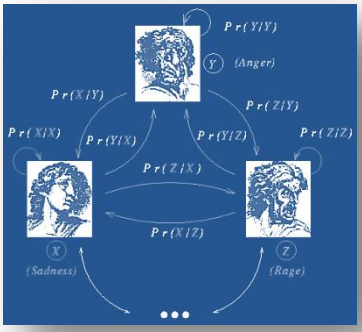

The experiments conducted and the development made to MRF models in this thesis will lead to enhanced understanding of its performance in feature extraction. The combined approach of the fuzzy and MRF models and its extension to multisource image classification takes the central innovation in this work. This chapter provides the answers to the research questions based on the findings with a detail summery. Several very important observations we made during this experiments are highlighted with the recommendations for the future research directives.

6.1 Research questions and the findings

First we look at the research questions we formulated prior to the study and the possible answers and conclusions made from the experiments.

1. What are the statistical similarities and dissimilarities in the class conditional distributions for both optical and SAR images?

   Optical and SAR images fundamentally provide different image statistics. This is mainly due to the difference in image acquisition and the different range of electromagnetic spectrum they are operating in. The main characteristic of SAR images is that the noise variance $\sigma_y{}^2$ of the pixel intensity Y is proportional to $\mu_y{}^2$ which is the square of the mean of this pixel. The true intensity μ_y is proportional to power return from the pixel in the absence of noise. The ramification of proportionality of mean and variance is that the targets with higher intensity have higher noise variances, and can be concluded that noise power is a function of the signal power. This prevents the use of additive white Gaussian noise (AWGN) model, where signal power and noise power are assumed to be independent. SAR images belong to the category of speckle images. If y be a random variable representing observed pixel intensity from SAR imagery, the PDF of y is exponential with the mean μ, where μ is the true intensity of the target to which this pixel belongs. When pixel intensities of neighboring pixels from the same target are uncorrelated and independent, most SAR systems obtain more than one independent sample of detected power from single target for each pixel. The number of independent samples L is referred to as "Number of looks per pixel" The recorded pixel intensity Y, is obtained by averaging these identically

distributed independent samples $Y = \frac{1}{L}\sum_{i=1}^{L} y_i$. The PDF of Y is expressed by a Gamma distribution.

As a summery the probability distribution of the land cover classes can be modelled by using multivariate Gaussian distribution for optical data and MAR based texture (Logarithmic SAR intensity) while using Gamma distribution for multilook SAR intensity. This is the fundamental rule used and implemented in this work.

2. What are the methods available to measure the fuzzy class membership grades for multisource satellite image pixels?

   This is a broad area to be researched, because it is not possible to propose an ideal approach for the membership grade estimation for the optical or SAR imagery. The two main methods proposed in this thesis for the membership grade determination is the Spectral Angle (SA) based sub pixel class fraction and the fuzzy c-means (FCM) clustering approach. Both these approaches showed promise to determine the pixel belongingness to a class. SA is advantageous for optical images as it is a method which is free from atmospheric attenuation. In most of the experiments conducted in this work, we preferred the FCM clustering mainly due to its feasibility to cluster images at different order of fuzzy membership grades, which allows different membership for each pixel (type 1 or type 2 fuzzy sets).

3. How can we model the posterior probability distributions separately for both optical and SAR images in an MRF using fuzzy class definitions?

   The possibility to model PDF using class fuzzy mean and the covariance is proposed for the first time in this study. This provides better estimation for the PDF function. In the case of Gamma distribution this is a stronger implementation as the Gamma distribution is mainly controlled by the class mean values only. Hence replacing this by the fuzzy mean vector is more convenient. In the case of multivariate Gaussian distribution for the multispectral data both the mean and the covariance will be fuzzified to have stronger estimation of the PDF. This implementation gives the user a new parameter to determine the classification performance. The most important aspect of this implementation is that the fuzzy and conventional class means and covariance's can be interchanged depending on the feature (land cover class) to be extracted.

4. What ancillary information (SAR- Texture) is available from SAR imagery, for MRF based parameter estimations and classification?

   The study proposes ancillary information (mainly SAR-texture) that can be used for the multisource classification mechanism. They are the autoregressive and autocorrelation texture. The results presented in this study only includes the MAR based texture, the spatial autocorrelation based texture measure has not been implemented. The discussions were made to show that these parameters can also be included in the multisource classifications and experiments can be conducted to find the performance of it. Moreover the GIS based vector information can also be used as ancillary information. One of the most useful and simple capability of the multisource model proposed is that, many spatial data types can be fused if the statistical properties are known.

5. What is the importance of the smoothing parameter in SRM and the sensor reliability factor in multisource fusion model (λ), for the MRF model?

The solution to determine the best smoothness parameter for the SRM is discussed in detail. Mainly the smoothness parameter relates heavily to the scale factor, the small scale factors tested in this study in the range of 2-3, yields large smoothness parameters for the optimal solution of the SRM.

In the case of the sensor reliability criteria (which can be considered as the second nature of the smoothness parameter, λ), the solution for the best reliability is not very clear. There are many methods proposed in literature but the practicability of them is tedious and time consuming. The idea for the best reliability value was generate by using the classification accuracy as an index. The best classification accuracy resulted by using each source is assigned to the corresponding reliability criteria. Nevertheless the class seperability index can also be an interesting index to determine the optimal sensor reliability criteria. Transform divergence or the Kullback–Leibler divergencecan can be proposed for such purposes. For both SAR intensity and texture the reliability criteria estimation is a trial and error process.

6. How to formulate the combined fuzzy MRF (FMRF) based feature extraction model for the optical and SAR imagery (MIC)?

   The combined model of the multisource data was performed using the theory of the MRF. The possibility to model the posterior energy and the equivalence between the MRF and the Gibbs distribution was the fundamental base for this integration. The detailed explanation of this integration is given in Chapter 4. This was fundamentally developed by considering the MRF mechanism to be a pixel labelling problem.

Three main experiments were discussed and presented in this thesis. In the first it investigated the performance of the MRF based SRM technique with the integration of the fuzzy class parameters. The fuzzy class parameters were defined using the SA and FCM techniques. Testing was carried out using a Worldview-2 data set over a semi urban environment initially. The main assumptions made in the study were the selected training pixels to be pure elements of their representative land cover classes, the fine resolution pixels (**y**) are conditionally independent, fuzzy membership grade of a pixel (**x**) for a particular class is its proportion within that pixel and the observed pixel vector x_m of the multispectral image is having a Gaussian distribution with mean $\overline{\mu(x)}$ and covariance $\overline{\sum(x)}$ ((Eq. 3.20) and (Eq. 3.21)) defined using fuzzy definitions. The healthy class spectral seperability with TD and JM close to 1.9 and 2.0 respectively suggested the least spectral confusion among the classes in the study area. This improves the selection of the pure spectral elements or the end members to define the reference pixel spectra for the SA based membership determination. Minimization of the posterior energy for the optimum SRM ***c*,** (Eq. 3.25) was achieved using SA with Metropolis-Hasting sampler (Geman and Geman 1984, Tso and Mather 2009). The main parameter which controls the annealing schedule of SA technique is the initial temperature T_0 and the cooling schedule parameter (K) which controls the rate of temperature decrease (Li 2009). Regardless of the low complexity of the classification problem in this study, we have implemented a slow annealing process for better results as a precaution. The use of SA and FCM for fuzzy class parameter determination is mainly due to the difficulty in determining the best membership determination and to avoid the model being subjective to such definitions. Finding out the best membership definition method is outside the focus of this study. We test the fuzzy and conventional MRF models for a range of λ values from 0.3 to 0.9. SRM generated for each of these λ parameters is a

configuration of different spectral and contextual information combination. As a benchmark these SRM results were comprehensively evaluated with respect to a standard parametric classification technique (MLC) at both pixel and sub pixel levels. In both the cases at a $\lambda = 0.9$ the optimum SRM's were generated. The use of PSNR and SSIM image quality indexes to investigate the structural similarity in classified fractional images is significantly novel. Further research work and studies are needed for better understanding of the SSIM index in different image processing algorithms. The results demonstrate the significant improvements in the fuzzy MRF model, with smoother classification results. The FCM based fuzzy parameters produce slightly accurate images with respect to the SA based method for λ=0.3 to 0.8. But very clearly both these methods produce the optimal SRM with a more of a same accuracy. This suggests that the sensitivity of the methods to varying fuzzy membership determinations can have little effect on the optimal result. But to strictly confirm this, extended work is needed. After carefully reviewing the MLC based results, experiments were drawn-out to compare the results with SVM and NN classifications. The validation of the fuzzy MRF based SRM with the SVM based reference images have shown healthy classification agreement. The definition of the fuzzy mean and the covariance information for the classes has improved the spectral information modelled by the likelihood energy (Eq. 3.25) of the MRF model. The findings made by using the NN classification have shown slightly different results. In this case both the fuzzy and conventional MRF models have not been able to provide significantly different results, yet they did not deviate significantly on the basis of accuracy. Their agreement with the reference images are more of the same. As it has been pointed out earlier the generation of the reference data using NN to validate the MRF should be improved. The training samples used to determine the fuzzy and conventional mean and covariance parameters of the representative classes to model the PDF in the MRF is kept same for fuzzy as well as the conventional approaches. But it is understood that to improve the inherent classification accuracy of the NN based reference images it is better to use proper ground truth data, prior to the accuracy assessment. This kind of implementation can significantly change this result. The overall results suggested that the proposed SA approach to generate the fuzzy functional images is reasonable. It has produced results close in agreement with the well-known fuzzy C-means clustering membership grades. Using membership grades for the training pixels is observed to be advantageous as it also reduce the amount of representative training samples needed for the classification. The contextual information integration and the improvement of the class parameters using fuzzy definitions in the MRF based SRM technique, is proved to be more effective with better classification accuracy. For vague land cover interpretations this approach can be very advantages due to its capabilities to reach higher classification accuracies at the sub pixel level. Further work is needed to test the performance of the method at a coarser resolution scale with heterogeneous land cover classes with strong similarity and also to validate the results with reference images having higher accuracy at sub pixel levels.

The extended application of the method on AVNIR-2 image can be considered as the first application of an SRM in Japanese remote sensing satellite imagery. The experiments show promising SRM results with the reduction in the PSF effects. Features in the urban area, such as buildings, trees and homogeneous grass and exposed soil classes were classified with higher degree of certainty. According to the SSIM matrices it was observed that the fuzzy class parameters affect more to the classes with strong mixture than the most pure pixels.

Fuzzy parameter integrated MRF based SRM technique employs an improved classification mechanism over the more reliable and frequently used classification methods such as MLC, SVM and NN. It is a

classification technique which operates on a finer spatial resolution than that of the input image. As a relatively new field in Remote Sensing, different SRM techniques have shown the promise in determining thematic information using low resolution satellite data. Improving the technique to perform reliably in different applications is essential. In this work, certain efforts were taken to minimize the uncertainties sneak into the SRM models due to vague land cover interpretations as well as the PSF using fuzzy definitions. The study went on to show that smoother and superior SRM maps could be resulted with the use of fuzzy parameters.

MAR model parameters since their introduction have been used successfully with Markov Random Filed base classification mechanisms for better contextual smooth classification outputs from multisource data. Yet their capabilities in time series data analysis especially to detect contextual changes in land cover have not been investigated fully. In this respect the main goal of the texture based time series data analysis was to investigate the performance of MAR texture measures of SAR data, to extract contextual changes resulting from disasters. The study proposes the use of MAR based texture for time series SAR data change analysis independent of polarimetric approaches. Affected area of the Tohoku, earthquake and tsunami in the year 2011 off the pacific coast of Japan was chosen as the study site (site 2). Four different techniques to detect the structural changes using MAR based texture measures were presented in this study. A significant finding of the study is the changes in the shape and height of the variograms from a spherical to exponential depending on the damages to the structure. Hence extensive use of variograms with MAR base texture at different transects over the study region can predict the areas exposed to major changes. The noise free setup of the MAR based texture provides the feasibility to use the SSIM for the study; this can be observed with the use of SSIM in Lee filtered SAR data. The change areas always represent the dissimilarity between the pre and the post disaster scenes. The temporal changes extracted from the SSIM based analysis corresponds similar to the change detection results of the MRD. Finally MRD extracts the change pixels from the no-change one. The visual inspection shows the MAR texture parameters are more sensitive to the small scale variations of the change. Noise free results with better smoothing can be observed in the MAR texture, comparative to the PCA and normalized ratio based approaches. It can be useful to apply the technique for different disaster situations with proper ground truth information for further evaluation. MAR based SAR texture preserves the original SAR information and provides a better discrimination for the changed and no changes classes.

The MRF model proposed in this study for multisource data considers the fuzzy membership grades for SAR intensity pixels to model the conditional energy using a Gamma distribution. Initial pixel labelling was done by using the maximum representative class fraction within an AVNIR-2 image pixel. Method was tested over an urban area in the north east coast of Japan, heavily affected by an earthquake and tsunami. The FMRF model shows its improvements over the MRF model for the multisource data with better contextual smoothening and class discrimination ability. Several important conclusions can be made from the findings of this work. Bothe the MRF and FMRF approaches show promising results for the multisource data classification. But as a main difference between the two, grade of memberships for pixels can be used to discrimination vague land cover classes (ex, water, farm lands). For a particular class which is not possible to be discriminated in the MRF, a better option is to use its fuzzy mean vector. This also means that we can replace specific class means with fuzzy means without replacing the whole conventional mean vector to model its conditional energy much more sensitively (adaptive mean vector). The combined annealing schedule shows the promise for practical applications with faster annealing and better energy minimization. The variation of the reliability factor λ is not clear with the experiments

conducted. It will be interesting to see its variation with different approaches such as genetic algorithms or class seperability index as mentioned above. We conclude that the use of membership weighted pixels to model the energy functions in MRF can bring an additional parameter in the form of an adaptive class mean vector to provide better classification accuracies. This also provides the possibility to incorporate uncertainty in MRF due to effects such as point spread function (PSF) as well as speckle.

6.1 Recommendations

The MRF based image analysis techniques tested in detail within this work has carried out MRF approach to new dimensions leading to extensive understanding about its performance, parameters and the compatibility toward different image sensor data (Multispectral and Microwave). The thesis details the MRF model theoretically as well as at the application level. This will be a good reading for most of the research work for the development of this method. The text in this thesis summarizes most of the major development in the history of the MRF modelling in image analysis (especially in Image classification and fusion). Several recommendations are pointed out in from the experiments conducted in this study.

One of the main recommendations is the development of a comprehensive classification accuracy measure to validate both the SRM and multisource data classification results using MRF. The validation task of the MRF process is the most tedious in the setup. Very few works have been done to justify the most suitable classification accuracy assessment for the SRM maps. The major difficulty is the current classification mechanisms fail to address the validation task when it comes advance classification mechanisms.

Secondly the development of Isotropic MRF models for multisource remote sensing image classification. The proposed method in this work undertakes the classification at SAR sensor resolution level. Hence it can be seen as one directional approach. It is also possible to make it work at the higher resolution (optical image). This is an area to work on in the future. Because it can yield SRM maps with the SAR information which has not been attempted up to now.

The third is the use of autocorrelation texture measures for the MRF modelling. This will be a new direction of multisource classification mechanism as the proposed recent spatial autocorrelation texture measures (Moran's I_i, Geary's C_i and Getis-Ord G_i) show strong advantageous to detect urban land cover regions. In such a setup it will be necessary to consider these texture measures close to GIS data formats.

The experiments discussed and shown in this thesis provide a comprehensive framework of MRF modelling. The integration of fuzzy and MRF models and the development of MRF models for multisource data classification is the central novelties of the thesis. Many improvements are still left in this work but the foundation is same as shown in this work. Interestingly this model is very simple that can integrate many remote sensing images in single frame work, but it is interesting to test more faster and accurate optimization approaches other than simulated annealing (SA). The model also provides the framework to inject the lost information due to atmospheric attenuations in optical imagery using SAR imagery. This is a very useful and powerful character of the multisource MRF classification mechanism.

Appendix A

- MRF and GRF equivalence

Let P(ω) be a Gibbs distribution on the set of sites (image pixels) S with respect to the neighborhood system N. Consider the conditional probability defined by

$$P(\omega_i|\omega_{S-i}) = \frac{P(\omega_i,\omega_{S-i})}{P(\omega_{S-i})} = \frac{P(\omega)}{\sum_{\omega_i' \in \mathcal{L}} P(\omega')} \quad (1)$$

$\omega' = \{\omega_1, \ldots\ldots, \omega_{i-1}, \omega_i', \ldots\ldots, \omega_m\}$ any configuration that agrees with ω at all sites except i, and $\mathcal{L}$ set of labels.

$$P(\omega) = \frac{\exp[-\sum_{c\in C} V_c(\omega)]}{Z} \quad (2)$$

Similarly

$$P(\omega') = \frac{\exp[-\sum_{c\in C} V_c(\omega')]}{Z}$$

Substituting Eq., 2 in Eq., 1

$$P(\omega_i|\omega_{S-i}) = \frac{\exp[-\sum_{c\in C} V_c(\omega)]}{\sum_{\omega_i' \in \mathcal{L}} \exp[-\sum_{c\in C} V_c(\omega')]} \quad (3)$$

Dividing clique C in to two sets A and B, with A consisting of pixels containing r and B being the pixels not containing r, Eq., 3 becomes

$$P(\omega_i|\omega_{S-i}) = \frac{\exp[-\sum_{c\in A} V_c(\omega)] \times \exp[-\sum_{c\in B} V_c(\omega)]}{\sum_{\omega_i' \in \mathcal{L}} \{exp[-\sum_{c\in A} V_c(\omega')]\} \times \{\exp[-\sum_{c\in B} V_c(\omega')]\}} \quad (4)$$

Since $V_c(\omega) = V_c(\omega')$ for any set of pixels c that does not contain pixel r, following terms of the Eq., 4 can be removed.

$$exp\left[-\sum_{c\in B} V_c(\omega)\right] \text{ and } exp\left[-\sum_{c\in B} V_c(\omega')\right]$$

Hence this probability only depends on the potential function V_c of the pixels containing r.

$$P(\omega_i|\omega_{S-i}) = \frac{\exp[-\sum_{c\in A} V_c(\omega)]}{\sum_{\omega_i' \in \mathcal{L}} [exp[-\sum_{c\in A} V_c(\omega')]]} \quad (5)$$

- Multisource classification mechanism theory-

Let x_m and y_m denotes the observed optical (X) and SAR (Y) image pixel gray level values at a pixel location *m* respectively. Label of a pixel is represented by class ω.

$P(\omega|x,y) \propto P(x,y|\omega)P(\omega)$

$U(\omega|x,y) = U(x,y|\omega) + U(\omega)$

$P(x_m,y_m|\omega_m) \propto P(x_m|\omega_m) \times P(y_m|\omega_m)$

$P(x_m,y_m|\omega_m) \propto P(x_m|\omega_m)^{\lambda_1} \times P(y_m|\omega_m)^{\lambda_2}$

$P(x_m,y_m,z_m|\omega_m) \propto P(x_m|\omega_m)^{\lambda_1} \times P(y_m|\omega_m)^{\lambda_2} \times P(z_m|\omega_m)^{3}$

$U(x_m,y_m,z_m|\omega_m) = \lambda_1 \times U(x_m|\omega_m) + \lambda_2 \times U(y_m|\omega_m) \times \lambda_3 \times U(z_m|\omega_m)$

Hence the conditonal probaility for SAR intensity can be defined as

$$P(y_m|\omega_m) = \frac{L^L}{\mu_{\omega(L-1)!}^L} y_m^{L-1} \exp(-\frac{L}{\mu_\omega} y_m)$$

$$P(y_m|\omega_m) = \frac{1}{Z} \exp(-\frac{U(y_m|\omega_m)}{T})$$

$$Z = \sum_{all\ possible\ cofigerations\ of\ \omega} \exp\left[-\frac{U(\omega)}{T}\right]$$

$$Log(P(y_m|\omega_m)) = Log(\frac{1}{Z}\exp\left(-\frac{U(y_m|\omega_m)}{T}\right))$$

$$U(y_m|\omega_m) = -Log\big(P(y_m|\omega_m)\big)$$

$$= -Log\left(\frac{L^L}{\mu_{\omega(L-1)!}^L} y_m^{L-1} \exp\left(-\frac{L}{\mu_\omega} y_m\right)\right)$$

$$= \frac{L}{\mu_\omega}\ y_m - Log\left(\frac{L^L}{\mu_{\omega(L-1)!}^L} y_m^{L-1}\right)$$

$$= \frac{L}{\mu_\omega}\ y_m - Log\left(\frac{L}{\mu_\omega^L} y_m^{L-1}\right)$$

$$= \frac{L}{\mu_\omega}\ y_m - (L-1)Log(y_m) - (-Log(\mu_\omega^L))$$

$$U(y_m|\omega_m) = \frac{L}{\mu_\omega{}^l} y_m - (L-1)\log(y_m) + Llog(\mu_\omega)$$

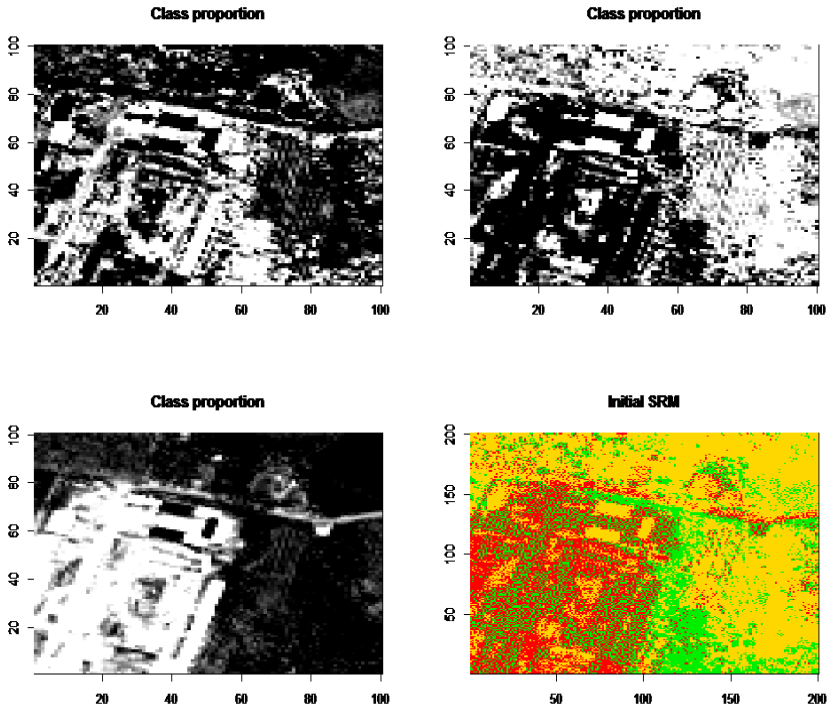

Figure A.1 Class fractions and the initial MRF filed for Worldview-2 imagery

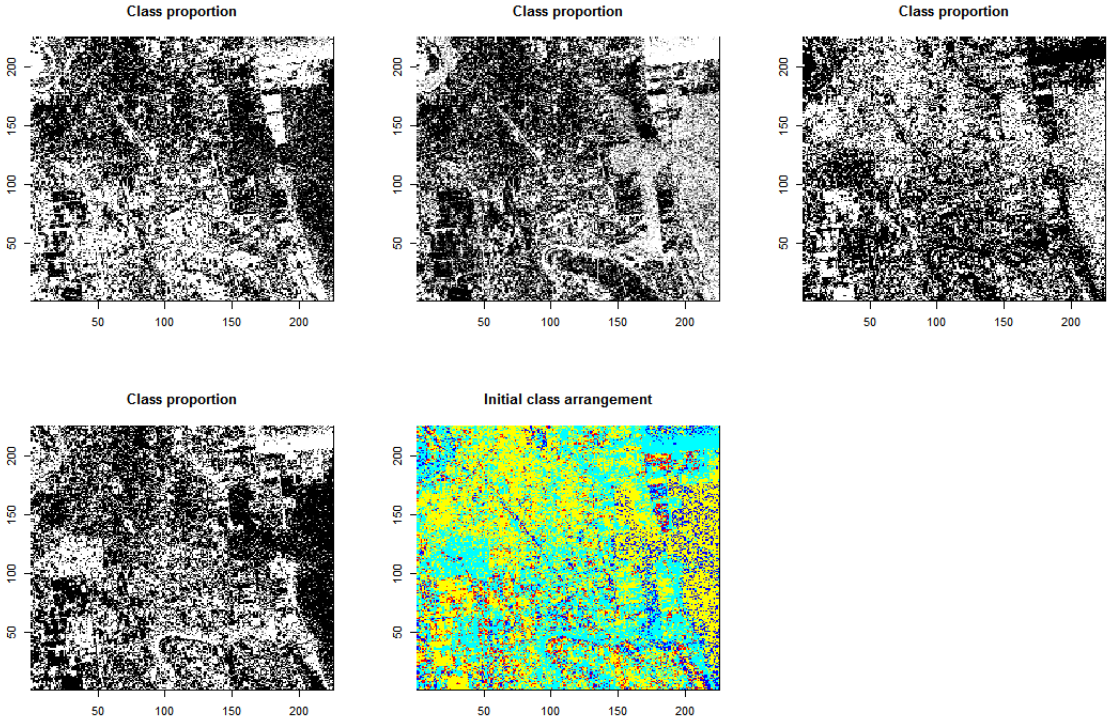

Figure A.2 Class fractions and the initial MRF filed for AVNIR-2 pre disaster imagery

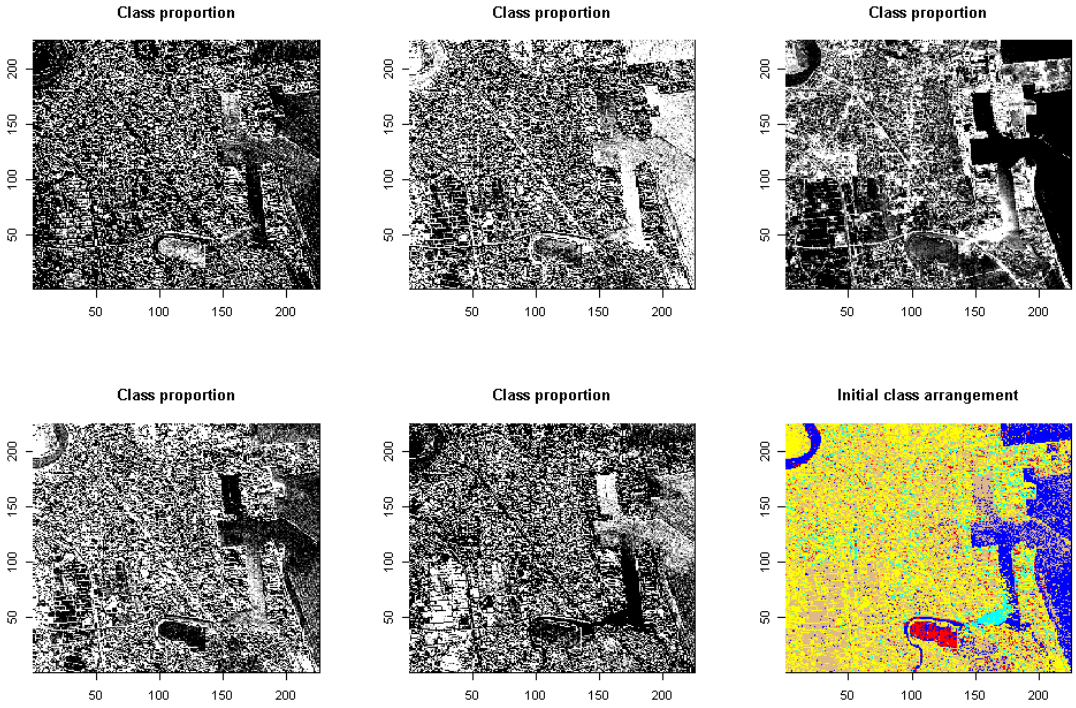

Figure A.3 Class fractions and the initial MRF filed for AVNIR-2 pre disaster imagery

Pseudo cord of the SA based optimization

Begin

Determine neighborhood system (usually only clique C_2 is used), and parameters **(Parameters for energy function)**

(1) Choose an initial temperature T.

(2) Initialize image of configuration w for each pixel by choosing w_r as the class at site r that minimizes the non-contextual energy term

$$U\left(d_r \middle| w_r\right) = \frac{1}{2}\left(d_r - u_k\right)\sum_k^{-1}\left(d_r - u_k\right)$$ as given in Eq. **3.25**

(3) For all pixels r, perturb w_r by label w_r', which is randomly selected from the label set ι. Define energy difference Δ as

$$\Delta = U(w_r|d_r) - U(w_r'|d_r)$$

Both energy functions are calculated in terms of Equation (**3.27**

If $\Delta > 0$ replace w_r by w_r',

else if $\exp(\Delta/T) \geq$ random [0,1] replace w_r by w_r';

(4) Repeat (3) N_{inner} times.

(5) Let $T = f(T)$ where f is a decreasing function.

(6) Repeat (3)–(5) until frozen, $T \rightarrow 0$;

End

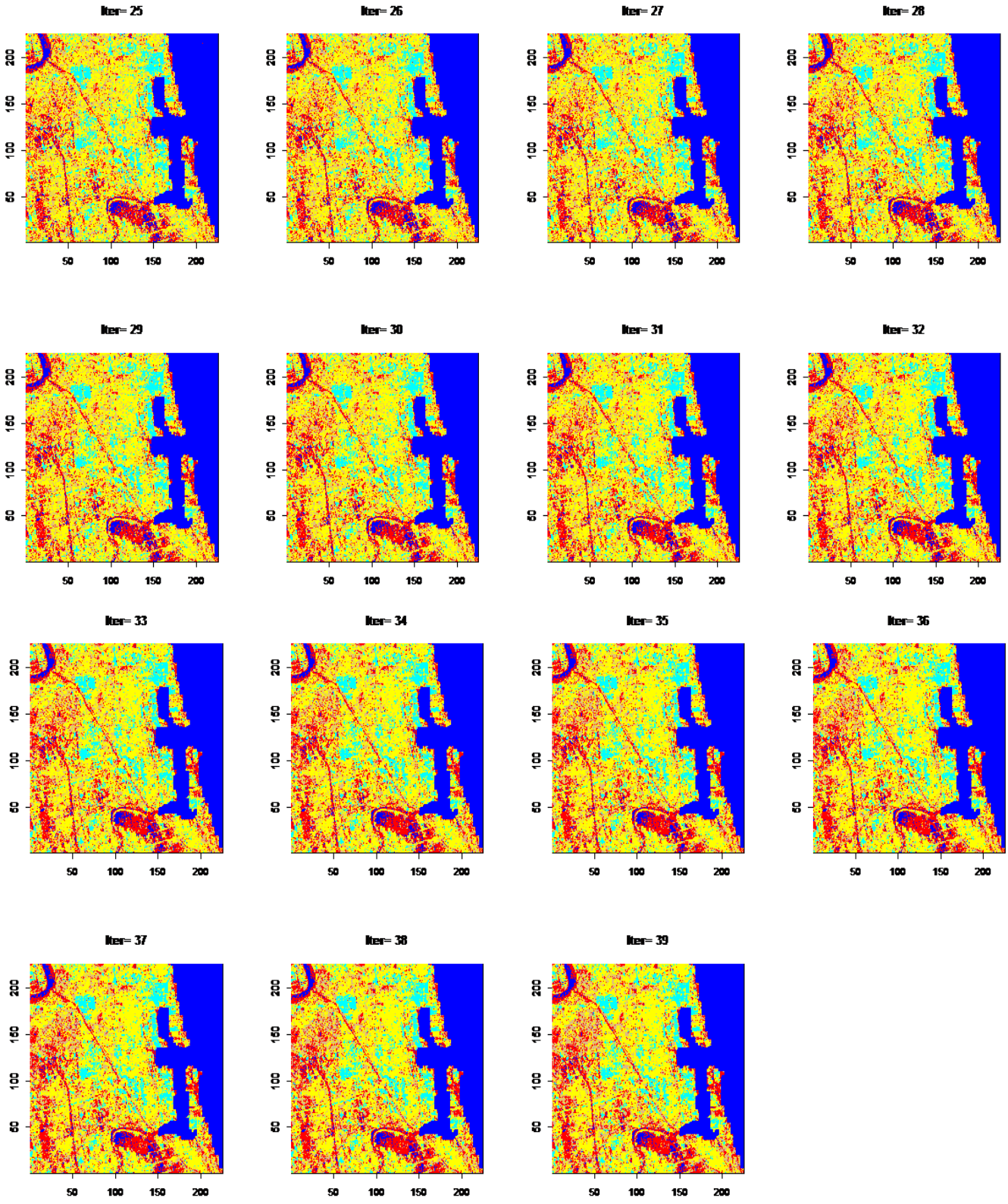

Figure A.4 SA based total iteration process for optimal class labelling post disaster AVNIR-2 image and SAR HH+VV/2

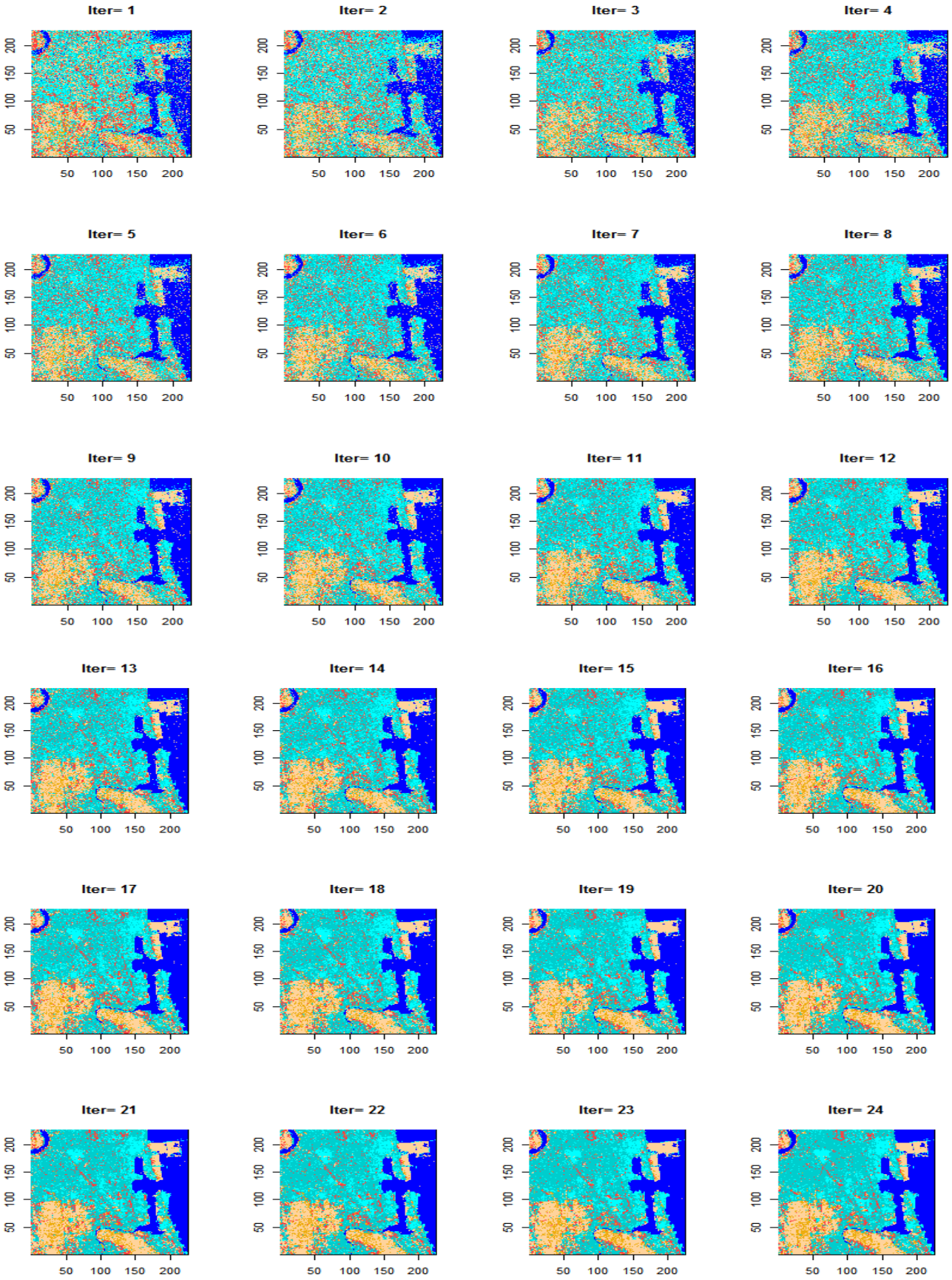
Iter= 1
Iter= 2
Iter= 3
Iter= 4
Iter= 5
Iter= 6
Iter= 7
Iter= 8
Iter= 9
Iter= 10
Iter= 11
Iter= 12
Iter= 13
Iter= 14
Iter= 15
Iter= 16
Iter= 17
Iter= 18
Iter= 19
Iter= 20
Iter= 21
Iter= 22
Iter= 23
Iter= 24
50
100
150
200

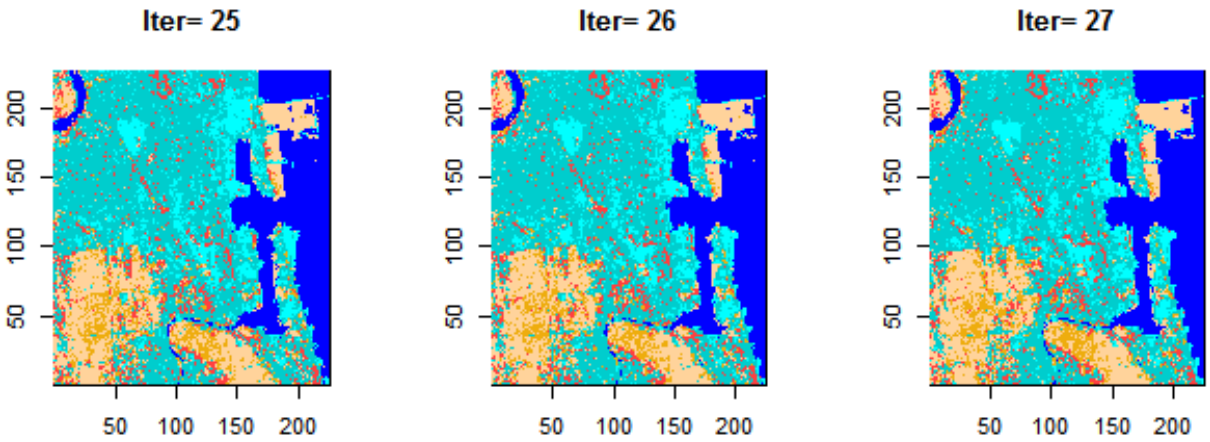

Figure A.5 SA based total iteration process for optimal class labelling pre disaster AVNIR-2 , ALOS PALSAR HH+VV/2 and MAR texture

Appendix B- Mathematical notations

Chapter 2

X={F,L}	F intensity process and L line process in the original image
G	Given degraded data
$\boldsymbol{Z_m}$	$m \times m$ integer lattice (F $\in Z_m$)
$\boldsymbol{\mathcal{F}}$	Neighborhood system
T	Temperature
S	Set of sites
$\boldsymbol{s}$	element of site S
$\boldsymbol{\mathcal{G}_s}$	Neighborhood system for site s
$\boldsymbol{r \neq s}$	Two different sites
$\mathbb{C}$	Set of cliques
$\boldsymbol{C}$	Cliques for $\boldsymbol{\mathcal{G}}$
$\boldsymbol{i,j}$	Pixel coordinate
D	Set of Line site
$\boldsymbol{Q}$	Neighborhood system for line process
$\boldsymbol{\Lambda}$	Common state space
$\boldsymbol{L}$	pixel intensity levels
$\boldsymbol{\Omega}$	Set of all possible labels (configurations)
$\boldsymbol{\omega}$	Pixel label
$\boldsymbol{U(\omega)}$	Energy Function
$\boldsymbol{Y}$	Coarser spatial resolution image
$\boldsymbol{X}$	Super resolution map

$\boldsymbol{M \times N}$	Input image dimensions
$\boldsymbol{a}$	Scale factor
$\boldsymbol{t}$	Time
$\boldsymbol{S}$	Set of all sites (i.e., pixels) belonging to observed image
$\boldsymbol{J}$	Set of all sites (i.e., pixels) belonging to SRM
$\boldsymbol{\mathcal{L}}$	Numbers of land cover classes
$\boldsymbol{V_c(X)}$	Gibbs potential function (clique potential)
$\boldsymbol{\mu(s)}, \boldsymbol{\Sigma(s)}$	Class mean vector and covariance matrix
$\boldsymbol{b_l(s)}$	Proportions of land cover classes ($l \in \mathcal{L}$)
$\mathbf{Z}$	Partition function (normalizing constant)
$\boldsymbol{Y_s, \theta_{kl}, \sigma^2, \mu_y}$	Parameters of the SAR textural model (MAR)

There are few exceptions to the interpretation of the symbols in chapter 2, especially in the definitions of the multisource classification mechanism; they are specified in Table 2.1

Chapter 3

$\boldsymbol{d}$	Set of random variables (ex, pixel DN values), family *d* is a random field
$\boldsymbol{\omega}$	Pixel label
$\mathbf{C}$	Super resolution map (SRM)
$\boldsymbol{S}$	Set of all sites (i.e., pixels) belonging to observed image
$\boldsymbol{V_c(X)}$	Gibbs potential function (clique potential)
$\boldsymbol{N_i}$	The set of sites neighboring i
$\boldsymbol{\mathcal{L}}$	Numbers of land cover classes
$(\boldsymbol{C_1})\ \boldsymbol{c} = \{\boldsymbol{i}\}$	Single site clique
$(\boldsymbol{C_2})\ \ \boldsymbol{c} = \{\boldsymbol{i}, \boldsymbol{i'}\}$	Pair of neighboring sites
$\boldsymbol{U(\omega)}$	Energy Function
$\mathbf{Z}$	Partition function (normalizing constant)
$\boldsymbol{K}$	Number of sensor bands

$\boldsymbol{f_{\omega}(\mathbf{X})}$	Fuzzy grade of membership
$\boldsymbol{l}$	Number of land cover classes
T_0	Initial temperature
$\boldsymbol{K}$	Cooling schedule parameter
$\boldsymbol{t}$	Iteration number
$\boldsymbol{\theta}$	Weighting parameter
$\boldsymbol{\sigma_u^2}$	Noise variance
$\boldsymbol{\delta_x}$	Mean value of log estimated SAR intensity
w	Membership weighting exponent
Ω	Fuzzy subset of the universe of discourse
f_{ω}	Fuzzy membership grade for class ω

References

Ardila, J.P., Tolpekin, V. A, Bijker, W., and Stein, A., 2011. Markov-random-field-based super-resolution mapping for identification of urban trees in VHR images. *ISPRS Journal of Photogrammetry and Remote Sensing* **66 (6)**, 762-775.

Ardila, J. P., Tolpekin, V. A, Bijker, W., and Stein, A., 2012. Quantification of crown changes and change uncertainty of trees in an urban environment. *ISPRS Journal of Photogrammetry and Remote Sensing*, **74**, 41-55.

Atkinson, P. M., 2004. Super-resolution land cover classification using the two-point histogram. *Geostatistics for Environmental Applications*, 15-28.

Atkinson, P. M., 2005. Super-resolution target mapping from soft classified remotely sensed imagery, *Photogrammetric Engineering and Remote Sensing* **71**, 839-846.

Atkinson, P. M., 2009. Issues of uncertainty in super-resolution mapping and their implications for the design of an inter-comparison study, *International Journal of Remote Sensing* **30(20)**, 5293-5308.

Atkinson, P.M., 2004 Resolution manipulation and sub-pixel mapping in Remote Sensing Image Analysis: Including the Spatial Domain, Kluwer Academic, Dordrecht, 51-70.

Bastin, L., Fisher. P., and Wood, J., 2002. Visualizing uncertainty in multi-spectral Remotely Sensed imagery. *Computers & Geosciences* **28** (3), 337-338.

Bateson, A., Curtiss, B., 1996. A Method for Manual Endmember and Spectral Unmixing Selection, *Remote Sensing of Environment* **55**, 229-243.

Benediktsson, J.A., Swain, P.H., 1989. A method of statitical multisource classification with a mechanism to weight the influence of the data sources, *Geoscience and Remote Sensing Symposium, 1989. IGARSS'89. Vancouver, Canada* , 517-520.

Besag, J., 1974. Spatial interaction and the statistical analysis of lattice systems (with discussions). *Journal of the Royal Statistical Society*, Series B36, 192–236.

Boardman, J. W., 1989. Inversion of imaging spectrometry data using singular value decomposition, *Geoscience and Remote Sensing Symposium, 1989. IGARSS'89. 12th Canadian Symposium on Remote Sensing, 1989 Vancouver, Canada* , 2069-2072.

Boucher, A. A., Kyriakidis, P.C., Cronkite-Ratcliff, C.C., 2008, Geostatistical solutions for super-resolution land cover mapping. *IEEE Transactions on Geoscience and Remote Sensing* **46**, 272-283.

Bremaud, P. (1999).Markov chains Gibbs field, Monte Carlo simulation, and queues. New York' Springer-Verlag.

Bruzzone, L., Prieto,F.F., 2000, Automatic analysis of the difference image for unsupervised change detection. *IEEE Transactions on Geoscience and Remote Sensing* **38(3)**

Bujor, F., Trouve, E., Valet, L.,Nicolas, J.M., Rudant, J.P., 2004, Application of Log-Cumulants to the detection of spatiotemporal discontinuities in multitemporal SAR images. *IEEE Transactions on Geoscience and Remote Sensing* **38(3)**

Canty, M. J., 2010. Image Classification, and Change Detection in Remote Sensing with algorithms for ENVI/IDL. CRC Press, Boca Raton.

Calabresi, G., 1996. The use of ERS data for flood monitoring: An overall assessment. Second ERS application workshop, London, UK, 237–241.

Chellappa, R.,Chatterjee, S., 1985, Classification of Texture using Gaussian Markov Random Field, *IEEE Transaction on Acoustics and Signal Processing*, **33(4)**, 959-963.

Congalton, R. G., 1991. A review of the assessing the accuracy of classification of Remotely Sensed data. *Remote Sensing of Environment* **37 (1)**, 35-46.

Cross, G.R., Jain., A. K. 1983, Markov Random Field Texture Models, *IEEE Transaction on Pattern Analysis and Machine Intelligence*, **PAMI-5(1)**, 25-39.

Curran, P. J. 1988. The Semivariogram in Remote Sensing: An Introduction, *Remote Sensing of Environment* **21**, 493-507.

DigitalGlobe., 2011. www.digitalglobe.com (Accessed 20 February, 2011)

Dierking, W., Skiver, H., 2002, Change Detection for thematic mapping by means of airborn multitemporal polarimetric SAR imagery, *IEEE Transaction of Geoscience and Remote Sensing* **40(3)**, 618-636.

Del Frate, F. D., Pacifici, F., Solimini, D., 2008. Monitoring Urban Landcover in Rome, Italy, and its change by single-polarization Multitemporal SAR images, *IEEE Journal of Selected Topics Applied Earth Observation and Remote Sensing*, **2(1)**, 87-97.

Deng, H., Clausi, D.A., 2004. Unsupervised image segmentation using a simple MRF model with a new implementation scheme. Pattern Recogniton. 37, 2323-2335

Deng, H., Clausi, D.A., 2005. Unsupervised segmentation of synthetic aperture radar sea ice imagery using a novel Markov Random Field model. *IEEE Transactions on Geoscience and Remote Sensing* **43(3)**, 528-538.

Dekker, R. J. 2003, Texture analysis and classification of ERS SAR images for map updating of urban areas in The Netherlands, *IEEE Transaction of Geoscience and Remote Sensing*, **49(9)**, 1950-1958.

Derin, H., H. Elliott., 1987. Modeling and segmentation of noisy and textured images using Gibbs random fields. *IEEE Transactions on Pattern Analysis and Machine Intelligence* **9 (1)**, 39–55.

Dubes, R. C., A. K. Jain., 1989. Random field models in image analysis. *Journal of Applied Statistics* **16 (2)**, 131–164

Duda, R.O., Hart, P.E., Stork, D.G., 2000, Pattern classification, second ed, Wiley-Interscience, New York

Dubes, R. C., Jain, A. K., Nadabar, S. G., Chen, C. C., 1990. *MRF Model-Based algorithm for image segmentation, 10th International Conference on Pattern Recognition, Atlantic City, NJ*, 808 - 814

Duggin, M. J., Robinove , C. J.,1990. Assumptions implicit in Remote Sensing data acquisition and analysis. *International Journal of Remote Sensing* **11** (10), 1169-1694.

Ehrlich, D., Guo, H. D., Molch, K., Ma, J. W., Pesaresi, M. 2009, Identifying damage caused by the 2008 Wenchuan Earthquake from VHR remote sensing data, *International Journal of Digital Earth*, **2(4)**, 309-326.

Fisher, P., 1997. The pixel: a snare and a delusion. *International Journal of Remote Sensing* **18(3)**, 679-685.

Fisher, P., 2010. Remote Sensing of land cover classes as type 2 fuzzy sets. *Remote Sensing of Environment* **114 (2)**, 309-321.

Fisher, P., Arnot, C., Wadsworth, R., Wellens, J., 2006. Detecting change in vague interpretations of Landscapes. *Ecological Informatics* **1 (2)**, 163-178.

Fisher, P. F., Pathirana, S., 1990. The evaluation of fuzzy membership of land cover classes in the suburban zone. *Remote Sensing of Environment* **34 (2)**, 121-132.

Foody , G. M., 1997. Fully fuzzy supervised classification of land cover from Remotely Sensed imagery with Artificial Neural Network. *Neural Computing & Applications* **5 (4)**, 238-247.

Foody, G. M., 1998. Sharpening fuzzy classification output to refine the representation of sub-pixel land cover distribution. *International Journal of Remote Sensing*, **19(13)**, 2593 – 2599.

Foody, G.M., Matur, A., 2006. The use of small training sets containing mixed pixels for accurate hard image classification: Training on Mixed spectral responses for classification by a SVM. *Remote Sensing of Environment* **103 (2)**, 179-189.

Forster, B., 1983. Some urban measurements from Landsat data. *Photogrammetric Engineering and Remote Sensing* **49**, 1693-1707.

Franknote, R.T., Chellappa, R., 1987. Lognormal Random-Field Models and their applications to radar image synthesis, *IEEE Transaction of Geoscience and Remote Sensing*, **GE-25(2)**, 195-207.

Gamba, P., Aldrighi, M.,2012. SAR Data Classification of Urban Areas by Means of Segmentation Techniques and Ancillary Optical Data, *IEEE Journal of Selected topics in Applied Earth Observation and Remote Sensing*, Vol. *5*, No. 4, 1140-1148.

Gamba, P., Acqua, F.D., Trianni, G., 2007. Rapid damage detection in the Bam area using multitemporal SAR and exploiting ancillary data, *IEEE Transactions on Geoscience and Remote Sensing*, **45(6)**, 1582-1589.

Geman, S., Geman, D., 1984. Stochastic relaxation, Gibbs distribution, and the Bayesian restoration of images. *IEEE Transactions on Pattern Analysis and Machine Intelligence* **6 (6)**, 721-741.

Geman, D., Reynolds, G., 1992. "Constrained restoration and the recovery of discontinuities". *IEEE Transactions on Pattern Analysis and Machine Intelligence* **14 (3)**, 767–783.

Henderson, F. M., Xia, Z. G., 1997. SAR applications in human settlement detection, population estimation and urban land use pattern analysis: A status report. *IEEE Transactions on Geoscience and Remote Sensing*, **35**, 79–85.

Herralick,R.M., Shanmugam, K., Dinetein, I., 1973. Textural features for image classification. *IEEE Transactions on systems, man and cybernetics.* **SMC-3(6)**, 610-621.

Hore, A., Ziou, D., 2010. Image quality matrices: PSNR vs. SSIM, in *2010 International Conference on Pattern Recognition*, 2366-2369.

Hou, Y., Yang, Y., Rao, N., Lun, X., Lan, J 2011. Mixture model and Markov random field-based remote sensing image unsupervised clustering method, *Opto−Electronics Review* **19(1)**, 83-88.

Huang, C., Townshend, J.R.G., Liang, S., Kalluri, S.N.V., DeFries, R. S., 2002. Impact of sensor's point spread function on land cover characterization assessment and deconvolution, *Remote Sensing of Environment* **96 (3-4)**, 302-314.

Inglada, J., and Mercier, G., 2007. A new statitical similarity measure for chage dtection in multitemporal SAR images and its extension to multiscale change analysis, *IEEE Transaction of Geoscience and Remote Sensing*, **45(05)**, 1432-1445.

Jiang, L., Liao, M., Lin, H., Yang, X.,L., 2009. Synergistic use of optical and InSAR data for urban impervious surface mapping: a case study in Hong Kong, *International Journal of Remote Sensing* **30(11)**, 2781-2796.

Jaynes, E., 1982. On the rationale of maximum-entropy methods. *Proceedings of IEEE* **70**, 939–952.

Jakubowicz, O., 1988, Autonomous reconfiguration of sensor systems using neural nets, *In Proc. SPIE: Sensor Fusion*, 197-203, Orlando, Florida.

Kasyap, R. L., Chellappa, R. 1983. Estimation and Choice of Neighbors in Spatial-Interaction models of Images, *IEEE Transaction on Geoscience and Remote Sensing*, **IT-29 (1)**, 60-72.

Kasyap, R. L., Chellappa, R., Khotanzad, A. 1982. Texture Classification using features derived from random field models, *Pattern Recognition Letters*, **1**, 43-50.

Kasetkasem, T., Arora, M. K., Varshney, P. K., 2005. Super-resolution land cover mapping using a Markov Random Field based approach, *Remote Sensing of Environment* **96 (3-4)**, 302-314.

Kasetkasem, T., Varshney, P. K., 2002. An Image Change Detection Algorithm based on Markov Random Field Model. *IEEE Transactions on Geoscience and Remote Sensing* **40(8)**, 1815-1823.

Krus, F. A., Lefkoff, A. B., Boardman, J. W., Heidebrecht, K. B., Shapiro, A. T., Barloon, P. J., Goetz, A. F.H., 1993. The Spectral Image Processing System (SIPS)- Interactive visualization and analysis of imaging spectrometer data. *Remote Sensing of Environment* **44 (2-3)**, 145-163.

Kong, J.A., Yueh, S.H., Lim, H.H., Shin, R.T., Van Zyl, J.J., 1990. Classification of earth terrain using polarimetric synthetic aperture radar images. Progress In Electromagnetics Research **3**. 327-370

Leinenkugel, P., Esch, T., and Kuenzer, C., 2011. Settlement detection and impervious surface estimation in the Mekong Delta using optical and SAR remote sensing data. *Remote Sensing of Environment*, **115**, 3007–3019.

Li, S. Z., 2009. Markov Random Field Modelling in Image Analysis, thired ed, Springer-Verlag, London.

Liu, Y., Nishiyama, S.,Yano, T., 2004. Analysis of four change detection algorithms in bi-temporal space with a case study, *International Journal of Remote Sensing*, **25(11)**, 2121-2139

Ling, F., Du, Y., Xiao, F.,Xue, H., Wu, S., 2010**.** Super-resolution land-cover mapping using multiple sub-pixel shifted remotely sensed images, *International Journal of Remote Sensing* **31(19)**, 5023–5040.

Magnussen, S., Boudewyn, P., Wulder, M, C., 2004. Contextual classification of Landsat TM images to forest inventory cover types, *International Journal of Remote Sensing* **25**, 2421-2440.

Maselli, F., Conese, C., Filippis, T.D., Norcini, S., 1995. Estimation of Forest Parameters Through Fuzzy Classification of TM Data. *IEEE Transactions on Geoscience and Remote Sensing* **33 (1)**, 77-84.

Melin, P., Castillo, O., 2013. A review on the applications of type-2 fuzzy logic in classification and pattern recognition, *Expert Systems with Applications* **40**, 5413-5423.

Mertens, K.C., Verbeke, L.P.C., Ducheyne, E.I.,De Wulf, R.R., 2003.Using genetic algorithms in sub-pixel map-ping, *International Journal of Remote Sensing*, 24 (21), 4241–4247.

Mertens, K. C., Verbeke, L.P.C., Westra, T., De Wulf, R.R., 2004. Sub-pixel mapping and sub-pixel sharpening using neural network predicted wavelet coefficients. *Remote Sensing of Environment* **91**, 225-236.

Muad., A. M., Foody, G. M., 2012. Impact of Land Cover Patch Size on the Accuracy of Patch Area Representation in HNN-Based Super Resolution Mapping. *IEEE Journal of Selected Topics in Applied Earth Observations and Remote Sensing* **5(5)**, 1418-1427.

Nguen, M. Q., Atkinson, P.M., Lewis, H.G., 2006. Super-resolution mapping using a Hopfield neural network with fused images, *IEEE Transactions on Geoscience and Remote Sensing* **44**, 736–749.

Nishii, R., 2003. A Markov random field-based approach to decision-levelfusion for remote sensing image classification. IEEE Transactions on Geoscience and Remote Sensing, **41(10)**, 2316 – 2319.

Ord, K.1975, Estimation Methods for models of spatial interaction, *Journal of the American Statistical Association*, Vol. *70*, No. 349, pp.120-126.

Pal, M., Mather, P. M., 2004. Assessment of the Effectiveness of Support Vector Machines for Hyperspectral data. *Future Generation Computer Systems* **20 (7)**, 1215-1225.

Park, S.E., Lee, T.H., Hong, S.Y., and Moon, W.M. 2001. Investigation of April 2000 forest fire in Kang-won province, Korea using RADARSAT data, paper presented at In Geoscience and Remote Sensing Symposium. IGARSS '01. international, Sydney, NSW.

Plaza, A., Du, Q., Bioucas-Dias, J.M., Jia, X., Kruse, F. A., 2011. Foreword to the Special Issue on Spectral Unmixing of Remotely Sensed Data, *IEEE Transactions on Geoscience and Remote Sensing* **49(11)**, 4103-4110.

Plaza, A., Martínez, P., Pérez, R., Plaza, J., 2004. A quantitative and comparative analysis of endmember extraction algorithms from Hyperspectral data, *IEEE Transactions on Geoscience and Remote Sensing*, **42(3)**, 650-663.

Qiu, F., Berglund, J., Jensen, J. R., Thakkar, P., Ren, D., 2004. Speckle Noise Reduction in SAR Imagery Using a Local Adaptive Median Filter, *GIScience and Remote Sensing*, **41**. 244-266

Rashed. T., Jurgens. C., 2010 Remote Sensing of urban and suburban areas, Springer Berlin.

Richards, J. A., Jia, X., 2006. Remote Sensing Digital Image Analysis, fourth ed. Springer-Verlag.

Ridd, M. K., 1995. Exploring a V-I-S(Vegetation-impervious surface-soil) Model for Urban Ecosystem Analysis through Remote Sensing: comparative anatomy for cities. *International Journal of Remote Sensing* **16(12)**, 2165-2185.

Rosenield, G. H., Fitzpatrick-Lins, K., Ling, H.S., 1982. Sampling for thematic map accuracy testing. *Photogrammetric Engineering and Remote Sensing* **48**, 131–137.

Sarkar, A., Biswas, M. K., Kartikeyan, B., Kumar, V., Majumder, K. L.,Pal, D. K. 2002. A MRF model-based segmentation approach to classification for multispectral imagery. *IEEE Transactions on Geoscience and Remote Sensing*, **40(5)**, 1102 – 1113

Singh, H., 1989. Digital change detection using remotely-sensed data, *International Journal of Remote Sensing*, Vol, *10*, No, 06, pp. 989-1003.

Small, C. 2001. Estimation of urban vegetation abundance by spectral mixture analysis, *International Journal of Remote Sensing* **22(7)**, 1305-1334.

Sohn, Y., Moran, E., Gurri, F., 1999. Deforestation in North-Central Yucatan (1985-1995): Mapping secondary succession of forest and agricultural land use in sotuta using the cosine of the angle concept. *Photogrammetric Engineering and Remote Sensing* **65(8)**, 947-958.

Solberg , A. H. S., Taxt, T., Jain, A. K., 1996. A Markov Random Field model for classification of multisource satellite imagery. *IEEE Transactions on Geoscience and Remote Sensing* **34(1)**, 100-113.

Solberg , A. H. S., Taxt, T., Jain, A. K., 1997. Texture Fusion and Feature Selection Applied to SAR Imagery. *IEEE Transactions on Geoscience and Remote Sensing* **35(1)**, 475-479

Soergel, U. 2010. Radar remote sensing of urban areas. Heidelberg: Springer, 133–159

Stasoll, M., and Gamba, P. 2008. Spatial Indexes for the Extraction of Formal and Informal Human Settlements From High-Resolution SAR Images, *IEEE Journal of Selected topics in Applied Earth Observation and Remote Sensing*, Vol.1, No. 2, pp.98-106.

Tang, J., Wang, L., Myint, S. W., 2007. Improving urban classification through fuzzy supervised classification and spectral mixture analysis. *International Journal of Remote Sensing* **28(18)**, 4047-4063.

Tatem, A.J.,Lewis, H.G.,Atkinson, P.M., Nixon, M.S., 2001. Super-resolution target identification from remotely sensed images using Hopfield Neural network. *IEEE Transactions on Geoscience and Remote Sensing*, **39**, 781–796.

Tatem, A. J., Hugh, G., Atkinson, P. M., Nixon, M. S. (2002a). Superresolution land cover pattern prediction using a Hopfield neural network. *Remote Sensing of Environment*, **79**, 1 – 14.

Tatem, A. J., Lewis, H. G., Atkinson, P. M., Nixon, M. S. (2002b). Super-resolution land cover mapping from remotely sensed imagery using a Hopfield neural network. In G. M. Foody, & P. M. Atkinson (Eds.), Uncertainty in Remote Sensing and GIS. Chichester' Wiley.

Tison, C., Nicolas, J. M., Tupin, F., & Maitre, H., 2004. A new statistical model for Markovian classification of urban areas in high-resolution SAR images. *IEEE Transactions on Geoscience and Remote Sensing*, 42, 2046–2057.

Tolpekin, V. A., Hamm, N.A.S., 2008. Fuzzy super resolution mapping based on Markov random fields. In: Proceedings of IGARSS 2008 : International Geoscience and Remote Sensing Symposium : Geoscience and remote sensing, the next generation, 6-11 July 2008 Boston, MA, USA. Piscataway : IEEE, 2008. ISBN 978-1-4244-2807-6. pp. 875-878.

Tolpekin, V. A., Stein, A., 2009. Quantification of the effects of land-cover-class spectral separability on the accuracy of Markov-Random-Field-Based Superresolution Mapping. *IEEE Transactions on Geoscience and Remote Sensing* **47(9)**, 3283-3297.

Tso, B., Mather, P. M., 2009. Classification Methods for Remotely Sensed data, second ed. CRC Press, Boca Raton.

Tso, B., Mather, P. M., 1999. Classification of Multisource Remote Sensing Imagey Using a Genetic Algorithm and Markov Random Fields. IEEE Transactions on Geoscience and Remote Sensing **37(3)**, 1255-1260.

Tso, B., Olson, R.C., 2005a. Combining spectral and spatial information into hidden Markov models for unsupervised image classification. *International Journal of Remote Sensing* **26**, 2113-2133.

Tupin, F., Maitre, H., Mangin, J.F.,Nicolas, J.M., Pechersky, E., 1998. Detection of linear features in SAR images: Application to road network extraction. *IEEE Transactions on Geoscience and Remote Sensing* **36**, 434–454.

Ulaby, F. K., Kouyate, F., Brisco, B., and Lee Williams, T.H. 1986, Textural Information in SAR Images, *IEEE Transaction on Geoscience and Remote Sensing*, Vol. *GE-24*, No.2,pp. 235-245.

Wang, F., 1990. Fuzzy Supervised Classification of Remote Sensing Images. I*EEE Transactions on Geoscience and Remote Sensing* **28(2)**, 194-201.

Wang, Z., Bovik, A.C., Sheikh, H. R., Simoncelli, E. P., 2004. Image quality assessment: from error visibility to structural similarity. *IEEE Transactions on Image Processing* **13(4)**, 1-14.

Wang, Z., Li, Q., 2011. Information content weighting for perceptual image quality assessment, *IEEE Transactions on image processing*, **20(5)**, 1185-1198.

Welikanna, D. R., Tolpekin, V. A., Kant, Y., 2008. Analysis of the effectiveness of spectral mixture analysis and the Markov Random Field based Super Resolution Mapping over an Urban Environment, *International Archives of Photogrammetry, Remote Sensing and Spatial Information Sciences* **37 (part B7)**, 641-650.

Welikanna, D. R., Tamura, M., Tolpekin, V. A., Susaki, J., Maki, M., 2012. Improving Markov Random Field based super resolution mapping through fuzzy parameter intergration, ISPRS Annals of the Photogrammetry, Remote Sensing and Spatial Information Sciences, **1(7)**, 183-189.

Winkler, G. (1995).Image analysis random fields and dynamic Monte Carlo methods. New York' Springer-Verlag.

Jiang, L. M., Liao, M. S., Lin, H., and Yang, L. M., 2009. Synergistic use of optical and InSARdata for urban impervious surface mapping: A case study in Hong Kong. *International Journal of Remote Sensing*, **30**, 2781–2796.

Weng, Q., 2012. Remote Sensing of impervious surface in the urban areas: Requirements, methods and trends. *Remote Sensing of Environment*, **117**, 34-49.

Weng, Q., Hu, X., 2008. Medium spatial resolution satellite imagery for estimating and mapping urban impervious surfaces using LSMA and ANN. *IEEE Transactions on Geoscience and Remote Sensing*, **46(8)**, 2397-2406.

Weng, Q., Hu, X., Liu, H., 2009. Estimating impervious surface using linear spectral mixture analysis with multitemporal ASTER images. *International Journal of Remote Sensing* **30(18)**, 4807-4830.

Wood, T. F., Foody, G. M., 1993. Using cover-type likelihoods and typicalities in a Geographic Information System data structure to map gradually changing environments, *Landscape Ecology and GIS*, 141-146.

Woodcock, C.E., Strahler, A.H., and Jupp, D.L.B. 1988a. The Use of Variograms in Remote Sensing:I Scene Models and Simulated Images, *Remote Sensing of Environment*, **25**, 323-348.

Woodcock, C.E., Strahler, A.H., and Jupp, D.L.B. 1988a. The Use of Variograms in Remote Sensing:II Real Digital Images, *Remote Sensing of Environment*, **25**, 349-379.

Wu, C., 2004. Normalized spectral mixture analysis for monitoring urban composition using ETM+ imagery, *Remote Sensing of Environment*, 93(4), 480-492.

Wu, C. and Murray, A.T., 2003. Estimating impervious surface distribution by spectral mixture analysis, *Remote Sensing of Environment*, **84(4),**493-505

Wu, C. and Yuan, F., 2007. Seasonal sensitivity analysis of impervious surface estimation with satellite imagery, Photogrammetric Engineering and Remote Sensing, **73(12),**1393-1401

Xu, M., Chen, H., Varshney, P. K., 2011. An image fusion approach based on Markov Random Fields. *IEEE Transactions on Geoscience and Remote Sensing* **49(12)**, 5116-5127.

Yang, L., Jiang, L., Lin, H.,Liao, M., 2009. Quantifying sub-pixel urban impervious surface through fusion of optical and InSAR imagery. GIScience & Remote Sensing. **46(2)**, 161-171.

Yang, X., Clausi, D. A., 2012. Evaluating SAR sea ice image segementation using edge-preserving region-based MRFs. IEEE Journal of Selected Topics in Applied Earth Observation and Remote Sensing. **5(5)**, 1383-1393.

Jiang, L. M., Liao, M. S., Lin, H., and Yang, L. M., (2009). Synergistic use of optical and InSAR data for urban impervious surface mapping: A case study in Hong Kong. *International Journal of Remote Sensing*, **30**, 2781–2796.

Zadeh, L. A., 1965. Fuzzy Sets. Information and Control **8 (3)**, 338-353.

Zhang, B., Sun, X., Gao, L.,Yang, L., 2011. End member extraction of Hyperspectral Remote Sensing Images based on the Ant Colony Optimization (ACO) algorithm. *IEEE Transactions on Geoscience and Remote Sensing* **49(7)**, 2635-2646.

Zhang, J., Foody, G. M., 2001. Fully-fuzzy supervised classification of sub-urban land cover from remotely sensed imagery: statistical and artificial neural network approach. *International Journal of Remote Sensing*, **22 (4)**, 615-628.

Zhou, W., Bovik, A.C., Sheikh., H.R., and Simoncelli, E.P. 2004, Image Quality Assessment: From Error Visibility to Structural Similarity, *IEEE Transaction on Image Processing*,**13(4)**. 1-14

Tison, C., Nicolas, J. M., Tupin, F., and Maitre, H., 2004. A new statistical model for Markovian classification of urban areas in high-resolution SAR images. *IEEE Transactions on Geoscience and Remote Sensing*, **42**, 2046–2057.